Dual-energy cone-beam CT for proton therapy

Gloria Vilches Freixas

N°d'ordre NNT : 2017LYSEI099

THESE de DOCTORAT DE L'UNIVERSITE DE LYON
opérée au sein de
l'INSA de LYON

Ecole Doctorale N° 160
ELECTRONIQUE, ELECTROTECHNIQUE, AUTOMATIQUE

Spécialité/ discipline de doctorat :
Traitement du Signal et de l'Image

Soutenue publiquement le 27/10/2017, par :

Gloria Vilches Freixas

Dual-energy cone-beam CT for proton therapy

Devant le jury composé de :

Parodi, Katia	Professeur des Universités, Ludwig-Maximilians-Universität, Munich	Rapporteur
Verhaegen, Frank	Professeur des Universités, MAASTRO Clinic, Maastricht	Rapporteur
Dauvergne, Denis	Directeur de Recherche, CNRS, Grenoble	Examinateur
Biston, Marie-Claude	Docteur Centre Léon Bérard, Lyon	Examinatrice
Létang, Jean Michel	Maître de Conférences, INSA-LYON, Villeurbanne	Directeur de thèse
Rit, Simon	Chargé de Recherche, CNRS, Villeurbanne	Co-directeur de thèse

Département FEDORA – INSA Lyon - Ecoles Doctorales – Quinquennal 2016-2020

SIGLE	ECOLE DOCTORALE	NOM ET COORDONNEES DU RESPONSABLE
CHIMIE	**CHIMIE DE LYON** **http://www.edchimie-lyon.fr** Sec : Renée EL MELHEM Bat Blaise Pascal 3e etage secretariat@edchimie-lyon.fr Insa : R. GOURDON	M. Stéphane DANIELE Institut de Recherches sur la Catalyse et l'Environnement de Lyon IRCELYON-UMR 5256 Équipe CDFA 2 avenue Albert Einstein 69626 Villeurbanne cedex directeur@edchimie-lyon.fr
E.E.A.	**ELECTRONIQUE, ELECTROTECHNIQUE, AUTOMATIQUE** **http://edeea.ec-lyon.fr** Sec : M.C. HAVGOUDOUKIAN Ecole-Doctorale.eea@ec-lyon.fr	M. Gérard SCORLETTI Ecole Centrale de Lyon 36 avenue Guy de Collongue 69134 ECULLY Tél : 04.72.18 60.97 Fax : 04 78 43 37 17 Gerard.scorletti@ec-lyon.fr
E2M2	**EVOLUTION, ECOSYSTEME, MICROBIOLOGIE, MODELISATION** **http://e2m2.universite-lyon.fr** Sec : Sylvie ROBERJOT Bât Atrium - UCB Lyon 1 04.72.44.83.62 Insa : H. CHARLES secretariat.e2m2@univ-lyon1.fr	M. Fabrice CORDEY CNRS UMR 5276 Lab. de géologie de Lyon Université Claude Bernard Lyon 1 Bât Géode 2 rue Raphaël Dubois 69622 VILLEURBANNE Cédex Tél : 06.07.53.89.13 cordey@univ-lyon1.fr
EDISS	**INTERDISCIPLINAIRE SCIENCES-SANTE** **http://www.ediss-lyon.fr** Sec : Sylvie ROBERJOT Bât Atrium - UCB Lyon 1 04.72.44.83.62 Insa : M. LAGARDE secretariat.ediss@univ-lyon1.fr	Mme Emmanuelle CANET-SOULAS INSERM U1060, CarMeN lab, Univ. Lyon 1 Bâtiment IMBL 11 avenue Jean Capelle INSA de Lyon 696621 Villeurbanne Tél : 04.72.68.49.09 Fax :04 72 68 49 16 Emmanuelle.canet@univ-lyon1.fr
INFOMATHS	**INFORMATIQUE ET MATHEMATIQUES** **http://infomaths.univ-lyon1.fr** Sec :Renée EL MELHEM Bat Blaise Pascal 3e etage infomaths@univ-lyon1.fr	Mme Sylvie CALABRETTO LIRIS – INSA de Lyon Bat Blaise Pascal 7 avenue Jean Capelle 69622 VILLEURBANNE Cedex Tél : 04.72. 43. 80. 46 Fax 04 72 43 16 87 Sylvie.calabretto@insa-lyon.fr
Matériaux	**MATERIAUX DE LYON** **http://ed34.universite-lyon.fr** Sec : M. LABOUNE PM : 71.70 –Fax : 87.12 Bat. Direction Ed.materiaux@insa-lyon.fr	M. Jean-Yves BUFFIERE INSA de Lyon MATEIS Bâtiment Saint Exupéry 7 avenue Jean Capelle 69621 VILLEURBANNE Cedex Tél : 04.72.43 71.70 Fax 04 72 43 85 28 jean-yves.buffiere@insa-lyon.fr
MEGA	**MECANIQUE, ENERGETIQUE, GENIE CIVIL, ACOUSTIQUE** **http://mega.universite-lyon.fr** Sec : M. LABOUNE PM : 71.70 –Fax : 87.12 Bat. Direction mega@insa-lyon.fr	M. Philippe BOISSE INSA de Lyon Laboratoire LAMCOS Bâtiment Jacquard 25 bis avenue Jean Capelle 69621 VILLEURBANNE Cedex Tél : 04.72 .43.71.70 Fax : 04 72 43 72 37 Philippe.boisse@insa-lyon.fr
ScSo	**ScSo*** **http://recherche.univ-lyon2.fr/scso/** Sec : Viviane POLSINELLI Brigitte DUBOIS Insa : J.Y. TOUSSAINT Tél : 04 78 69 72 76 viviane.polsinelli@univ-lyon2.fr	M. Christian MONTES Université Lyon 2 86 rue Pasteur 69365 LYON Cedex 07 Christian.montes@univ-lyon2.fr

*ScSo : Histoire, Géographie, Aménagement, Urbanisme, Archéologie, Science politique, Sociologie, Anthropologie

To my daughter Claudia

Abstract

Proton therapy is a promising radiation treatment modality that uses proton beams to treat cancer. Current treatment planning systems rely on an X-ray computed tomography (CT) image of the patient's anatomy to design the treatment plan. The proton stopping-power ratio relative to water (SPR) is derived from CT numbers (HU) to compute the absorbed dose in the patient. Protons are more vulnerable than photons to changes in tissue SPR in the beam direction caused by movement, misalignment or anatomical changes. In addition, inaccuracies arising from the planning CT and intrinsic to the HU-SPR conversion greatly contribute to the proton range uncertainty. In clinical practice, safety margins are added to the treatment volume to account for these uncertainties at the expense of losing organ-sparing capabilities. The use of dual-energy (DE) in proton therapy was first suggested in 2009 to better estimate the SPR with respect to single-energy X-ray imaging.

The aim of this thesis work is to investigate the potential improvement in determining proton SPR using DE to reduce the uncertainty in predicting the proton range in the patient. This PhD work is applied to a new imaging device, the Imaging Ring (IR), which is a cone-beam CT (CBCT) scanner developed for image-guided radiotherapy (IGRT). The IR is equipped with a fast kV switching X-ray source, synchronized with a filter wheel, allowing for multi-energy CBCT imaging.

The first contribution of this thesis is a method to calibrate a model for the X-ray source and the detector response to be used in X-ray image simulations. It has been validated experimentally on three CBCT scanners. Secondly, the investigations have evaluated the factors that have an impact on the outcome of the DE decomposition process, from the acquisition parameters to the post-processing. Both image- and projection-based decomposition domains have been thoroughly investigated, with special emphasis on projection-based approaches. Two novel DE decomposition bases have been proposed to estimate proton SPRs, without the need for an intermediate variable such as the effective atomic number. The last part of the thesis proposes an estimation of proton SPR maps of tissue characterization and anthropomorphic phantoms through DE-CBCT acquisitions with the IR. A correction for X-ray scattering has been implemented off-line, and a routine to linearly interpolate low-energy and high-energy sinograms from sequential and fast-switching DE acquisitions has been proposed to perform DE material decomposition in the projection domain with real data. DECT-derived SPR values have been compared with experimentally-determined SPR values in a carbon-ion beam.

Resumé

La proton thérapie est une modalité de traitement du cancer qui utilise des faisceaux de protons. Les systèmes de planification de traitement actuels se basent sur une image de l'anatomie du patient acquise par tomodensitométrie (Computed Tomography en anglais, CT). Le pouvoir darrêt des protons relatif à l'eau (Stopping Power Ratio en anglais, SPR) est déterminé à partir des unités Hounsfield (Hounsfield Units en anglais, HU) pour calculer la dose absorbée au patient. Les protons sont plus vulnérables que les photons aux modifications du SPR des tissus dans la direction du faisceau dues au mouvement, au mauvais positionnement ou aux changements anatomiques. De plus, les inexactitudes issues du CT de planification et intrinsèques à la conversion HU-SPR contribuent énormément à l'incertitude sur la portée des protons. Dans la pratique clinique, des marges de sécurité s'ajoutent au volume de traitement pour tenir compte de ces incertitudes au détriment de la capacité dépargner des tissus sains autour de la tumeur. L'usage de l'imagerie bi-énergie en proton thérapie a été proposé pour la première fois en 2009 pour mieux estimer le SPR du patient par rapport à l'imagerie mono-énergie.

Le but de cette thèse est d'étudier l'amélioration potentielle de l'estimation du SPR des protons en utilisant l'imagerie bi-énergie pour réduire l'incertitude dans la prédiction de la portée des protons dans le patient. Cette thèse est appliquée à un nouveau système dimagerie, l'Imaging Ring (IR), un scanner tomodensitométrique conique (Cone-Beam CT en anglais, CBCT) développé pour la radiothérapie guidée par l'image. L'IR est équipé d'une source de rayons X avec un système d'alternance rapide du voltage, synchronisé avec une roue contenant des filtres de différents matériaux qui permet des acquisitions CBCT multi-énergie.

La première contribution est une méthode pour calibrer les modèles de source et la réponse du détecteur pour être utilisés en simulations d'imagerie X. Deuxièmement, les recherches ont évalué les facteurs qui peuvent avoir un impact sur les résultats du processus de décomposition bi-énergie, des paramètres d'acquisition au post-traitement. Les deux domaines, de la tomodensitométrie et des projections, ont été étudiés, avec un accent particulier sur les approches basées dans le domaine des projections. Deux nouvelles bases de décomposition ont été proposées pour estimer le SPR, sans avoir besoin d'une variable intermédiaire comme le nombre atomique effectif. La dernière partie propose une estimation du SPR des fantômes de caractérisation tissulaire et d'un fantôme anthropomorphique à partir d'acquisitions avec l'IR. Il a été implémenté une

correction du diffusé, et il a été proposé une routine pour interpoler linéairement les sinogrammes de basse et haute énergie des acquisitions bi-énergie pour pouvoir réaliser des décompositions en matériaux avec données réelles. Les valeurs reconstruites du SPR ont été comparées aux valeurs du SPR expérimentales déterminées avec un faisceau d'ions de carbone.

Acknowledgements

Writing this part of the manuscript means the end of this exciting trip of three years that has been the adventure of the thesis. Return to being a student after a few years working has been challenging and difficult at the beginning, but I do not regret the decision. These years spent in Lyon have been enriching from the professional and personal point of view. I would like to acknowledge some people because this thesis is the result of a team work.

First of all, I would like to express my gratitude to Jean-Michel Létang and Simon Rit, my PhD supervisors, for being a winning tandem while guiding me during these years, for teaching me so many things, for the quality of our discussions on the white board and the good mood during the meetings.

My sincere thanks also goes to all the members of the jury for agreeing to evaluate my research work and for the valuable insights, comments and discussions: Prof. Katia Parodi and Prof. Frank Verhaegen as rapporteurs, Dr. Denis Dauvergne as president of the jury and reviewer, and Dr. Marie-Claude Biston as reviewer.

I would like to thank David Sarrut, who leads the CLB-Team 4 of CREATIS, for the opportunity to work within this multidisciplinary team. I warmly thank all CREATIS colleagues and friends for all the discussions and good moments we shared inside and outside working hours, with a special mention to Cath, Brent, Eugenia, Adrien, Thomas "2", Marie, Cyril, Loriane, Ilaria, Edwardo, Benoît, Thomas "1", Fabien and Nicolas.

I would also like to thank all the people from medPhoton, especially: Phil Steininger, Peter Keuschnigg, Daniel Kellner, Heinz Deutschmann and Ivan Messner, for the fruitful discussions and explanations of the Imaging Ring, for their technical support, for their help during the experimental sessions in Salzburg and Wienner-Neustad and for the *Augustiner* beers we shared afterwards.

A special thanks also to Vicki Taasti from Aarhus for sharing the same passion for dual-energy as I do and for the nice discussions we had (and still have) on its application in proton therapy.

Last but not least, I would like to thank my parents for always believing in me and for teaching me the value of effort. Thanks also to the artist of the family, Judit, for

having made a special drawing for the PhD book cover. Thanks also to my family in law for always supporting me, especially in the final stretch. *Merci*, *Thank you*, *Gràcies*, *Gracias* and *Grazie* to all the family and friends that I did not explicitly mention, but who are also part of this success.

In the end of this period I have two babies: the dual-energy thesis and a lovely daughter that changed our lives, who let me write 95% of the thesis before coming into the world. Gràcies Claudia per existir. I would like to finish with a special and big thank you to my life-partner for his endless support, help and love, without whom anything would have been possible: Gràcies Xavi.

Contents

List of Tables

List of Figures

Acronyms

AF Adult Female

ALARA As Low As Reasonably Achievable

AMK Alvarez and Macovski, and Kanematsu

ANR Agence Nationale de la Recherche

APT Adaptive Proton Therapy

ASIC Application-Specific Integrated Circuit

BMD Basis Material Decomposition

BP Bragg Peak

CBCT Cone Beam Computed Tomography

CNR Contrast-to-Noise Ratio

CREATIS Centre de Recherche En Acquisition et Traitement de l'Image pour la Santé

CSDA Continuous Slowing Down Approximation

CT Computed Tomography

CTV Clinical Target Volume

CV coefficient of variation

DDD Depth Dose Distribution

DDS Dose Delivery System

DE Dual-Energy

DECT Dual-Energy Computed Tomography

DER Dual-Energy Radiography

DEXTER Dual-Energy X-ray imaging for TargEting Radiotherapy

DLD Dual-Layer Detector

DSCT Dual-Source CT

FBP Filtered-Back Projection

FFD Fixed-Forced Detection

FKVS Fast Kilo-Volt Switching

FOV Field Of View

FWF Austrian Science Fund or Fonds zur Förderung der wissenschaftlichen Forschung

GTV Gross Tumor Volume

HU Hounsfield Units

HVL Half-Value Layer

ICRP International Commission on Radiological Protection

IGRT Image Guided Radiotherapy

IMPT Intensity Modulated Proton Therapy

IMRT Intensity Modulated Radiation Therapy

IR Imaging Ring

kV Kilo-voltage

MC Monte Carlo

MCS Multiple Coulomb Scattering

MLP Most Likely Path

MRI Magnetic Resonance Imaging

NDT Non-Destructive Testing

NTCP Normal Tissue Complication Probability

OAR Organ At Risk

PCD Photon-Counting Detector

PET Positron Emission Tomography

PMU Paracelsus Medical University

PPS Patient Positioning System

PSF Point-Spread Function

PTCOG Particle Therapy Cooperative Group

PTV Planning Target Volume

QA Quality Assurance

radART Institute for Research and Development on Advanced Radiation Technologies

RBE Relative Biological Effectiveness

RED Relative Electron Density

RMS Root-Mean Squared

RMSE Root-Mean Squared error

ROI Region-Of-Interest

RT Radiation Therapy or Radiotherapy

SE Single-Energy

SECT Single-Energy Computed Tomography

SEM Standard Error of the Mean

seTLE split exponential Track Length Estimator

SI International System of Units

SK Saito and Kanematsu

SKS Scatter Kernel Superposition

SNR Signal-to-Noise Ratio

SOBP Spread Out Bragg Peak

SPP Stopping Power Parametrization

SPR Stopping Power Ratio

TCP Tumor Control Probability

TFT Thin Film Transistor

TPS Treatment Planning System

VM Virtual Monochromatic

VMAT Volumetric Modulated Arc Therapy

WEPL Water Equivalent Path Length

Introduction

Computed tomography (CT) images provide the spatial distribution of the linear attenuation coefficient of the object being imaged. Two objects having different mass density and elemental composition might exhibit the same photon attenuation value and, therefore, cannot be distinguished in a CT scan. However, by exploiting the dependence on energy of the attenuation coefficient of tissues, two materials might be differentiated when recording the attenuation at different beam spectra. This is the basic principle of dual-energy imaging, which was already mentioned in 1973 by Sir Hounsfield in the paper describing the invention of the CT scanner.

Proton therapy is a cancer treatment modality that uses proton beams to damage cancer cells, preventing them from growing and dividing. In principle, the finite and controllable range of protons (by adjusting their kinetic energy) and the reduced integral patient dose with respect to photons, for the same target dose, allow for a more conformal radiotherapy. Current treatment planning systems rely on an X-ray CT image of the patient's anatomy to design the treatment plan. The proton stopping-power ratio relative to water (SPR) is derived from CT numbers (HU) to compute the absorbed dose in the patient. Protons are more vulnerable than photons to changes in tissue SPR in the beam direction caused by movement, misalignment or anatomical changes. In addition, inaccuracies arising from the planning CT and intrinsic to the HU-SPR conversion greatly contribute to the proton range uncertainty. In clinical practice, safety margins are added to the treatment volume to account for these uncertainties at the expense of losing organ-sparing capabilities. The use of dual-energy imaging for proton treatment planning was first proposed in 2009 to better estimate the patient SPR with respect to single-energy imaging.

In this work, the main motivation has been to investigate the potential improvement in determining proton SPR using dual-energy to reduce the uncertainty in predicting the proton range in the patient. This PhD work is applied to a new imaging device, the Imaging Ring (IR), which is a cone-beam CT (CBCT) scanner developed for image-guided radiotherapy (IGRT). The IR is equipped with a fast-kV switching X-ray source, synchronized with a filter wheel, allowing for multi-energy CBCT imaging.

This work is organized as follows: Chapter 1 starts out by providing an introduction

to radiotherapy developments in the last century, an overview of proton-matter interactions and the clinical rationale for proton therapy. We then proceed in describing the role of CT in radiation treatment planning, an overview of photon-matter interactions, the sources of uncertainty in proton therapy and an outline of the existing imaging modalities to minimize these uncertainties.

To set the basis for further discussion, Chapter 2 describes the principles and technical approaches to perform dual-energy imaging, provides an overview of the clinical and industrial applications with special mention to radiotherapy applications, and a review of the existing decomposition methods for material segmentation and dose calculation in both the image- and the projection- domain.

Chapter 3 then deals with the first objective of this PhD work, that is to provide a model for the source and the detector response of the IR system. A procedure to calibrate and validate kilo-voltage CBCT models is described, as well as a procedure to simultaneously assess the validity of the source and the detector response models. In addition, a scatter-mitigation technique for the IR data, implemented off-line, is illustrated.

We then proceed, in Chapter 4, in reviewing the existing methods to determine the SPR from dual-energy data and we compared them with two novel approaches. We also compared image- and projection-based decomposition domains in terms of SPR accuracy. The last part of this chapter shows the results of the second objective of this PhD work: the estimation of proton SPR maps of tissue characterization and anthropomorphic phantoms through dual-energy CBCT acquisitions with the IR system.

Chapter 5 deals with the third objective of the thesis, that is to investigate the main factors that would have an impact on the outcome of the dual-energy decomposition process, from the acquisition protocols to the post-processing.

Chapter 6 reviews some of the works that have studied the influence of the mean excitation energy of human tissues on the proton range, and evaluates the feasibility of an experimental setup to extract volumetric distributions of the I-value of patients by combining two tomographic imaging modalities: proton CT and dual-energy CT.

This document ends with a synthesis of the conducted work and the future prospects.

Chapter 1

Thesis context

Contents

The main objective of this thesis was to improve the estimation of the range of protons in patients using Dual-Energy Computed Tomography (DECT) for proton therapy treatment planning. This thesis was part of the Dual-Energy X-ray imaging for TargEting Radiotherapy (DEXTER) project, a collaboration between Institute for Research and Development on Advanced Radiation Technologies (radART) (Salzburg, Austria) and Centre de Recherche En Acquisition et Traitement de l'Image pour la Santé (CREATIS) (Lyon, France) co-funded by Agence Nationale de la Recherche (ANR) and Austrian Science Fund or Fonds zur Förderung der wissenschaftlichen Forschung (FWF). Most of the work has been conducted in the Léon Bérard Cancer Center in Lyon.

The aim in this chapter is to describe the key elements for establishing the context of the Ph.D. thesis:

- radiotherapy developments in the last century, proton-matter interactions, clinical rationale for proton therapy;
- radiation treatment planning and the role of computed tomography, photon-matter interactions, sources of uncertainty in proton therapy, imaging modalities to minimize range uncertainties and to verify proton range in the patient.

1.1 Clinical context

1.1.1 Radiotherapy: from X-rays to particle therapy

Radiotherapy, also known as radiation therapy or radiation oncology, is a cancer treatment modality that uses ionizing radiation to damage cancer cells, preventing them from growing and dividing. The most limiting factor in radiotherapy is the normal tissue radiation tolerance. To ensure the success of radiotherapy, the main goal is to conform the dose, i.e., to deliver the maximum radiation dose to the tumor while minimizing the dose delivered to the surrounding healthy tissues.

Radiotherapy came out shortly after the discovery of X-rays by Wilhelm Röntgen in 1895. A year later, in 1896, Henri Becquerel discovered that certain elements spontaneously emit energetic particles or radiation from matter, property named spontaneous radioactivity. For this discovery, Henri Becquerel together with Marie Curie and Pierre Curie received the Nobel Prize in Physics in 1903. One of their findings was the cutaneous damage induced by the continuous exposition to radium. This evidence of biological and harmful effects suggested that radiation could be used to treat diseases [Slater, 2012]. A

new era of research began. In the following decades, the growing interest in understanding radiation response, radiobiological damage and how to optimize the use of radiation for therapeutic purposes yield to tremendous developments in radiotherapy.

X-rays or gamma-rays (cobalt sources) were the first radiation sources employed in radiotherapy. In 1940, electron beam therapy became also a therapeutic option. Due to the low energy available, a limitation of the first X-ray machines was the difficulty to treat deeply-seated tumors without producing excessive skin reactions. In the 1960s, low energy X-ray machines were substituted by high energy mega-voltage (MV) treatment units, known as linear accelerators or linacs. Linacs were also suited to produce electron beams ideal to treat superficial tumors up to 4 cm depth.

The introduction of new imaging modalities, such as Computed Tomography (CT) and Magnetic Resonance Imaging (MRI) in the 1970s and Positron Emission Tomography (PET) in the 1980s, along with computer-assisted Treatment Planning System (TPS), allowed large improvements. Treatment planning shifted from 2D to 3D and CT-based planning improved target tumor and Organ At Risk (OAR) delineation, allowing dose distributions better conformed to the tumor [Thariat et al., 2012]. Image Guided Radiotherapy (IGRT) started in the 1980s with the introduction of portal imaging.

In concomitance with technological developments, the improved knowledge in radiobiology introduced dose fractionation schemes, which have proven to increase survival rates and to reduce radiation side effects. With the advent of linacs equipped with a gantry, a rotating structure around an horizontal axis, multiple beams pointing to the target center were used in clinical routine to irradiate deep-seated tumors and to better conform the dose.

Another development towards delivering therapeutic doses with higher precision, and thus avoiding normal tissue irradiation, was the introduction of Intensity Modulated Radiation Therapy (IMRT) in the late 1990s and Cone Beam Computed Tomography (CBCT) at the beginning of the XXI century. Volumetric Modulated Arc Therapy (VMAT) was introduced in the last years as an evolution of IMRT. The so-called mega-voltage era is still in continuous technological development looking for machines and techniques to produce better conformed dose plans.

In the context of improving radiotherapy by better targeting the tumoral volume and sparing the surrounding tissues, the performance of other particle beams such as neutrons, protons, pions or heavier ions early aroused interest [Amaldi and Kraft, 2005]. This led to the birth of particle therapy.

Particle therapy or hadron therapy encompasses those techniques of external radiotherapy that use hadrons, non elementary particles composed of quarks such as neutrons, protons or light nuclei, to irradiate solid tumors.

In 1938, low energy neutrons were the first hadrons used in radiotherapy. It was observed in clinical trials that neutrons produced better tumor control rate, especially for radio-resistant tumors, thanks to the high Relative Biological Effectiveness (RBE)[1]

[1]The Relative Biological Effectiveness (RBE) of a given radiation is the ratio of dose of reference

[Stone et al., 1940]. Nevertheless, as the depth-dose distribution of fast-neutrons is similar to that of X-ray beams (see Figure 1.1), the high biological effective dose behaved as a double-edge sword causing severe side effects due to the difficulty of sparing healthy tissues. Radiotherapy with neutrons was abandoned until mid-1970's where the interest in fast neutrons was renewed.

Between the 1940s and the 1970s, physicists and biologists demonstrated the superiority of charged particle beams with respect to photon and neutron beams [Slater, 2012]. Negative pions were then studied. Despite an increase of dose at the end of the range, pions were soon abandoned mainly due to the difficulty to produce pions and also because clinical trials showed no improved tumor control rate with respect to conventional photon therapy.

In 1946, Robert Wilson proposed the clinical use of proton and carbon ion beams [Wilson, 1946]. He observed that these charged particle beams presented an inverse depth-dose profile with respect to X-rays, with a maximum dose deposit at the end of their range, near the so-called Bragg Peak (see Figure 1.1). The first treatment with proton beams was carried out at the Lawrence Berkeley National Laboratory (Berkeley, California, U.S.A.) in 1954. Three years later, in 1957, treatments with helium beams started. Other particle beams, such as neon ions, were used for treatment in 1975. Heavy ion therapy in Berkeley was done at the Bevalac, a combination of linear accelerator with a Bevatron, i.e. a weakly focusing synchrotron. Other laboratories accelerated particle beams using a cyclotron, which produces a fixed beam energy, and passive shaping systems such as energy absorbers, scatterers, compensators and collimators were used to shape the beam to the target volume.

Most of the clinical data available with carbon ion beams derive from the clinical activity started in 1994 at the Heavy Ion Medical Accelerator Center (HIMAC, Chiba, Japan), using the passive shaping technique. In 1997, the active beam delivery technique, which consists in using magnetic fields to deflect hadron beams across the treatment volume, was started at the Gesellschaft für Schwerionenforschung (GSI, Darmstadt, Germany) and at the Paul Scherrer Institute (PSI, Villigen, Switzerland).

One advantage of particle beams with respect to photons is the possibility to better spare normal tissues when treating deep-seated tumors or close to organs at risk [Paganetti, 2011]. Consequently, in the last twenty years, interest in proton and carbon ion therapy has significantly increased worldwide. At present[2], 61 proton facilities and 10 carbon ion therapy facilities are in operation. Around 40 proton facilities and 3 carbon ion facilities are under construction, and more than 15 proton facilities are in the planning stage worldwide. The Particle Therapy Cooperative Group (PTCOG) reported that, by the end of 2015, 131240 patients had been treated with protons and 19376 patients had been treated with carbon ions worldwide[3]. Despite some clinically proved advantages [Tsujii et al., 2004; Okada et al., 2010], the main reason of the limited

radiation (photons) to that of test (e.g. neutrons) required to produce a defined biological response. This quantity is used to compare the biological effects of different radiation sources.

[2]According to www.ptcog.ch. Last update: November 2016.

[3]According to www.ptcog.ch. Last update: December 2015.

spread of heavy ion therapy around the world is cost-efficiency. The cost of building such a facility, generally a synchrotron, is two to three times higher than building a proton facility.

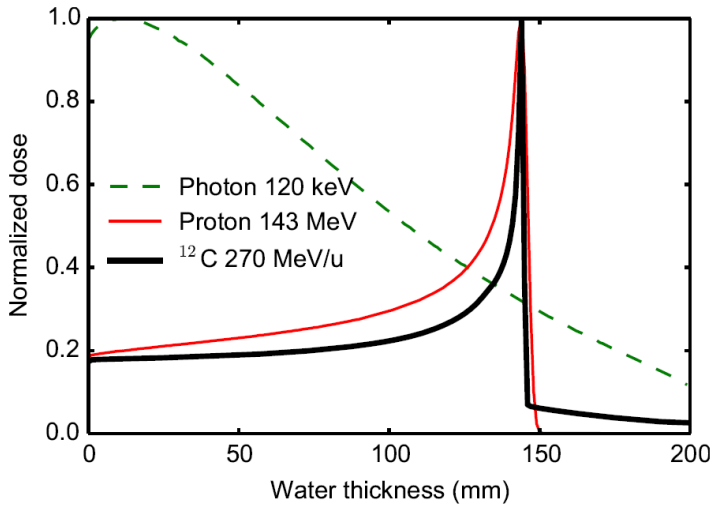

Figure 1.1: Normalized central axis depth dose profiles from several particle beams. Proton and carbon ion beams exhibit relatively low entrance dose, followed by a region where dose increases slowly with depth (*plateau* region), until reaching the maximum dose deposit in depth, in the so-called *Bragg peak*. Photons present a maximum dose deposit close to the patient skin and afterwards an exponential decay. Protons present a sharp edge at the end of the range whereas carbon ions show a sharper Bragg peak than protons, and a non negligible tail due to nuclear fragmentation. Figure from [Quiñones, 2016].

1.1.2 Physics of proton interactions in matter

A proton is a subatomic particle with a positive charge. A therapeutic proton beam has an initial kinetic energy comprised between 60 MeV and 250 MeV. In this energy range, the mechanisms that describe the energy transfer from the proton beam to the traversed matter are:

1. *Energy loss* in inelastic Coulomb interactions with electrons of the medium: excitation and ionization of target atoms.

2. *Multiple Coulomb scattering* due to elastic interactions with the target nuclei.

3. *Elastic and inelastic nuclear interactions* with the target nuclei.

In general terms, protons continuously lose kinetic energy through frequent collisions with atomic electrons; while most of the changes of direction are due to repulsive elastic Coulomb interactions with the atomic nuclei. Inelastic nuclear interactions between protons and atomic nuclei also occur but are less frequent. A schematic illustration of the mechanisms that govern proton interactions with matter in the therapeutic energy range is shown in Figure 1.2 and a more detailed description of each mechanism is provided in the following subsections.

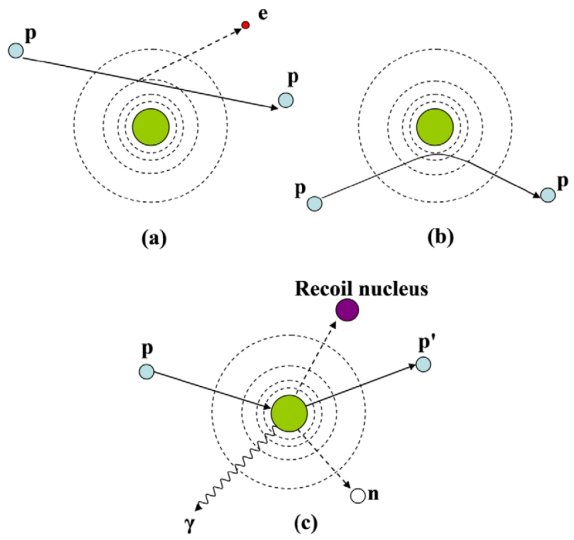

Figure 1.2: Illustration of proton-matter interaction mechanisms: a) energy loss via inelastic Coulomb interactions with electrons; b) deflection of the proton trajectory via repulsive elastic Coulomb interactions with the atomic nuclei; c) absorption of the primary proton by the nucleus and creation of secondary particles via inelastic nuclear interactions (p: proton, e: electron, n: neutron, γ: gamma rays). Figure from [Newhauser and Zhang, 2015].

1.1.2.1 Energy loss

Protons primarily lose kinetic energy due to frequent inelastic Coulomb interactions with the electrons of the medium. When a proton traverses matter, it collides with electrons causing the excitation and ionization of atoms. The range of the secondary electrons produced is less than 1 mm (except delta-rays [Newhauser and Zhang, 2015]), so dose is locally absorbed along the proton path. Protons travel following an almost straight line because there is no significant deflection of protons by electrons. As proton mass is much higher than electron mass[4], protons lose a small fraction of their energy

[4] $\mu = m_p/m_e = 1836.15267389(17)$ is the proton-electron mass ratio which is the rest mass of the proton m_p divided by that of the electron m_e. Retrieved from *The NIST Reference on Constants, Units, and Uncertainty.* US National Institute of Standards and Technology. November 2016.

in each interaction causing a continuous slowing down.

The *linear stopping power* (S) is the quantity that defines the rate of energy loss (dE) of a proton beam per unit length (dx) in a homogeneous material, expressed in MeV/cm. S increases as protons slow down (valid in the high velocity regime, i.e. $v >> v_e$, where v is the velocity of the projectile and v_e the velocity of the electrons of the medium) and it depends on the kinetic energy and the target material. The stopping power is defined for a beam, not for a single particle.

Another useful quantity, independent of the mass density ρ, is the *mass stopping power* (S/ρ) expressed in MeV/g·cm^2 defined as

$$\frac{S}{\rho} = -\frac{1}{\rho}\left\langle \frac{dE}{dx} \right\rangle . \tag{1.1}$$

The *mean electronic energy loss* of charged particles in a homogeneous medium is described by the Bethe-Bloch equation ([Bethe, 1930; Bloch, 1933]) which is valid for projectile energies above $\sim$ 1 MeV/u:

$$S = -\left\langle \frac{dE}{dx} \right\rangle = 4\pi r_e^2 m_e c^2 \rho_e \frac{z^2}{\beta^2}\left[\ln \frac{2m_e c^2 \beta^2}{I(1-\beta^2)} - \beta^2 - \frac{\delta}{2} - \frac{C}{Z}\right] \tag{1.2}$$

where r_e is the classical electron radius, m_e is the mass of an electron, c is the speed of light in vacuum, ρ_e is the electron density of the medium, z is the charge of the projectile ($z = 1$ for protons), $\beta = v/c$ where v is the velocity of the projectile, Z is the atomic number of the medium, I is the mean excitation energy of the medium, $\delta/2$ is a density correction term and C/z is a shell correction term. Correction terms were added to the initial formulation to account for the quantum mechanical effects. The density effect term $\delta/2$ is important at high energies (typically outside the therapeutic range, i.e. 1% for 500 MeV protons [ICRU, 1993]) and it corrects for the fact that the electric field of the projectile tends to polarize the target atoms along its path. As a consequence, electrons far from the projectile path would feel less the electric field of the projectile and would contribute less to the energy loss, reducing the stopping power. The shell correction term C/Z is important at very low energies, it depends on the medium and on the projectile velocity [Leo, 1994], and corrects for the assumption that target electrons are at rest. When the projectile velocity is comparable or smaller than the orbital velocity of the bound electrons, the probability that the projectile collides with the orbital electrons decreases and so does the stopping power (i.e. up to 6% for protons between 1 MeV and 100 MeV [Ziegler, 1999]).

Due to the loss and capture of electrons from the target when the projectile velocity is comparable to the electron orbital velocity ($\simeq$ 0.008 c), to extend the Bethe-Block formula to lower energies, the projectile charge z is replaced by an *effective charge* z_{eff}. The dependency of z_{eff} with the projectile velocity can be approximated by the Barkas formula [Barkas and Evans, 1963]:

$$z_{eff} = z(1 - e^{-a\beta z^{-2/3}}) \tag{1.3}$$

where $a \simeq 125$.

The quasi-continuous energy loss determines the proton range in the patient (see section 1.1.3.2). Looking at Equation 1.2, it is easy to understand the typical depth dose distribution of charged particle beams (see Figure 1.1). Energy loss is governed by the projectile's characteristics and the properties of the absorber material. In particular, energy loss is proportional to the inverse square of the projectile's velocity ($1/\beta^2$) and to the square of its charge z, but it is independent of the projectile's mass. In other words, the energy loss rate increases as the kinetic energy of the particle decreases along the penetration depth (*plateau* region), followed by a steep rise at low residual energies at the end of the particle range (*Bragg peak* region). At very low energies, the effective charge z_{eff} is rapidly reduced according to Equation 1.3, causing an abrupt drop of the stopping power (*sharp edge*). Moreover, the energy loss rate is directly proportional to the density of electrons in the absorber medium (ρ_e) (see section 1.1.3.4) and it also depends on the logarithm of the mean excitation energy I of the target (see section 1.1.3.5).

Clinical applications require to deliver a uniform dose to the target volume. This is achieved by adding fluence-weighted proton beams of different energies –Bragg peaks at different depths– which results in a Spread Out Bragg Peak (SOBP) (see Figure 1.3). As cyclotrons produce a fix beam energy, a range modulator wheel is used to adjust Bragg peak positions in depth; whereas synchrotons produce beams of variable energy.

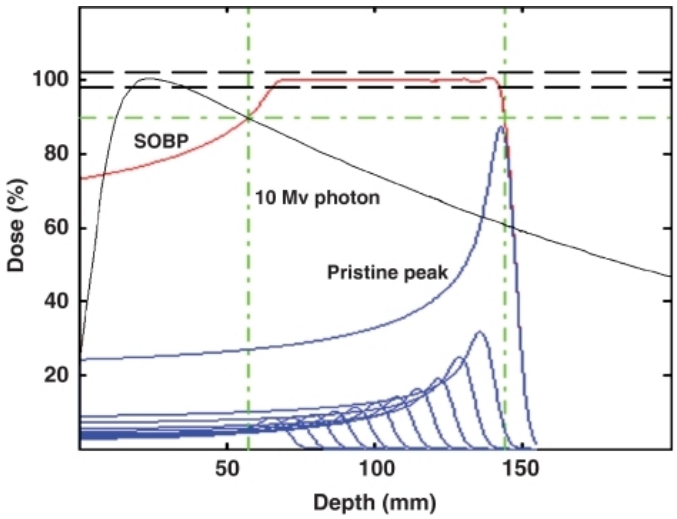

Figure 1.3: Depth dose distribution for a Spread Out Bragg Peak (SOBP, red) generated by adding fluence-weighted pristine Bragg peaks (blue), and a 10 MV photon beam (black). Figure from [Levin et al., 2005].

1.1.2.2 Multiple Coulomb scattering

When protons slow down and pass close to the target nuclei, they also interact with the electromagnetic Coulomb field of target nuclei (repulsive force). In these collisions, protons lose little energy, but change direction due to multiple scattering with atomic nuclei. A lateral divergence of the beam is observed after many scattering events ($\geqslant$20). The beam angular distribution with respect to the incident direction after traversing a certain thickness of material can be interpreted as the summation of small angle deflections (highly probable) and large angle deflections (rare events) [Leo, 1994].

For small deviation angles, the most complete theory was proposed by Molière in 1948. Assuming that scattered protons are mainly emitted at small deflection angles ($\sin\theta \approx \theta$) the beam angular deviation can be approximated by a Gaussian distribution [Gottschalk, 2004]. Based on Molière's theory, Highland in 1978 derived a formula to quantify the scattering angle θ_0 after traversing a thickness L of material (with $L \ll$ proton range) expressed in radians:

$$\theta_0 = \frac{14.1 \text{ MeV}}{pv}\, z \sqrt{\frac{L}{X_0}} \left[1 + \frac{1}{9}\log_{10}\left(\frac{\mathrm{L}}{\mathrm{X_0}}\right)\right] \tag{1.4}$$

where z, p and v are the charge ($z = 1$ for protons), the initial momentum and the velocity of the projectile, respectively. X_0 is the radiation length of the target material, which is a value characteristic of electromagnetic processes at high energy (in particular bremsstrahlung), i.e. it is proportional to Z^2; and L is the target thickness in the same units (g/cm^2).

As $\theta_0 \propto 1/pv$, the scattering angle θ increases as the kinetic energy T of the proton beam ($pv \simeq 2T$) decreases. To reach the same depth, massive particles (e.g. carbon ion beams) require more kinetic energy than lighter ones (e.g. protons). Consequently, at a given penetration depth, carbon ion beams show little lateral scattering, while protons exhibit an angular spread approximately three times larger. Moreover, the scattering angle is inversely proportional to $X_0^{1/2}$ of the traversed material.

Multiple Coulomb Scattering (MCS) is responsible for the lateral divergence of the beam (lateral penumbra) and of the growth of the lateral spot size of a scanned beam in depth.

1.1.2.3 Nuclear interactions

Besides the electromagnetic mechanisms hereabove described, protons can undergo elastic and inelastic nuclear reactions with the atomic nuclei. In the therapeutic energy range, these interactions contribute significantly less to energy loss than electromagnetic processes. In elastic interactions, the incident projectile scatters off the target nucleus, with the total kinetic energy conserved. In inelastic interactions, the proton is absorbed by the nucleus, whereas the nucleus is irreversibly transformed (i.e. left in an excited state and then fragmented). Most of the secondary particles resulting from proton-nucleus interactions are protons, neutrons, γ rays, heavy fragments such as alphas,

short-lived isotopes such as positron emitters, e.g. predominantly ^{15}O and ^{11}C for proton irradiations, and recoiling residual nuclei. Active research is being conducted to test if the distribution of γ rays (prompt gammas), and ^{15}O and ^{11}C isotopes can be used for *in vivo* range verification during proton treatment delivery (see section 1.2.5.2) [Knopf and Lomax, 2013].

The main consequence of nuclear interactions is a gradual decrease of the number of primary protons before reaching the depth of the Bragg Peak (i.e. about 1% of the incident protons are removed from the beam per centimeter of range in water [Lomax, 2009]). In other words, at a depth of 20 cm in water, the primary proton fluence is reduced by about 20%.

1.1.3 Quantities of interest

In this section, some useful quantities that will be referenced to in the rest of the manuscript are defined.

1.1.3.1 Energy and range straggling

Statistical fluctuations in the proton-electron interactions (see section 1.1.2.1) result in small variations in the energy loss rates of individual protons. This phenomenon is known as *range or energy straggling* and results in a broadening of the measured Bragg peak with respect to the Bragg peak determined with Equation 1.2. The range straggling depends on the mass of the projectile and it varies approximately as the inverse of the square root of the particle mass. Thus, Bragg peaks for carbon ion beams are narrower in the direction of the beam compared with protons beams (see Figure 1.1). Moreover, range straggling increases with the penetration depth in a given material, resulting in Bragg peaks of larger width and smaller height for higher initial energy (see Figure 1.4).

1.1.3.2 Average range

The range is intrinsically an average quantity, defined for a beam and not for individual protons. The range is defined as the depth at which half of the protons of a beam have come to rest [Newhauser and Zhang, 2015] (see Figure 1.5). For a monoenergetic beam, the depth at which 50% of the protons have stopped coincides with the 80% fall-off position [Paganetti, 2012].

To a good extent (if neglecting lateral scattering), proton path can be approximated by a straight line. Under this assumption and the assumption that protons lose energy in a continuous manner, i.e. the Continuous Slowing Down Approximation (CSDA), the range R can be computed as:

$$R(E) = \int_0^E S(E')^{-1} dE' \tag{1.5}$$

where E is the proton initial kinetic energy. This equation gives the length of proton path which, for most clinical situations, is a good approximation of the *average proton range*.

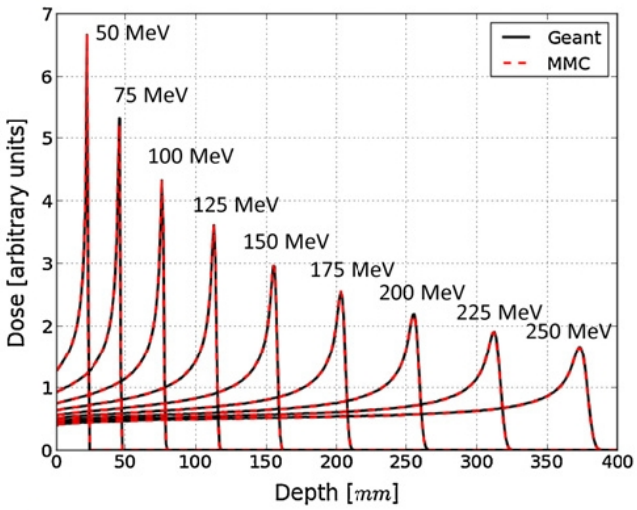

Figure 1.4: Depth dose distributions in water for different proton beam energies. Figure from [Fix et al., 2013]. Range straggling increases with the penetration depth. MMC: macro Monte Carlo.

1.1.3.3 Absorbed dose

The *absorbed dose* is a quantity that measures the energy deposited in a medium by primary and secondary particles (e.g. electrons, see section 1.1.2.1) per unit mass. In most situations, secondary electron equilibrium prevails, i.e., the energy carried in and out of a volume of interest by secondary electrons is on average the same. Under this assumption and discarding nuclear interactions, the macroscopic dose D delivered to a medium of density ρ by a fluence ϕ of mono-energetic charged particles is proportional to the mean energy loss of the particle beam:

$$D = \frac{\phi}{\rho} \left\langle \frac{dE}{dx} \right\rangle \tag{1.6}$$

1.1.3.4 Electronic density

The *electronic density* ρ_e, expressed in electrons/cm^3, of a compound or mixture composed of N elements is given by:

$$\rho_e = \rho \, N_A \sum_{i=1}^{N} \omega_i \frac{Z_i}{A_i} \tag{1.7}$$

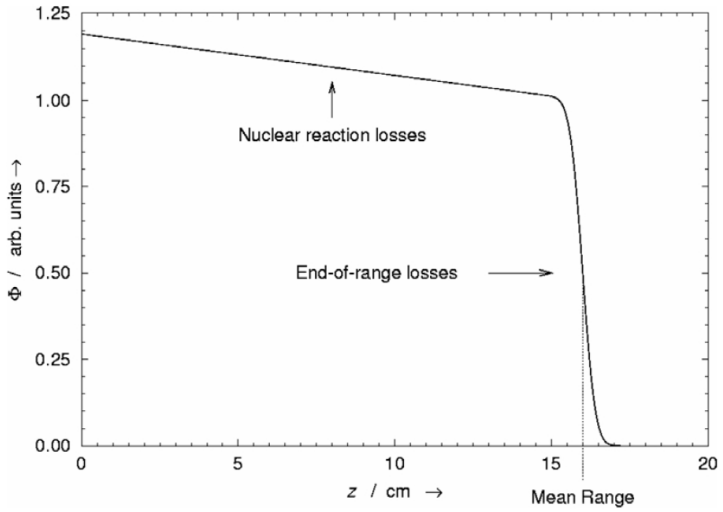

Figure 1.5: Proton beam fluence ϕ (in arbitrary units) as a function of depth z in water. Nuclear interactions are responsible of the gradual decrease of the number of primary protons. The sharp distal edge is caused by ions being absorbed by the medium when running out of energy. Range straggling and stochastic energy loss variations of individual protons within the beam results in the sigmoid shape of the distal fall-off. Figure from [Newhauser and Zhang, 2015].

where ρ is the mass density (in g/cm^3) of the compound, N_A is the Avogadro's number[5], ω_i, Z_i and A_i are the fraction by weight, the atomic number and the molar mass (in g/mol) of the i-th element, respectively.

Z/A varies by about 16%, from 0.5 to 0.42, for the main elements present in the human body. Hydrogen is an exception with 0.99, but the concentration of hydrogen in the human body is low (about 10%) and nearly uniform thorough the body [ICRU, 1992].

1.1.3.5 Mean excitation energy

The *mean excitation energy*, sometimes referred to as *average ionization potential* or *I-value*, expressed in electron volts (eV)[6], is defined as the mean energy required to excite an atomic electron from its initial ground state E_0 to an excited state E_i. Its value

[5]The Avogadro's number or constant represents the number of constituent particles, usually atoms or molecules, that are contained in one mole of substance. In the International System of Units (SI) it has the value of $6.022140857(74) \times 10^{23}$, expressed in atoms or molecules per mol.

[6]An electron volt (eV) is the amount of energy gained by an electron moving across an electric potential difference of one volt: $1\ \text{eV} = 1.6 \times 10^{-19}$ J.

is usually the energy difference between final and initial state: $I = \langle E_i - E_0 \rangle$.

The knowledge of the mean excitation energy or I-value of a medium is necessary to compute the stopping power (Equation 1.2) and, therefore, the range (Equation 1.5) of charged particle beams penetrating the medium. The I-value is a quantity independent of the properties of the projectile, and it only depends on the properties of the medium [ICRU, 1993].

Atomic electrons bounded to atomic nuclei can be described as individual oscillator systems with a characteristic resonance frequency. The excitation energy spectrum of atoms or molecules is discontinuous and each energy transition– from its ground state to a certain excited state– (or oscillator frequency) has a certain probability (named *dipole oscillator strength*). Based on this representation, Fano [Fano, 1964] defined the mean excitation potential as:

$$\ln I = \sum_i f_i \ \ln E_i \tag{1.8}$$

where f_i and E_i are the dipole oscillator strength and the excitation energy of the transition from its ground state to the excited state i, respectively. Most elements have excitation energies (E_i) in the range 10 eV to 1000 eV and the difficulty of this computation relies on the knowledge of oscillator strengths (f_i) in this energy range [Hsu, 1979].

Bloch [Bloch, 1933] suggested the semi-empirical formula

$$I(Z) = k \cdot Z \tag{1.9}$$

where $k \simeq$15 eV for low Z absorbers and $k \simeq$10 eV for high Z absorbers, which applies quite well for high Z atoms ($Z > 20$), as shown in Figure 1.6.

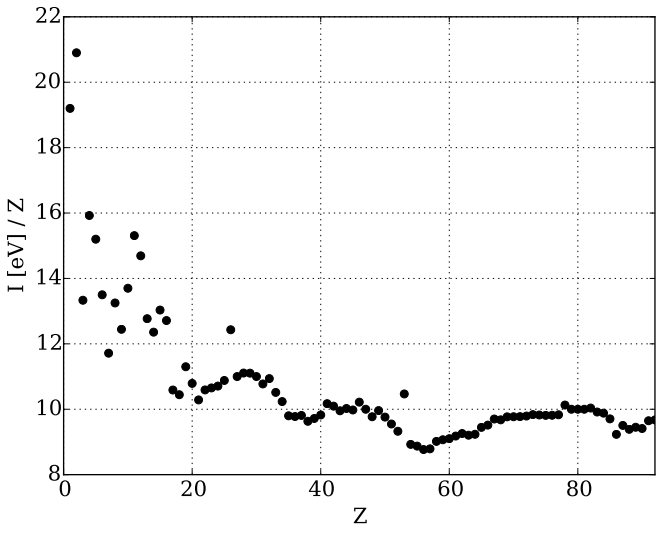

Figure 1.6: Mean excitation energy I divided by the atomic number Z as a function of Z. I-values taken from ICRU Report 49 [ICRU, 1993].

Mean excitation energies are most commonly determined experimentally through: 1) the measurement of the stopping power relative to a reference absorber, 2) the absolute stopping power or 3) the particle range [Hsu, 1979; ICRU, 1993]. First, the determination of the relative stopping power requires to measure the energy lost by charged particles in the test absorber and in the reference absorber (e.g. aluminum or copper [Hsu, 1979] and water, see section 1.1.3.6). In addition, it is necessary to know the I-value and the shell corrections for the reference absorber. Second, the absolute stopping power of an absorber can be obtained by a direct measurement of the energy lost by charged particles in the absorber. Then, the I-value is determined using Equation 1.2. Third, the I-value can be determined through range measurements of monoenergetic charged particles in an absorber material, neglecting scattering (CSDA formalism) and solving Equations 1.5 and 1.2 for I.

The determination of the I-value for compounds, either experimentally or theoretically, has a large associated uncertainty (i.e. on the order of 10-15% for human tissues [Andreo, 2009]). Consequences on how this uncertainty affects particle range estimation and dose calculation are addressed in Chapter 6.

Alternatively, and to a good approximation, the I-value of compounds can be determined using the *Bragg additivity rule* [ICRU, 1993]:

$$\ln I = \frac{\sum_i \omega_i \ (Z_i/A_i) \ \ln I_i}{\sum_i \omega_i \ (Z_i/A_i)} \tag{1.10}$$

where $\ln I_i$ is the logarithm of the mean excitation energy of i-th element. This relation adds the contributions from different atoms although it ignores the influence of chemical bonds.

In ICRU Reports 37 [ICRU, 1984] and 49 [ICRU, 1993], to improve the agreement with experimental data, the I-value for atomic constituents of compounds was given a different value (i.e. $\simeq 13\%$ higher) with respect to the I-value of the same atoms in the elemental state. In these reports, there is also the distinction between compounds in gas and in condensed phases (liquid or solid).

According to the Bragg additivity rule, the mass stopping power (Equation 1.1) for a compound can be approximated by a linear combination of the mass stopping powers (S_i/ρ_i) for the atomic constituents [ICRU, 1993]:

$$\frac{S}{\rho} = \sum_i^N \omega_i \ \frac{S_i}{\rho_i} \tag{1.11}$$

1.1.3.6 Stopping Power Ratio

In proton therapy, a useful quantity to determine the range in the patient and to compute the absorbed dose (see section 1.2.1) is the proton Stopping Power Ratio (SPR) to water[7]. For human tissues in the therapeutic energy range, the SPR in a medium

[7] Water is commonly used as reference medium. Human bodies are assumed to be composed of water by about 70%.

m can be approximated by the ratio of stopping powers given by Equation 1.2 without shell and density corrections [Schneider et al., 1996; Yang et al., 2012]:

$$SPR_m = RED_m \frac{\left[\ln \frac{2m_e c^2 \beta^2}{I_m(1-\beta^2)} - \beta^2\right]}{\left[\ln \frac{2m_e c^2 \beta^2}{I_{\mathrm{w}}(1-\beta^2)} - \beta^2\right]} \tag{1.12}$$

where I_m and I_{w} are the mean excitation energies of the medium m and water, respectively. The Relative Electron Density (RED) is the ratio of electronic densities (see section 1.1.3.4) of the medium m and water, respectively:

$$RED_m = \frac{\rho_{e,m}}{\rho_{e,\mathrm{w}}}. \tag{1.13}$$

1.1.4 Clinical rationale for proton therapy

In the previous section (section 1.1.2), the physical processes responsible of the spatial distribution, i.e. both lateral and longitudinal, of energy deposited and absorbed dose in the patient caused by incident proton beams were introduced. The physics of protons is precisely the central rationale for the increased interest in proton therapy observed in the last ten years.

The highly conformal and uniform dose to the target volume is no longer the main advantage of protons over photons because recent developments in conventional radiotherapy (see section 1.1.1) provide comparable target coverage [Newhauser and Zhang, 2015]. The main advantages of proton therapy are the finite range of protons, the possibility to control the penetration depth by adjusting the proton energy, the flat dose distribution in correspondence of the tumor location by overlapping several Bragg peaks, the lower integral dose[8], the possibility to treat deep-seated tumors with high doses which results in an increased Tumor Control Probability (TCP), and the superior capabilities to spare healthy tissues with respect to photons and thus increased patient tolerance (see Figure 1.7). By exploiting the sparing in normal tissues with proton therapy, it should be possible to reduce the incidence of treatment-related complications such as secondary cancers, cardiovascular diseases, fertility complications, growth and muscular problems in children and other long-term side effects [Paganetti and Bortfeld, 2005; Levin et al., 2005; Amaldi and Kraft, 2005; Oeffinger et al., 2006; Paganetti, 2011; Slater, 2012; Newhauser and Zhang, 2015].

The survival rate in pediatric oncology has increased in the last decades, i.e. 58% in the mid-1970s to more than 80% nowadays[9]. Hence, the main goal in pediatric oncology is to reduce late side effects and toxicity to ensure a better and long-standing quality of life. For these reasons, children are ideal candidates to benefit from proton therapy [Zhang et al., 2013; Rombi et al., 2014; Indelicato et al., 2016].

[8] The integral dose is the total energy deposited in a patient for a given target dose.
[9] Retrieved from www.cancer.org – Key statistics for childhood cancers. December 2016.

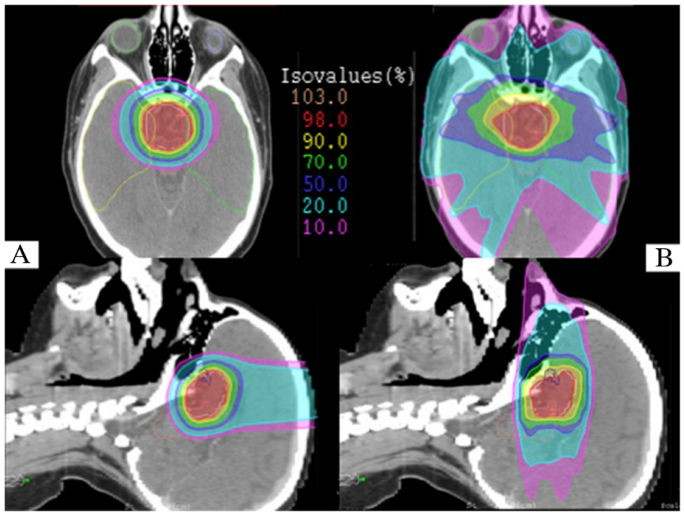

Figure 1.7: Comparison of highly conformed isodose distributions obtained with a 3 beams Intensity Modulated Proton Treatment (IMPT) plan (A) and with a 7 beams Intensity Modulated Radiotherapy (IMRT) plan (B). The IMPT plan improved sparing of temporal lobes, orbital structures and optical nerves. Moreover, the integral dose to the brain tissue was reduced with IMPT. Figure extracted from [Rombi et al., 2014].

Nowadays, only proton and carbon ion beams are used clinically. A debate is ongoing on which are the most suited ions for cancer therapy. From one side, ions with atomic number greater than 6 (carbon) are less prone to be used clinically due to the fragmentation tail after the Bragg Peak and the high RBE already in the entrance region [Jäkel, 2006]. On the other hand, some studies reveal that ions with an atomic number between 1 and 6 might be good candidates, such as Helium beams [Jäkel et al., 2003; Thariat et al., 2012; Slater, 2012; Krämer et al., 2016]. This is a very interesting discussion but it is beyond the scope of this thesis which is focused on improving proton therapy treatment planning, even-though the findings could be extrapolated to other ion species.

1.1.5 Conclusion

More than one century after the discovery of X-rays, technological developments in radiotherapy together with improved knowledge of biological effects of radiation have resulted in the delivery of highly conformal dose plans with maximized healthy tissue preservation. Radiotherapy with high energy photons and with charged particle beams have experienced a parallel development over time and, nowadays, both techniques are available. Due to the physical characteristics of proton beams when interacting with matter as compared to photons, protons present a superior advantage in sparing healthy tissues, particularly when treating deeply seated-tumors, which can reduce long-term

side effects. Each treatment modality presents advantages and limitations and both techniques have specific clinical indications. This thesis is focused on minimizing one of the main drawbacks of proton therapy –range uncertainty– in order to take full benefit of proton therapy.

1.2 Radiation treatment planning

The first step of a radiation treatment, named *simulation*, consists of acquiring a CT scan of the patient without any contrast agent and with all the contention items that would be used during the whole treatment (e.g. mask, head or legs holder, bite block, bolus, etc). The patient has to be placed in a comfortable and reproducible manner in order to be positioned exactly in the same way during all treatment fractions. This CT receives the name of *planning CT*. It gives information on the internal anatomy of the patient and it allows to account for heterogeneities during the treatment planning stage. CT with contrast agent, MRI and PET images are additionally acquired and registered with the planning CT to provide additional anatomical or functional information.

In the second step, named *contouring and prescription*, the physician delineates the target volume and the OARs on the planning CT and prescribes the dose to the tumor volume. The ICRU Report N.62 [ICRU, 1999] defines the target volumes to which dose has to be prescribed: the Gross Tumor Volume (GTV) is the macroscopic tumor, visible on the planning CT; the Clinical Target Volume (CTV) contains the GTV and sub-clinical tumor extensions at a certain probability level, not visibles; the Planning Target Volume (PTV) is a geometrical concept introduced for treatment planning to ensure that the prescribed dose to the CTV is actually delivered despite uncertainties in the treatment delivery. A schematic illustration of the different volumes is provided in Figure 1.8.

The third step of a radiation treatment is the *planning stage* in which medical physicists design the treatment plan, i.e. decide the most appropriate beam entrances, the number of fields and the optimization method. For example, due to range uncertainties in the patient, caused by inhomogeneities or patient positioning, beams stopping in front of an OAR are avoided in particle therapy. Afterwards, the absorbed dose in the patient is calculated on the planning CT by the TPS and validated by the physician.

Next, the *plan verification* step is part of the Quality Assurance (QA) program to ensure that the dose distribution calculated by the TPS is actually delivered to the patient, and to discard potential errors in the treatment delivery chain.

The last step is the *treatment delivery* where the position of the patient is checked prior and during treatment using X-ray imaging. Patient position defined in the simulation stage, at which the planning CT has been acquired, has to be reproduced in each treatment fraction.

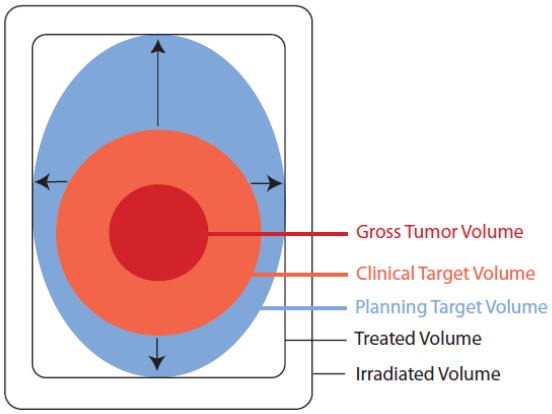

Figure 1.8: Volume definition according to the ICRU. GTV: Gross Tumor Volume, CTV: Clinical Target Volume, PTV: Planning Target Volume. GTV and CTV are oncological concepts, whereas PTV is a geometrical concept. Figure extracted from [ICRU, 2004].

1.2.1 The role of computed tomography in radiation treatment planning

CT images play an important role in radiation treatment planning. As mentioned before, the planning CT is used to define the treatment volumes and the OARs, and to compute the absorbed dose.

CT images provide the spatial distribution of photon attenuation coefficients μ of the scanned object. CT scanners are commonly calibrated with respect to water and CT numbers are expressed according to the Hounsfield Units (HU)[10] scale. In a voxel with average linear attenuation coefficient μ_x, the corresponding HU value is given by:

$$HU_x = 1000 \cdot \frac{\mu_x - \mu_{\mathrm{w}}}{\mu_{\mathrm{w}} - \mu_a} \tag{1.14}$$

where μ_{w} and μ_a are the linear attenuation coefficient of water and air, respectively. According to Equation 1.14, a 1 HU variation represents a 0.1% variation of the attenuation coefficient of water, since the attenuation coefficient of air is nearly zero. By definition, the HU value of water is 0 and the HU value of air is -1000. These two points are used to calibrate the CT scanner at different photon spectra.

Most TPSs report dose to water or water-equivalent dose and human bodies are assumed to be composed of water with varying mass density, electron density or stopping

[10]Named after Sir Godfrey Hounsfield who shared the Nobel Prize in Physiology or Medicine in 1979 with Allan Cormack for the invention of the X-ray CT.

power [Paganetti, 2009]. Consequently, in conventional photon therapy, each voxel of the patient CT scan is converted into mass density or RED (Equation 1.13); whereas in proton therapy treatment planning, TPSs require the conversion of HU values into proton SPRs relative to water (Equation 1.12).

CT-based treatment planning and dose computation is the clinical standard in radiotherapy. However, at present, many groups are also evaluating the feasibility of using MR images for treatment planning. MRI-based treatment planning has the advantage to be radiation-less and it has superior soft-tissue contrast compared to CT [Schmidt and Payne, 2015].

In the next sections the main processes that govern photon-matter interactions and some useful quantities that would be referenced to in the following sections of the manuscript are described.

1.2.2 Physics of photon interactions in matter

When a photon –X-ray beam or gamma radiation– traverses an object, three situations might occur:

1. It penetrates through the object without interacting.
2. It interacts with matter and it is completely absorbed.
3. It interacts with matter, it is scattered or deflected with respect to its initial direction and deposits part of its energy.

The process in which some of the photons are removed from the beam due to photon interactions is known as *attenuation*. The probability of photon interaction with matter per unit path length is given by the *linear attenuation coefficient* μ expressed in cm^{-1}. μ is related to the mean free path[11] τ in the target, the atomic cross-section σ_a (expressed in cm^2/atom) and the electronic cross-section σ_e (expressed in cm^2/electron) by the following expression [Jackson and Hawkes, 1981]:

$$\mu = \frac{1}{\tau} = n \cdot \sigma_a = n \cdot Z \cdot \sigma_e \tag{1.15}$$

where n is the number of atoms per unit volume of the absorber ($n = \rho \cdot N_A/A$) and $n \cdot Z = \rho_e$ is the electron density (expressed in electron/cm^3).

Another useful quantity, which is independent of the mass density of the absober material, is the *mass attenuation coefficient* μ/ρ expressed in cm^2/g.

The mass attenuation coefficient of a mixture, for a given photon energy or spectrum, is computed through the so-called *mixture rule* [Jackson and Hawkes, 1981]:

$$\left(\frac{\mu}{\rho}\right)_{med} = \sum_i \omega_i \left(\frac{\mu}{\rho}\right)_i \tag{1.16}$$

[11] τ is the average distance a photon travels between collisions with atoms of the target material.

where ω_i is the fractional weight of the i-th element of the mixture.

There are four major effects which lead to the attenuation of a photon beam: the photoelectric effect, the Compton effect or incoherent scattering, the Rayleigh or coherent scattering and the pair production. All mechanisms satisfy the laws of conservation of energy and momentum.

The total electronic cross-section for X-ray collisions can be written as the sum of the cross-sections for the processes contributing to the attenuation:

$$\sigma_e = \sigma_e^{\mathrm{ph}} + \sigma_e^{\mathrm{C}} + \sigma_e^{\mathrm{R}} + \sigma_e^{\mathrm{P}} \tag{1.17}$$

where the labels ph, C, R and P denote the photoelectric, the Compton, the Rayleigh and the pair production electronic cross sections, respectively.

1.2.2.1 Photoelectric effect

The photoelectric effect is an interaction between an incoming photon and a tightly bound electron, typically from the K or L shells. The energy transfer is a two-steps process. First, the photon transfers practically all of its energy E_{ph} to the electron and it ceases to exist. Second, the electron departs with most of the energy from the photon ($E_e = E_{ph} - E_{binding}$) and deposits its energy in the surrounding matter by ionizing the neighboring molecules. Since the interaction creates a vacancy in one of the electron shells, an electron moves down to fill in and this drop in energy often produces a characteristic X-ray photon (see Figure 1.9), also named fluorescence radiation, or the liberation of an Auger electron from an external shell. These are the so-called *atomic relaxation* processes.

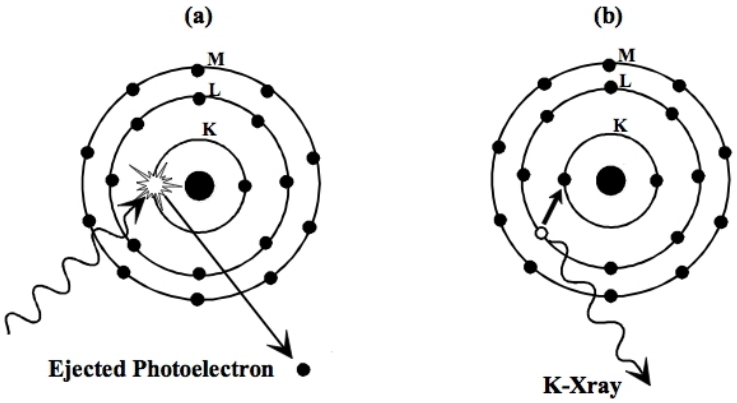

Figure 1.9: Photoelectric effect: a) photon absorption and electron ejection; b) fluorescent X-ray emission.

This interaction depends on the energy of the incoming photon and the atomic number (Z) of the tissue. The atomic cross section of the photoelectric effect is proportional

to:

$$\sigma_a^{ph} \propto \frac{Z^n}{E^m} \tag{1.18}$$

where $n \simeq$4-5 and $m \simeq$2-3. The lower the energy and the higher the atomic number of the target, the more likely a photoelectric effect (see Figure 1.11).

1.2.2.2 Compton effect or incoherent scattering

The Compton effect is an interaction where an incoming photon collides preferably with a loosely bound electron. In this interaction, both the photon and the electron are scattered. The photon has lost some of its energy but can continue to undergo additional interactions. The electron begins to ionize the surrounding media with the energy given by the photon.

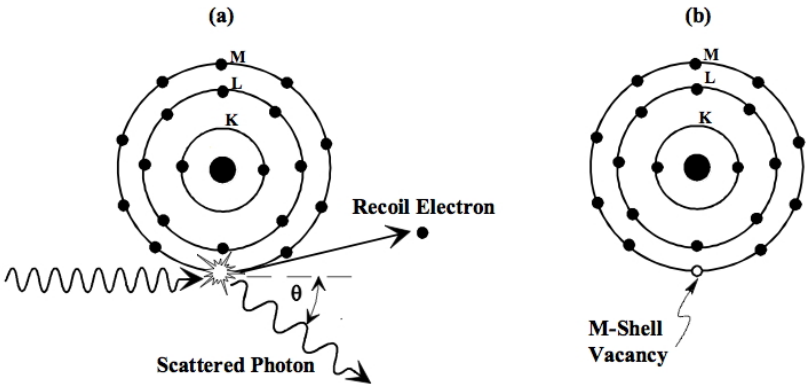

Figure 1.10: Compton effect: a) scattered photon and electron; b) ionized atom.

The probability of a Compton interaction is inversely proportional to the energy of the incoming photon and it is independent of the atomic number (Z) of the target material. The electronic cross section of the incoherent scattering is described by the Klein-Nishina formula f_{KN}, given by:

$$\sigma_e^C = f_{KN} = 2\pi r_e^2 \left[\frac{1+\alpha}{\alpha^2} \left(\frac{2(1+\alpha)}{1+2\alpha} - \frac{\ln(1+2\alpha)}{\alpha} \right) + \frac{\ln(1+2\alpha)}{2\alpha} - \frac{1+3\alpha}{(1+2\alpha)^2} \right] \tag{1.19}$$

with $\alpha = E/(m_e c^2)$ the normalized incident photon energy and r_e the classical electron radius. For the case of water this effect is predominant from 25 keV to 25 MeV (see Figure 1.11).

1.2.2.3 Rayleigh or coherent scattering

Rayleigh scattering is a process where an incoming photon is scattered by bound atomic electrons and in which the atom is neither ionized nor excited. The scattered photon is forward peaked and it hardly changes the initial photon field [Jackson and

Hawkes, 1981]. This process is maximum at low energies (E <25 keV) and for high-Z materials (Z >6):

$$\sigma_a^R \propto \frac{Z^2}{E^2} \tag{1.20}$$

For diagnostic CT energies (i.e. from 30 keV to 150 keV), Rayleigh scattering is usually neglected but, for mammography applications, where X-ray energies between 15 keV and 30 keV are used, this effect is not negligible (for the case of water).

1.2.2.4 Pair production electron-positron

This effect takes place when an incoming photon interacts with the nucleus of an atom. The photon gives its energy to the nucleus and, in the process, creates a pair of electron-positron. The positron ionizes until it combines with a free electron. This generates two photons that are emitted in opposite directions.

The probability of a pair production is proportional to the atomic number of the material and there is an energy threshold below which no pair production can occur, equal to twice the rest mass energy of an electron ($E = 2m_ec^2 = 1.022$ MeV):

$$\sigma_a^P \propto Z^2 \tag{1.21}$$

For the case of water this effect is predominant for energies superior to 25 MeV (see Figure 1.11) so, for most kV imaging applications (i.e. diagnostic CT), this effect is usually neglected.

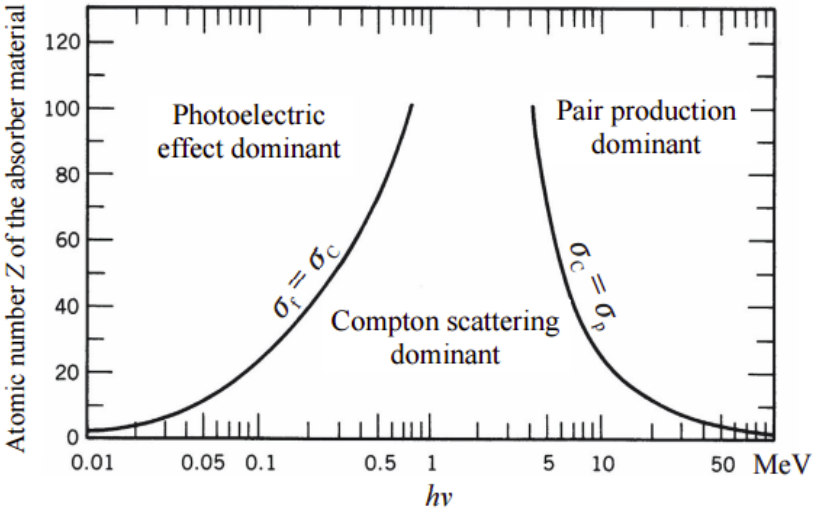

Figure 1.11: Illustration of the relative importance of the main three mechanisms of photon-matter interaction as a function of the incident photon energy ($h\nu$) and the atomic number Z of the absorber.

1.2.2.5 Beer-Lambert attenuation law

When a photon beam traverses a slice of material, some of the photons interact with the material and some simply pass through without interactions. The attenuation of monochromatic photons, collimated into a narrow beam, traversing a thickness of absorber is governed by the exponential decay law, known as the *Beer-Lambert law*:

$$I = I_0 \cdot e^{-\mu \Delta_x} \tag{1.22}$$

where I_0 is the flux of photons emitted by the X-ray source, I is the flux of photons measured by the detector after traversing a thickness Δ_x of absorber, and μ is the linear attenuation coefficient.

This equation can also be expressed as:

$$-\ln \frac{I}{I_0} = \mu \Delta_x. \tag{1.23}$$

When a polychromatic photon beam passes through an heterogeneous object, Equation 1.22 can be written as:

$$I(\boldsymbol{y}) = \int_0^E S(E) \exp\left(- \int_{L_{\boldsymbol{y}}} \mu(\boldsymbol{x}_l, E)\ \mathrm{d}l \right) \mathrm{d}E \tag{1.24}$$

where S is the polychromatic spectrum, $L_{\boldsymbol{y}}$ is the line-segment between the source and a detector pixel $\boldsymbol{y}$ and $\boldsymbol{x}_l$ is a point in space of the object.

1.2.3 Stopping-power conversion from single-energy CT

As earlier discussed (see section 1.2.1), analytical TPSs require the conversion of each voxel of the patient CT scan into electron density relative to water (RED) for photon dose calculations and into proton stopping power ratios (SPR) relative to water for proton dose calculations. In the literature, there are several ways to convert patient CT numbers into SPR using Single-Energy Computed Tomography (SECT) or DECT (see chapter 4). In the case of SECT, two main approaches have been proposed: a direct calibration using a dedicated phantom (see section 1.2.3.1) and the stoichiometric calibration [Schneider et al., 1996] (see section 1.2.3.2).

1.2.3.1 Empirical calibration

This approach consists in establishing a relation between CT numbers of human tissue surrogates with the measured stopping power ratio (SPR) relative to water through a calibration curve. The generation of the calibration curve is a three-steps procedure. First, a CT scan of a phantom containing tissue equivalent materials, such as the CIRS Model 062M Electron Density Phantom (CIRS Inc., Norfolk, U.S.A)[12], using the CT

[12]The CIRS Model 062M Electron Density Phantom consists of two concentric disks made of plastic water, that can represent both head and abdomen configurations, with seventeen holes to place tissue equivalent inserts with mass densities ranging from 0.2 g/cm^3 (lung) to 4.51 g/cm^3 (titanium).

scanner and the imaging protocols used for radiotherapy treatment planning is done. Then, the average HU value inside each insert is taken. In a second step, the SPR of each sample of known thickness a is determined experimentally by measuring the shift in the Bragg peak position when interposing this material to the beam (BP_x) with respect to the Bragg peak position in water without insert ($BP_{w/o}$) using a water-column device (e.g. PTW PeakFinder):

$$SPR_x = \frac{BP_{w/o} - BP_x}{a} = \frac{\Delta P}{a} \tag{1.25}$$

where ΔP and a have to be expressed in the same units (e.g. mm), because SPR is dimensionless. Finally, a piece-wise linear fit between the measured SPR values and the corresponding CT numbers is done for each CT protocol evaluated. The curve exhibits two main slopes: materials with HU lower than zero and higher than zero (see Figure 1.12). The reason of these two segments is the dependency of the photoelectric effect on the atomic number: for materials with HU lower than zero (e.g. lung tissues), the linear attenuation coefficient depends little on the atomic number, but for materials with HU higher than zero (such as bone inserts) there is a Z^3 dependency because the photoelectric effect is predominant. Materials with high atomic number have a higher I-value and, according to Equation 1.12, a reduced SPR value with respect to RED, which explains the reduced slope for increasing HU values. In the transition of the two segments, which corresponds to the soft tissue region, there is some fitting ambiguity between CT numbers and SPR values because the atomic number of inserts does not necessarily increase with RED [Paganetti, 2009; Tremblay et al., 2014]. This is an opposite behavior to materials with HU higher than zero (e.g. bone) where a well-defined correlation exists between RED and atomic number [Chen et al., 1979].

The accuracy of this method strongly depends on how much the elemental composition of tissue equivalent materials differs from that of human tissues and it is also sensitive to the tissue substitutes used for the calibration [Schneider et al., 1996].

1.2.3.2 Stoichiometric calibration

To overcome the above-mentioned limitations, Schneider *et al* proposed the *stoichiometric calibration* [Schneider et al., 1996], which is the most widely used calibration method in clinical practice. The method consists in scanning a set of materials with known physical density and chemical composition, not necessarily body-like tissues, in the CT scanner. The measured HU values are then used to determine some coefficients of a parametric model of the linear attenuation coefficient. Then, the theoretical HU values of real tissues can be computed through this parametrization. With tabulated composition data of the selected human tissues [Woodard and White, 1986; White et al., 1987; ICRU, 1992; ICRP, 2009], the theoretical SPR can be determined through equation 1.12. Finally, the calibration curve is generated by making an appropriate fit between theoretical CT numbers and SPR values.

Nevertheless, this method is not exempt of uncertainty, as pointed out by Yang *et al* [Yang et al., 2012]. In particular, the method is sensitive to the goodness of the

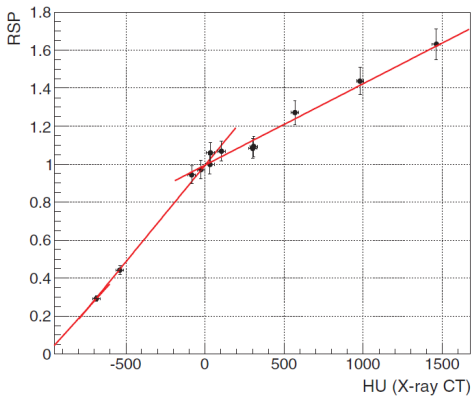

Figure 1.12: Example of bi-linear curve fitting between Hounsfield Units (HU) and proton stopping power ratio (SPR) relative to water using human tissue surrogates. In the soft tissue region (HU$\simeq$0), there is a fitting ambiguity due to the lack of one-to-one relation between HU and SPR values. Figure extracted from [Arbor et al., 2015].

parametric model used to model the CT scanner, and to variations in the human tissue composition and mass density. Despite the improvement with respect to the direct calibration approach [Schneider et al., 1996], the HU-SPR degeneracy in the soft tissue region still persists (Figure 1.13). Another source of uncertainty is related to the ongoing discussion on how to compute the theoretical SPR values of human tissues. The Bethe's equation without correction terms is used in the stoichiometric calibration, however, there are other approaches in the literature that employ different correction terms and different I-values, i.e. Bichsel *et al* 1972 [Bichsel, 1972], Janni *et al* 1982 [Janni, 1982] and ICRU Report 49 [ICRU, 1993]. On the one hand, Oden *et al* [Ödén et al., 2015] concluded that it is safe to use the Bethe's formula without correction terms as the errors obtained for biological tissues were below 0.1%. On the other hand, substantial differences in terms of the SPR have been reported when comparing the four existing approaches and the different sets of elemental I-values available [Ödén et al., 2015; Doolan et al., 2016], being larger when using the approach proposed by Schneider *et al* in the stoichiometric calibration [Doolan et al., 2016].

The range uncertainty associated to this procedure using animal tissues was found to be 1.8% for bone tissues and 1.1% for soft tissues, which means a range error between 1 mm and 3 mm [Schaffner and Pedroni, 1998].

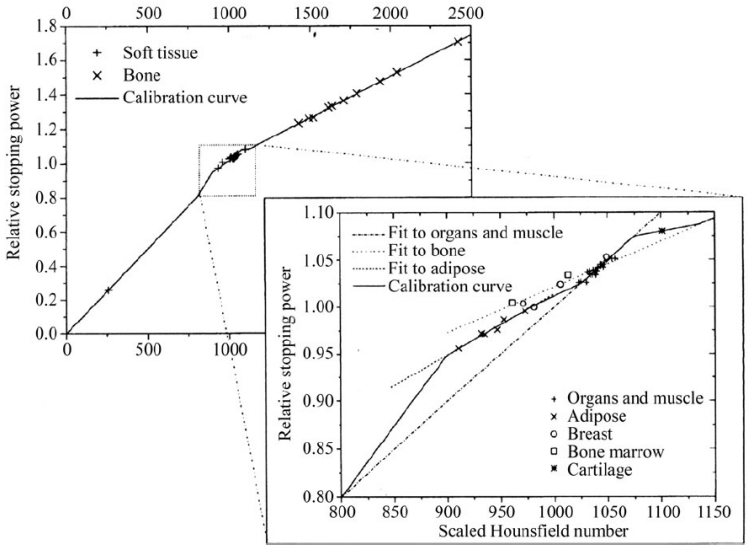

Figure 1.13: Conversion of Hounsfield Units (HU) to proton stopping power ratio (SPR) relative to water obtained though the stoichiometric calibration [Schneider et al., 1996]. On the right, zoom in the region of HU numbers close to zero (scaled to 1000 in this figure). The ambiguity of this conversion in the soft tissue region is visible by the five lines used to fit the data. Figure extracted from [ICRU, 2007].

1.2.4 Uncertainties in proton therapy

In theory, the finite and controllable range of protons –by adjusting the position of the Bragg peak– and the reduced integral dose with respect to photons allow a precise dose delivery (see section 1.1.4). However, uncertainties in treatment planning and in treatment delivery have dosimetric consequences and might cause severe damages to the patient, such as target miss or accidental exposure of OAR.

Uncertainties in proton therapy can be classified according to the source of errors [Both, 2012]:

1. Patient-related: setup or geometric errors, errors in target definition, target and organ motion, tumor regression or growth during the treatment course, and tissue inhomogeneities (e.g. different organ filling) along the beam path and in the transverse direction.

2. Physics-related: conversion of CT numbers into SPR values (see section 1.2.3), dose calculation approximations and dose uncertainties.

3. Machine-related: Dose Delivery System (DDS) tolerances, Patient Positioning System (PPS) tolerances, beam energy tolerance, etc.

4. Biology-related: RBE is assumed to be constant and equal to 1.1. However, it is not constant as it depends on dose, cell type and clinical endpoint.

Patient-related sources of uncertainty are common to conventional photon radiotherapy. For setup errors and systematic uncertainties, such as target definition errors and machine-related uncertainties, the geometrical concept of the PTV (see section 1.2) is applicable. Safety margins are added to the target volume to ensure that the CTV receives the prescribed dose.

Due to the sharp dose gradient at the distal edge of the Bragg peak (see Figure 1.1), the effect of tissue inhomogeneities or changes in density along the proton beam path is superior for protons than for photons [Goitein, 1982] and it has a severe impact on the proton range (see Figure 1.14). To limit the consequences of tissue inhomogeneities and biological uncertainties, particularly after the Bragg peak position, beams stopping in front of OARs are avoided. In addition, range uncertainty margins are added in the treatment planning stage. Besides the uncertainties in the longitudinal direction, density changes perpendicular to the beam direction might also have a dosimetric impact in proton therapy dose calculations.

X-ray CT-based treatment planning is one of the major sources of uncertainty in proton therapy [Jäkel, 2006]. Since photons and protons interact differently inside the human body, there is no clear functional relation between CT numbers and SPRs. A piece-wise linear relation exists between HU and SPRs for low density and bone materials, whereas it is not unique for soft tissues (see Figure 1.13). The conversion of HU to SPR using the stoichiometric calibration introduces a range error of 1.1% for soft tissues and 1.8% for bone tissues [Schaffner and Pedroni, 1998]. Stochastic (i.e. noise) and systematic variations of the CT numbers (i.e. drifts of the scanner with time) can also affect the calibration curve [Yang et al., 2012]. This relation also depends on the CT scanner, the CT resolution and the parameters of the imaging protocol. HU values can also be wrongly assigned because of beam hardening [Schaffner and Pedroni, 1998], scattering inside the patient and reconstruction artifacts due to high-Z materials (e.g. metallic implants, prosthesis, dental filling) [Jäkel, 2006]. Proper corrections have to be implemented in the reconstruction pipeline before treatment planning. Moreover, the choice of the reconstruction algorithm and the detector sensitivity might also influence the accuracy of HU numbers [Doolan et al., 2016].

There are also uncertainties related to dose calculation. On the one hand, most commercial TPSs are based on analytical pencil-beam dose calculation algorithms [Paganetti, 2012]. To compute the range of protons stopping at a certain point, these algorithms typically scale the depth-dose distribution in water by the water-equivalent depth in the patient, computed from the patient CT, using straight proton trajectories and neglecting the relative position of heterogeneities in depth [Schaffner et al., 1999; Paganetti, 2012]. MCS is typically approximated by a sum of two Gaussian functions and it can have an impact on the lateral beam penumbra and on the dose distributions because range degradation is not correctly predicted. Compared with Monte Carlo (MC) algorithms, these algorithms are less sensitive to complex geometries and density variations, particularly near the interface of two materials [Grevillot, 2011; Paganetti, 2012;

Schuemann et al., 2014]. The uncertainty in the proton range due to dose calculations using analytical algorithms was estimated to be 2.7% for homogeneous geometries and 4.6% for heterogeneous geometries [Paganetti, 2012]. Therefore, dose uncertainties could be reduced by using MC dose calculations which provide a higher level of accuracy with respect to analytical algorithms [Paganetti, 2012]. The main drawback is that they are not fast enough for clinical applications [Mairani et al., 2013]. Another source of dose uncertainty resides in the mean excitation energy values of water and tissues necessary to compute the SPR (see section 1.1.3.6). Recommended I-values of water by ICRU Report 37 [ICRU, 1984], 49 [ICRU, 1993], 73 [ICRU, 2005] and *Errata and Addenda* of Report 37 [Sigmund et al., 2009] are 67 eV, 75 eV, 80 eV and 78 eV, respectively. Based on the range of possible values, Andreo [Andreo, 2009] studied the influence of this variation on the Bragg peak position for proton and carbon ions. Excluding the smallest value, the uncertainty in the I-value for water results in a SPR variation between 0.8% and 1.2% in the therapeutic energy range [Paganetti, 2012]. For tissues, the uncertainty in the I-value was estimated to be $\sim 10-15\%$ [Andreo, 2009] which might result in a range uncertainty of 1.5% in tissue [Paganetti, 2012]. Another source of dose calculation uncertainty associated to some TPS algorithms is to not account for the SPR dependency on the proton energy (see section 1.1.3.6). [Yang et al., 2012] concluded that when ignoring the SPR variation with the proton energy along the beam path, range errors were about 0.5%.

Range uncertainty margins are clinically used in proton treatment planning and depend from one proton facility to another. Typical margins are 3.5% + 1 mm, 3.5% + 3 mm or 2.5% + 1.5 mm [Paganetti, 2012]. [Goitein, 1985] introduced the generic margin recipe of 3.5% + 1 mm. The 1 mm margin was introduced to compensate for patient-related uncertainties and beam-modifying compensator errors. The 3.5% was obtained from the quadratic sum of errors:

$$\sqrt{(2\%)^2 + (1\%)^2} \times 1.5\sigma \cong 3.5\% \tag{1.26}$$

where 2% is the uncertainty associated to the HU determination in the early 1980s [Schuemann et al., 2014], and 1% comes from the conversion between CT numbers and SPR. A 1.5 standard deviation margin was chosen to characterize a 85% confidence limit, which was found to be reasonable for some clinical applications [Goitein, 1985]. However, this margin recipe does not account for dose calculation uncertainties [Schuemann et al., 2014]. To take full benefit of proton therapy, some authors are arguing that generic margins should be replaced by site-specific margins based on the specific geometry and beam angle [Park et al., 2013; Schuemann et al., 2014].

With a better understanding of range uncertainties and by using appropriate mitigation techniques such as *in vivo* imaging (i.e. IGRT and range verification techniques) during the treatment fraction, adaptive radiotherapy and robust optimization treatment planning (e.g. multiple beams to reduce the sensitivity to range uncertainties [Knopf and Lomax, 2013] and beam-specific PTVs [Park et al., 2012]), it would be possible to deal with movements and range errors due to internal anatomical changes, to reduce treatment volumes and thus decrease the Normal Tissue Complication Probability

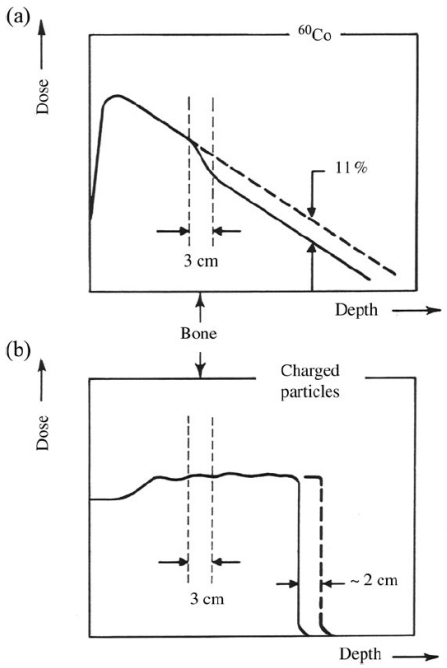

Figure 1.14: Effect of a 3 cm slab of bone placed in: a Cobalt-60 beam (a); and in the SOBP of a proton beam (b). The photon beam intensity is reduced by 11% but still penetrates deeply, whereas the proton beam range is reduced by 2 cm due to the high density object interposed along the beam path. Figure extracted from [ICRU, 2007]. Analogously, an air cavity in the proton path would result in a high dose deposit at the distal edge whereas the photon tail would be almost unaltered.

(NTCP).

1.2.5 Imaging modalities to reduce uncertainties

Several sources of uncertainty in proton therapy have been listed in section 1.2.4. This section briefly describes two imaging approaches aiming at mitigating these uncertainties but in different phases of the proton treatment: before (in the planning stage) and during treatment delivery.

1.2.5.1 Imaging alternatives in treatment planning

Treatment planning systems require SPR information of the patient to compute dose distributions and proton ranges. At present, SPR values are estimated from CT numbers of the planning CT through a calibration procedure (see section 1.2.3). To circumvent range uncertainties associated to this conversion, at least two imaging modalities could be used instead: proton CT and multi-energy CT (e.g. dual-energy).

Proton CT Proton CT is an attractive alternative in treatment planning as it directly reconstructs the SPR map of the patient. It consists in irradiating the patient with high energy protons, in order to place the Bragg peak position outside the patient (i.e. from 200 MeV for the head to 250 MeV for the trunk), and measure the energy lost by the protons after traversing the patient. The Water Equivalent Path Length (WEPL) can be derived and the SPR map reconstructed. The idea of using protons for imaging was early proposed in the 1960s [Cormack, 1963]. However, due to the poor spatial resolution of first reconstructed images and the high cost of those scanners, X-ray imaging prevailed over protons. In the late 1990s, a renewed interest in proton imaging was experienced [Quiñones et al., 2016]. Despite the active research of last years, no commercial proton CT scanner is currently available; there are just prototypes.

Multi-energy CT A recent approach in X-ray CT imaging is *multi-energy CT* which encompasses all those imaging modalities in which attenuation data of an object is measured at two (i.e. *dual-energy CT*, see chapter 2) or more energies (e.g. *spectral CT*, see section 2.2.6). The main idea behind these imaging modalities is that, since photon attenuation depends both on the elemental composition and the density of an object (see section 1.2.2), two materials might not be distinguished in a CT scan, e.g. if one contains a high-Z element and the other has a high density [Heismann et al., 2012]; however, as the attenuation for these materials does not have the same energy dependency (see Figure 2.1), they can often be differentiated when having CT measurements at different energies. Therefore, having attenuation measurements at two or more energies allows material discrimination and can improve diagnostic information. The use of Dual-Energy (DE) in proton therapy was first suggested in 2009 [Bazalova et al., 2009; Beaulieu et al., 2009]. One year later, Yang [Yang et al., 2010] demonstrated that DECT could provide a better estimate of the SPR with respect to single-energy X-ray CT imaging (see chapter 4).

1.2.5.2 Image-guided radiotherapy

"Image-guided radiotherapy (IGRT) is the process of frequent imaging (i.e. 2D or 3D) the patient in the treatment room during a course of radiotherapy to guide the treatment process" [Verellen et al., 2007]. The purpose of IGRT in proton therapy is two-fold. First, IGRT is used in areas of the body that are prone to movements and it allows the physician to track interfractional tumor motion, and to eventually adjust the patient position or the beam position to target the tumor more precisely. CBCT systems mounted on the treatment couch are used for this purpose. Another approach, MRI-guided proton therapy, which uses MRI instead of X-rays to obtain anatomical information of the patient, is currently being investigated [Lagendijk et al., 2014]. Second, imaging in the treatment room can be used to verify protons range and dose distributions. Integrated online PET systems are an attractive and non-invasive possibility to image the dose delivered by protons. Due to nuclear interactions (see section 1.1.2), a small fraction of protons create positron emitting isotopes (e.g. ^{11}C, ^{13}N and ^{15}O) [Knopf and Lomax, 2013]. PET imaging is based on the coincident detection

of gammas resulting from the annihilation of emitted positrons with electrons. A 3D distribution of the induced activity in the patient is thus obtained and it is subsequently compared with predicted PET activity distribution calculated with MC simulations. However, physiological wash-out in the tissues has to be correctly modeled to achieve an accurate comparison and the low statistics problem has to be solved. Another approach for *in vivo* range verification is *prompt gamma* imaging which consists in monitoring the emitted gammas produced in the inelastic collisions between the incident particle and the medium (see section 1.1.2). Prompt gamma emission is almost isotropic and can be detected instantaneously (few nanoseconds) after the nuclear interaction [Knopf and Lomax, 2013; Huisman et al., 2016]. However, due to the low prompt gamma signal and the low efficiency of current detectors, the clinical application of prompt gamma for range verification is still under development. Other solutions under development are ionoacoustic characterization of the Bragg Peak position [Assmann et al., 2015] and interaction vertex imaging [Henriquet et al., 2012].

1.2.6 Conclusion

Protons are more vulnerable than photons to changes in density and tissue inhomogeneities in the beam direction caused by movement, misalignment or anatomical changes. Image-guidance in the treatment room can be beneficial to mitigate motion and to verify proton ranges in the patient during the treatment fraction. Current treatment planning systems rely on X-ray CT image information of patient's anatomy to design the treatment plan. To calculate the proton range in the patient and to compute the absorbed dose, patient SPR information derived from CT numbers is required. Inaccuracies arising from the planning CT and intrinsic to this conversion are an important source of range uncertainty. To account for these uncertainties, safety margins are added in the planning stage. The aim of this thesis is to investigate the benefits of using dual-energy CBCT to reduce uncertainties in predicting the proton range in the patient.

Chapter 2

Dual-energy CT

Contents

This chapter describes the principles and technical approaches to perform dual-energy CT. A brief overview of the clinical and industrial applications of dual-energy CT with special mention to clinical applications for radiotherapy purposes is given. A review of the decomposition solutions for material segmentation and dose calculations, either in the image domain or in the projections domain, is also provided.

2.1 Principles

When scanning an object, the measured CT number in a voxel is related to its linear attenuation coefficient (see Equation 1.14). As the attenuation depends both on the mass density and the elemental composition of the scanned object (see section 1.2.2), similar HU can be measured at a certain photon energy for different materials and, as a consequence, cannot be distinguished in a CT scan. However, by exploiting the differences of X-ray attenuation coefficients of tissues at different energies (see Figure 2.1), materials can be distinguished when recording the attenuation at different energies or beam spectra.

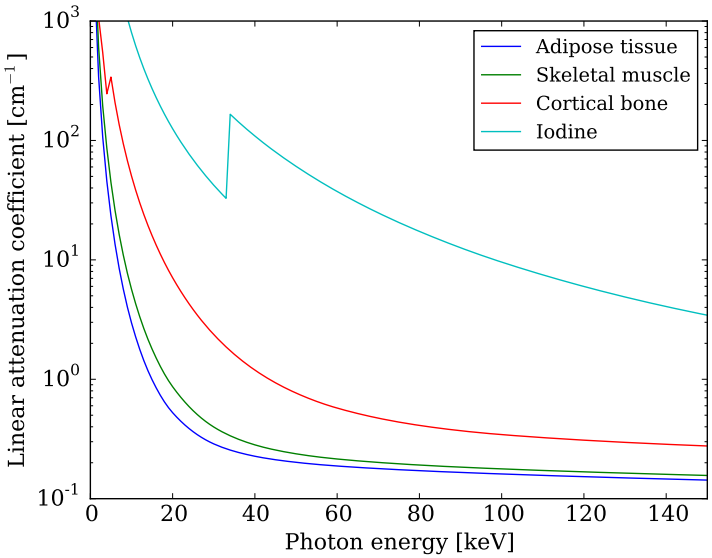

Figure 2.1: Linear attenuation coefficient as a function of the photon energy for some human tissues and iodine. Data retrieved from NIST database [Hubbell and Seltzer, 2004].

In 1973, Sir Hounsfield mentioned in his paper describing the invention of the CT scanner [Hounsfield, 1973] the possibility to distinguish between materials having different atomic number (e.g. calcium and iodine) when scanning an object at two different beam spectra (e.g. 100 kV and 140 kV).

The basic principle of dual-energy consists in acquiring two datasets from the same anatomical area with different X-ray voltages (see sections 2.2.1, 2.2.2 and 2.2.3) or with one voltage but recording different portions of the spectrum (see sections 2.2.4 and 2.2.5) or energy windows (see section 2.2.6).

The theoretical basis for dual-energy CT (DECT) was established in the late 1970s. First studies were published in 1976 by Alvarez and Macovski [Alvarez and Macovski, 1976] and by Rutherford *et al* [Rutherford et al., 1976]. In both papers, they proposed the decomposition of the linear attenuation coefficient into terms describing the two main interaction processes for X-ray photons in the diagnostic CT range: photoelectric

absorption and Compton scattering (see section 1.2.2). The approaches differed in the sense that Alvarez and Macovski directly decomposed projection data obtained from the CT scan, prior to image reconstruction whereas Rutherford *et al* decomposed into photon interactions the reconstructed images at low and high energy voltages and then estimated the effective atomic number and the effective electron density of the scanned object. An approach similar to Rutherford's was chosen by Brooks [Brooks, 1977]. These approaches can be classified as *projection-based* or *pre-processing* methods and *image-based* or *post-processing* methods, respectively. Lehmann *et al* [Lehmann et al., 1981] applied the decomposition theory to Dual-Energy Radiography (DER). In the following years, papers describing the potential of dual-energy for tissue characterization and quantification [Chiro et al., 1979; Cann et al., 1982; Dunscombe et al., 1984] and for beam hardening reduction [Hemmingsson et al., 1986] were published. Furthermore, a two-material decomposition basis was alternatively proposed to the photon interactions basis, such as aluminum and plastic [Marshall et al., 1984; Kalender et al., 1987] or water and calcium chloride [Hawkes et al., 1986].

Despite the clinical potential of dual-energy, its implementation was slow due to limitations of the first DECT scanners such as low resolution, sensitivity to movement artifacts [Heismann et al., 2012] and decomposition algorithms suffering from noise amplifications [Kelcz et al., 1979; Chuang and Huang, 1988]. At the very beginning, sequential acquisitions at different voltages were used, but suffered from spatial and temporal misregistration of the two datasets. DECT imaging did not find its way into clinical routine until 2006 when the first commercial dual-energy scanner was built by Siemens Healthcare (Forchheim, Germany) [Flohr et al., 2006].

2.2 Technical approaches

A CT scanner consists of an X-ray tube and a detector. Detectors can be classified into two main groups: *energy-integrating* or *energy-resolved*. Energy-integrating detectors integrate the X-ray signal over time with an energy weighting factor (named *detector response*) and, therefore, they do not provide energy resolution [Heismann et al., 2012] (see Chapter 3). These detectors convert X-rays to light via a thin scintillator layer (typically Cesium Iodide or Gadolinium Oxysulfide) and then to charge by an amorphous silicon photodiode (indirect conversion) or directly to charge through a Thin Film Transistor (TFT) array (direct conversion). On the other hand, energy-resolved detectors are able to distinguish individual photons coming from a polychromatic spectrum within given energy thresholds. These detectors typically use high speed semiconductors –e.g. Cadmium Telluride (CdTe) or Cadmium Zinc Telluride (CZT)– combined with fast readout Application-Specific Integrated Circuit (ASIC)s, with an electronic chain for each pixel of the detector [Wang et al., 2011]. In other words, with just one X-ray tube voltage acquisition, energy-resolved detectors are capable to record attenuation data from multiple energy bins, whereas with energy-integrating detectors acquisitions with different X-ray tube voltages are necessary to obtain the same kind of information.

Since its initial conception in 1976, several technical approaches have been developed

to perform DECT imaging. The previous distinction of detector's technology eases the classification of the existing modalities to acquire dual-energy data: sequential acquisitions with a conventional CT scanner, dual-source CT systems, twin beam systems and fast-kV switching systems are based on energy-integrating detectors, whereas dual-layer detectors and photon-counting systems are based on energy-resolved detectors. A brief description of each approach or scanner is given in the following subsections.

2.2.1 Sequential Acquisition

The simplest way to acquire dual-energy data consists in performing two consecutive scans of the same anatomical area at different tube potentials. Initial DECT studies employed this technique. Different filtration can be applied to the low and the high tube voltage. The main limitation of this approach is that, as patient data is not acquired at the same time interval, patient movement may compromise the quality of the decomposition [McCollough et al., 2015]. Non-rigid anatomical registration could reduce motion artifacts [Heismann et al., 2012]. This approach is still appropriate for imaging anatomical regions not prone to movement.

2.2.2 Dual-Source CT systems

A Dual-Source CT (DSCT) scanner is equipped with two X-ray tubes mounted with an angular offset of about 90° and the corresponding detectors. The two X-ray source/detector systems rotate simultaneously around the patient and each X-ray tube can have independent filtration. The first commercially available DECT system was a DSCT scanner (Figure 2.2). In first generation DSCT scanners, the Field Of View (FOV) of the high voltage was smaller than the low voltage's FOV due to gantry space limitations [Flohr et al., 2006] to avoid irradiating the electronics. Last generation DSCTs have overcome this limitation by increasing the angle between X-ray tubes (i.e. from 90° to 95°). Second generation scanners still present a limited FOV (i.e. 33 cm) which might be a problem to image large patients, but third generation scanners (such as the DSCT Siemens Somatom Force) can have a full FOV of 50 cm[1]. Another downside of DSCT scanners is the cross-scattered radiation between the orthogonal X-ray tubes and detectors, which can reduce the Contrast-to-Noise Ratio (CNR) of the images. These artifacts can be reduced by placing anti-scatter grids and with proper scatter modeling [Heismann et al., 2012; McCollough et al., 2015].

2.2.3 Fast Kilo-Volt Switching systems

Fast Kilo-Volt Switching (FKVS) systems are equipped with an X-ray tube capable of switching voltage and current settings between consecutive projections of the same scan. This system enables nearly simultaneous acquisition of the same anatomical region with two different beam spectra. Low and high voltage projections are interleaved,

[1]From the technical specifications of the "DSCT Somatom Force scanner". Retrieved from www.healthcare.siemens.com

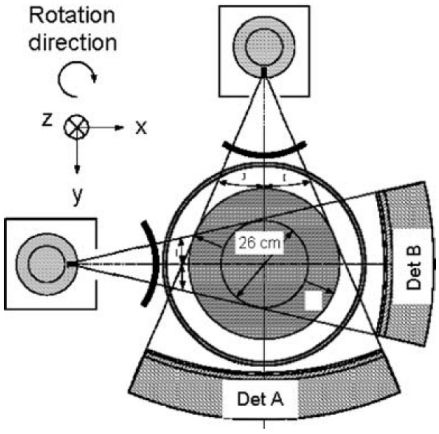

Figure 2.2: Illustration of the first Dual-Source CT scanner. Figure from [Flohr et al., 2006]. Detector A covers the entire field-of-view (FOV) with a diameter of 50 cm, whereas detector B is restricted to a smaller and central FOV to avoid irradiating the electronics of detector A.

i.e. acquired at consecutive projection angles (see Figure 2.3). The first FKVS scanner was conceived in 1986 [Kalender et al., 1986], but technical limitations such as the impossibility to change current settings between consecutive projections, and the required fast response of the tube and the detector, limited its clinical implementation [Zou and Silver, 2008; Heismann et al., 2012; McCollough et al., 2015]. GE Healthcare (Waukesha, Wisconsin, U.S.A.) overcame some of these limitations with the CT750 HD scanner [Zhang et al., 2011]. One downside of this system is the poor spectral separation of the low and the high voltage projections due to technical limitations in filtering differently the two spectra when using a single X-ray source. A recent development, the Imaging Ring (IR) X-ray system (medPhoton, Salzburg, Austria), which is a FKVS scanner equipped with a filter wheel synchronized with the beam pulse, allows different filtration of the low and the high voltage projections. A detailed description of the IR system is provided in Chapter 3.

2.2.4 Dual-Layer Detector systems

A Dual-Layer Detector (DLD) system consists of a single X-ray tube and a so-called *dual-layer* detector. Dual-layer detectors, also named *sandwich* detectors, are composed of two scintillator detectors where the top layer predominantly collects low-energy X-ray photons and the bottom layer mainly detects high-energy X-ray photons (see Figure 2.4). The main advantage of this scanner is the simultaneous acquisition of low and high

Figure 2.3: Principle of fast kV switching systems to acquire dual-energy CT data. Figure from [Heismann et al., 2012]. Low (green) and high (orange) voltage projections are acquired at consecutive projection angles.

energy projections. The performance of dual-energy imaging with this system depends on the capabilities to provide separate beam spectra, with small overlap, and similar Signal-to-Noise Ratio (SNR) for the low and the high voltage projections [Heismann et al., 2012; McCollough et al., 2015]. Detector thicknesses are different to achieve the same noise level in low and high energy images. However, the optimal thicknesses of the layers depend on the beam spectrum and also vary with the size and composition of the imaged object.

2.2.5 Twin beam systems

Another technical solution to perform dual-energy imaging with a single X-ray source CT scanner is the so-called *twin beam* technology proposed by Siemens Healthcare (Forchheim, Germany). In this system, the X-ray beam is filtered by two different materials, i.e. gold (Au) and tin (Sn), before reaching the patient. In the longitudinal direction, the rows of the detector are divided into two parts: one half of the rows collect the X-ray photons filtered with gold and the other half detects X-ray photons filtered with tin (see Figure 2.5). The K-edge of tin and gold are at 29 keV and 81 keV, respectively. Consequently, tin filters out more low energy photons (detects the high energy spectrum) than gold which eliminates more high energy photons (detects the low energy spectrum).

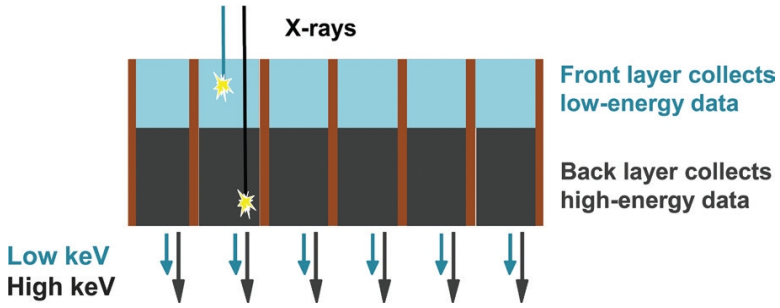

Figure 2.4: Illustration of the dual-layer detector principle. The front layer predominantly collects low-energy X-ray photons, while the back layer predominantly collects high-energy X-rays photons capable to pass through the front layer. Figure from [McCollough et al., 2015].

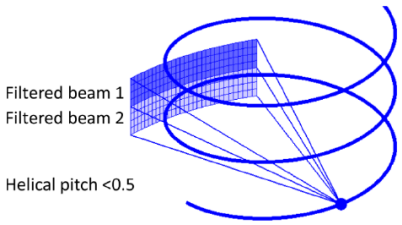

Figure 2.5: Illustration of a twin-beam acquisition using a single source CT system. Figure from [Yu et al., 2016]. X-ray beam is split in two: half is filtered with gold and half is filtered with tin. Half-rows of the detector collect the X-ray photons filtered with gold and the other half the X-ray photons filtered with tin.

2.2.6 Photon-Counting Detector systems

Photon-Counting Detector (PCD) systems consist of an X-ray source and an energy-resolving photon-counting detector. Photon-counting detectors are capable of counting discrete photon interactions according to the associated photon energy. The detector is divided into N energy channels or bins, determined by consecutive N+1 energy thresholds, where each one has an independent detector response function (i.e. probability of a photon with energy E to be detected at energy E) [Taguchi and Iwanczyk, 2013]. Photons detected within one bin are then counted (see Figure 2.6). These systems are still under development, there is no commercial system yet but small animal prototypes.

Detector's technology has to solve two main limitations: pulse pile-up when the count rate is too high, and charge sharing between adjacent energy bins. Photon-counting technology with energy discrimination thresholds opens up the potential transition from dual-energy CT to *multi-energy CT* or *spectral CT* imaging, which would allow multi-material segmentation [Schlomka et al., 2008; Heismann et al., 2012; McCollough et al., 2015; Van Elmpt et al., 2016].

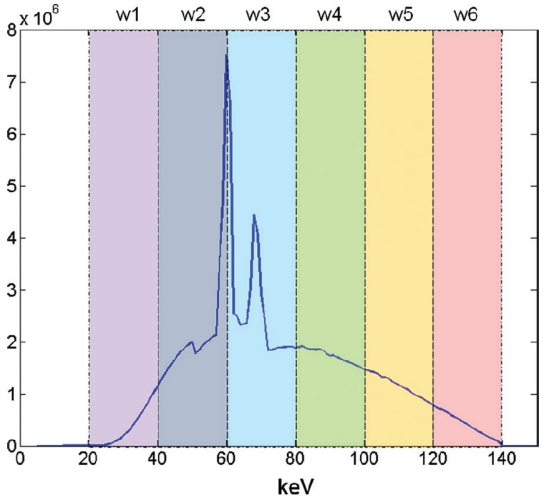

Figure 2.6: Schematic illustration of the binning of the incident polychromatic spectrum into six energy windows. Figure from [McCollough et al., 2015].

2.3 Applications

Dual-energy CT imaging has two main fields of application: medical and industrial. Dual-energy techniques are used in many industrial Non-Destructive Testing (NDT) applications. Quantitative DECT imaging of composite materials consisting of two or few materials is used to detect eventual material defects (e.g. wrong thicknesses or missing fibers) [Létang et al., 2004]. Among other applications, DECT is also employed in airports for the inspection of luggages to detect the presence of arms or explosives [Rebuffel and Dinten, 2007].

Dual-energy imaging has many clinical applications: from diagnosis to radiotherapy applications. Estimation of the contrast agent uptake (e.g. iodine) in suspected lesions, fat quantification or bone densitometry are examples of quantitative imaging. After material decomposition one can remove a basis material from the image, such as the contrast agent, to generate contrast-free images without necessity of acquiring a second set of images, or bone- and calcium-subtracted images to improve lesion characterization [Karçaaltncaba and Akta, 2011; McCollough et al., 2015; Van Elmpt et al., 2016]. DECT is also used to synthesize monoenergetic images of the patient at certain effective energies to improve diagnosis [Yu et al., 2012]. These images are less affected by beam hardening,

can improve the CNR [Li et al., 2012; McCollough et al., 2015] and, in the presence of prostheses or high density materials, show reduced metal artifacts with respect to conventional single energy CT [Bamberg et al., 2011; Pessis et al., 2015].

Besides many diagnostic applications, DECT imaging is also used in radiotherapy [Van Elmpt et al., 2016]. As discussed in section 1.2.1, analytical TPSs require the conversion of each voxel of the patient CT scan into electron density to water (RED) for photon dose calculations and into proton stopping power ratios (SPR) for proton dose calculations. The single-energy stoichiometric calibration (see section 1.2.3.2) is currently the clinical standard. However, the HU-SPR or HU-RED degeneracy, particularly in the soft tissue region, introduces some range errors that need to be accounted for in the treatment safety margins. Monte Carlo-based TPSs require more information than RED or mass density maps to compute the material specific cross sections, such as the chemical composition or the elemental fraction by weight in every CT voxel. One approach is to segment the HU-RED curve into several segments, where each segment has a single tissue assigned with well-known chemical composition and mass density [Schneider et al., 2000]. However, due to the above-mentioned lack of one-to-one relation between HU and RED values, particularly in the soft tissue region, wrong tissue assignment might occur with dosimetric consequences. To solve this ambiguity and to improve material discrimination or segmentation, additional tissue information, such as the effective atomic number Z_{eff}, can be extracted from DECT imaging [Bazalova et al., 2008a,b; Bazalova and Verhaegen, 2009; Beaulieu et al., 2009]. Thus, radiotherapy applications include material segmentation for Monte Carlo dose calculations, improved brachytherapy dose calculations by decomposition into photon interaction cross sections, SPR estimation for proton therapy treatment planning, and quantification of carbon content in tissues to improve proton range verification using PET imaging [Van Elmpt et al., 2016].

In the following, the manuscript is focused on radiotherapy applications of DECT, particularly for proton therapy treatment planning. A review of the existing decomposition algorithms is provided in the next section.

2.4 Decomposition algorithms: review of methods

The two main approaches to perform dual-energy were proposed in 1976 (see section 2.1) and they mainly differ in the order of the decomposition and the reconstruction step. Since then, many algorithms to decompose DECT data into the required variables for radiotherapy purposes, e.g. the relative electron density (RED) and the effective atomic number (Z_{eff}), have been proposed. Some methods directly decompose into these two variables, some decompose into two material mass densities or concentrations, and some decompose into photoelectric effect and Compton scattering cross sections. Up to now, for radiotherapy applications, most of the proposed methods are image-based (section 2.4.1).

Depending on whether scanner specific information is known or not *a priori*, a further classification of the decomposition approaches can be made. The here-named *model-based* methods are based on *a priori* knowledge of source energy spectrum and detector

response, whereas *calibration-based* methods rely on a calibration using materials with known properties to obtain parameters that indirectly characterize the energy spectrum and the detector response of the CT scanner.

2.4.1 Image-based

Image-based methods use linear combinations of the reconstructed images to obtain material-selective DECT images. The methods listed below mainly differ on the level of complexity of the parametrization of the linear attenuation coefficient, and whether or not they rely on a calibration or on the exact knowledge of scanner properties. Unlike projection-based methods, image-based methods require a beam-hardening correction in the reconstruction pipeline. Beam hardening artifacts occur because the energy dependency of the linear attenuation coefficient is neglected (see equation 1.24).

Rutherford *et al* [Rutherford et al., 1976] proposed a parametric model of the monochromatic linear attenuation coefficient as a function of two parameters: the effective atomic number Z_{eff} and the effective number of atoms per unit volume N^*. By scanning an object at two voltages (i.e. 120 kVp and 140 kVp), a system of two equations of $\mu(E_1)$ and $\mu(E_2)$ with two unknowns (Z_{eff} and N^*) can be numerically solved, where E_1 and E_2 are the effective energies of the incident spectra. The *effective energy* of a beam is the monochromatic energy at which a given material will exhibit the same attenuation coefficient as measured on the CT scanner with a polychromatic beam. Brooks [Brooks, 1977] proposed the decomposition of the scanned object into Compton and photoelectric coefficients images. His approach is based on the quality factor Q of the X-ray spectrum, determined through a calibration process with known materials, which avoids the need of defining an effective energy of the beam. In 2003, Torikoshi *et al.* [Torikoshi et al., 2003] proposed a dual-energy X-ray CT decomposition method into electron density and effective atomic number using synchrotron radiation. The advantage of using monochromatic X-ray beams is that reconstructed CT images are exempt of beam hardening effect. Since then, many dual-energy approaches that decompose into effective atomic number and relative electron density using commercial DECT scanners have been proposed. To cite some, in 2008, Bazalova *et al* [Bazalova et al., 2008b] extended the decomposition formalism proposed by Torikoshi for polychromatic X-ray beams, which resulted in an improved tissue segmentation with respect to the conventional HU-RED curve. This method requires perfect knowledge of the beam spectrum and the detector response of the system. To limit beam hardening artifacts, the incident spectrum was filtered with 16 cm of solid water (one half of the phantom diameter) and, for high-Z materials, a semi-empirical correction for beam hardening was proposed. Most image-based methods rely on a beam hardening correction (typically a water precorrection function at the projections level) implemented in the image reconstruction step [Brooks and Di Chiro, 1976]. Maaß *et al* [Maaß et al., 2009] proposed an image-based decomposition method based on generalized precorrection functions that are not optimized to correct for beam hardening but to generate material-selective images, which resulted in material-decomposition images less affected by beam hardening. In 2012, Saito [Saito, 2012] proposed a dual-energy decomposition method based on a

weighted difference of CT numbers at low and high voltages (ΔHU) to extract the relative electron density (RED). The proposed $\Delta\text{HU} - \text{RED}$ curve showed a low dependence on the object size used for the calibration. Hünemohr *et al* [Hünemohr et al., 2014a] adapted the formalism of Alvarez and Macovski [Alvarez and Macovski, 1976] in the image-domain. They proposed a decomposition method into Z_{eff} and RED based on a calibration, not requiring the *a priori* knowledge of the source spectrum. Landry *et al* [Landry et al., 2013b] proposed a calibration-based approach to compute Z_{eff}, without need to estimate the CT scanner spectrum, by establishing a relation between the ratio of measured CT numbers at low and high voltages and Z_{eff}. Bourque *et al* [Bourque et al., 2014] adapted the stoichiometric calibration method of Schneider *et al* [Schneider et al., 1996] to dual-energy CT data. This method was further implemented by Tremblay *et al* [Tremblay et al., 2014] to monochromatic images previously generated through a projection-based approach. Mendonça *et al* [Mendonça, 2014] extended the material decomposition and discrimination capability of dual-energy CT to more than two materials, based on the assumption that the mix of materials in the human body behaves as an ideal solution, for which mass and volume-preservation laws apply. Unlike other approaches, where a simplified parametrization of the linear attenuation coefficient was used, van Abbema *et al* [Van Abbema et al., 2015] extended the full description of the X-ray total cross section proposed by Jackson and Hawkes [Jackson and Hawkes, 1981] with additional fit functions to derive Z_{eff} and RED values from reconstructed CT images with an iterative procedure. Ramos-Garcia *et al* [Ramos Garcia et al., 2016] proposed another parametrization of the linear attenuation coefficient to decompose dual-energy data into Z_{eff} and RED. Han *et al* [Han et al., 2016] extended the representation of the linear attenuation coefficient as a linear combination of energy-dependent basis functions of two-materials, initially proposed by Alvarez and Macovski [Alvarez and Macovski, 1976] and first implemented in the image-domain by Williamson *et al* [Williamson et al., 2006], to estimate RED and $\ln(I)$ values for proton stopping-power computations.

2.4.2 Projection-based

Projection-based methods pass the two-energy raw-data sets through a decomposition function to generate DECT specific sinograms. Afterwards, the image reconstruction step produces material-selective images. This approach requires that projections for the low and the high energy spectrum are sampled at the same angle (i.e. effectively matched or accurately interpolated).

The theoretical framework for projection-based methods was established by Alvarez and Macovski in 1976 [Alvarez and Macovski, 1976]. The key idea of this approach, which is based on the mixture rule (see Equation 1.16), is that the linear attenuation coefficient of the scanned object at a location $\boldsymbol{x}$ can be expressed as a linear combination of energy-dependent basis functions $f_i(E)$ with energy-independent coefficients a_i, with

$i = 1, 2, ..., n$:

$$\mu(E, \boldsymbol{x}) = \sum_{i=1}^{n} a_i(\boldsymbol{x})\ f_i(E) \tag{2.1}$$

For the particular case of dual-energy, $n = 2$, a set of two basis functions with two energy-independent coefficients has to be chosen. Alvarez and Macovski concluded that the choice of the basis functions was empirical [Alvarez and Macovski, 1976]. They suggested the decomposition into the photoelectric effect and Compton scattering cross sections, which was later generalized into a two-material decomposition method [Heismann et al., 2012] (see section 2.4.2.1).

Unlike image-based methods, where many different ways to combine the reconstructed CT images have been proposed, the formalism of projection-based methods remains unaltered. Projection-based methods differ in the way of solving the dual-energy problem (i.e. generation of DECT-specific sinograms): through a numerical process or based on a calibration (see section 2.4.2.2).

As the energy dependency is factored out in this decomposition process (see equation 2.1), the basis-images should not be affected by beam-hardening (with respect to the image-based ones). Consequently, projection-based approaches do not require a beam hardening correction prior to image reconstruction.

2.4.2.1 Forward problem

Photoelectric and Compton effect decomposition In the diagnostic energy range, the linear attenuation coefficient of materials can be represented by a linear combination of the photoelectric effect and Compton scattering cross sections. If no absorption edges are located in the energy range of CT imaging, the photoelectric cross section can be approximated by $f_{\text{ph}} \propto E^{-3}$ (see Equation 1.18), and the Compton cross section by the Klein-Nishina formula f_{KN} (see Equation 1.19):

$$\mu(E, \boldsymbol{x}) = a_1(\boldsymbol{x})\ \frac{1}{E^3} + a_2(\boldsymbol{x})\ f_{\text{KN}} \tag{2.2}$$

where the coefficients a_1 and a_2 have a physical meaning [Alvarez and Macovski, 1976]:

$$a_1 = \frac{K_1\ \rho\ Z^n}{A} = \frac{K_1\ \rho_e\ Z^{n-1}}{N_A};\ \ n \approx 4 \tag{2.3}$$

$$a_2 = \frac{K_2\ \rho\ Z}{A} = \frac{K_2\ \rho_e}{N_A};\ \ K_2 = 2\pi r_e^2 \tag{2.4}$$

with $[\text{A}] = \text{u} = (\text{g/mol})/N_A$ and $1\ \text{u} = 1.660539\ 10^{-24}$ g.

The line integrals A_{ph} $(= A_1)$ and A_{C} $(= A_2)$ of the energy-independent terms of the photoelectric and Compton contributions can be expressed as:

$$A_{\text{ph}}(\boldsymbol{u}, \theta) = \int_{L(\boldsymbol{u},\theta)} K_1'\ \rho_e(\ell)\ Z^m(\ell)\ \mathrm{d}\ell; \qquad m = n - 1; \qquad K_1' = K_1/N_A \tag{2.5}$$

$$A_{\mathrm{C}}(\boldsymbol{u},\theta) = \int_{L(\boldsymbol{u},\theta)} K_2' \; \rho_e(\ell) \; \mathrm{d}\ell; \qquad K_2' = K_2/N_A \tag{2.6}$$

where $\ell \in L(\boldsymbol{u},\theta)$ is the line-segment between the source and a detector pixel located at position $\boldsymbol{u}$ for a given projection angle θ.

Once A_{ph} and A_{C} are known for each projection angle θ, the effective atomic number and the electron density can be extracted from equations 2.5 and 2.6 after reconstruction.

It is worth mentioning that in the presence of elements with high atomic numbers (typically the contrast agent), having a K-edge discontinuity in the diagnostic energy range, equation 2.2 is no longer valid. A third term describing the attenuation properties of this element has to be added [Roessl and Proksa, 2007]. This new formulation requires to perform attenuation measurements at least at three different energy spectra (in case of energy-integrating systems) or to use energy-resolved photon-counting systems. Alternatively, Mendonça *et al* [Mendonça, 2014] proposed an image-domain multi-material decomposition method for DECT based on the assumption that human body materials behave as an ideal solution, that can be described as a mixture of at most three materials for which volume and mass preservation laws apply, and some regularity constraints. Based on this idea, some authors proposed a multi-material decomposition using statistical methods such as penalized-likelihood reconstruction with edge-preserving regularization for each material on the projection-domain [Long and Fessler, 2014] and in the image-domain [Xue et al., 2017].

Two-materials decomposition Equation 2.1 can also be written as a linear combination of energy-dependent basis functions of two materials with energy-independent coefficients. The basis functions $f_i(E)$ can either be the energy-dependent mass attenuation coefficients or the linear attenuation coefficients of the i-th material and, the coefficients, the mass density or the fraction of each material i of the basis, respectively. The two-materials decomposition method is also called Basis Material Decomposition (BMD) and the linear attenuation coefficient is given by:

$$\mu(E,\boldsymbol{x}) = \varrho_1(\boldsymbol{x}) \left(\frac{\mu}{\rho}\right)_1 (E) + \varrho_2(\boldsymbol{x}) \left(\frac{\mu}{\rho}\right)_2 (E) \tag{2.7}$$

where (μ/ρ) represents the mass attenuation coefficient of the i-th material, and ϱ_i the corresponding mass fraction per volume.

The projection of the mass density ϱ_1 and ϱ_2 can be expressed as follows:

$$A_1(\boldsymbol{u},\theta) = \int_{L(\boldsymbol{u},\theta)} \varrho_1(\ell) \; \mathrm{d}\ell \tag{2.8}$$

$$A_2(\boldsymbol{u},\theta) = \int_{L(\boldsymbol{u},\theta)} \varrho_2(\ell) \; \mathrm{d}\ell. \tag{2.9}$$

The choice of the material basis is very important. Typically, to represent most of the biological tissues in the human body, a combination of water and bone mineral, or

soft tissue and cortical bone, or water and iodine in presence of iodine-based contrast agents, are chosen [Heismann et al., 2012].

Once the set of line integrals A_1 and A_2 are known for all projection angles θ, it is possible to reconstruct the mass density images using, for example, a filtered backprojection (FBP) reconstruction algorithm.

Li *et al* [Li et al., 2012] decomposed scatter-corrected CBCT projections into material selective images of water and bone, water and PMMA or water and iodine to synthesize virtual monochromatic CBCT projections, which were then used to reconstruct virtual monochromatic CBCT images. The resulting CBCT images showed a substantial metal artifact reduction and improved image contrast compared to a single-energy scan of equivalent dose.

2.4.2.2 Inversion

When performing a dual-energy acquisition, two sinograms of the same object at two different energy spectra are available. The logarithmic transmission or attenuation of an X-ray beam after traversing an object is expressed as:

$$m_{\mathrm{LE}} = -\ln\left(\mathrm{I}/\mathrm{I}_0\right)_{\mathrm{LE}} = -\ln\int_E S_{\mathrm{LE}}(E)\ \exp\left(-A_1\ f_1(E) - A_2\ f_2(E)\right)\ \mathrm{d}E \tag{2.10}$$

$$m_{\mathrm{HE}} = -\ln\left(\mathrm{I}/\mathrm{I}_0\right)_{\mathrm{HE}} = -\ln\int_E S_{\mathrm{HE}}(E)\ \exp\left(-A_1\ f_1(E) - A_2\ f_2(E)\right)\ \mathrm{d}E \tag{2.11}$$

where m_{LE} and m_{HE} are the logarithmic transmission values at low and high energy voltages respectively, I and I_0 the measured intensities with and without object, S_{LE} and S_{HE} the normalized energy spectra weighted by the detector response, A_1 and A_2 the line integrals that we want to solve and f_1 and f_2 the energy-dependent basis functions.

The unknowns A_1 and A_2 can be determined numerically by solving the system of equations 2.10-2.11, e.g., using the *simplex method* of Nelder and Mead [Nelder and Mead, 1965] following [Schlomka et al., 2008], assuming that the energy spectra and the detector response are well known (model-based). The performance of this approach relies on the accuracy of the model describing the scanner.

An alternative approach is to express the system of equations 2.10-2.11 as a polynomial expansion of two variables. From one side, Alvarez and Macovski [Alvarez and Macovski, 1976] proposed the following expansion:

$$m_{\mathrm{LE}} = b_0 + b_1\ A_1 + b_2\ A_2 + b_3\ A_1^2 + b_4\ A_2^2 + b_5\ A_1\ A_2 + b_6\ A_1^3 + b_7\ A_2^3 \tag{2.12}$$

$$m_{\mathrm{HE}} = c_0 + c_1\ A_1 + c_2\ A_2 + c_3\ A_1^2 + c_4\ A_2^2 + c_5\ A_1\ A_2 + c_6\ A_1^3 + c_7\ A_2^3 \tag{2.13}$$

where the unknown coefficients b_i and c_i can be determined experimentally through a calibration procedure. Once the coefficients are determined, the system of equations 2.12-2.13 can be numerically solved for A_1 and A_2 (using e.g. Newton-Raphson iteration method). On the other hand, the areal density values or thicknesses can be expressed as a polynomial function of the logarithmic transmission values at low and high energy

voltages [Lehmann et al., 1981; Chuang and Huang, 1988]:

$$A_1 = \widehat{b}_0 + \widehat{b}_1\ m_{\mathrm{LE}} + \widehat{b}_2\ m_{\mathrm{HE}} + \widehat{b}_3\ m_{\mathrm{LE}}\ m_{\mathrm{HE}} + \widehat{b}_4\ m_{\mathrm{LE}}^2 + \widehat{b}_5\ m_{\mathrm{HE}}^2 + \widehat{b}_6\ m_{\mathrm{LE}}^3 + \widehat{b}_7\ m_{\mathrm{HE}}^3 \tag{2.14}$$

$$A_2 = \widehat{c}_0 + \widehat{c}_1\ m_{\mathrm{LE}} + \widehat{c}_2\ m_{\mathrm{HE}} + \widehat{c}_3\ m_{\mathrm{LE}} \cdot m_{\mathrm{HE}} + \widehat{c}_4\ m_{\mathrm{LE}}^2 + \widehat{c}_5\ m_{\mathrm{HE}}^2 + \widehat{c}_6\ m_{\mathrm{LE}}^3 + \widehat{c}_7\ m_{\mathrm{HE}}^3 \tag{2.15}$$

With this representation, for any given pair of attenuation measurements of an object, one can directly determine the corresponding areal density or thickness in the basis materials, without need of numerical solving.

In both methods, the unknown coefficients b_i, c_i, $\widehat{b}_i$ and $\widehat{c}_i$ can be determined experimentally through a calibration procedure in the least square sense. The calibration is performed in the following way: attenuation measurements (m_{LE} and m_{HE}) are performed for two different photon spectra (labeled LE and HE) and different areal density values A_1 and A_2 of two well-known materials (or thicknesses if $f_i = \mu$). Slabs of plastic (e.g. PMMA) and aluminium of variable thicknesses are commonly used for the calibration due to its ease of production and because they represent quite well the attenuation properties of soft tissue and bone, respectively. Nevertheless, these calibration-based approaches present also some disadvantages: sensitivity to the order of the polynomial, to the use of crossed-terms in the polynomial, to the exact thickness of the interposed slabs of two materials, to the number of points of the calibration curve, etc. [Cardinal and Fenster, 1990].

A variant of the previous calibration-based method consists in dividing the range of thicknesses of the two materials used for the calibration into a number of subregions (e.g. 10 subregions) [Chuang and Huang, 1988]. Then, for each subregion, different coefficients b_i and c_i are determined in the least square sense. The rationale for using subregions is that beam hardening increases with the thickness of the irradiated object and, therefore, the resulting polynomial would be more accurate. However, to avoid artifacts, a proper treatment of the transition between adjacent subregions has to be implemented.

2.4.3 Joint decomposition and reconstruction

Some authors are also evaluating the possibility to decompose and reconstruct spectral CT data in one single step based on iterative algorithms, e.g., [Schmidt et al., 2015; Sidky et al., 2016; Foygel Barber et al., 2016]. With this approach, the intermediate step of decomposing the measured sinograms into material-specific sinograms, followed by tomographic reconstruction, is not required. On the other hand, it is computationally demanding as the spectral transmission data coming from different energy channels has to be treated simultaneously. One of the advantages is that, unlike projection-based approaches, registered projections are not required.

2.5 Conclusion

Dual-energy formalism was early proposed in the 1970s, but it was not clinically implemented until 2006 when the first commercial DECT scanner was placed on the market. Among several industrial and clinical applications, DECT imaging has promising applications in radiotherapy. By adding an extra measurement at a different energy, DECT imaging can provide additional tissue information, such as the effective atomic number, to improve material discrimination, dose calculation and SPR estimation for proton therapy applications. In recent years, more image-based than projection-based DECT algorithms have been proposed. One explanation is that projection-based methods require to have access to dual-energy raw data, which cannot be accessible in most commercial CT scanners. In addition, low and high energy projections need to be sampled at the same angle or accurately interpolated which is not trivial for dual-source scanners or fast-kV switching systems. However, with the advent of dual-layer systems and photon-counting detector technology, projection-based methods are becoming more attractive since the projections from the different energy spectra are obtained without angular separation. In this thesis, special emphasis was given to projection-based dual-energy approaches to improve proton SPR estimation in the patient.

Chapter 3

Imaging Ring system

Contents

The DEXTER project is built around a new scanner, the Imaging Ring (IR) system, developed by medPhoton, a spin-off company of the Paracelsus Medical University (PMU), for image-guided radiotherapy (IGRT). The aim in this chapter is to describe:

- the Imaging Ring system;
- a parametric model for the source and the detector response;
- a procedure developed to calibrate and validate kilo-voltage cone-beam CT models applied to three commercial systems;

- a procedure developed for the Imaging Ring to assess the validity of the source and the detector response models;

- a scatter-mitigation technique implemented off-line for the Imaging Ring image data.

3.1 Description of the Imaging Ring system

The Imaging Ring (IR) system is a cone-beam CT (CBCT) scanner developed for image-guided radiotherapy (IGRT) (see section 1.2.5.2) by medPhoton GmbH (Salzburg, Austria), a spin-off company of the PMU. The source and the flat panel detector of the system are fixed to a ring, which is mounted on the treatment couch, and can translate longitudinally along the table to image all patient areas. Some features of this system are that the source and the detector can independently rotate along circular trajectories and that the system is equipped with dynamic X-ray collimation jaws. The Field Of View (FOV) of the source and the detector trajectories can be off-centered with respect to the center of rotation of the scanner and, in combination with synchronized collimation, it allows large FOV irradiations (i.e. the IR is able to cover the full body outline, also in thorax region including the shoulders) and off-centered acquisitions which allow reduction of patient dose as unnecessary areas of the patient are not irradiated. Another characteristic of this system is the possibility to adjust the tube current, the tube voltage and the spectrum filtration at each beam pulse thanks to the fast-kilovolt switching capabilities of the source (see section 2.2.3) and the synchronized filter wheel which allows multi-energy imaging. The filter wheel is positioned before the collimator jaws and contains four holes to place filters (i.e. air, copper, aluminium, copper and silver).

The X-ray source is capable of emitting energies between 40 kV and 120 kV at two focal spot sizes of 0.3 mm and 0.6 mm with tube currents comprised between 5 mA and 120 mA. The amorphous silicon flat panel detector has a Cesium Iodide scintillator and an active area of 41×41 cm^2. For a detailed description of the system geometry and the CT reconstruction algorithm with off-centered FOV acquisitions refer to [Rit et al., 2016], and for the nine-degrees of freedom flexmap with independent movable source and detector refer to [Keuschnigg et al., 2017].

3.2 Procedure for the calibration and validation of kilovoltage cone-beam CT models

This work has been published in the *Med. Phys.* journal in a Technical Note format [Vilches-Freixas et al., 2016a] (see Appendix A).

Figure 3.1: Imaging Ring system installed at MedAustron (Wiener Neustadt, Austria). Photo courtesy of medPhoton GmbH.

3.2.1 Introduction

Several devices have been developed to acquire images of the patient in the treatment room for image-guided radiation therapy (IGRT). Kilo-voltage (kV) cone-beam computed tomography (CBCT) provides volumetric images of the patient to correct for the treatment position and to assess changes in the internal anatomy. Implementation of dual-energy capabilities in CBCT units is finding diagnostic applications to improve material segmentation and enhance contrast. A model of the kV CBCT unit is required to optimize the imaging device, to simulate and correct for scatter radiations [Poludniowski et al., 2009a], to optimize single [Ding et al., 2010] and dual-energy acquisition protocols, to compute the patient imaging dose [Alaei and Spezi, 2015] and for material decomposition in dual-energy CT.

Verification of CBCT models has been carried out in different manners in the literature [Alaei and Spezi, 2015]. To validate the X-ray source model, some authors performed Half-Value Layer (HVL) measurements [Poludniowski et al., 2009a] [Spezi et al., 2009], but only the first HVL is commonly checked. In a recent work [Randazzo and Tambasco, 2015], the authors proposed an original experimental setup to rapidly characterize X-ray sources by acquiring angular-dependent HVLs and fluence data. Others compared the Monte Carlo calculations with measured depth dose distributions and dose profiles [Downes et al., 2009; Ding et al., 2007]. A solution to validate the detector model is the method proposed by Granton *et al* [Granton et al., 2012] which consists of recording image intensities over a wide range of X-ray tube voltages and comparing them to predicted image intensities using the source and the detector models.

Even though some works in the literature have assessed either the accuracy of the source model or the detector model separately, we believe that it is necessary to provide a general procedure to validate both models in a simple manner. The purpose of this study is to propose a concise experimental approach to calibrate and validate a given

model for the source and the detector of a CBCT scanner. If the model is pre-calibrated or if precise manufacturer information is available, the degrees of freedom of the model tend to zero and, then, this procedure can be used exclusively for model validation. As example of application, the proposed method has been applied to the models of three different CBCT scanners and the results are discussed.

3.2.2 Materials and methods

3.2.2.1 Procedure

The calibration and validation of the CT model is a two-step protocol: the source model then the detector model. The source model at each voltage is represented by the photon energy spectrum $\Phi_{0,k}(E, \theta, \phi)$, i.e. the number of photons per energy E for the k-th voltage and without additional filtration (index 0) in a direction (θ, ϕ) expressed in spherical coordinates. The detector model is represented by the detector response $S_p(E, \beta)$ which is defined for each pixel p and is a function of the incident photon energy E and the angle β between the normal to the detector and the incident ray.

Source The procedure to validate the source model is as follows: first, a series of dose measurements in air is performed with varying filter thicknesses and materials in front of the source. High-purity sheets of aluminum (Al), copper (Cu) and silver (Ag) are used. This procedure is repeated for several tube voltages (kV), tube current (mA) and exposure times (ms). The absorbed dose in air $D^{exp}_{j,k}$ of the j-th setup of filters ($j = 1, ..., J$) and k-th voltage is measured using a dosimeter working in the range of energies of interest. The energy dependence of the dosimeter used for the experimental measurements is assumed to be negligible at this range of voltages. The theoretical dose in air is calculated using

$$D^{theo}_{j,k}(\theta, \phi) = \sum_i (\mu_{en}/\rho)_{air}(E_i) \cdot \Phi_{j,k}(E_i, \theta, \phi) \cdot E_i \tag{3.1}$$

where $D^{theo}_{j,k}$ is the theoretical dose in air, i is the index of energy bins of the spectrum with E_i the corresponding energy, $(\mu_{en}/\rho)_{air}$ is the energy-dependent mass energy absorption coefficient of air taken from the NIST database [Hubbell and Seltzer, 2004] and $\Phi_{j,k}$ is the polychromatic spectrum of the j-th setup computed from $\Phi_{0,k}$ and the known thicknesses of filters. A subset of acquired data, e.g., dose measurements without filter in front of the source ($j = 0$), might be used for calibrating the source model. The last step of the validation process consists in giving a figure of merit (e.g. the percentage relative difference) of the comparison between experimental and calculated dose values for each voltage, filter material and filter thickness.

The proposed method can be used to perform both a single point dose comparison (e.g. $\theta = 0°, \phi = 0°$) and a two-dimensional (2-D) dose comparison (θ, ϕ). For the latter, the irradiation area is discretized and the validation procedure repeated by shifting the

dosimeter accordingly (step-and-shoot technique). Another option is to substitute the punctual dosimeter by a 2-D dosimetric film or an array detector.

Detector The validation of the detector model assumes that the source model is calibrated and validated. A set of image acquisitions is performed with varying filter materials and tube voltages. Like the source validation procedure, high-purity sheets of aluminum, copper and silver are placed in the beam to modify the source spectrum $\Phi_{0,k}$. For each setup j ($j = 1, ..., J$), more than 500 frames are acquired to reach the plateau-regime of the lag [Starman et al., 2012]. A temporal median is then performed over the last frames where the image intensity remains constant (i.e. the last 100 frames) to compute the measured pixel value $P^{exp}_{j,k}(p)$. The predicted pixel values are determined as follows

$$P^{theo}_{j,k}(p) = \sum_i \Phi_{j,k}(E_i, \theta_p, \phi_p) \cdot S_p(E_i, \beta_p) \tag{3.2}$$

where $P^{theo}_{j,k}(p)$ is the predicted pixel value for the j-th filter setup and the k-th voltage, θ_p and ϕ_p are the spherical coordinates of pixel p in the coordinate system of the source, $S_p(E_i, \beta_p)$ the detector response at energy E_i and β_p, which is uniquely defined by the scanner geometry and (θ_p, ϕ_p). Parameters of the detector model might be calibrated against a subset of experimental data if necessary. Then, predicted and measured pixel values for each voltage and spectrum filtration are compared using a goodness of fit indicator, such as the percentage relative difference.

The detector response (total absorbed energy) is considered locally deposited, and not spread like it should be if scatter in the detector was accounted for [Poludniowski et al., 2011]. Consequently, Equation 3.2 can only be used to validate the energy response of the detector, not its spatial response.

3.2.2.2 Application

Experimental setups The current procedure was applied to the three kV-CBCT scanners of Table 3.1. All flat panel detectors had CsI:Tl scintillators. The filters in front of the X-ray source were slabs of aluminum (nominal thicknesses: 0.5 mm, 1 mm and 2 mm), copper (nominal thickness: 0.1 mm) and silver (nominal thickness: 0.125 mm). All filters were of high-purity ($\geq$99.9%). The exact thickness t of each high-purity filter material of known density ρ was obtained from precise measurements of the mass m and the area A. Moreover, two dosimeters working in the range of voltages of interest, i.e., from 50 to 130 kV, specifically the Nomex (PTW GmbH, Freiburg, Germany) and the MagicMax (Ion Beam Applications S.A., Louvain-la-Neuve, Belgium) multimeters, were used for the source model verification. Acquistions were performed with three filter combinations: f_1) no filter, f_2) 8 mm Al, and f_3) 0.3 mm Cu + 0.5 mm Ag.

A prerequisite of implementing this procedure is to have a model that needs to be validated. The proposed method can be used with any given model of source and detector response. To illustrate its application, a model for the source and for the detector

#	System	X-ray tube	Flat panel
1	Elekta XVI	Dunlee D604	Perkin Elmer XDR1622(Al)
2	medPhoton ImagingRing	IAE RTM70HS	Perkin Elmer XDR1642(Al)
3	IBA PT Gantry CBCT test bench	Varian GS2075	Thales Pixium4343RF

Table 3.1: kV-CBCT units

response is proposed below. The unknown parameters of the models are determined through calibration against experimental data. Finally, the agreement between the experimental data and the model output is measured by quantifying the relative differences between the measures and the predictions.

Source model Proprietary information, such as the inherent filtration (stoichiometric composition and thickness) and the anode angle of the X-ray source, is either not provided or it is given with big uncertainties. To overcome this restriction, the unknown tube filtration of the systems under study was described as a linear combination of two known materials. Aluminum (Al) and copper (Cu) were chosen as basis because they are commonly employed in commercial X-ray tubes as filter materials. In this study, the X-ray source was modeled by a photon energy spectrum parameterized by the anode angle, the tube voltage and the thicknesses of the basis materials (Al, Cu) which represent the inherent filtration. Using the program SpekCalc [Poludniowski et al., 2009b], photon fluence spectrum were generated without any filtration for different voltages at 10 kV step and for anode angles from 5° to 22° at 1° interval. Then, each spectrum was filtered with all possible thickness combinations of Al (from 0.1 to 8.0 mm at 0.1 mm step) and Cu (from 0.005 mm to 0.5 mm at 0.005 mm step). Finally, the experimental data was used to calibrate the model. The optimal tuple of parameters for each imaging system (anode angle, Al and Cu thicknesses) was determined by minimizing the following cost function:

$$F_{source} = \sum_{j,k} \left(\frac{D_{j,k}^{exp} - D_{j,k}^{theo}}{D_{j,k}^{exp}} \right)^2 \tag{3.3}$$

where the indices j and k refer to the j-th filter setup and k-th voltage, respectively. $D_{j,k}^{exp}$ are the experimental dose values and $D_{j,k}^{theo}$ are the theoretically determined dose values.

Dose measurements were carried out with a narrow beam geometry using: the filter cassette M2 (system # 1), the dynamic collimation jaws (system # 2) and lead slabs (system # 3). A dosimeter was attached to the flat panel detector and placed at the central beam axis. Thus, only the spectrum along the beam central axis ($\theta = 0°$) was considered. The absolute photon yield was adjusted by weighting the SpekCalc spectrum, filtered only with the inherent filtration, with the ratio of measured and theoretical

dose in air without additional filtration (j=0) for the corresponding (kV,mA,ms) tuple of source parameters.

Detector response model The detector response was modeled as the average contribution to the pixel value of one incident photon as a function of its energy. It was assumed that pixel values were proportional to the energy deposit in the scintillator. The detector response was generated using Monte Carlo simulations. The flat panel detector was modeled in GATE [Jan et al., 2004] v7.2 (based on Geant4 v10.1, physics list: emlivermore) as a stack of layers of user-defined materials according to the manufacturer's description (stoichiometry and thickness). The response of the detector was obtained by measuring the energy deposited in the scintillator layer with monoenergetic pencil beams of energies ranging from 1 to 140 keV [Roberts et al., 2008], perpendicular to the detector. In the 20-140 keV energy range, the statistical uncertainty of the simulated detector response was below 0.5% for all detectors (10^{10} photons). To provide an absolute value of the deposited energy on the detector, no calibration nor corrections, i.e. bad pixels and gain, were applied to the acquired projections, only offset correction. Then, a parameter was used in the model to relate the detector signal to the predicted value, i.e. a multiplicative factor δ_p for each pixel p of the detector determined in the least square sense:

$$\delta_p = \frac{\sum_{j,k} P^{theo}_{j,k}(p)}{\sum_{j,k} P^{exp}_{j,k}(p)} \tag{3.4}$$

$P^{theo}_{j,k}(p)$ is the predicted pixel value for setup j-th and k-th voltage with p the pixel index and $P^{exp}_{j,k}(p)$ is the measured pixel value for setup j-th and k-th voltage. To manage bad pixels, $P^{exp}_{j,k}(p)$ was determined by taking the spatial median of the signal in a 3×3 pixels area perpendicular to the beam central axis. Moreover, as the exact thickness of the CsI scintillator layer was not perfectly known, the detector response was computed for scintillator lengths ranging from 200 to 900 µm at steps of 50 µm. The experimental data was used to determine the optimal CsI length that minimized the following cost function:

$$F_{detector} = \sum_{j,k} \left(\frac{\delta_p P^{exp}_{j,k} - P^{theo}_{j,k}}{\delta_p P^{exp}_{j,k}} \right)^2 \tag{3.5}$$

where the index j and k refers to the setup j-th and k-th voltage, respectively.

Sensitivity analysis The term "sensitivity analysis" refers here to the study of the variations of the model accuracy (cost function) around its optimum. In particular, once the optimal tuple of source model values (mm Al, mm Cu, anode angle) were determined for each system, small variations (i.e. up to ± 0.3 mm Al, ± 0.01 mm Cu, ± 3 degrees) around the optimal values at a time were introduced for each parameter. For the detector response model, the scintillator length was varied from 200 µm to 900 µm.

3.2.3 Results

The source model was calibrated using dose measurements in air with increasing thicknesses of aluminum, with the beam filtrations f_1 (no filter) and f_3 (0.3 mm Cu + 0.5 mm Ag). For each imaging system, the parameters of the source model were determined by minimizing the cost function described in Equation 3.3 and are summarized in Table 3.2. In Figure 3.2, plot of two representative X-ray spectra and the detector response in energy, obtained after calibration, for each system.

System	Anode angle (°)	mm Al	mm Cu	CsI length (μ)
#1	18	7.2	0.01	750
#2	11	0.3	0.06	350
#3	11	3.0	0.01	450

Table 3.2: Model parameters of each imaging system (see Table 3.1) determined through minimization.

The results of the point-by-point dose comparison between experimental and theoretical values are summarized in Table 3.3. This is illustrated visually in Figure 3.3. Averaging over all setups, all imaging systems showed an agreement between theoretical absorbed dose in the dosimeter and measurements within 1.5 %.

	Source			Detector			
System	Total	f_1	f_3	Total	f_1	f_2	f_3
#1	1.4 ± 5.1	2.9 ± 1.7	-12 ± 5.4	1.8 ± 6.5	-2.1 ± 2.4	4.0 ± 1.3	3.6 ± 10
#2	-0.48 ± 3.5	-1.2 ± 1.6	0.78 ± 5.1	-3.7 ± 9.9	-2.3 ± 4.0	-2.8 ± 5.8	-6.9 ± 19
#3	0.45 ± 2.8	0.97 ± 2.1	-6.3 ± 1.1	-2.4 ± 5.7	-0.86 ± 1.3	0.63 ± 4.2	-7.5 ± 7.3

Table 3.3: For all systems (see Table 3.1), results of the source and the detector model verification expressed in terms of the relative difference (in %) averaged over all voltages. The total relative difference, averaged over all filtration, and the relative to each filtration are shown in separate columns.

For the detector response verification, three irradiation setups were evaluated: f_1 (no filter), f_2 (8 mm Al) and f_3 (0.3 mm Cu + 0.5 mm Ag). For each imaging system, the scintillator length, which was an unknown parameter of the detector model, was determined by minimizing the cost function described in Equation 3.5. The resulting CsI lengths are shown in Table 3.2. The results of the detector response model verification are summarized in Table 3.3 and it is illustrated in Figure 3.4. In general, good agreement between the theoretical and the measured energy deposited in the detector is obtained for setup f_1 and f_2. For the setup f_3, larger discrepancies are observed, particularly for the imaging system #2. Nevertheless, when taking into account all the setups, the

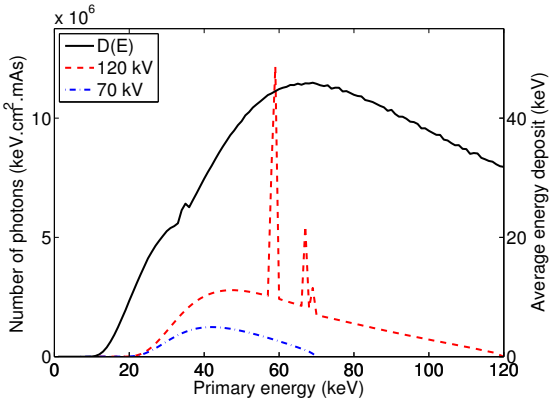

(a)

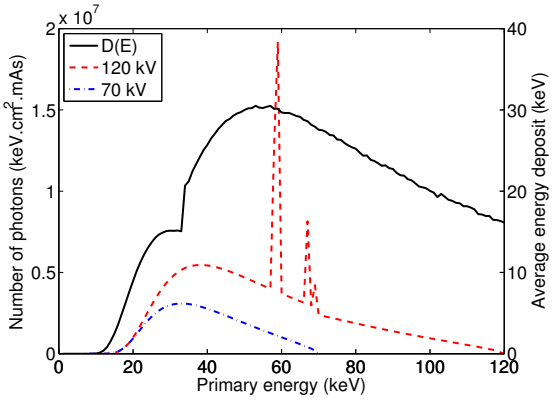

(b)

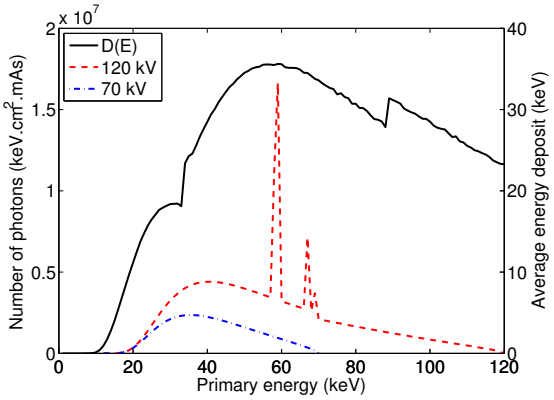

(c)

Figure 3.2: Source and detector response models built for the kV-CBCT unit of system # 1 (a), # 2 (b) and # 3 (c) (see Table 3.1). Left axis: plot of the 70 kV and 120 kV X-ray source spectra. Right axis: Monte Carlo simulated detector response in energy.

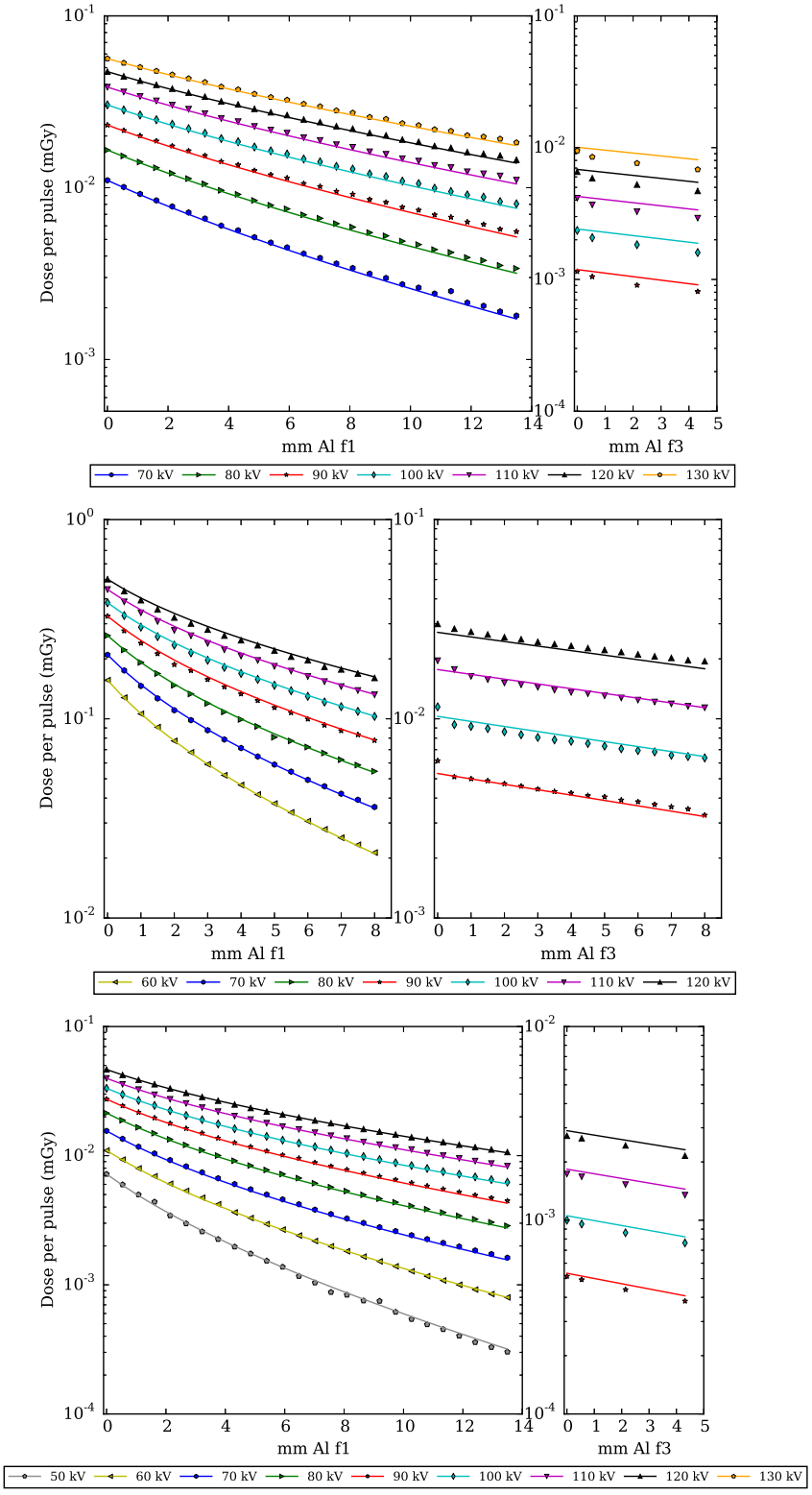

Figure 3.3: From top to bottom: results of the source model verification for the imaging system # 1, # 2 and # 3 (see Table 3.1). Semi-logarithmic plot of the absolute dose per pulse as a function of the aluminum thickness interposed in the beam for several tube voltages. Left: original beam spectrum (i.e. filtration f_1); right: spectrum with filtration f_3. Markers represent the experimental dose readouts and the continuous lines the theoretical dose values.

theoretical total energy deposit in the detector agreed with measurements to within 4% for all imaging systems.

The results of the sensitivity analysis for the three imaging systems are shown in Figure 3.5. Systems # 2 and # 3 are more sensitive to variations in the anode angle, inherent filtration and scintillator length than system # 1.

3.2.4 Discussion

In this work, an experimental procedure has been developed to calibrate and validate any model of source and detector responses of a CBCT unit.

In the application example, the unknown parameters of the models were determined by minimizing a defined cost-function using the procedure measurements. The results of the source model verification showed worse agreement of the f_3 filter setup for the imaging system #1 compared to the others. Either the process of minimizing the cost function did not provide the optimal inherent filtration thicknesses, because there were fewer data points in f_3 compared to f_1, or the f_3 data set points out an error in the model for highly hardened beams. In the detector model verification, larger discrepancies were observed for the setup f_3, particularly for the imaging system #2. This could be due to a limitation or error in the model, e.g., a wrong density or thickness estimation in the simulated stack of layers. Nevertheless, even if the source model accuracy for the different setups was not optimal, it seems to have little influence on the detector model accuracy.

The main difference between our method and those found in the literature is that we generate many data points using different filtering materials. Moreover, the measurement and the prediction of doses in air are compared for each filter setup instead of comparing the HVLs only. Due to the discontinuities in the spectrum range, materials such as silver, gold and tungsten, modulate the initial spectrum in a different way compared to aluminum. The introduction of copper and silver filtration in the verification process seems to highlight errors or limitations in the source and in the detector model that were not noticeable with the aluminum filtration only.

The materials required to set the experimental framework are easily accessible and often available in hospitals, i.e., attenuation filters of different materials for both models, and a dosimeter working in the range of CT imaging voltages. This procedure is interesting for the physicists that need a forward model benchmarked against experimental data, a prerequisite in many applications, some of which have been listed in the introduction.

The protocol has only been illustrated to a single direction for the source and the detector of three CBCT scanners but other directions may be validated by repeating the procedure, using 2D dose detectors or applying the method developed by Randazzo *et al* [Randazzo and Tambasco, 2015] which is complementary to the current protocol. To compute the theoretical dose values in the 2D plane and thus, to account for the heel effect in the anode-cathode direction, analytic models of the heel effect that require few dose points measurements in the 2D plane might be used [Braun et al., 2010].

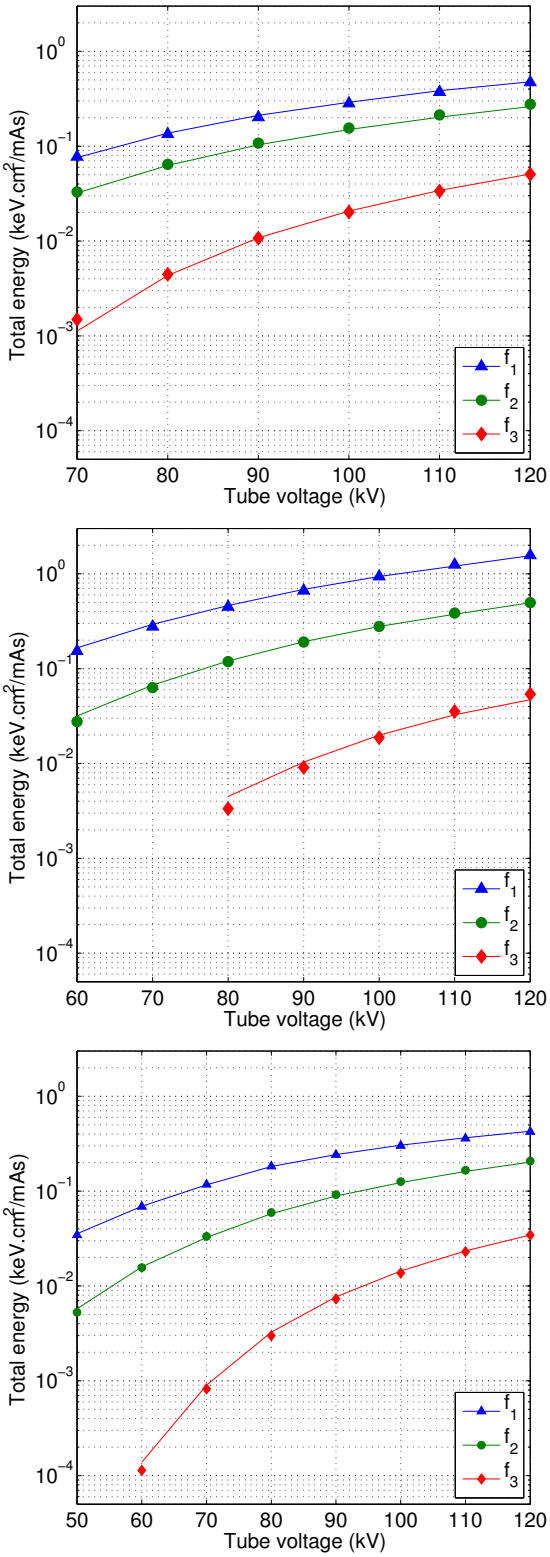

Figure 3.4: From top to bottom: results of the detector response verification for the imaging system # 1, # 2 and # 3 (see Table 3.1). Semi-logarithmic plot of the theoretical (continuous line) and measured (markers) energy deposited in the detector for increasing X-ray tube potentials divided by the mAs. The method was repeated using different spectra filtration: f_1, f_2, f_3.

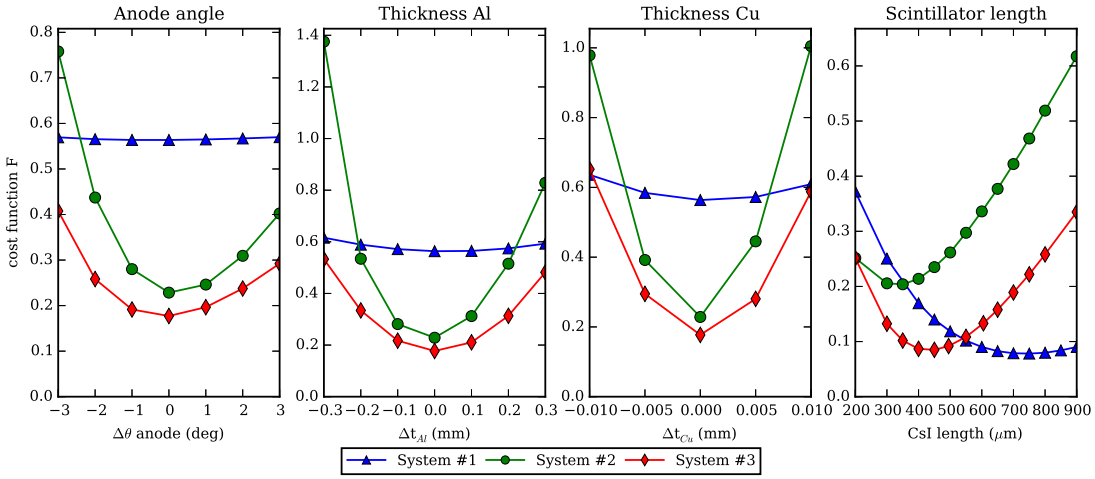

Figure 3.5: Sensitivity analysis results in terms of the cost function as a function of the parameters of the source and the detector model. Variations were centered at the optimal values, summarized in Table 3.2, determined previously in the model calibration stage.

According to the sensitivity analysis, very hardened beams (e.g. system # 1) are less sensitive to variations in the source model parameters because anode angle or inherent filtration variations do not introduce significant changes in the photon yield. The detector response was sensitive to the scintillator length but it was characterized by a flat cost function around the optimum. In other words, the scintillator lengths in the 10% interval of the optimal CsI length would produce similar results.

The limitation of the current validation procedure is that when parametric models with many unknowns are used, like in the application example (section II.B), the experimental data are also used for the model calibration. In such cases, one needs to have independent sets of measurements for the validation. Otherwise, this procedure is only an indicator of the goodness of fit of our calibration. However, if the model of the CBCT scanner is pre-calibrated, this procedure can be exclusively used for validation. Presumably, the user would anyway further validate the model depending on its use, e.g. using a beam stop array for scatter simulations. To complement our sensitivity analysis, it would be of additional value to evaluate the impact of measurement uncertainties.

3.2.5 Conclusion

In this work, a calibration and validation procedure for any model of the source and the detector of a CBCT unit has been described. The experimental procedure requires instruments and equipments that are readily available in many clinical or research facilities. The protocol has been successfully applied to simple models of three commercial X-ray imaging systems.

3.3 Assessment of the Imaging Ring model validity

In the framework of this PhD. thesis, a model for the Imaging Ring system was required to perform image-simulations in GATE and to perform dual-energy decomposition with real data. Reliable information from the manufacturer is required to built the models of the source and the detector response of the CBCT unit. Unfortunately, most of the time this information is not available or it is provided with big uncertainties (e.g. CsI length from 550 µm to 800 µm). Consequently, the parametric models for the source and the detector response described in the previous section were considered. The model with three unknowns, i.e. anode angle, thickness of Al and thickness of Cu (which represent the inherent tube filtration), referred to the *bi-material* model in the following, was built for the X-ray source. The thickness of the scintillator layer (CsI) was the unknown of the parametric model for the detector.

In the course of this work, the Imaging Ring unit used for dual-energy acquisitions underwent some upgrades and modifications. For example, a flattening filter made of aluminum with an optimized shape was installed in the last set of experiments to reduce the heel effect (Figure 3.6). Consequently, after every major modification, it was required to check the Imaging Ring models determined in Section 3.2.

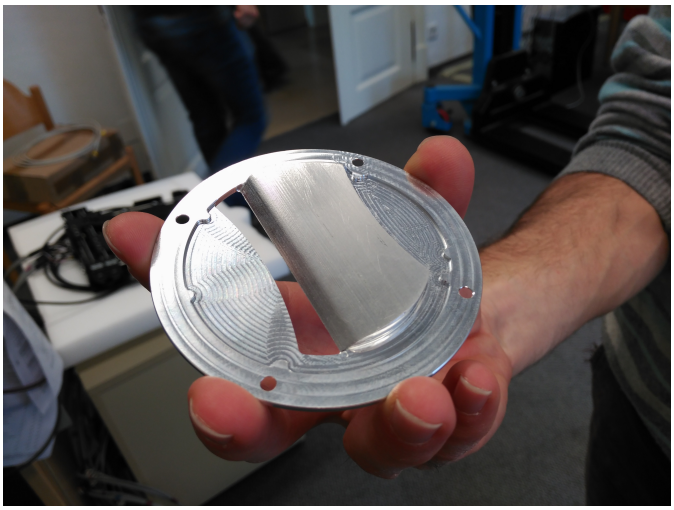

Figure 3.6: Flattening filter to reduce the heel effect.

To that end, a simplified procedure was implemented to simultaneously assess the source and the detector models validity.

3.3.1 Experimental setup

1. The same high-purity ($\geq$99.9%) filters of Al, Cu and Ag of known thicknesses used in Section 3.2 were arranged following a staircase pattern. Three different filter arrangements were considered to have as much filter combinations as possible. X-ray collimation jaws were adjusted to illuminate only the desired portion of filters

and thus reduce scatter contamination (see Figures 3.7, 3.8 and 3.9).

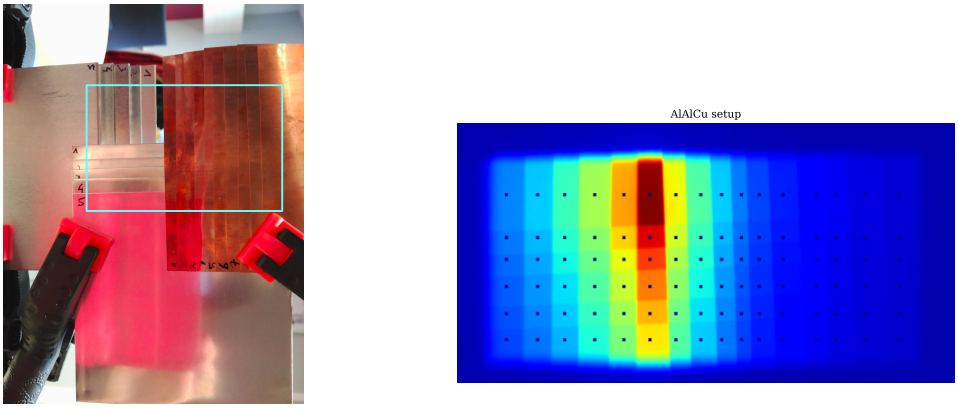

(a) (b)

Figure 3.7: a) Picture showing the first filter arrangement: (Al 2 mm, Al 0.5 mm, Cu). The blue rectangle shows the collimator aperture. b) Figure showing the ROIs placement on transmission images.

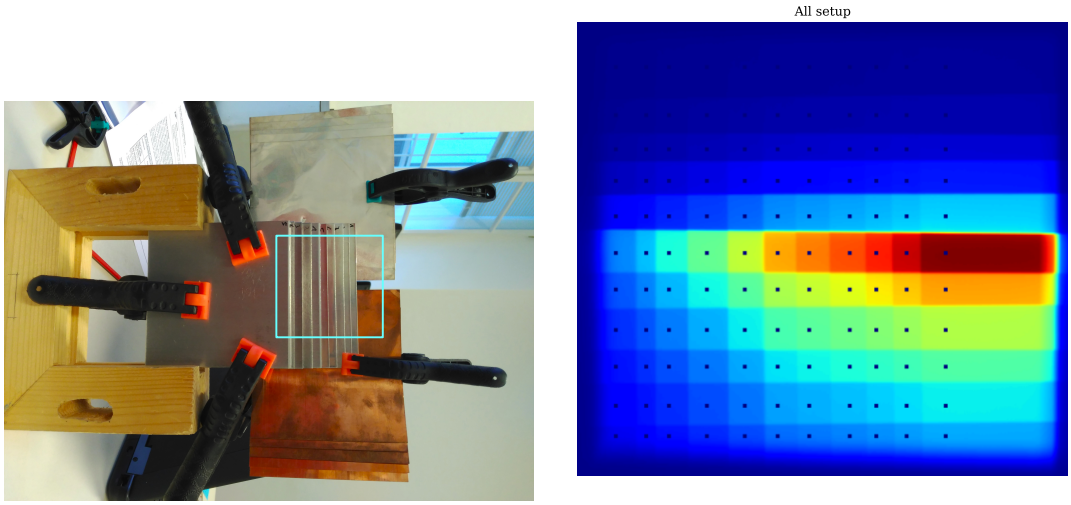

(a) (b)

Figure 3.8: a) Picture showing the second filter arrangement: (Al 2 mm, Al 0.5 mm, Cu, Ag). The blue rectangle shows the collimator aperture. b) Figure showing the ROIs placement on transmission images.

2. The source and the flat panel detector were oriented in front of each other according to the irradiation geometry employed in dual-energy acquisitions (see Figure 3.10).

3. For each filter setup and tube voltage, between 200 and 400 transmission images

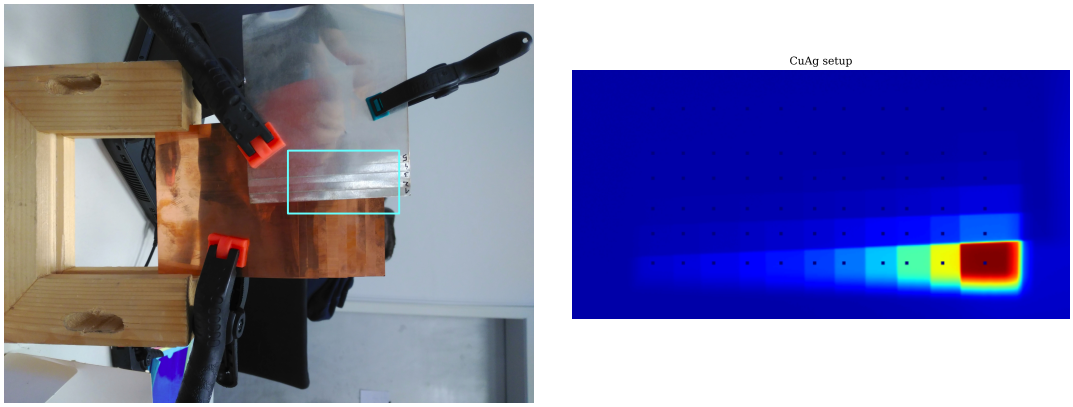

(a) (b)

Figure 3.9: a) Picture showing the third filter arrangement: (Cu, Ag). The blue rectangle shows the collimator aperture. b) Figure showing the ROIs placement on transmission images.

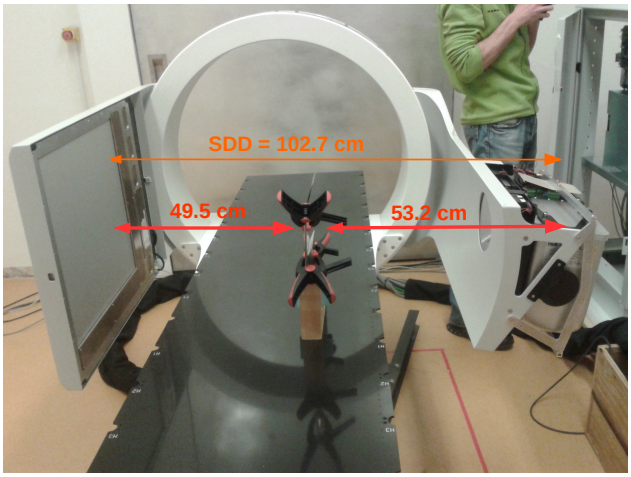

Figure 3.10: Irradiation setup to assess the source and the detector models validity.

were acquired with all corrections activated, i.e. lag, fluence and bad pixels.

3.3.2 Post-processing

1. A 3×3 pixels Region-Of-Interest (ROI) was placed at the center of each homogeneous area of the image, corresponding to one step of the step-phantom. All transmission images (I) were normalized to the transmission value of the ROI placed in air (I_0), without filtration. The spatial mean of the signal in each ROI and the temporal mean of the signal over all frames was computed.

2. To reduce the degrees of freedom, the nominal anode angle of 10° was considered. Non-filtered spectra at 10° and tube voltages ranging from 60 kV to 120 kV at 10 kV steps were retrieved from SpekCalc. These spectra were further filtered with 102.7 cm of air (source-to-detector distance of the Imaging Ring system). The *bi-material* source model described in Section 3.2 was used. The unknown parameters of this model, which were the thicknesses of Cu and Al, were determined through a minimization process with the step-phantom transmission measurements.

3. The detector response in energy was generated in GATE for scintillator thicknesses of CsI ranging from 350 µm to 800 µm (unknown parameter of the detector model) as described in Section 3.2. The CsI thickness was determined through a minimization process with the step-phantom transmission measurements.

4. The inherent Al filtration was increased from 0.0 to 3.0 mm at steps of 0.1 mm, the inherent Cu filtration was increased from 0.0 to 0.3 mm at steps of 0.01 mm, and the CsI length was varied from 350 to 800 µm at steps of 50 µm. A minimization process of the following cost function was carried out to determine the optimal model parameters:

$$F = \sum_{j,k} \left(\frac{att_{j,k}^{\text{exp}} - att_{j,k}^{\text{theo}}}{att_{j,k}^{\text{exp}}} \right)^2 \tag{3.6}$$

   where the index j and k refers to the j-th filter setup and k-th voltage, respectively. $att_{j,k}^{\text{exp}}$ are the experimentally determined attenuation values and $att_{j,k}^{\text{theo}}$ are the theoretically computed attenuation values making use of the source and the detector models. The attenuation values were computed as $-\ln(\text{I}/\text{I}_0)$, where I are transmission values and I_0 the transmission values of the ROIs positioned in air.

5. This procedure was implemented twice along the duration of the thesis. For the experimental session conducted in March 2016, the inherent filtration of the bi-material source model (Al and Cu) and the CsI length that minimize the cost function F were **0.3 mm Al**, **0.06 mm Cu** and **550** µm, respectively; whereas, for the experimental session conducted in November 2016, after the installation of the flattening filter, the parameters of the model were **0.6 mm Al**, **0.15 mm Cu** and **550** µm. These parameters differ from the ones determined in section 3.2 because the changes made to the system modified the photon yield. These new values and the corresponding models were used to decompose dual-energy real data.

3.4 Scatter correction

One of the well-known limitations of CBCT imaging is the scatter contamination in the projection images due to the large X-ray illumination volume [Zhu et al., 2009].

The physical phenomenon responsible of these image artifacts is Compton scattering (see section 1.2.2.2) and the main consequences are: shading and streak artifacts, loss of CNR and wrong HU quantification [Ohnesorge et al., 1999; Siewerdsen and Jaffray, 2001; Siewerdsen et al., 2006; Sossin et al., 2014]. Scatter contamination can either come from the object being imaged or from the flat-panel detector. In the CT diagnostic energy range, scatter within the flat-panel detector and housing cause a low-spatial frequency signal superimposed to the primary signal, known as *scatter-glare*, visible in the acquired images [Poludniowski et al., 2011]. In the high energy range, typically used in industrial NDT, the contribution of the detector scatter becomes more substantial and cannot be neglected [Bhatia et al., 2016].

On the detector side, scatter mitigation techniques include the use of anti-scatter grids, which prevent a certain fraction of scattered photons to reach the detector at the cost of attenuating the flux of primary radiation and increasing patient dose [Kyriakou and Kalender, 2007], and the air-gap method which consists in increasing the distance between the object and the detector at the cost of reducing the size of the FOV and increasing the source intensity for divergent beams. On the source side, scatter can be reduced by proper collimation and employing bow-tie filters [Rührnschopf et al., 2011; Ruhrnschopf and and Klingenbeck, 2011].

Scatter correction procedures consist of two steps: scatter estimation and scatter compensation through data post-processing [Rührnschopf et al., 2011; Ruhrnschopf and and Klingenbeck, 2011]. Scatter can be estimated by measurement or by mathematical modeling. Beam-blockers or collimator-shadow techniques are used to estimate the scatter empirically. Mathematical modeling techniques include scatter deconvolution and scatter modeling (i.e. either analytically or based on MC simulations).

Scatter deconvolution methods, also referred to as Scatter Kernel Superposition (SKS), model the X-ray cone beam as an array of pencil beams that interact with the object and each one has its own Point-Spread Function (PSF) or scatter kernel [Ohnesorge et al., 1999; Bertram et al., 2006; Star-Lack et al., 2009; Sun and Star-Lack, 2010]. The PSFs can be determined either experimentally or through MC simulations. Typically, these kernels are assumed to be symmetric and invariant all along the image. However, as the magnitude and spatial distribution of scatter is object dependent, some authors showed that this assumption can lead to important scatter estimation errors and, thus, adaptive asymmetric kernels are preferred to improve the scatter transport modeling [Star-Lack et al., 2009; Sun and Star-Lack, 2010].

The IR has a scatter deconvolution method implemented in the image reconstruction pipeline. Its scatter kernels are estimated through transmission measurements (field size of 5×5 cm^2) interposing several slabs of solid water to the X-ray beam and recording the scatter-to-primary ratio. Transmission signal is described as the sum of the primary signal and the scatter contribution. Due to the geometry and the position of the collimation jaws, there is more head scatter in the u-direction than in the v-direction. This effect is partially solved by collimating the jaw in the u-direction. The scatter signal is fitted by two Gaussian distributions and substracted to the transmission signal by deconvolution in a pixel-by-pixel basis.

Thanks to the dynamic collimator jaws, the IR system offers the possibility to perform dual-energy CBCT acquisitions with a slit of 2 cm or 3 cm at the isocenter simulating a fan beam acquisition. Technically, it would be possible to collimate much tighter but then a correction model for the penumbra of the jaws would be required. In this thesis, to take advantage of the signal behind the jaws, which the scatter correction implementation in the IR pipeline does not use, the *collimator-shadow* technique proposed by Siewerdsen *et al* [Siewerdsen et al., 2006] has been implemented off-line to correct for the remaining scatter when performing CBCT acquisitions using the dynamic collimator jaws. Some comparative studies have concluded that the collimator-shadow approach was one of the most accurate empirical techniques available [Akbarzadeh et al., 2010].

The method proposed by Siewerdsen *et al* [Siewerdsen et al., 2006] consists in measuring the scatter fluence in the shadow of the collimation. It assumes that the signal behind the collimator jaws is exclusively due to X-ray scatter and that the transmission through the collimator leaves is negligible. We define v as the rotation axis (second coordinate of each projection) and u as its orthogonal direction (first coordinate of each projection). The 2D scatter fluence $S(u, v)$ is determined by fitting a polynomial between pixel values measured along the top and the bottom edges of the detector behind the collimator jaws (S_{top} and S_{bot} in Figure 3.11). A longitudinal fit (in the v direction) is performed for each row in the u direction. The same operation is repeated for each projection m in order to get a 3D scatter fluence $S(u, v, m)$. As transmission values are equal to the sum of primary signal and scatter contribution, the scatter fluence is substracted from each measured projection $M(u, v, m)$ to estimate the primary radiation contribution $P(u, v, m)$ to the detector signal:

$$P(u, v, m) = M(u, v, m) - S(u, v, m). \tag{3.7}$$

The position of the collimation jaws is provided by the IR system for each projection. Using Siewerdsen's notation, the scatter signal was measured behind the top and the bottom jaws in a $S_{\text{top}} = S_{\text{bot}}$=15 mm region with a z_0=3 mm margin to account for the jaws penumbra and uncertainties in the jaws positions. The other parameters of the algorithm were: v_{fit}=2 order of the polynomial fit, θ_{fit}=1 no projection-to-projection smoothing and u_{fit}=7 pixels of lateral smooting with a Gaussian filter.

To illustrate the implementation of the method, a set of 610 projection images of the CIRS Dynamic Thorax Phantom Model 008A (Norfolk, VA, Norfolk, VA, United States of America) acquired at 120 kV filtered with Cu and Ag with a slit of 3 cm at the isocenter was selected. This set of acquisitions was chosen among others due to the larger scatter contamination. Images of the linear attenuation coefficient were reconstructed using the Filtered-Back Projection (FBP) algorithm implemented in RTK. The phantom was segmented into the four main materials (plastic water, lung, trabecular bone and cortical bone) and the reference image at 120 kV/CuAg was computed at the effective monochromatic energy of the spectrum (calculated accounting for the detector response and the polychromatic energy spectrum of the IR) using the chemical composition and mass density values of each material provided by the manufacturer.

Figure 3.12a shows the second order polynomial fits along v for different u values for

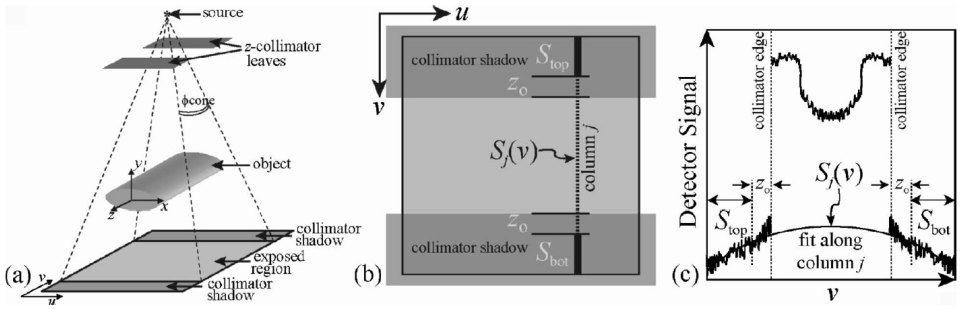

Figure 3.11: a) Schematic illustration of a cone-beam CT irradiation. Collimator jaws limit the FOV in the longitudinal direction (v) and shadow the top (S_{top}) and bottom (S_{bot}) edges of the detector. b) Top view of the detector in which the detector regions shadowed by the collimator blades are visible. c) Signal between top and bottom collimator shadows columnwise interpolated in the v direction ($S_j(v)$) to estimate the 2D scatter fluence $S(u, v)$ across the FOV. Figure extracted from [Siewerdsen et al., 2006].

a projection image, whereas Figure 3.12b shows the line profiles for a given u relative to the transmission signal (primary + scatter), the primary signal and the scatter signal. The scatter contribution is about 20% of the primary signal.

Figure 3.13 shows the reconstructed images of the linear attenuation coefficient without scatter correction (left), with Siewerdsen's scatter correction (middle) and with the current scatter correction version implemented in the IR reconstruction pipeline (right). It is worth to mention that the IR scatter correction at the time of the experimental session was insufficiently configured, especially regarding the integrated scatter distance correction –which is required for accounting for the varying object to detector distance in non-isocentric datasets. Figure 3.14 shows two line profiles across the reference image, the uncorrected image and the two scatter corrected images. As reported in the literature [Akbarzadeh et al., 2010], due to scattered radiation, a reduction of the attenuation coefficient is observed for most tissues.

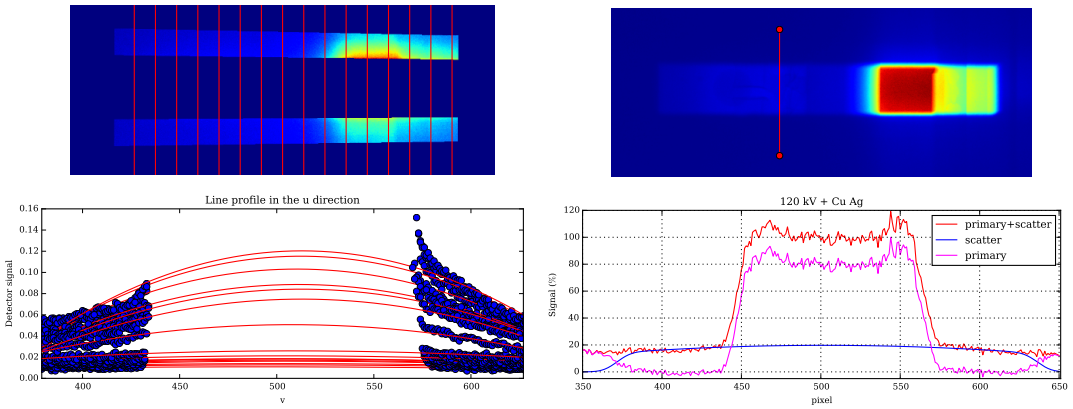

(a) Top: signal behind the collimation jaws; bottom: second order polynomial fits along v for different u values to derive the scatter fluence $S(u, v)$.

(b) Top: transmission signal and line profile for a given u (red); bottom: transmission signal, primary signal and scatter contribution in percentage with respect to the primary signal.

Figure 3.12: Example of implementation of the collimator-shadow scatter correction method. Projections relative to the CIRS Thorax phantom acquisitions at 120 kV filtered with Cu and Ag. The scatter contribution within the object (blue area) is about 20% of the primary signal.

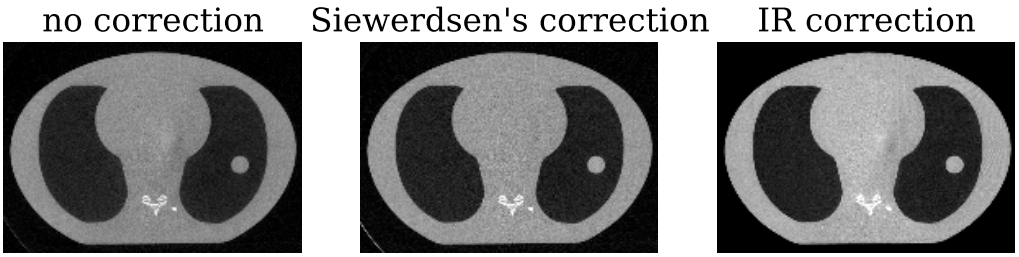

Figure 3.13: Comparison of reconstructed CT images without scatter correction (left), scatter corrected using Siewerdsen's method (middle) and with the IR scatter correction implemented at the time of the experiment (right). Colorbar from [0, 0.3] cm^{-1}.

When testing Siewerdsen's method to projections of the CIRS Electron Density Phantom Model 062M (Norfolk, VA, United States of America) acquired with a slit of 3 cm at the isocenter, no improvement was observed. The CIRS phantom is only 5 cm in the v direction and, therefore, there is a sharp edge in the S_{top} and S_{bot} areas used for the scatter estimation. In the part where there is no phantom, a larger amount of scatter escapes the object and reaches the detector compared to the part between the jaws where most of the scatter is attenuated by the object itself. The larger amount of

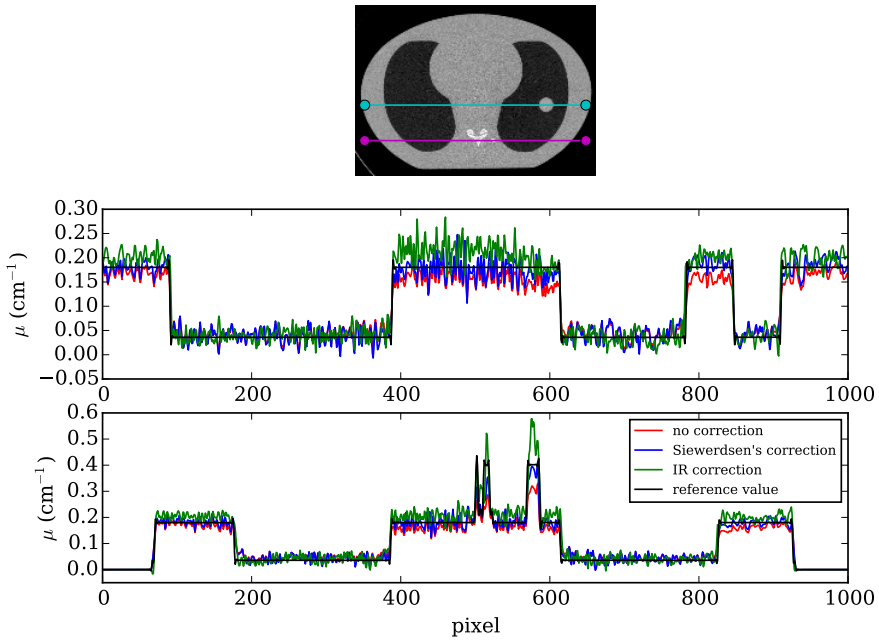

Figure 3.14: Line profile comparison of reconstructed CT images without scatter correction (red), with Siewerdsen's scatter correction (blue) and with the IR scatter correction implemented at the time of the experiment (green), with respect to the reference value (black). Middle plot corresponds to the cyan line profile and bottom plot to the magenta line profile. Colorbar from [0, 0.3] cm^{-1}.

scatter near the edges of the object than behind the object is a known phenomenon that can be observed with MC simulations, e.g., in Fig.1 of [Thing et al., 2013]. Nevertheless, Siewerdsen's approach was found adequate to correct IR CBCT acquisitions using the dynamic collimation jaws when the object shape being imaged was slowly varying around the jaw borders.

3.5 Conclusion

The main features of the Imaging Ring (IR) system, a scanner developed for IGRT and at the center of this work, have been described. This CBCT unit presents additional features such as a X-ray source with fast-kV switching capabilities synchronized with a filter wheel which allows multi-energy imaging. In particular, the thesis is focused on exploiting the dual-energy CBCT capabilities of this system for proton therapy applications. To that end, a parametric model for the source and the detector response of the IR system were proposed. These models were further calibrated and validated through an experimental procedure, tested also on other two commercial CBCT units. A simplified experimental procedure was developed to simultaneously assess the validity of the IR models after system upgrades. Finally, to take advantage of the signal behind

the jaws when performing dual-energy CBCT phantom acquisitions with a 3 cm slit at the isocenter, i.e. simulating a fan beam acquisition, the collimator-shadow technique was implemented off-line to correct for the remaining scatter with convincing results.

Chapter 4

Stopping-power estimation from dual-energy CT

Contents

The range of protons in patients is determined from the stopping-power ratio (SPR) of tissues relative to water along the beam path. The stoichiometric calibration proposed by [Schneider et al., 1996] has been widely adopted in the current practice to convert planning X-ray CT images into SPR maps based on single-energy CT (SECT). However, a 3.5% range uncertainty has been associated with this conversion [Yang et al., 2012]. The proton SPR can be derived from dual-energy CT (DECT) data and it has been shown that DECT imaging has the potential to improve the accuracy of the SPR estimation compared to conventional single-energy CT (SECT) [Yang et al., 2010; Hansen et al., 2015; Hünemohr et al., 2013; Zhu and Penfold, 2016]. Several algorithms based on DECT have been proposed to predict the SPR or the intermediate variables required to compute the SPR with the aim of improving the accuracy of proton dose calculations, e.g., the relative electron density (RED), the effective atomic number (Z_{eff}) or the logarithm of the mean excitation energy [Yang et al., 2010; Saito, 2012; Hünemohr et al., 2014a,c; Landry et al., 2013b; Bourque et al., 2014; Van Abbema et al., 2015; Ramos Garcia et al., 2016; Han et al., 2016; Möhler et al., 2016; Taasti et al., 2016]. Section 2.4 described in detail the two main approaches to perform dual-energy decomposition, i.e. image- and projection-based decomposition domains. In projection-based methods, material decomposition is performed prior to image reconstruction, and for image-based methods the decomposition takes place after image reconstruction. Today, no consensus has emerged as to what the best decomposition method and domain are for the SPR estimation. The aim in this chapter is to:

- list the existing definitions for the effective atomic number;

- review the existing methods to determine the SPR from DECT data;
- describe two novel approaches to determine the SPR from DECT;
- compare the existing and novel approaches in terms of SPR accuracy;
- compare the image- and the projection-based decomposition domains in terms of SPR accuracy;
- determine the SPR from real data using the Imaging Ring system.

4.1 Effective atomic number definition

Many equations describing the radiation-matter interaction processes are dependent on the atomic number (see sections 1.1.2 and 1.2.2). To describe these interactions for compounds (e.g. water) or mixtures (e.g. soft tissue or bone), it is necessary to define an *effective* atomic number (Z_{eff}). For photon interactions, the effective atomic number was first introduced by [Mayneord, 1937]. In the literature, there are mainly two definitions for the Z_{eff}: a power law approach (section 4.1.1) and based on the parametrization of the electronic cross section (section 4.1.2).

4.1.1 Power law equation

To calculate the Z_{eff} of a compound or mixture, a power law method was proposed [Mayneord, 1937]:

$$Z_{\text{eff}} = \left[\sum_i^N \lambda_i \cdot Z_i^m \right]^{1/m} ; \qquad \lambda_i = \frac{\omega_i \cdot \frac{Z_i}{A_i}}{\sum_i^N \omega_i \cdot \frac{Z_i}{A_i}} \tag{4.1}$$

where λ_i is the fractional contribution of the i-th element to the total number of electrons in the mixture, such that $\sum_i \lambda_i = 1$, ω_i is the mass fraction of the i-th element having atomic number Z_i and atomic mass A_i (g/mol).

This is an approximate expression and the exponent m is an empirically determined parameter affected by the spectra of photon beams. A short literature overview was conducted to list the different m-exponent values. In the 1930s, photon sources were restricted to low energy X-ray units, i.e. with photon energies ranging from 30 to 80 keV where the photoelectric effect is dominant over the Compton process. For this reason, a m-exponent value of 2.94, that came from an empirical formula for the photoelectric process [Khan, 2003], was recommended by Mayneord. In 1977, Brooks [Brooks, 1977] provided an example on how to determine the m-exponent. In Fig. 1 of [Brooks, 1977], there is a log-log plot of the atomic cross section σ_p (barns/atom) for photoelectric absorption, coherent scattering and binding energy correction as a function of the energy, for various elements. Empirical fits to the data using the equation $\sigma_p = B\ E^A$ resulted in a slope of A=-2.8 (i.e. $\sigma_p = B\ E^{-2.8}$) for a number of common elements. In Fig. 2

of [Brooks, 1977], the log-log plot of the energy independent term of the atomic cross section (B) as a function of the atomic number for 11 elements resulted in a slope of 4.1 (i.e. $\sigma_p \propto Z^{4.1}$). A multiplicative factor equal to $10^{-24}\rho_e/Z$ was required to convert from σ_p in barns/atom to linear attenuation coefficient μ_p in cm^{-1}, which resulted in the final m-exponent of 3.1. In 1983, Johns and Cunningham [Johns and Cunningham, 1983], using the elemental compositions of a variety of materials and the tabulated values for the elemental electronic cross sections, computed the Z_{eff} for air, water, fat, muscle, bone, polystyrene, Lucite, LiF and ferrous sulfate for energies from 30 to 80 keV. The value of m that gave the best fit ranged from 3.4 to 3.8 with most of the best fit values around 3.5. Finally, in most dual-energy decomposition algorithms, the Z_{eff} of a compound or mixture is defined using the power law of Equation 4.1. However, multiple m-exponent values are used in these publications (see Table 4.1) because, depending on the interaction processes considered and the photon energy range, the m-exponent differs.

Publication	m-exponent
[Bazalova et al., 2008b]	3.5
[Yang et al., 2010]	3.3
[Landry et al., 2011]	3.3
[Saito, 2012]	3.5
[Hünemohr et al., 2014c]	3.1

Table 4.1: m-exponents used in some dual-energy CT publications.

4.1.2 Parametrization of the electronic cross section

To avoid the ambiguity in determining the m-exponent value, Bourque *et al* [Bourque et al., 2014] proposed another definition of the Z_{eff} for mixtures and compounds based on a parametrization of the electronic cross section σ_e (section 1.2.2). For polychromatic radiations, the electronic cross section averaged over a given spectrum $\overline{\sigma_e}$ is given by:

$$\overline{\sigma_e}(Z) \equiv \int_0^{E_{max}} \sigma_e(Z,E)\ S(E)\ dE \tag{4.2}$$

where $\sigma_e(Z,E)$ represents the electronic cross section for a specific photon energy E and $S(E)$ is the normalized photon spectrum at energy E with $\int_0^{E_{max}} S(E) = 1$.

For any Z ($Z \in \mathbb{R}$, $Z \geq 1$) and for a given photon spectrum or monochromatic energy, Bourque *et al* defined the parametric electronic cross section $\widehat{\sigma_e}$ as follows:

$$\widehat{\sigma_e}(Z) \equiv \sum_{m=1}^{M} a_m\ Z^{m-1} \tag{4.3}$$

where the coefficients a_m were obtained using a least square fit on tabulated electronic cross section data from the NIST database [Hubbell and Seltzer, 2004] over a range

$Z \in [Z_{\min}, Z_{\max}]$. M is the order of the fit that guarantees $\widehat{\sigma_e}(Z) = \sigma_e(Z)$ for Z integers. There is a one-to-one relation between the electronic cross section, either averaged over a polychromatic spectrum or for a monochromatic energy, and the atomic number over a range $Z \in [Z_{\min}, Z_{\max}]$. It means that there is an inverse function $\widehat{\sigma_e}^{-1}$ such that

$$Z = \widehat{\sigma_e}^{-1}(\sigma_e). \tag{4.4}$$

By analogy with the mixture rule [Jackson and Hawkes, 1981], the electronic cross section of a compound or mixture $\sigma_{\text{e,med}}$ can be computed as follows:

$$\sigma_{\text{e,med}} = \sum_i \lambda_i \ \sigma_e(Z_i) \tag{4.5}$$

In practice, if the electronic cross section of a compound or mixture is known for a given photon spectrum, the effective atomic number of a medium Z_{med} is defined as follows: *the parametric electronic cross section* $\widehat{\sigma_e}$ *evaluated at* Z_{med} *equals the electronic cross section of the medium averaged over the spectrum* $\sigma_{\text{e,med}}$

$$\widehat{\sigma_e}(Z_{\text{med}}) = \sigma_{\text{e,med}} \tag{4.6}$$

and thus:

$$Z_{\text{med}} \equiv \widehat{\sigma_e}^{-1}(\sigma_{\text{e,med}}) \tag{4.7}$$

One can note that, if $\widehat{\sigma_e}$ is a bijective function, this definition yields a unique Z_{med}. For this reason, the fit of $\widehat{\sigma_e}(Z)$ has to be limited in a region where there are no discontinuities with Z due to K-shell (or others) discontinuities. Despite the fact that this definition depends on the photon energy spectrum, Z_{med} of human tissues weakly varies with the photon spectrum in the range of CT imaging energies [Bourque et al., 2014].

4.2 State of the art

Many DECT-derived SPR prediction approaches determine the proton SPR from Bethe's equation without correction terms (see Equation 1.12) [Schneider et al., 1996; Yang et al., 2010]. To calculate SPRs from this equation, the relative electron density (RED) and the logarithm of the mean excitation energy of tissues (ln I_m) and water (ln I_{w}) are needed as input. Most DE algorithms decompose into RED [Saito, 2012], Z_{eff} [Landry et al., 2013b] or RED and Z_{eff} [Bazalova et al., 2008b; Yang et al., 2010; Landry et al., 2011; Hünemohr et al., 2013, 2014a,c; Bourque et al., 2014; Van Abbema et al., 2015; Ramos Garcia et al., 2016].

Yang *et al* [Yang et al., 2010] proposed a linear relationship between Z_{eff} and ln I_m based on a calibration with known human biological tissues extracted from [ICRU, 1989; White et al., 1987]. The Z_{eff} of human tissues was computed through equation 4.1 using an m-exponent of 3.3 and the tabulated chemical composition. The ln I_m of tissues was calculated through the Bragg additivity rule using the tabulated chemical composition

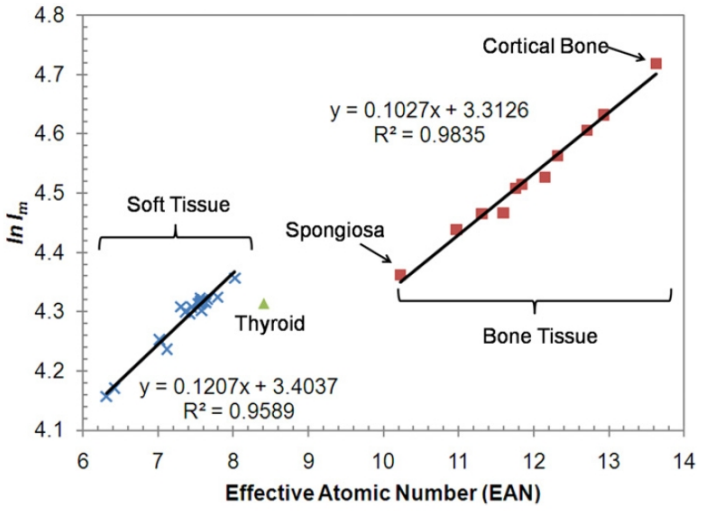

Figure 4.1: Linear relationship between ln I_m and Z_{eff} of 34 standard human biological tissues extracted from [ICRU, 1989; White et al., 1987]. The value of ln I_m is calculated through the Bragg additivity rule. Two separate linear relationships are proposed: soft tissue and bone tissue groups. Figure extracted from [Yang et al., 2010].

of tissues and the elemental I-values were taken from Table 2.8 and 2.11 in the [ICRU, 1993]. One limitation of this approach is the gap between the group of soft tissues and the group of bone tissues (see Figure 4.1). Due to volume averaging, CT voxels of a patient might fall within this Z_{eff} gap [Möhler et al., 2016] and, therefore, the ln I_m would not be defined.

To overcome this limitation, Bourque *et al* [Bourque et al., 2014] improved the relationship between Z_{eff} and I_m by proposing a continuous empirical parametrization for human tissues. In their implementation, the Z_{eff} of human tissues was computed through equation 4.7. Then, the Z_{eff}-range was divided into three regions and three piece-wise relations were proposed to fit the data (see Figure 4.3-1):

$$I(Z) = \begin{cases} e_1 Z + e_2 & \text{for Z} < \text{Z}_{min} \\ e_3 Z^5 + e_4 Z^4 + e_5 Z^3 + e_6 Z^2 + e_7 Z + e_8 & \text{for Z}_{min} \leq \text{Z} \leq \text{Z}_{max} \\ e_9 Z + e_1 0 & \text{for Z} > \text{Z}_{max} \end{cases} \tag{4.8}$$

In a pixel-by-pixel basis, Hünemohr *et al* [Hünemohr et al., 2014c] derived the mass fraction of the six main constituent elements of body tissues (i.e. hydrogen, carbon, nitrogen, oxygen, calcium, and phosphorus) from linear fits with RED and Z_{eff} information obtained through dual-energy decomposition. Afterwards, the Bragg additivity rule was used to compute the logarithm of the tissues I-value and Bethe's equation without any correction terms was used to compute the SPR assuming an I-value for water of 75 eV.

Kanematsu *et al* [Kanematsu et al., 2012] proposed a direct conversion between the RED and the SPR by establishing piece-wise linear relations between the RED and the SPR over RED of human tissues. A selection of 92 ICRU46 tissues of known chemical composition and mass density [ICRU, 1992], excluding obsolete and artificially extracted materials, were used for the calibration. To implement this curve (Figure 4.3-2), theoretical SPR values of these body tissues were computed using Bethe's equation for protons of 200 MeV. For proton energies in the range between 80 and 300 MeV, the variation of SPR with proton energy is negligible ($< 1\%$) [Arbor et al., 2015]. Consequently, this conversion can be assumed energy-independent [Farace, 2014].

Recently, Taasti *et al* [Taasti et al., 2016] proposed an empirical parametrization of the proton SPR directly based on the CT numbers of the low and the high energy DE spectra, avoiding all intermediate variables and steps. This method was found more robust to noise compared to other approaches [Hansen et al., 2015; Han et al., 2016]. A brief description of this method is provided in section 4.5.2.2.

4.3 Novel approaches

In the framework of the PhD thesis, two novel calibrated relations have been proposed to determine the proton SPR of tissues from dual-energy data. The starting point of both approaches is the output of the BMD projection-based decomposition method (see section 2.4.2.1), i.e. mass density images ϱ_i of the two basis materials (e.g. i=1: soft tissue and i=2: cortical bone). Electron density images relative to water (RED) can be derived from these mass density images for each pixel coordinate $\boldsymbol{x}$ as follows:

$$\mathrm{RED}(\boldsymbol{x}) = \frac{\varrho_1(\boldsymbol{x}) \left[\sum_i w_i \frac{Z_i}{A_i}\right]_1 + \varrho_2(\boldsymbol{x}) \left[\sum_i w_i \frac{Z_i}{A_i}\right]_2}{\rho_\mathrm{W} \left[\sum_i w_i \frac{Z_i}{A_i}\right]_\mathrm{W}} \tag{4.9}$$

where Z_i is the atomic number, A_i is the atomic mass and w_i is the elemental weight fraction for element i of the tabulated compounds 1, 2 and water (represented with the index W); ρ_W is the mass density for water. Furthermore, Virtual Monochromatic (VM) images at any energy E can be directly derived from the parametrization of the linear attenuation coefficient proposed by the BMD method:

$$\mu(\boldsymbol{x}, E) = \varrho_1(\boldsymbol{x}) \left(\frac{\mu}{\rho}\right)_1 (E) + \varrho_2(\boldsymbol{x}) \left(\frac{\mu}{\rho}\right)_2 (E). \tag{4.10}$$

From the existing relation between the linear attenuation coefficient and the electronic cross section (see Equation 1.15) [Jackson and Hawkes, 1981], an image of the electronic cross section at any energy E σ_e can also be determined from the reconstructed $\mu(E)$ image as follows:

$$\sigma_e(\boldsymbol{x}, E) = \frac{\mu(\boldsymbol{x}, E)}{N_A \left(\varrho_1(\boldsymbol{x}) \left[\sum_i w_i \frac{Z_i}{A_i}\right]_1 + \varrho_2(\boldsymbol{x}) \left[\sum_i w_i \frac{Z_i}{A_i}\right]_2\right)} \tag{4.11}$$

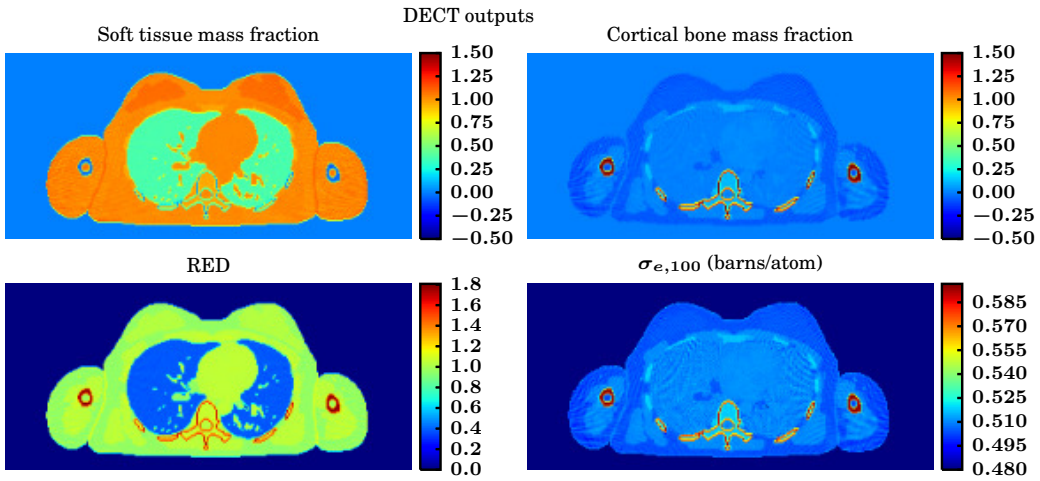

Figure 4.2: Dual-energy outputs of the BMD projection-based decomposition. From top to bottom and from left to right: soft tissue mass fraction image, cortical bone mass fraction image, relative electron density (RED) image and electronic cross section ($\sigma_{e,100}$) image reconstructed at 100 keV. Images relative to one slice of the ICRP female computation phantom.

Figure 4.2 shows the outputs of the BMD decomposition, i.e. mass fraction images of soft tissue and cortical bone of one slice of the International Commission on Radiological Protection (ICRP) female computational phantom [ICRP, 2009], and the derived outputs, i.e., the RED image and the electronic cross section image reconstructed at 100 keV ($\sigma_{e,100}$).

4.3.1 SPR from RED and ln(I)

This method consists in determining the proton SPR from the RED and the logarithm of the mean excitation energy using Bethe's equation without correction terms. The former is a direct BMD decomposition output, whereas the latter is derived through a novel piece-wise calibrated relation between σ_e and ln I_m for tabulated human tissues [ICRU, 1992] as illustrated in Figure 4.3-3. A 100 keV photon energy is chosen to perform the calibration because, in the presence of heavy metal objects, this photon energy falls within the optimal VM energy range to reduce metal artifacts [Li et al., 2012; Yu et al., 2012]. The ln I of human tissues is derived through the Bragg additivity rule using the tabulated chemical composition and the elemental I-values from Table 2.8 and 2.11 in the [ICRU, 1993]. The electronic cross section of a compound or mixture is computed through Equation 4.5 [Bourque et al., 2014].

An approach similar to this one, i.e. avoiding the derivation of the intermediate variable Z_{eff} and directly determining the ln I_m from DECT data, has been followed by two recently published works [Möhler et al., 2016; Han et al., 2016]. Han *et al*

[Han et al., 2016] proposed two linear models to determine the RED and the ln I_m as a function of the basis material images derived from the DECT BMD decomposition approach implemented in the image-domain [Williamson et al., 2006]. Two different materials basis were used: water and polystyrene for soft tissues, while water and aqueous $CaCl_2$ solution were chosen for bone tissues. On the other hand, Möhler *et al* [Möhler et al., 2016] factorized the SPR into RED and relative stopping number $\widehat{L}$ such that $\widehat{L} = L(I_m, \beta)/L(I_w, \beta)$. To derive the RED they suggested the approach of Hunemöhr *et al* [Hünemohr et al., 2014a], whereas for the $\widehat{L}$ they proposed a calibrated relation between the relative electron cross section $\widehat{\sigma_e}$ (obtained by dividing the measured relative attenuation coefficient by the RED) and the $\widehat{L}$ using known tissue base components or body tissues [Woodard and White, 1986; White et al., 1987].

4.3.2 SPR from RED and σ_e

The second method consists in directly determining the SPR from the RED and the σ_e images at a given energy E by establishing a relationship between σ_e and SPR over RED obtained through calibration with known human tissues [ICRU, 1992] (see Figure 4.3-4). As for the other method, the calibration is performed at a photon energy of 100 keV.

4.4 Comparison of SPR estimators

Two simulation-based studies were designed to compare, in terms of accuracy and precision, the procedures described in the previous section to estimate the SPR from DECT data.

The four calibrated relations that have been compared are illustrated in Figure 4.3 and they are summarized in Table 4.2. The first approach was the calibrated relation between the logarithm of the mean excitation energy of tissues I_m and Z_{eff} (Z_{eff}, ln I_m) proposed by Yang *et al* [Yang et al., 2010] and Bourque *et al* [Bourque et al., 2014]. The second approach consisted in the direct conversion of RED into SPR through the (RED, SPR/RED) relation proposed by Kanematsu *et al* [Kanematsu et al., 2012]. The last two approaches were based on the reconstructed image of the electronic cross section at 100 keV, hereafter labeled $\sigma_{e,100}$, from the BMD results (see section 4.3). In particular, in the third approach, a calibrated relation between $\sigma_{e,100}$ and ln I_m values ($\sigma_{e,100}$, ln I_m) was proposed, whereas the last method involved a calibration curve between $\sigma_{e,100}$ and SPR/RED.

4.4.1 Comparative study on a tissue characterization phantom

4.4.1.1 Materials and Methods

In this study presented at the ESTRO 35 conference [Vilches-Freixas et al., 2016b], the image-based method of Bazalova *et al* [Bazalova et al., 2008b] and the projection-based method of Alvarez and Macovski [Alvarez and Macovski, 1976], hereafter referred

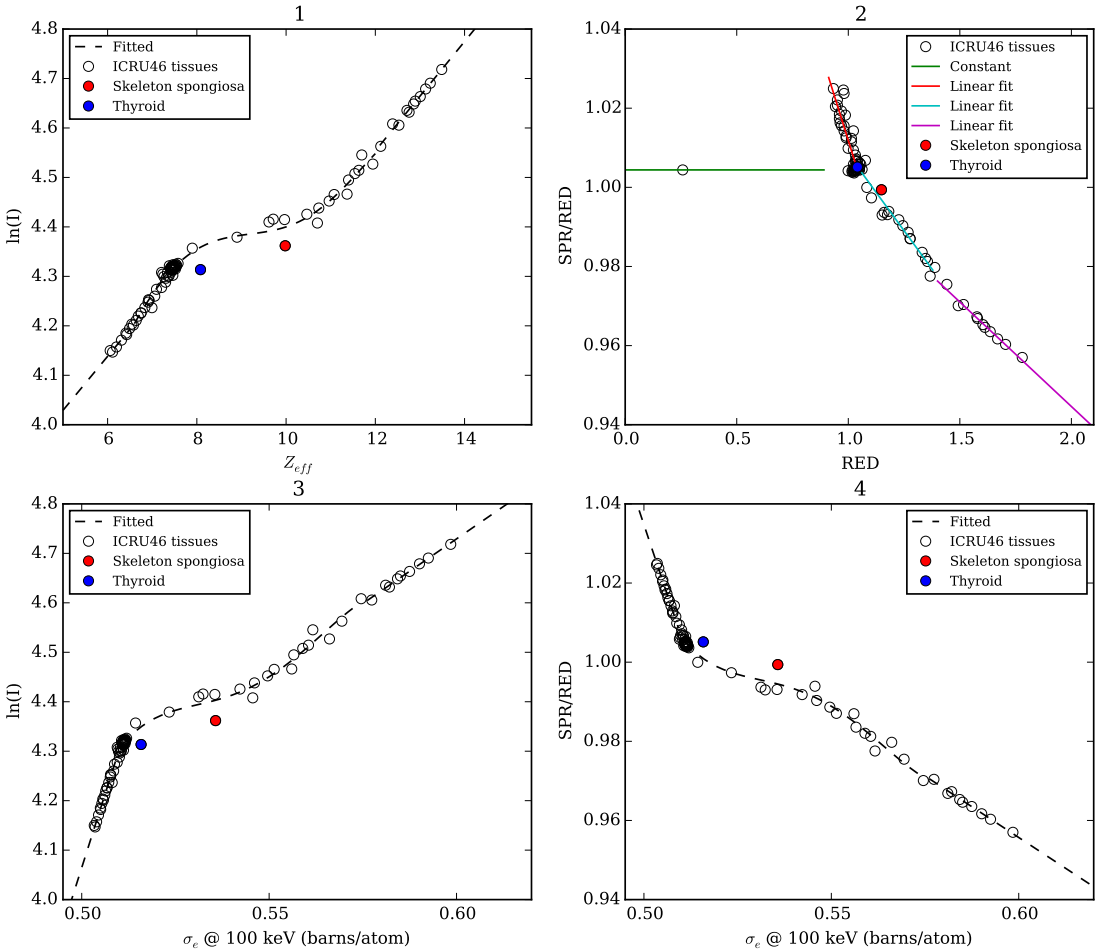

Figure 4.3: Calibrated relations using 92 tabulated human tissues [ICRU, 1992] (empty dots) to convert dual-energy outputs into the required variables to compute the proton SPR through Bethe's equation or to directly determine the SPR. 1) Piece-wise relation between the effective atomic number (Z_{eff}) and the logarithm of the mean excitation energy ($ln\ I$) [Bourque et al., 2014]. For Z_{eff} <6.2 linear fit, for 6.2≤ Z_{eff} ≤12 fifth-degree polynomial fit and for Z_{eff} >12 linear fit; 2) Piece-wise linear fitting to convert from RED to SPR over RED [Kanematsu et al., 2012]. RED limits: 0.9, 1.055 and 1.4; 3) Piece-wise relation between the electronic cross section at 100 keV ($\sigma_{e,100}$) and the logarithm of the mean excitation energy. For $\sigma_{e,100}$ <0.51 linear fit, for 0.51≤ $\sigma_{e,100}$ ≤0.575 fifth-degree polynomial fit and for $\sigma_{e,100}$ >0.575 linear fit; 4) Piece-wise relation between the electronic cross section at 100 keV and the ratio of SPR over RED. For $\sigma_{e,100}$ <0.51 linear fit, for 0.51≤ $\sigma_{e,100}$ ≤0.575 fifth-degree polynomial fit and for $\sigma_{e,100}$ >0.575 linear fit.

Method	Calibration curve
1	(Z_{eff}, $ln\ I$)
2	(RED, SPR/RED)
3	($\sigma_{e,100}$, $ln\ I$)
4	($\sigma_{e,100}$, SPR/RED)

Table 4.2: Method label with the corresponding calibrated relation to convert dual-energy output into the required variables to determine the SPR.

to BMD, were investigated. For the BMD (section 2.4.2.1), two variants were considered: water and compact bone basis (W/CB), and photoelectric and Compton basis (Ph/Co). For the image-based method, which produces RED and Z_{eff} images as output, photon beam spectra were additionally filtered with 16 cm of water and a beam-hardening correction was applied for materials with Z >10, as suggested by [Bazalova et al., 2008b]. Both projection-based methods assume that the linear attenuation coefficient at any energy can be obtained by a linear and energy-independent combination of these basis functions. For each decomposition method, the four empirical relationships to convert dual-energy outputs into SPR images (described in sections 4.2 and 4.3) were evaluated. For the projection-based (W/CB) method, the Z_{eff}-image was derived using the reconstructed σ_e image at 100 keV and the definition proposed by Bourque *et al* [Bourque et al., 2014] (equation 4.7 at 100 keV). For the projection-based (Ph/Co) method, the Z_{eff} image was derived from the reconstructed photoelectric basis image considering a Z-exponent of 3.3 and equation 2.5. The exponent was optimized for the given dual-energy spectra following the approach proposed by Tremblay *et al* [Tremblay et al., 2014].

Virtual DECT acquisitions of the Imaging Ring system (medPhoton, Salzburg, Austria) of the tissue characterization phantom Gammex 467 (Gammex, Middleton, WI) were carried out by means of deterministic simulations in GATE with realistic detector response model [Vilches-Freixas et al., 2016a]. The dual-energy spectra used in this study were: 80 kV for the low energy (LE) acquisition and 140 kV+Sn for the high energy (HE) acquisition. Scatter-free fan-beam acquisitions from 360 projections were considered. Realistic Poisson noise corresponding to a 20 mGy central dose, with an equal dose split between the LE and the HE acquisitions, was applied to the projections (for further details see Appendix B.1). The workflow of the study is illustrated in Figure 4.4.

4.4.1.2 Results and Discussion

Table 4.3 shows the relative SPR errors, (SPR-SPR_{ref})/SPR_{ref}, over all Gammex phantom inserts for each decomposition method, in terms of the mean error (μ) ± Root-Mean Squared error (RMSE). The values in brackets are the μ ± RMSE excluding lungs, as lung tissue inserts showed the maximum relative error due to its low density. Those pixel values with I_m, Z_{eff} and σ_e outside the human range of values were excluded from the computation. Figure 4.5 shows the SPR error maps relative to the calibrated

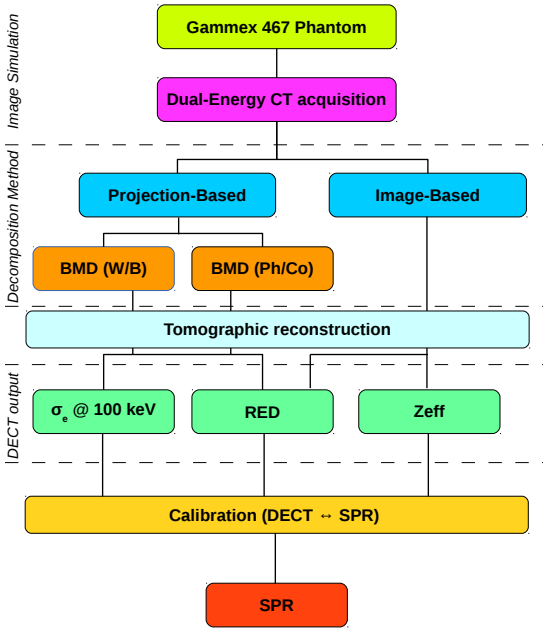

Figure 4.4: Workflow of the comparative study using the Gammex 467 phantom (section 4.4.1).

relation number 2 for the two projection-based methods and for the evaluated image-based method.

Method	BMD W/CB	BMD Ph/Co	Image-based
1	-0.2 ± 8.3 (-0.3 ± 7.7)	-5.4 ± 13.0 (-5.3 ± 12.0)	-2.7 ± 6.7 (-0.5 ± 4.5)
2	0.8 ± 5.1 (0.9 ± 3.2)	-0.3 ± 5.1 (-0.2 ± 3.2)	-2.3 ± 6.5 (-0.03 ± 3.8)
3	0.7 ± 5.7 (0.7 ± 4.2)	-1.2 ± 5.5 (-1.2 ± 4.0)	-
4	1.0 ± 5.2 (1.0 ± 3.4)	-0.8 ± 5.3 (-0.7 ± 3.5)	-

Table 4.3: Relative SPR errors averaged over the sixteen phantom Gammex inserts, expressed as μ ± RMSE (μ± RMSE excluding lung inserts), for two projection-based (BMD) and one image-based method, and for the four empirical relationships to convert DECT data into SPR (labeled as Method 1-4, see Table 4.2).

In terms of accuracy, the observed differences within the four empirical relationships were not statistically significant (p>0.05, Student t-test). The first method (Z_{eff}, ln I_m) was found to be the least appropriate in terms of precision for projection-based methods, but comparable to the second method for the image-based method. The second method, based on the RMSE, seems to be equally robust for image-based and projection-based methods. For all calibrated relations, no statistically significant differences were observed between the two BMD methods used in this study (W/CB and Ph/Co basis). The worst

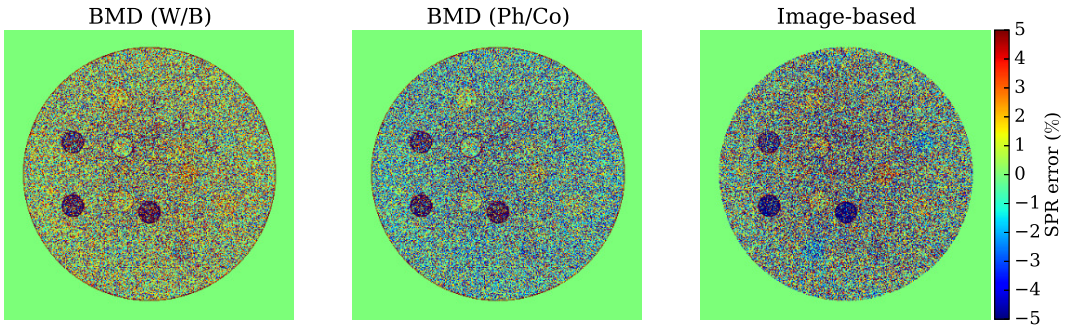

Figure 4.5: Percentage difference SPR maps estimated with the second method for all DECT approaches. Colorbar indicates the percentage error of the SPR.

result for the BMD Ph/Co method and the first approach could be due to a sub-optimal estimation of the Z_{eff} from the photoelectric basis image.

Even if the Gammex phantom used in this study contains sixteen inserts mimicking the attenuation properties of human tissues, the tissue distribution and the irradiation geometry is quite unrealistic with respect to a human body. This observation has motivated the second study.

4.4.2 Comparative study on an anthropomorphic phantom

4.4.2.1 Materials and Methods

In this second study, a more realistic setup was considered to compare the four calibrated relations to convert DECT outputs into SPR images. A thorax slice of the anthropomorphic female (AF) phantom from [ICRP, 2009] was used. Virtual DECT acquisitions of the Imaging Ring system using the same DE spectra and system characteristics as in the previous study were performed. Scatter-free fan-beam acquisitions from 720 projections were considered. Two situations were simulated: no noise in the projections (i.e. infinite dose) and realistic Poisson noise corresponding to a 20 mGy central dose applied to the projections (for further details see Appendix B.1). The BMD projection-based method, using a soft tissue and cortical bone pair as decomposition basis, was employed in this study.

The theoretical SPR image of the thorax slice was computed from the chemical composition and the mass density values provided in the ICRP publication [ICRP, 2009] and Bethe's equation at 200 MeV assuming an I-value for water of 78 eV [Sigmund et al., 2009].

4.4.2.2 Results and Discussion

Figures 4.6, 4.7, 4.8 and 4.9 plot the dual-energy decomposition outputs required by each empirical relation, the intermediate variables determined with the calibrated relations and the resulting SPR image.

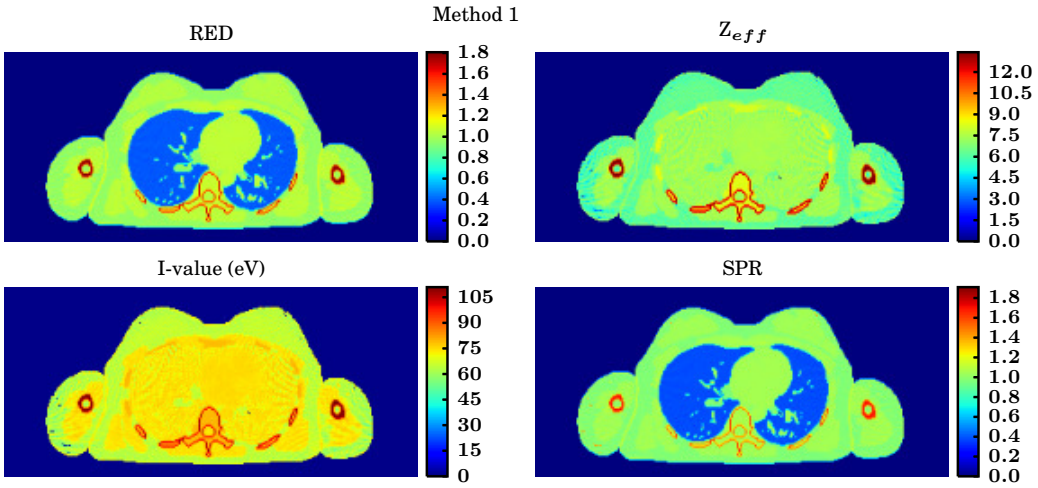

Figure 4.6: From top to bottom and from left to right: the RED and Z_{eff} images are the DECT outputs used by the first calibrated relation to estimate the SPR from DECT data. The I-value image is obtained from the empirical relationship between Z_{eff} and ln I_m, and the SPR image using Bethe's equation without correction terms. Images relative to the situation without noise in the projections.

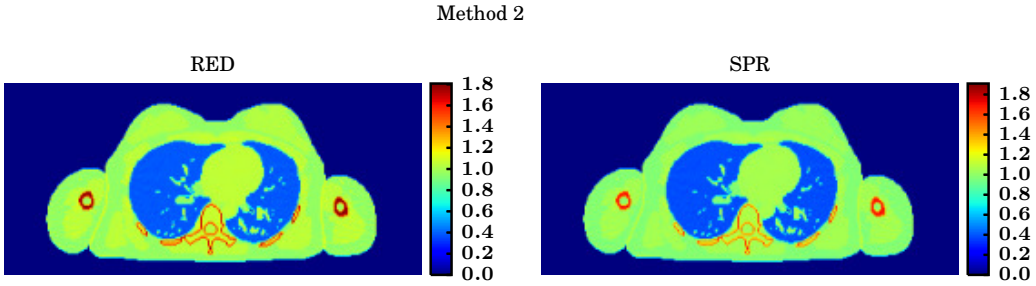

Figure 4.7: From left to right: the RED image is the DECT output used by the second calibrated relation to estimate the SPR from DECT data, and the SPR image using the empirical relationship between RED and SPR over RED. Images relative to the situation without noise in the projections.

In a pixel-by-pixel basis, the theoretical SPR image of the thorax slice was compared to the resulting SPR image for each calibrated relation and for each noise level (i.e. no noise or 20 mGy central dose). Figure 4.10 plots the histrograms of the absolute SPR errors for each empirical relation, without noise in the projections (top) and for a 20 mGy central dose (bottom). The Root-Mean Squared (RMS) errors and the maximum errors are provided in the legend for each calibrated relation.

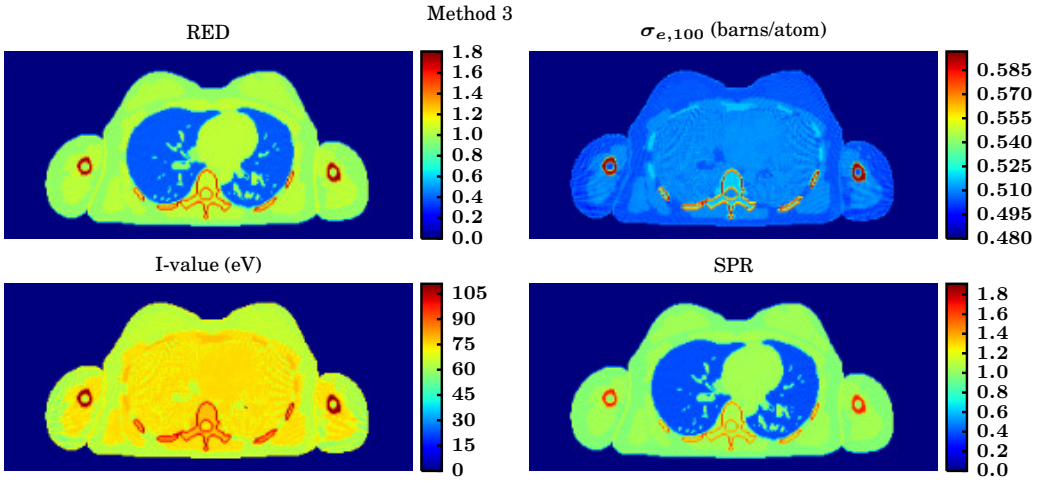

Figure 4.8: From top to bottom and from left to right: the RED and $\sigma_{e,100}$ images are the DECT outputs used by the third calibrated relation to estimate the SPR from DECT data. The I-value image is obtained from the empirical relationship between $\sigma_{e,100}$ and ln I_m, and the SPR image using Bethe's equation without correction terms. Images relative to the situation without noise in the projections.

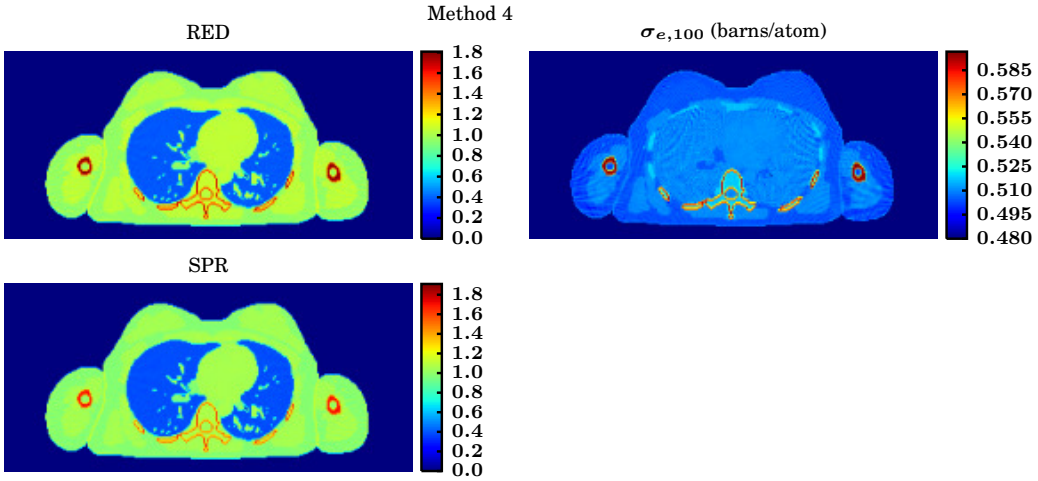

Figure 4.9: From left to right: the RED and $\sigma_{e,100}$ images are the DECT outputs used by the fourth calibrated relation to estimate the SPR from DECT data, and the SPR image using the empirical relationship between $\sigma_{e,100}$ and SPR over RED. Images relative to the situation without noise in the projections.

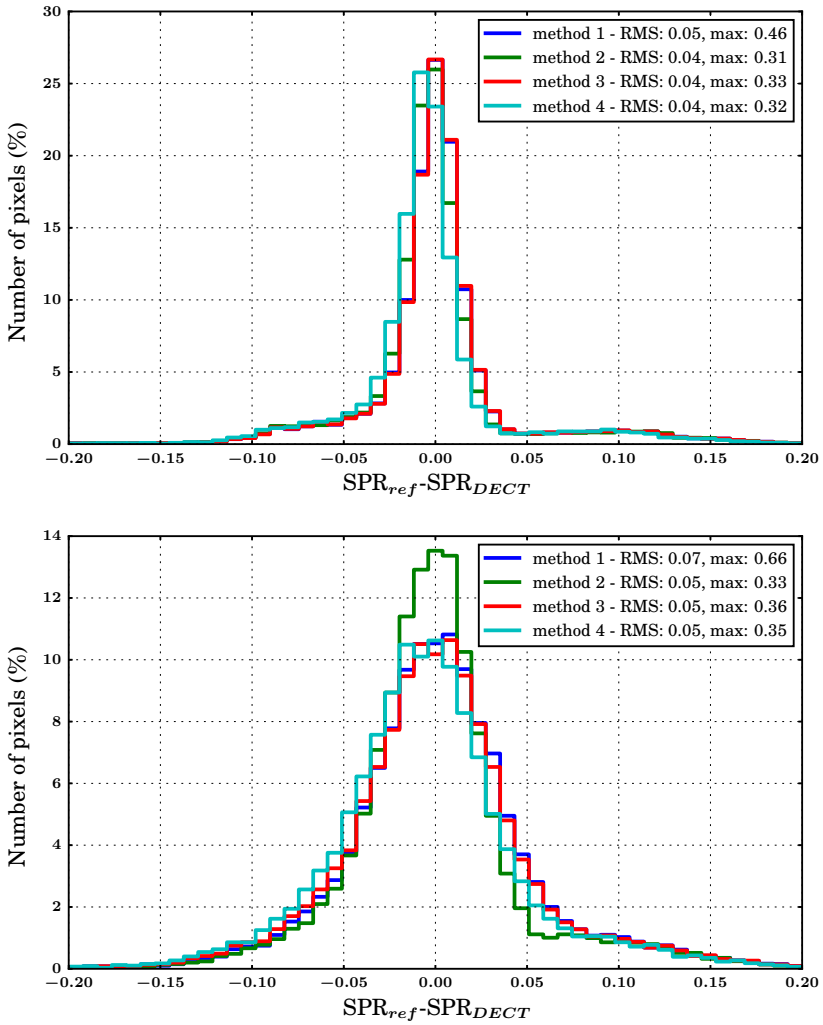

Figure 4.10: Histogram of the absolute SPR error distribution for each calibrated relation to convert DECT data into SPR images (see Figure 4.3). Results relative to the noiseless projections (top) and to Poisson noise corresponding to a 20 mGy central dose value (bottom). Root-mean square (RMS) and maximum SPR errors are provided in the legend for each method.

In terms of RMS error, no differences were observed between the four empirical relationships to convert DECT data into SPR. Maximum SPR differences were obtained for method 1. The presence of noise in the images only widens the error distributions and slightly increases the maximum differences, particularly for method 1.

4.4.3 Conclusions

Two studies were conducted to compare, in terms of accuracy and precision, different calibration methods to convert dual-energy data into SPR. Two existing methods in the literature, i.e. [Bourque et al., 2014] (originally proposed by [Yang et al., 2010]) and [Kanematsu et al., 2012], were compared to two novel relationships: ($\sigma_{e,100}$, ln I_m) and ($\sigma_{e,100}$, SPR/RED). A phantom with a simple irradiation geometry was used in the first study, whereas an anthropomorphic phantom representing an average female subject was used in the second study to validate the previous results. According to both studies, all methods behaved in a similar manner in terms of accuracy. Regarding the precision, the (Z_{eff}, ln I_m) approach was the least appropriate for projection-based methods. Kanematsu's approach (method 2) seems to be equally robust for image-based and projection-based methods. One advantage of this method is its simplicity as it only requires the reconstructed RED image as input to determine the SPR image. Farace [Farace, 2014] compared Kanematsu's approach with Hünemohr's and obtained comparable results in terms of SPR accuracy despite not explicitly taking into account the Z_{eff} information. Hünemohr *et al* [Hünemohr et al., 2014b] objected that for tissues having similar electron density values but different Z_{eff} (e.g. mammary gland or urine) the separation into electron density and atomic number would improve the accuracy in SPR prediction because these tissues can be well differentiated using DECT. Nevertheless, according to our results, it also seems not necessary to compute the intermediate variable Z_{eff} from DECT to have a good estimate of the SPR. Other authors have also proposed alternative DECT-derived SPR estimation approaches without reconstructing the intermediate Z_{eff} image [Han et al., 2016; Möhler et al., 2016]. Despite intensive research over the past years, our comparisons did not indicate that one method is advantageous over the other. The following section further investigates the comparison between projection- and image-based methods.

4.5 Comparison of projection- and image-based methods

Besides studying which was the most appropriate method to convert DECT output into SPR images, we investigated which decomposition domain, i.e. in the projections (before reconstruction) or in the CT images (after reconstruction), was more appropriate to estimate proton SPRs. To give an answer to this question, a collaboration with Vicki Trier Taasti, PhD. student from Aarhus University in Denmark, was carried out. This work has been presented in two international conferences and it has been published in the *PhiRo* journal in a full article format (see Appendix A).

4.5.1 Introduction

DECT methods can mainly be categorized into projection-based methods, where material decomposition is performed prior to image reconstruction, and image-based methods, where decomposition takes place after image reconstruction. As mentioned in section 2.4, both projection-based and image-based approaches can be further divided

into two main types: *model-based* where prior knowledge of source energy spectrum and detector response is required to solve analytically the system of equations; *calibration-based* where X-ray measurements of materials with known properties are performed to obtain parameters that characterize the energy spectrum and the detector response.

Nearly all DECT methods are image-based [Van Elmpt et al., 2016], possibly because image-based methods have the clear advantage that they can be performed on all DECT scanners, including conventional SECT scanners by acquiring two consecutive images at different kVp settings. In contrast, for projection-based methods, the low and the high energy projections need to be acquired at the same angle or be accurately interpolated. Nevertheless, with the advent of dual-layer systems and photon-counting detector technology, projection-based methods are becoming more attractive since the projections from the different energy spectra are obtained without angular separation and there cannot be any motion between the two (or more) projections per source position. Another reason is that projection-based methods require access to dual-energy projection data, which are not accessible in most commercial CT systems without the vendor agreement or reverse engineering. In a simulation study, Tremblay *et al* [Tremblay et al., 2014] concluded that combining the output of projection-based methods with the image-based stoichiometric calibration proposed by Bourque *et al* [Bourque et al., 2014] gave better accuracy for RED and Z_{eff} than a projection-based method alone.

The aim of the present study was therefore to investigate the impact on the SPR accuracy when using a projection-based method. We compared the performances of the SPR estimation and the corresponding proton range errors of one projection-based and two image-based DECT methods, through a simulation-based CT image acquisition framework with the measured detector response and dual-energy spectra of a commercial DECT scanner and realistic noise levels.

4.5.2 Materials and Methods

4.5.2.1 Virtual patient

The Adult Female (AF) reference computational phantom of the International Commission on Radiological Protection (ICRP) [ICRP, 2009] was used as a virtual patient to evaluate the performances of the SPR methods. This phantom, with voxel dimensions of $1.775 \times 1.775 \times 4.84$ mm^3, represented an average female subject structured with 140 organs made of 53 standard human tissues. The mass density and elemental weights of each tissue were provided in the ICRP Publication 110 [ICRP, 2009]. To evaluate a large number of tissue densities and compositions, four anatomical regions were selected: head, sternum, breast and pelvis (Fig. 4.11).

4.5.2.2 SPR estimation methods

Three DECT-based methods for SPR estimation were investigated, including one projection-based and two image-based approaches. The projection-based method relied on the two-material decomposition proposed by Alvarez and Macovski [Alvarez and

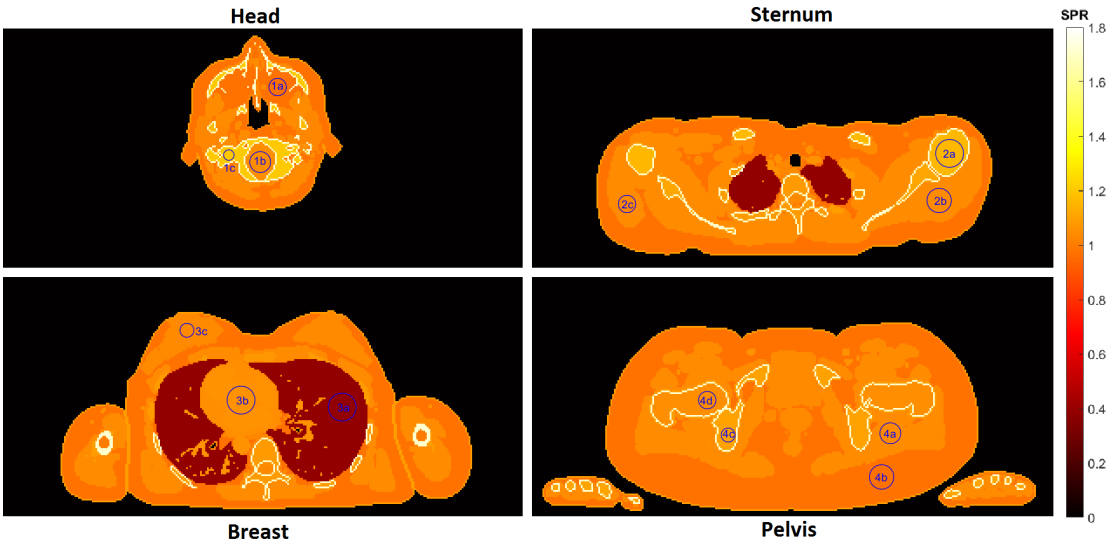

Figure 4.11: Reference SPR for the four slices used in the comparison. Placement of ROIs are shown by blue circles, three to four ROIs are placed in each slice.

Macovski, 1976] to estimate the RED and the conversion from RED to SPR proposed by Kanematsu *et al* [Kanematsu et al., 2012]. We will refer to this method as Alvarez and Macovski, and Kanematsu (AMK). The first image-based method used a parametrization for the SPR proposed by Taasti *et al* [Taasti et al., 2016]. This image-based method will be referred to as Stopping Power Parametrization (SPP). The second image-based approach was a combination of the methods proposed by Saito [Saito, 2012] to compute the RED and by Kanematsu *et al* [Kanematsu et al., 2012] to derive the SPR. We will refer to this method as Saito and Kanematsu (SK). The three SPR estimation methods are described in the following subsections.

Projection-based method (AMK) The method used to compute the SPR from dual-energy projection data is an adaptation of the two-step procedure proposed by Farace [Farace, 2014] in the image-domain. First, RED was derived from the reconstructed mass density images of soft tissue (ST) and cortical bone (CB) [Linstrom and Mallard, (retrieved December 6, 2016)], issued from the implementation of the two-material decomposition method in the projection domain [Alvarez and Macovski, 1976] (see section 2.4.2.1 for further details). Second, RED was converted into SPR using the poly-line relations proposed by Kanematsu *et al* [Kanematsu et al., 2012] (see section 4.2 for further details). This method was chosen for its simplicity and because it produced comparable results with respect to Hünemohr's approach [Farace, 2014]. Furthermore, in section 4.4, we concluded that this method was robust both for image- and projection-based methods.

The projection of the mass fractions ϱ_{ST} and ϱ_{CB} was expressed as follows:

$$A_{\mathrm{ST}}(\boldsymbol{u},\theta) = \int_{L(\boldsymbol{u},\theta)} \varrho_{\mathrm{ST}}(\ell)\ \mathrm{d}\ell \tag{4.12}$$

$$A_{\mathrm{CB}}(\boldsymbol{u},\theta) = \int_{L(\boldsymbol{u},\theta)} \varrho_{\mathrm{CB}}(\ell)\ \mathrm{d}\ell \tag{4.13}$$

where $\ell \in L(\boldsymbol{u},\theta)$ was the line-segment between the source and a detector pixel located at position $\boldsymbol{u}$ for a given projection angle θ.

When performing a dual-energy acquisition, two sinograms of the same object at two different energy spectra were available:

$$I_{\mathrm{LE}}(A_{\mathrm{ST}},A_{\mathrm{CB}}) = \int_{E_{\min}}^{E_{\max}} S_{\mathrm{LE}}(E)\ e^{-A_{\mathrm{ST}}\ \left(\frac{\mu}{\rho}\right)_{\mathrm{ST}}(E)-A_{\mathrm{CB}}\ \left(\frac{\mu}{\rho}\right)_{\mathrm{CB}}(E)}\ \mathrm{d}E \tag{4.14}$$

$$I_{\mathrm{HE}}(A_{\mathrm{ST}},A_{\mathrm{CB}}) = \int_{E_{\min}}^{E_{\max}} S_{\mathrm{HE}}(E)\ e^{-A_{\mathrm{ST}}\ \left(\frac{\mu}{\rho}\right)_{\mathrm{ST}}(E)-A_{\mathrm{CB}}\ \left(\frac{\mu}{\rho}\right)_{\mathrm{CB}}(E)}\ \mathrm{d}E \tag{4.15}$$

where I_{LE} and I_{HE} were the measured intensities for the low energy (LE) and the high energy (HE) spectrum, respectively, for a given projection angle; S_{LE} and S_{HE} were the normalized energy spectra weighted by the detector response.

The unknowns A_{ST} and A_{CB} were determined following [Schlomka et al., 2008] by solving the system of equations (4.14, 4.15) using the implementation of Nelder and Mead [Nelder and Mead, 1965] in RTK [Rit et al., 2014], assuming that the energy spectrum and the detector response were known (model-based decomposition).

Then, the mass fraction per volume of soft tissue (ϱ_{ST}) and cortical bone (ϱ_{CB}) was determined by reconstruction of A_{ST} and A_{CB} (see Section 4.5.2.4). The RED was derived for each pixel using equation 4.9 and the SPR using the piece-wise linear relations suggested by Kanematsu *et al* [Kanematsu et al., 2012] (see Figure 4.3-2).

Image-based method - SPR parametrization (SPP) The details of the image-based SPP method were described by Taasti *et al* [Taasti et al., 2016] (section 4.2), but the main principles are described here.

CT scans of a calibration phantom were required for the characterization of the X-ray energy spectrum (calibration-based decomposition). This calibration process was performed on simulated CT images of the Gammex 467 electron density calibration phantom (Gammex, Middleton, WI). Average CT numbers over ROIs inside the inserts in the reconstructed CT images were used.

Based on the known density and elemental composition of the inserts of the Gammex phantom, the effective energies of the used energy spectra were found using the CT numbers ($\mathcal{H}_j$) for the phantom inserts. The effective energy was defined as the energy which maximized the coefficient of determination, R^2, for the linear fit:

$$\frac{\mu(E_{\mathrm{eff},j})}{\mu_{\mathrm{W}}(E_{\mathrm{eff},j})} = \frac{\mathcal{H}_j}{A_j^t} + B_j^t \tag{4.16}$$

Here, subscript j refers to the energy spectrum ($j = \mathrm{LE}, \mathrm{HE}$), and A and B are fitting parameters. The linear attenuation coefficients, $\mu(E)$, for the Gammex inserts were calculated based on XCOM data [Berger et al., 2010]. From the effective energies, the Gammex inserts were divided into two categories, soft and bone tissues based on their CT numbers in the LE CT image. Then equation 4.16 was refitted for each tissue group, to find two sets of fitting parameters, A_j^t and B_j^t, where superscript $t \in \{\mathrm{soft}, \mathrm{bone}\}$ indicates the tissue group, using the effective energies $E_{\mathrm{eff},j}$ for each energy spectrum j. In this study, we used a separation point between the tissue groups of $\mathcal{H}_{\mathrm{LE}} = 150$ HU.

The attenuation ratios, u, for the 92 reference human tissues [ICRU, 1992] were calculated at the effective energies based on their density and elemental composition:

$$u \equiv \frac{\mu(E_{\mathrm{eff}})}{\mu_W(E_{\mathrm{eff}})} = \rho \, \frac{\sum_i w_i \left(\frac{\mu}{\rho}\right)_i (E_{\mathrm{eff}})}{\left[\sum_i w_i \left(\frac{\mu}{\rho}\right)_i (E_{\mathrm{eff}})\right]_{\mathrm{W}}} \tag{4.17}$$

These attenuation ratios were fitted to the SPR for the tissues based on the following equations:

$$\mathrm{SPR}^{\mathrm{est}}_{\mathrm{soft}} = (1+x_1)\,u_{\mathrm{HE}} - x_1 u_{\mathrm{LE}} + x_2 u_{\mathrm{LE}}^2 + x_3 u_{\mathrm{HE}}^2 + x_4 \left(u_{\mathrm{LE}}^3 + u_{\mathrm{HE}}^3\right) \tag{4.18}$$

$$\mathrm{SPR}^{\mathrm{est}}_{\mathrm{bone}} = (1+x_5)u_{\mathrm{HE}} - x_5 u_{\mathrm{LE}} + x_6 \frac{u_{\mathrm{LE}}}{u_{\mathrm{HE}}} + x_7 \left(u_{\mathrm{LE}}^2 - u_{\mathrm{HE}}^2\right) + x_8 \left(u_{\mathrm{LE}}^3 + u_{\mathrm{HE}}^3\right) \tag{4.19}$$

where the x_i's are fitting parameters. The fitting parameters used in this study can be found in Table 4.4. When these expressions were used to estimate the SPR for the AF phantom, the attenuation ratios were calculated using the fitting parameters found together with the effective energies, $u_j^t = \mathcal{H}_j / A_j^t + B_j^t$. The same separation between soft and bone tissue was used for the SPR estimation as for the calculation of the attenuation ratios.

Energy spectra characterization			SPR fitting parameters			
	LE (64 keV)	HE (96 keV)	Soft tissues		Bone tissues	
A^{soft}	988.8	991.3	x_1	3.161	x_5	0.8251
A^{bone}	971.8	984.8	x_2	1.176	x_6	0.03853
B^{soft}	1.006	1.007	x_3	−1.136	x_7	0.1150
B^{bone}	0.9803	1.004	x_4	−0.01883	x_8	−0.008910

Table 4.4: Calibration parameters used in the SPR parametrization; for the energy spectra characterization (equation 4.16), and for the SPR estimation (equations 4.18–4.19). The effective energies of the LE and HE spectra are given in parentheses.

Image-based method - Saito and Kanematsu's (SK) method This image-based DECT method is a combination of two methods originally presented by [Saito, 2012]

(calculation of the relative electron density, RED), and by [Kanematsu et al., 2012] (conversion from RED to SPR).

In Saito's method the RED was estimated as

$$\mathrm{RED} = a\,\frac{(1+\alpha)\,\mathcal{H}_{\mathrm{HE}} - \alpha\,\mathcal{H}_{\mathrm{LE}}}{1000} + b \tag{4.20}$$

The constants a, b and α were found by making calibration fits to the theoretical RED values for the 92 reference human tissues and their CT numbers calculated from equations 4.16 and 4.17. To take the low RED values for lung tissue into account, the constants were found by minimizing the relative deviations:

$$\frac{\mathrm{RED}_{\mathrm{theo}} - \mathrm{RED}_{\mathrm{est}}}{\mathrm{RED}_{\mathrm{theo}}} \tag{4.21}$$

The parameters used in this study can be found in Table 4.5. The CT numbers for the 92 reference human tissues used in the calibration were calculated from equation 4.17 and the effective energies given in Table 4.4.

a	b	α
1.0085	1.0091	0.5202

Table 4.5: Calibration parameters for Saito's method, found by minimization of equation 4.20. These parameters were used to compute the RED in the SK method.

As for the method presented in section 4.5.2.2, RED estimates were converted into SPR using the piece-wise linear relations suggested by Kanematsu *et al* [Kanematsu et al., 2012] (see Figure 4.3-2).

4.5.2.3 Calculation of reference SPR

Reference SPR values of the ICRP phantom were computed from the chemical composition and the density in a pixel-by-pixel basis using the Bethe equation without correction terms, as described by Schneider *et al* [Schneider et al., 1996]. A proton beam of 200 MeV kinetic energy was considered and the mean ionization energy of water was set to 78 eV [Sigmund et al., 2009]. The mean ionization energies of the tissues were calculated using the Bragg additivity rule [Schneider et al., 1996] and the I-values given in Table 2.8 and 2.11 in the ICRU49 report [ICRU, 1993].

4.5.2.4 CT imaging and CT reconstruction

Virtual CT projections of the Gammex and the ICRP phantom were generated in GATE [Jan et al., 2004] v7.2 (based on Geant4 v10.1, physics-list: emlivermore) using the *Fixed Forced Detection Actor*. This module deterministically computes digitally reconstructed radiographs using the reconstruction toolkit (RTK) v1.3.0 [Rit et al., 2014] and the Geant4 database of X-rays cross sections. Fan-beam projections with 600 views

of 2052 pixels subsequently re-binned to 1026 pixels of 1 mm^2 were acquired. The thickness of the detector row was 1 mm for the Gammex acquisitions and 2 mm for the ICRP phantom. The source-to-isocenter distance was 626 mm and the source-to-detector distance was 1026 mm. For the simulations of the CT projections, the measured dual-energy spectra (LE: 100 kVp, HE: 150 kVp + 0.6 mm Sn) and the measured detector response for the SOMATOM Force dual-source CT scanner were used, kindly provided by Siemens Healthcare (Forchheim, Germany). To represent a realistic scenario, Poisson distributed noise was applied to the projections. For each slice, a total central dose of 20 mGy was delivered with the dual-energy acquisition, with an equal dose split between the two energy spectra, i.e., a central dose of 10 mGy per energy spectrum; the calculation of the number of photons required to deliver a given dose is computed with Equation B.1. No bowtie filter was simulated.

CT images of the Gammex phantom and the AF slices were reconstructed using the LE and the HE sinograms, for the image-based method; and soft tissue and cortical bone density images of the AF slices, for the projection-based method. All reconstructions were performed using the filtered backprojection (FBP) reconstruction of RTK; for the reconstructions of the AF slices preserving the initial pixel dimension of 1.775×1.775 mm^2 and for the Gammex the pixel dimension of 1×1 mm^2.

Beam-hardening correction Prior to CT reconstruction, the LE and the HE sinograms of the Gammex and the AF phantom were corrected for beam hardening using the method described in [Brooks and Di Chiro, 1976], since it was found to be mandatory for the image-based methods. A look-up table linearizing the input projection values for water was created using the energy spectrum and the detector response of the CT scanner system and increasing water thicknesses.

4.5.2.5 SPR comparison

The performances of the SPR estimation with respect to the reference values were evaluated based on different criteria: relative SPR differences over defined ROIs, each covering a single tissue, and relative range errors computed over a whole slice. The placement of the ROIs can be seen in Fig. 4.11, and their reference SPRs are listed in Table 4.6. For each ROI, the mean error was calculated and its precision was assessed using the Standard Error of the Mean (SEM). To have a direct comparison of the three methods, the root-mean-square error (RMSE) over the mean relative SPR difference for the thirteen ROIs was taken; this gives a combined error measure for the thirteen defined ROIs.

To estimate the influence of the SPR deviations on the range calculation, we calculated the range errors along the proton beam path through the entire slice using the Radon transform implemented in MATLAB (The MathWorks Inc., Natick, MA). The Radon transform was computed on the absolute SPR difference images, for each angle in the interval from $0 - 179°$ in steps of $1°$. The SPR difference for pixels outside the body outline was set to zero. The Radon transform was also computed on the reference SPR

	ROI name	AF Material-ID	Tissue type	SPR_{ref}	N
Head	1a	49	Adipose tissue	0.972	75
	1b	32	Brain	1.051	111
	1c	8	Cranium, spongiosa	1.203	27
Sternum	2a	3	Humeri, upper half, spongiosa	1.157	195
	2b	29	Muscle tissue	1.046	147
	2c	29	Muscle tissue	1.046	75
Breast	3a	50	Lung tissue (compressed lungs)	0.384	195
	3b	28	Blood	1.055	195
	3c	48	Breast (mammary gland)	1.040	47
Pelvis	4a	29	Muscle tissue	1.046	111
	4b	49	Adipose tissue	0.972	147
	4c	14	Pelvis, spongiosa	1.100	47
	4d	9	Femora, upper half, spongiosa	1.053	75

Table 4.6: Reference data for the thirteen defined ROIs used for comparison of the relative SPR differences. N is the number of pixels in the ROI.

maps to calculate the water-equivalent path length (WEPL). To exclude beam paths entirely outside the body, an exclusion penalty was applied to pixels in the reference SPR sinogram with a WEPL of zero. The results for the range errors were given relative to reference WEPL maps, to take into account that the beam paths in different directions and slices were not of equal length.

4.5.3 Results

The RMSE over the mean relative error for each of the thirteen ROIs, placed in homogeneous tissue regions, was 0.54% for the AMK method, 0.68% for the SPP method and 0.61% for the SK method (Fig. 4.12). The bias (given by the signed mean error) for the head, sternum and breast slices was larger for the AMK method, however, for the pelvis slice (ROI4a-d) this method gave the smallest errors (Table 4.7). Considering all slices, the AMK method had the smallest bias. For all methods, the relative errors for ROIs in the pelvis slice (ROIs 4a-d) were larger than for the other slices.

The AMK method gave the lowest RMSEs for the relative range errors. For the AMK and SPP methods, the positive and negative range errors were nearly averaged out over the slice, such that the mean relative range errors were close to 0%; only for the head slice estimated by the SPP method, the 0% range error was not within the interquartile range (IQ), as shown by the blue boxes in Fig. 4.13. In contrast, for the image-based SK method, the range error distribution had a negative bias for all slices. Even though the mean relative range errors for the SPP method were fairly low, this method produced the widest error distributions (Fig. 4.13 and Table 4.8).

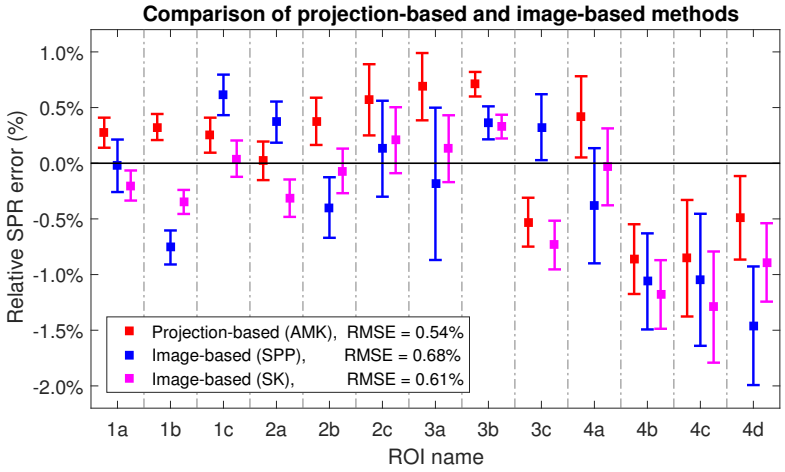

Figure 4.12: Relative SPR errors for each of the thirteen ROIs (for the placement see Fig. 4.11). The center squares show the mean of the relative SPR error over the ROI, and the error-bars show the standard error of the mean (SEM).

	PB (AMK) $\mu \pm \sigma$	IB (SPP) $\mu \pm \sigma$	IB (SK) $\mu \pm \sigma$
Head	0.28% ± 0.04%	-0.06% ± 0.69%	-0.17% ± 0.20%
Sternum	0.32% ± 0.28%	0.03% ± 0.39%	-0.06% ± 0.26%
Breast	0.29% ± 0.71%	0.17% ± 0.31%	-0.09% ± 0.57%
Pelvis	-0.45% ± 0.60%	-0.99% ± 0.45%	-0.85% ± 0.57%

	RMSE	μ	σ
PB (AMK)	0.54%	0.07%	0.56%
IB (SPP)	0.68%	-0.27%	0.65%
IB (SK)	0.61%	-0.33%	0.53%

Table 4.7: Comparison of relative SPR deviations over the defined ROIs. The upper part of the table gives the results averaged over the individual slices (signed mean ± standard deviation, $\mu \pm \sigma$, over the ROIs in each slice), while the lower part gives the results averaged over all four slices together (RMSE, mean (μ), and standard deviation (σ) over all thirteen ROIs). (PB: Projection-based, IB: Image-based).

4.5.4 Discussion

In this study, we have compared a projection-based and two image-based methods for computing SPR maps and deriving range error distributions. The image-based SPP method gave mean range errors comparable to the results for the projection-based method, but larger standard deviations. In contrast, the image-based SK method resulted in slightly biased results. Nevertheless, the differences between the three methods were not found significant ($p > 0.1$).

Method	Head (122.8 mm)		Sternum (162.5 mm)		Breast (162.1 mm)		Pelvis (181.7 mm)	
	$\mu \pm \sigma$ (%)	RMSE (%)	$\mu \pm \sigma$ (%)	RMSE (%)	$\mu \pm \sigma$ (%)	RMSE (%)	$\mu \pm \sigma$ (%)	RMSE (%)
PB (AMK)	-0.24±0.81	0.84	-0.01±0.64	0.64	-0.04±0.58	0.58	-0.14±0.80	0.82
IB (SPP)	-0.41±0.86	0.95	0.01±0.81	0.81	0.04±0.72	0.72	0.03±1.10	1.10
IB (SK)	-0.51±0.80	0.95	-0.28±0.63	0.69	-0.33±0.57	0.66	-0.44±0.80	0.91

Table 4.8: Comparison of the relative range errors over each image slice. The results are given as the signed mean errors ($\mu \pm \sigma$) and the root-mean-square errors (RMSE) in percentage. The range errors are taken relative to the reference water equivalent path length (WEPL); the mean reference WEPL for each slice is given in parentheses beneath the slice name. (PB: Projection-based, IB: Image-based).

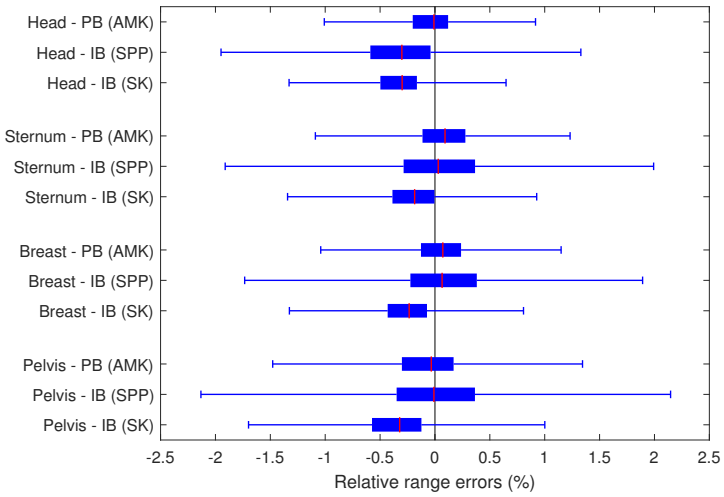

Figure 4.13: Box-plot of relative range error distribution, as calculated by the Radon transform for each anatomical slice using each of the three SPR estimation methods (PB: Projection-based, IB: Image-based). The blue boxes show the interquartile (IQ) range, i.e. from the 25%-percentile (Q1) to the 75%-percentile (Q3), and the red horizontal line represents the median. The whiskers go from Q1−2.5×IQ up to Q3+2.5×IQ. The outliers are not shown in the figure, but at most 8.8% of the data points (excluding the sinogram entries corresponding to a WEPL of zero) were outside the whiskers.

In our simulations, clinical polychromatic energy spectra, a realistic detector response and noise levels corresponding to a 20 mGy central dose were used. However, no bowtie filter was simulated. The material basis for the selected projection-based approach was optimized to give the best results (see section 5.2). To have a direct comparison between

projection-based and image-based calculations, we used an image-based method (the SK method) where the conversion from RED to SPR were performed in the same way as for the projection-based method, using the polyline fit proposed by [Kanematsu et al., 2012]. Further, we also used one of the latest image-based methods [Taasti et al., 2016], as this method was proven to give smaller SPR errors and to be more robust to noise than two other existing DECT methods [Han et al., 2016; Hansen et al., 2015]. For these reasons, we consider that the comparison was carried out under fair conditions.

The image-based SK method showed a net negative bias on the range accuracy that was not observed for the image-based SPP method. It has earlier been shown that the SPR accuracy using Saito's method in combination with an estimation of the effective atomic number is dependent on the calibration and evaluation materials and on the phantom size used for the calibration [Hansen et al., 2015]. Range errors seem to correlate well with SPR errors obtained for some tissues, such as breast tissue (ROI 3c), adipose tissue (ROI 4d) or pelvis spongiosa (ROI 4c), which were found in large proportions in the selected slices and, therefore, could also explain the observed bias in the SK range results. This suggests that accuracy errors add up along the proton beam path. The SPP method resulted in noisier SPR images and, thus, wider error distributions. In terms of RMSE, the projection-based approach produced better results for the SPR and the range with respect to the two image-based methods. Therefore, based on these results, we recommend increasing the consideration of projection-based approaches for proton SPR determination. However, the inherent limitation of each of the methods should be taken into consideration and, therefore, the most well-suited SPR estimation method for each facility might depend on the DECT technology available.

Beam hardening artifacts occur because the energy dependency of the linear attenuation coefficients is neglected. To overcome this approximation, image-based methods require a beam-hardening correction. In contrast, material decomposition in projection-based approaches is performed prior to reconstruction, and as the energy dependency is factored out in this decomposition process (equation 2.7) the basis-images should not be affected by beam-hardening. But this is not true unless a good choice of the basis-material decomposition is performed, such that the assumption that μ can be separated into an energy-dependent and an energy-independent part holds true. In the energy range of clinical CT scanners (i.e. from 40 to 150 keV) and for materials with $Z < 15$ this assumption is acceptable [Jackson and Hawkes, 1981]. In this study, the implemented strategy to correct for beam-hardening in the image-based method works well for water-equivalent tissues but might not be accurate enough for low- and high-density tissues. A more sophisticated beam-hardening correction might therefore improve the results for the image-based methods, but it would most likely require an iterative approach. Furthermore, if a better beam-hardening correction was applied, a LE spectrum with a lower mean energy might be more relevant than the 100 kVp spectrum used in this study.

The two image-based methods used in this study were calibration-based, and a calibration was needed to find the effective energies for the LE and HE spectrum. This calibration procedure is sensitive to the calibration phantom being comparable to the

object for which the SPR is to be estimated; i.e. the calibration phantom should be of a similar size and consist of materials with a composition comparable to human tissues, such that the phantom hardens the x-ray energy spectrum in the same way as the investigated anatomical site. For this study, only a single calibration phantom with a diameter of 16.5 cm was used for all four anatomical slices. This may be one cause for the larger relative SPR deviations in the pelvis slice for the image-based methods (Table 4.7).

For model-based image-based methods, the energy spectrum must also be properly hardened to reproduce the beam hardening of the scanned object. This issue is taken into account by additionally filtering the x-ray source for instance by water [Yang et al., 2010; Bazalova et al., 2008b]. Here, the amount of water may also be dependent on the anatomical region being investigated, since the performance of these methods will depend on the accuracy of this prior knowledge on the energy spectrum and the detector response [Yang, 2011]. Therefore, the input parameters must be tuned with care for both types of image-based methods. However, for calibration-based methods, this is more straight-forward since it only requires using a well-suited calibration phantom of the proper size.

For the projection-based method applied in this study, the system of equations (4.14, 4.15) was solved numerically assuming that the energy spectrum and the detector response were well-known. The same was assumed for the beam hardening correction of image-based methods. It was shown that projection-based methods are sensitive to alterations of the energy spectrum [Tremblay et al., 2014] and to the amount of noise [Brendel et al., 2016]. Tremblay *et al* [Tremblay et al., 2014] found that the accuracy of the RED was more degraded when the spectrum was altered for projection-based methods than for image-based. The projection-based results in the present work are therefore dependent on accurate knowledge of the energy spectrum and detector response. An alternative would be to approximate the system of equations (4.14, 4.15) by a polynomial expansion of two variables [Alvarez and Macovski, 1976; Chuang and Huang, 1988]. The unknown coefficients could be determined experimentally through a calibration procedure with increasing thicknesses of two well-known materials (see section 2.4.2.2 for further details). However, there would also be disadvantages with this approach, including sensitivity to the order of the polynomial, to the use of cross-terms in the polynomial, to the exact thicknesses of the interposed slabs of two materials and to the number of points of the calibration curve. It should also be noted that model-based approaches always rely on a pre-calibration of the model, e.g., the one presented in [Vilches-Freixas et al., 2016b].

Another ongoing discussion within the community is how to determine the reference SPR values. In this study, a 200 MeV proton energy was used to determine the SPR reference values as for proton energies in the range between 80 and 300 MeV, the variation of SPR with proton energy is negligible (<1%) [Arbor et al., 2015]. In addition, Yang [Yang, 2011] conducted a study with a 175 MeV initial kinetic energy beam and concluded that neglecting the SPR dependence with energy introduced a 0.5% range error.

4.5.5 Conclusion

In this simulation-based study, the dual-energy decomposition domains – the projection-domain (decomposition prior to image reconstruction) and the image-domain (decomposition after image reconstruction) – were compared in terms of the performance of extracting the SPR from DECT and the resulting WEPL. In terms of SPR accuracy and range errors, the observed differences obtained with projection- and image- based methods were not found statistically significant. With the advent of technological developments, projection-based methods are becoming more attractive. Most of the existing methods to compute the SPR are image-based but, based on these results, projection-based approaches should also be considered for proton SPR determination.

4.6 SPR estimation using the Imaging Ring system

The aim of this study was to determine the ability of the Imaging Ring (IR) system (medPhoton, Salzburg, Austria) (Chapter 3) to estimate the SPR of two tissue characterization phantoms and one anthropomorphic thorax phantom by performing dual-energy material decomposition. Sequential single-energy CBCT scans at different voltages and filtration and dual-energy CBCT FKVS acquisitions of these phantoms were acquired in Salzburg using the IR. Two experimental sessions were carried out: in March 2016 and in November 2016. Reconstructed SPR images of these phantoms were compared to the reference values, which were determined at the Heidelberg Ion-beam Therapy center (HIT, Germany) using a PeakFinder water column (PTW, Freiburg, Germany) and a carbon ion beam of 310.6 MeV/u initial kinetic energy in another experimental session (Appendix C).

4.6.1 Materials and Methods

4.6.1.1 Phantoms

Twelve inserts of the Gammex RMI 467 (Gammex, Middleton, United States of America) phantom (see Table C.2) and eighteen inserts of the CIRS 062 (CIRS, Norfolk, United States of America) phantom (see Table C.1) were positioned in the inner and outer disk of the CIRS 062 phantom. These inserts mimic human tissue attenuation properties and the chemical composition was provided by the manufacturer. Seventeen inserts at a time can be placed in the inner and outer disks of the CIRS phantom. Two phantom configurations were considered: 1) twelve Gammex phantom inserts and five CIRS phantom inserts were positioned as shown in Figure 4.14 a. Hereafter, this phantom will be referred to as *CIRS-Gammex*; 2) seventeen CIRS phantom inserts positioned as shown in Figure 4.14 b. We will refer to this phantom as *CIRS-CIRS*. The CIRS Dynamic Thorax phantom with a lung tumor insert (Figure 4.14 c), with known chemical composition and mass density, was also used to simulate a human body irradiation.

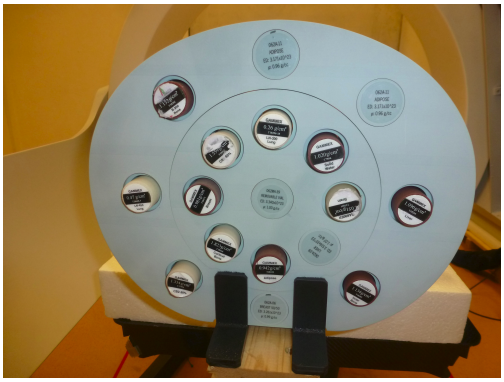

(a) CIRS-Gammex phantom

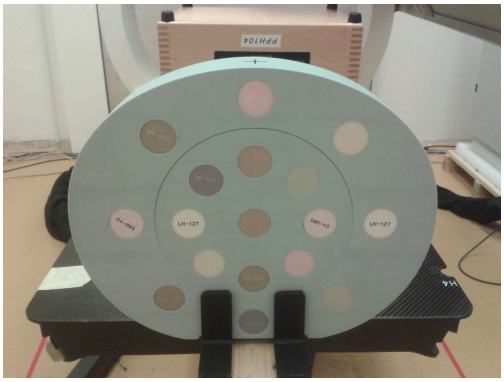

(b) CIRS-CIRS phantom

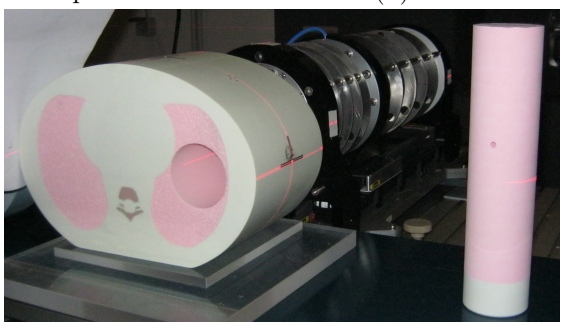

(c) CIRS dynamic thorax phantom (left) with lung tumor (right)

Figure 4.14: Phantoms used in this study.

4.6.1.2 Dual-energy CBCT sequential acquisitions

Single-energy CBCT scans at different voltages and filtration of these phantoms were sequentially acquired in Salzburg using the IR. CBCT scans were performed with a 2 cm or 3 cm slit aperture at the isocenter, using the dynamic collimation jaws to reduce scatter contamination, clock-wise rotation, acquisition time of about 60 s with $\Delta\theta$=0.6°, projection size of 1024×1024 pixels with pixel size of 0.4×0.4 mm^2 and fluence corrections activated. Single-energy CBCT acquisitions were grouped in order to reproduce dual-energy CBCT sequential acquisitions. Table 4.9 shows the acquisition parameters for the CIRS-CIRS phantom and the CIRS-Gammex phantom dual-energy acquisitions and Table 4.10 shows the acquisition parameters for the CIRS Thorax phantom dual-energy acquisitions. The acquisitions where a filter material of the wheel was used are indicated with an asterisk, whereas the acquisitions in which a high purity silver filter was placed after the collimator to additionally filter the spectrum are marked with a triangle. Fluence correction was not available for those projections acquired with a high purity silver filter.

The scatter correction proposed by [Siewerdsen et al., 2006] implemented off-line (see section 3.4) was applied to the projections of the CIRS Thorax phantom. As discussed in

section 3.4, the collimator-shadow scatter correction was not applied to the CIRS-CIRS and CIRS-Gammex acquisitions as it was found to be not suitable for these phantoms.

4.6.1.3 Dual-energy CBCT FKVS acquisitions

Dual-energy FKVS CBCT scans synchronized with the filter wheel of the CIRS-Gammex and the CIRS-CIRS phantoms were carried out. Figure 4.15 shows one resulting sinogram of the CIRS-CIRS phantom, with interleaved LE and HE projections, when performing a dual-energy FKVS acquisition. As for the single-energy acquisitions, to reduce scatter contamination, CBCT scans with a 3 cm slit aperture at the isocenter were considered. Table 4.9 shows additional acquisition parameters for each phantom acquisition. One (current) restriction of FKVS acquisitions is that the pulse length of the LE and the HE energy spectra has to be the same.

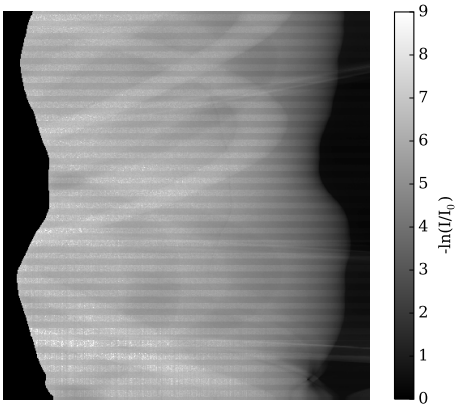

Figure 4.15: CIRS-CIRS phantom sinogram corresponding to the 80 kV/Air + 120 kV/Air FKVS acquisition. Interleaved LE and HE projections are visible.

Exp. session	Phantom	LE spectra	LE settings	HE spectra	HE settings	Frame number	Acq. type	Slit (cm)	RMS (%) all inserts	RMS (%) w/o lungs
03-2016	Cirs-Gammex	60 kV Al (*)	60 mA, 25 ms	120 kV Air	10 mA, 13 ms	600	sequential	2	4.6	4
03-2016	Cirs-Gammex	60 kV Al (*)	60 mA, 25 ms	120 kV Ag (△)	25 mA, 13 ms	600	sequential	2	9.3	9.6
03-2016	Cirs-Gammex	90 kV Air	20 mA, 15 ms	120 kV Air	10 mA, 13 ms	600	sequential	2	12.3	12.2
03-2016	Cirs-Gammex	90 kV Air	20 mA, 15 ms	120 kV Ag (△)	25 mA, 13 ms	600	sequential	2	17.4	18.2
03-2016	Cirs-Gammex	90 kV Al (*)	20 mA, 17 ms	120 kV Air	10 mA, 13 ms	600	sequential	2	6	3.6
03-2016	Cirs-Gammex	90 kV Al (*)	20 mA, 17 ms	120 kV Ag (△)	25 mA, 13 ms	600	sequential	2	13.7	14.2
03-2016	Cirs-Gammex	90 kV Ag (△)	60 mA, 16 ms	120 kV Air	10 mA, 13 ms	600	sequential	2	10.1	9.3
03-2016	Cirs-Gammex	90 kV Ag (△)	60 mA, 16 ms	120 kV Ag (△)	25 mA, 13 ms	600	sequential	2	15	15.7
03-2016	Cirs-Cirs	90 kV Air	20 mA, 15 ms	120 kV Air	10 mA, 13 ms	600	sequential	2	10.2	8.8
03-2016	Cirs-Cirs	90 kV Air	20 mA, 15 ms	120 kV Ag (△)	25 mA, 13 ms	600	sequential	2	16.1	17.5
03-2016	Cirs-Cirs	90 kV Al (*)	20 mA, 17 ms	120 kV Air	10 mA, 13 ms	600	sequential	2	7.7	4.7
03-2016	Cirs-Cirs	90 kV Al (*)	20 mA, 17 ms	120 kV Ag (△)	25 mA, 13 ms	600	sequential	2	12.1	13
03-2016	Cirs-Cirs	90 kV Ag (△)	60 mA, 16 ms	120 kV Air	10 mA, 13 ms	600	sequential	2	17.8	19.9
03-2016	Cirs-Cirs	90 kV Ag (△)	60 mA, 16 ms	120 kV Ag (△)	25 mA, 13 ms	600	sequential	2	12.8	13.8
11-2016	Cirs-Gammex	80 kV Cu (*)	25 mA, 20 ms	120 kV Cu+Ag (*)	25 mA, 20 ms	610	sequential	3	29.8	31.2
11-2016	Cirs-Gammex	80 kV Cu (*)	25 mA, 20 ms	120 kV Air	20 mA, 20 ms	610	sequential	3	18.2	18.2
11-2016	Cirs-Gammex	80 kV Air	25 mA, 20 ms	120 kV Cu+Ag (*)	25 mA, 20 ms	610	sequential	3	27.8	29.2
11-2016	Cirs-Gammex	80 kV Air	25 mA, 20 ms	120 kV Air	20 mA, 20 ms	610	sequential	3	13.1	12.9
11-2016	Cirs-Cirs	80 kV Cu (*)	25 mA, 20 ms	120 kV Cu+Ag (*)	25 mA, 20 ms	610	sequential	3	29.1	32.2
11-2016	Cirs-Cirs	80 kV Cu (*)	25 mA, 20 ms	120 kV Air	20 mA, 20 ms	610	sequential	3	15.6	15.5
11-2016	Cirs-Cirs	80 kV Air	10 mA, 20 ms	120 kV Cu+Ag (*)	25 mA, 20 ms	610	sequential	3	27.2	29.9
11-2016	Cirs-Cirs	80 kV Air	10 mA, 20 ms	120 kV Air	20 mA, 20 ms	610	sequential	3	13.5	10.5
11-2016	Cirs-Gammex	80 kV Air	25 mA, 20 ms	120 kV Air	20 mA, 20 ms	990	FKVS	3	8.4	6.7
11-2016	Cirs-Cirs	80 kV Air	10 mA, 20 ms	120 kV Cu+Ag (*)	25 mA, 20 ms	990	FKVS	3	17.3	10.9
11-2016	Cirs-Cirs	80 kV Air	20 mA, 10 ms	120 kV Air	15 mA, 10 ms	990	FKVS	3	11.3	7.6

Table 4.9: Parameters of the dual-energy sequential and FKVS CBCT acquisitions for the CIRS-Gammex and the CIRS-CIRS phantoms: LE and HE spectra (tube voltage and additional filtration), LE and HE settings (tube current and pulse length), number of frames and slit aperture at the isocenter. The acquisitions marked with an asterisk indicate that a filter material of the wheel was used, whereas the acquisitions in which a high purity silver sheet was placed after the collimator to additionally filter the spectrum are marked with a triangle. Last two columns show the relative SPR RMS errors accounting for all phantom inserts and excluding lung inserts, respectively.

Exp. session	Phantom	LE spectra	LE settings	HE spectra	HE settings	Frame number	Acq. type	Slit (cm)	RMS	max diff.
11-2016	Cirs Thorax	80 kV Cu (*)	25 mA, 20 ms	120 kV Cu+Ag (*)	25 mA, 20 ms	610	sequential	3	0.17	1.20
11-2016	Cirs Thorax	80 kV Cu (*)	25 mA, 20 ms	120 kV Air	10 mA, 20 ms	610	sequential	3	0.35	2.1
11-2016	Cirs Thorax	80 kV Air	10 mA, 20 ms	120 kV Cu+Ag (*)	25 mA, 20 ms	610	sequential	3	0.16	1.14
11-2016	Cirs Thorax	80 kV Air	10 mA, 20 ms	120 kV Air	10 mA, 20 ms	610	sequential	3	0.24	1.69

Table 4.10 Parameters of the dual-energy sequential acquisitions for the CIRS Thorax phantom: LE and HE spectra (tube voltage and additional filtration), LE and HE settings (tube current and pulse length), number of frames and slit aperture at the isocenter. The acquisitions where a filter material of the wheel was used to additionally filter the spectrum are indicated with an asterisk. Last two columns show the RMS error computed over the SPR difference image and the maximum SPR difference, respectively.

4.6.1.4 Sinogram interpolation

One assumption of projection-based dual-energy decomposition methods is that the same information per tube voltage has to be available at each projection angle (see section 2.4.2). To that end, LE and HE projections have to be properly interpolated to have the LE and the HE projections sampled at the same angle.

In this study, for the dual-energy CBCT sequential acquisitions, we decided to interpolate the HE projections with respect to the LE projections. The interpolation was performed with respect to the source angle value of each projection. As the source and the detector can rotate independently along circular trajectories [Rit et al., 2016], for each projection, there is a unique pair of source angle and detector angle values. This was checked by plotting the difference of the source angle and the detector angle with respect to the source angle position for a set of independent single-energy acquisitions performed in March 2016 and in November 2016. Acquisitions performed in November 2016 were perfectly consistent, whereas acquisitions performed in March 2016 were found to be less reproducible. In the light of these results, we concluded that a simple linear sinogram interpolation with respect to the source angle position was sufficient for the CBCT acquisitions performed in November 2016. For the acquisitions carried out in March 2016, a linear interpolation was performed as illustrated in Figure 4.16.

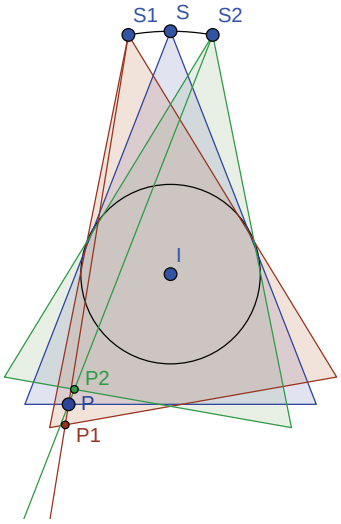

Figure 4.16: The projection at source position S is linearly interpolated from the backprojection onto the detector of the projections at source positions S1 and S2. For example, the value at point P is obtained from the linear combination of the values at P1 and P2.

For the dual-energy CBCT FKVS acquisitions, first, the LE and the HE projections were separated from the combined dual-energy sinogram of Figure 4.15 ($2N$ projections). Second, the LE and the HE sinograms (with N projections each) were linearly interpolated with respect to the $2N$ source angles, without resampling, in order to have a $2N$-projections LE sinogram and a $2N$-projections HE sinogram sampled at the same

angle.

4.6.1.5 SPR determination

We followed the procedure described in section 4.5.2.2 to reconstruct the SPR phantom images. Mass density images of two basis materials were reconstructed using the BMD projection-based dual-energy decomposition method proposed by [Alvarez and Macovski, 1976]. On a pixel-by-pixel basis, the RED image was derived from the reconstructed mass density images. Then, the SPR image was determined through a functional relation between the RED and the ratio of SPR and RED proposed by [Kanematsu et al., 2012]. Acrylic (PMMA) and aluminum (Al) were chosen as basis materials for all phantom acquisitions.

Reference SPR values of the phantom inserts used in this study were experimentally determined in a measurement session carried out at the Heidelberg Ion-beam Therapy center (HIT, Germany) in March 2016 (see Appendix C for further details). Reconstructed SPR images of the CIRS Thorax were compared to the reference SPR values in a pixel-by-pixel basis, whereas ROIs covering the inserts in a central slice of the CIRS-Gammex and the CIRS-CIRS phantoms were considered to compare reconstructed SPR images with experimentally determined SPR values.

4.6.1.6 SECT-derived SPR images

In order to investigate if DECT outperforms SECT, the CIRS-CIRS phantom image corrected for beam-hardening and reconstructed from the CBCT projections acquired at 120 kV/Air was used to generate a look-up table to convert HU into SPR (Figure 4.17). A ROI of 10 pixels radius was used to extract the HU value inside each phantom insert and the corresponding SPR was the experimentally determined value (see Appendix C).

To compare SECT- and DECT-derived SPR images, the HU-SPR curve was used to generate the SPR map of the scatter-corrected image of the CIRS Thorax phantom acquired at 120 kV/Air.

4.6.2 Results

4.6.2.1 Dual-energy CBCT sequential acquisitions

CIRS Thorax phantom In a pixel-by-pixel basis, the resulting SPR images for each dual-energy sequential acquisition were compared to the experimentally determined values. Table 4.10 shows the RMS error and the maximum SPR deviations computed over the SPR difference image of each dual-energy CBCT acquisition. Worse RMS errors and larger maximum errors were obtained for the dual-energy combinations with a HE spectrum of 120 kV/Air than with 120 kV/Cu+Ag. It might be explained by the increased energy gap between the incident dual-energy spectra when using a HE spectrum of 120 kV/Cu+Ag which results in a less noisy reconstructed SPR image. Figure 4.18 shows the reconstructed mass density images of PMMA and Al, the RED image and

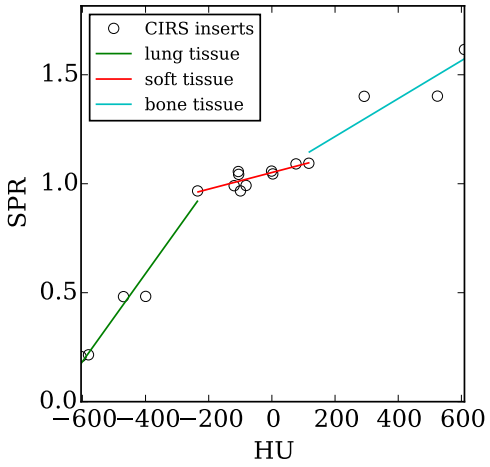

Figure 4.17: HU to SPR calibration curve computed from the CIRS-CIRS phantom image reconstructed from the CBCT projections acquired at 120 kV/Air. A piece-wise linear interpolation between HU and SPR values was used, divided in three segments: lung tissue (HU<-230), soft tissue (-230≤HU<120) and bone tissue (HU≥120).

the corresponding SPR image obtained from the scatter-corrected dual-energy CBCT sequential acquisition at 80 kV/Air + 120 kV/CuAg of the CIRS Thorax phantom.

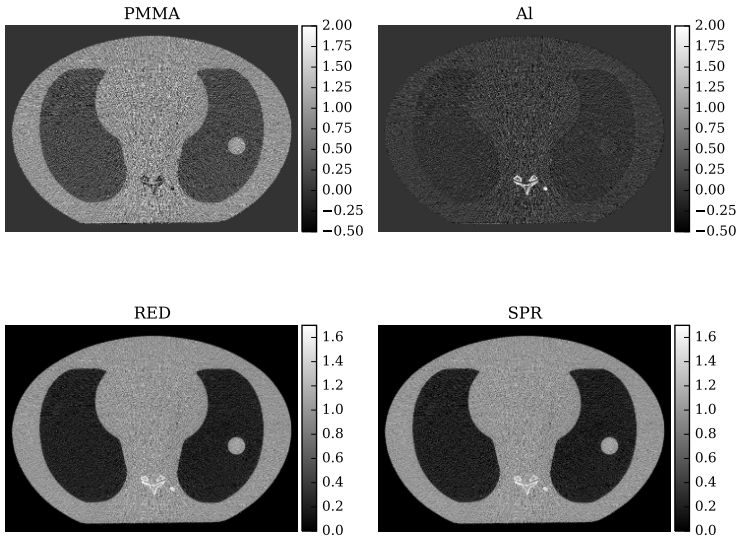

Figure 4.18: From top to bottom and from left to right: PMMA and Al mass density images, RED image and SPR image corresponding to the dual-energy CBCT sequential acquisition at 80 kV/Air + 120 kV/CuAg of the CIRS Thorax phantom.

Figure 4.19 plots a line profile comparing the reconstructed SPR image with the experimentally determined SPR values (a), and the histogram of the SPR difference image for the 80 kV/Air + 120 kV/CuAg CBCT acquisition (b). The SPR error histogram (Figure 4.19-b) is centered around zero, but it exhibits a peak around 0.3 which corresponds to the trabecular and cortical bone pixels. Unlike lung and plastic water inserts, for which the experimentally determined SPR values were considered (Appendix C), the theoretically determined SPR values (Equation 1.12) of bone inserts were used because they are mold in the phantom and they cannot be separated from other materials to estimate their SPR experimentally. A water I-value of 78 eV and a proton beam energy of 200 MeV were considered. Theoretical SPR values were found to be systematically higher than experimental values.

CIRS and Gammex phantoms For each phantom insert, the mean value and the standard deviation of the SPR were calculated in ROIs covering the inserts in a central slice of the phantom, and they were compared to the experimental values (Appendix C). Table 4.9 shows the relative RMS errors averaged over all phantom inserts and excluding lung inserts of each dual-energy sequential CBCT acquisition. For the dual-energy sequential acquisitions acquired in March 2016, the RMS errors averaged over all inserts (excluding lungs) ranged from 4.6% (3.6%) to 17.4% (18.2%) for the CIRS-Gammex phantom, whereas it varied from 7.7% (4.7%) to 17.8% (19.9%) for the CIRS-CIRS phantom. For the acquisitions performed in November 2016, the RMS errors varied from 13.1% (12.9%) to 29.8% (31.2%) for the CIRS-Gammex phantom, whereas they ranged from 13.5% (10.5%) to 29.1% (32.2%) for the CIRS-CIRS phantom.

Figure 4.20 shows the reconstructed mass density images of PMMA and Al, the RED image and the corresponding SPR image obtained from the dual-energy CBCT sequential acquisitions at 60 kV/Al + 120 kV/Air (a) and at 90 kV/Al + 120 kV/Air (b) performed in March 2016 (see Table 4.9) of the CIRS-Gammex phantom. Some Beam Hardening (BH)-like artifacts and streaks are visible in the reconstructed mass density images, specially for the 60 kV/Al + 120 kV/Air acquisition, which are less predominant in the reconstructed RED and SPR images.

Figure 4.21 plots the DECT-derived SPR values versus reference values for two dual-energy spectra (top) and the SPR residuals (bottom) for the CIRS-Gammex phantom inserts sorted by increasing SPR value. Lung inserts were excluded from the residual plot due to the large relative errors, i.e. up to 36% for the 60 kV/Al + 120 kV/Air dataset and up to -66% for the 90 kV/Al + 120 kV/Air dataset. RMS errors of 4.9% (all inserts) and 4.4% (excluding lung inserts) were obtained for the 60 kV/Al + 120 kV/Air acquisition, and RMS errors of 6.1% (all inserts) and 3.7% (excluding lung inserts) were obtained for the 90 kV/Al + 120 kV/Air acquisition. The SPR image derived from the 90 kV/Al + 120 kV/Air acquisition was noisier with respect to the 60 kV/Al + 120 kV/Air acquisition, i.e., the latter presents a larger incident energy gap. Chapter 5 studies in detail the influence of the incident energy gap, i.e., between the LE and the HE acquisitions, on the reconstructed images noise.

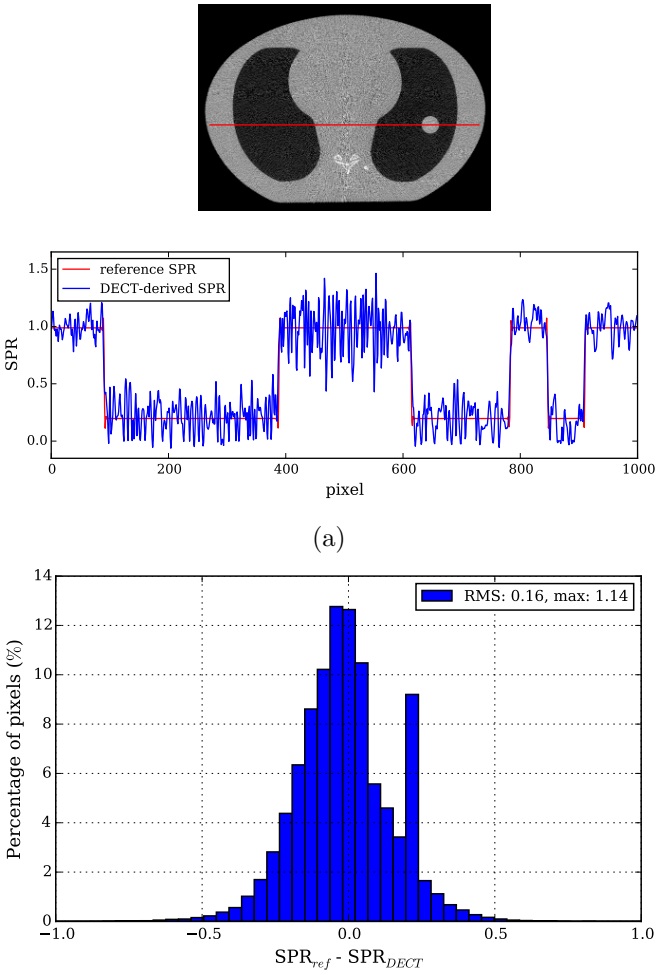

(a)

(b)

Figure 4.19: Results relative to the dual-energy CBCT sequential acquisition at 80 kV/Air + 120 kV/CuAg of the CIRS Thorax phantom. a) SPR profile comparing the reconstructed SPR image (blue) with the experimentally determined SPR values (red); b) histogram of the SPR difference image. The corresponding RMS and maximum errors are indicated in the figure legend.

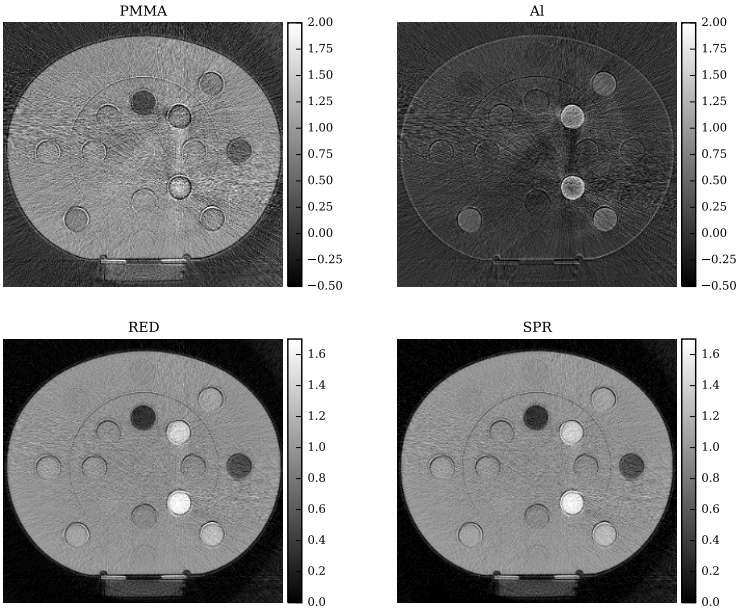

(a) 60 kV/Al + 120 kV/Air - CIRS-Gammex

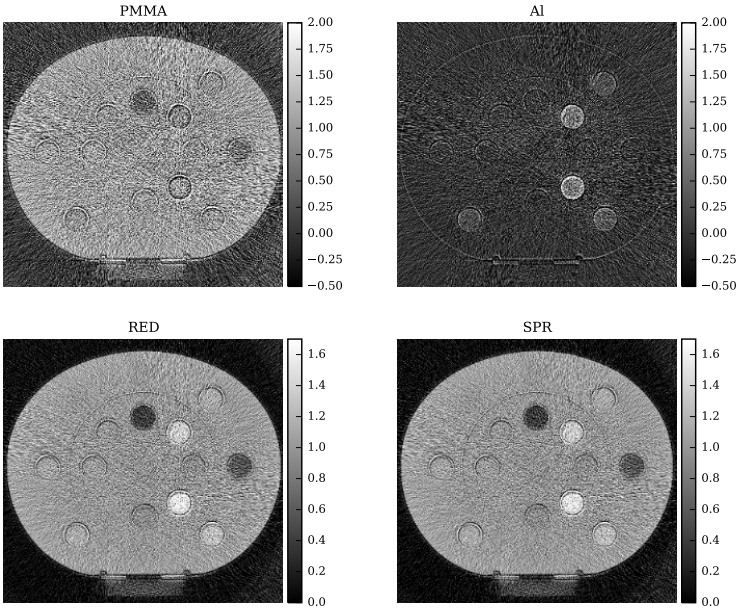

(b) 90 kV/Al + 120 kV/Air - CIRS-Gammex

Figure 4.20: Results corresponding to the dual-energy sequential acquisition at 60 kV/Al + 120 kV/Air (a) and at 90 kV/Al + 120 kV/Air (b) of the CIRS-Gammex phantom performed in March 2016. From top to bottom and from left to right: PMMA and Al mass density images, RED image and SPR image.

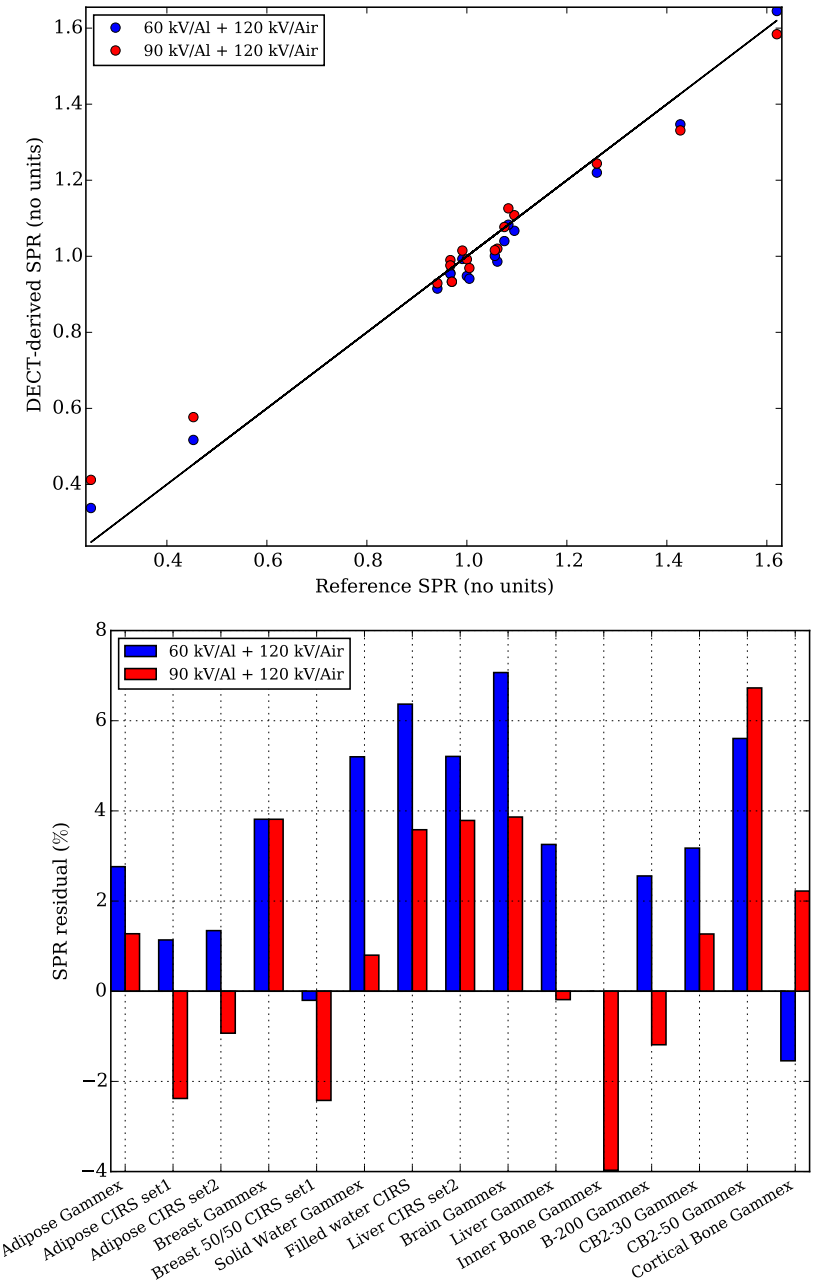

Figure 4.21: DECT-derived SPR values versus reference values for two dual-energy spectra (top) and SPR residuals (bottom) for the CIRS-Gammex phantom inserts sorted by increasing SPR value. Lung inserts were excluded from the residual plot.

4.6.2.2 Dual-energy CBCT FKVS acquisitions

CIRS and Gammex phantoms For each phantom insert, the mean value and the standard deviation of the SPR were calculated in ROIs covering the inserts in a central slice of each phantom. Table 4.9 shows the relative RMS errors averaged over all phantom inserts and excluding lung inserts of each dual-energy FKVS CBCT acquisition. For the CIRS-Gammex phantom, RMS errors of 8.4% (all inserts) and 6.7% (excluding lung inserts) were obtained. For the CIRS-CIRS phantom, RMS errors of 17.3% (all inserts) and 10.9% (excluding lung inserts) were computed for the 80 kV/Air + 120 kV/CuAg acquisition, whereas errors of 11.3% (all inserts) and 7.6% (excluding lung inserts) were obtained for the 80 kV/Air + 120 kV/Air acquisition.

Figure 4.22 shows the reconstructed mass density images of PMMA and Al, the RED image and the corresponding SPR image obtained from the dual-energy CBCT FKVS acquisition at 80 kV/Air + 120 kV/Air of the CIRS-Gammex phantom (a), and at 80 kV/Air + 120 kV/CuAg of the CIRS-CIRS phantom (b). There are some artifacts at the center of the mass density images compatible with scatter contamination. In addition, some BH-like artifacts are visible, specially for the 80 kV/Air + 120 kV/CuAg acquisition. Moreover, a moderate cupping is visible in the reconstructed images, i.e. enhanced phantom edges with respect to the central portion, particularly for the CIRS-CIRS phantom acquisition.

Figure 4.23 plots the DECT-derived SPR values versus reference values and the SPR residuals for both phantom inserts sorted by increasing SPR value. Lung inserts were excluded from the residual plot due to the large relative errors, i.e. up to -87% for the CIRS-Gammex phantom and up to -130% for the CIRS-CIRS phantom.

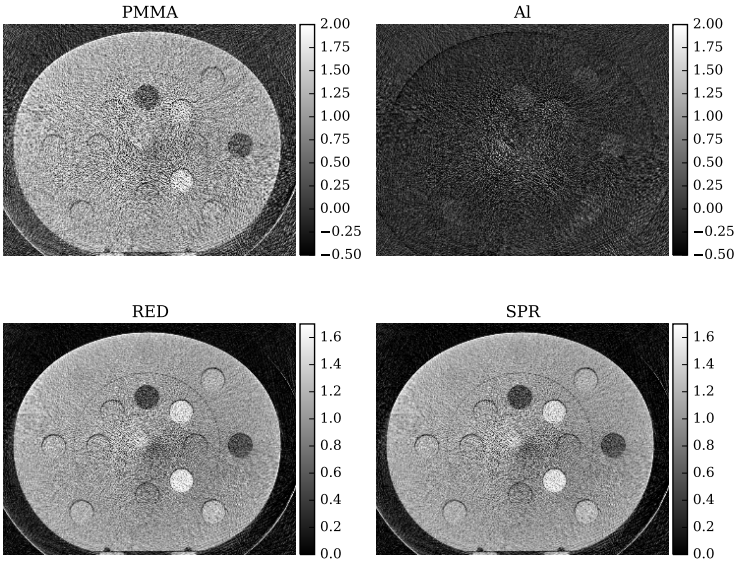

(a) 80 kV/Air + 120 kV/Air - CIRS-Gammex

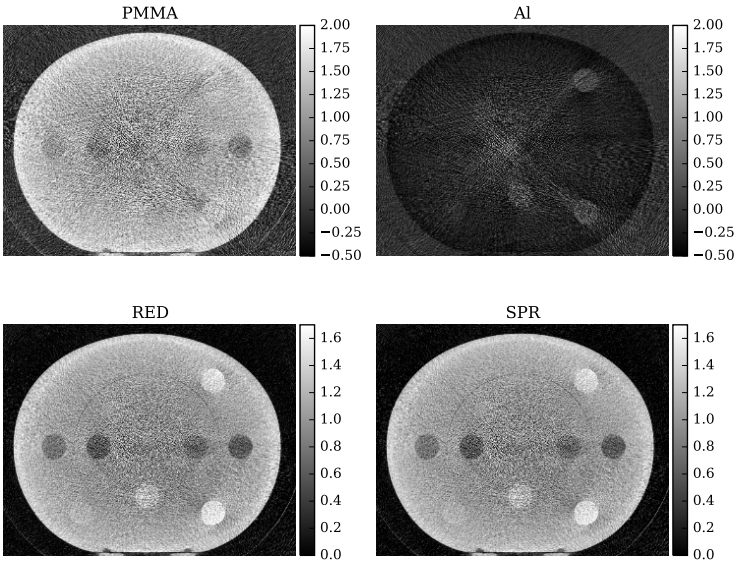

(b) 80 kV/Air + 120 kV/CuAg - CIRS-CIRS

Figure 4.22: Results corresponding to the dual-energy CBCT FKVS acquisition at 80 kV/Air + 120 kV/Air of the CIRS-Gammex phantom (a) and to the dual-energy CBCT FKVS acquisition at 80 kV/Air + 120 kV/CuAg of the CIRS-CIRS phantom (b). From top to bottom and from left to right: PMMA and Al mass density images, RED image and SPR image.

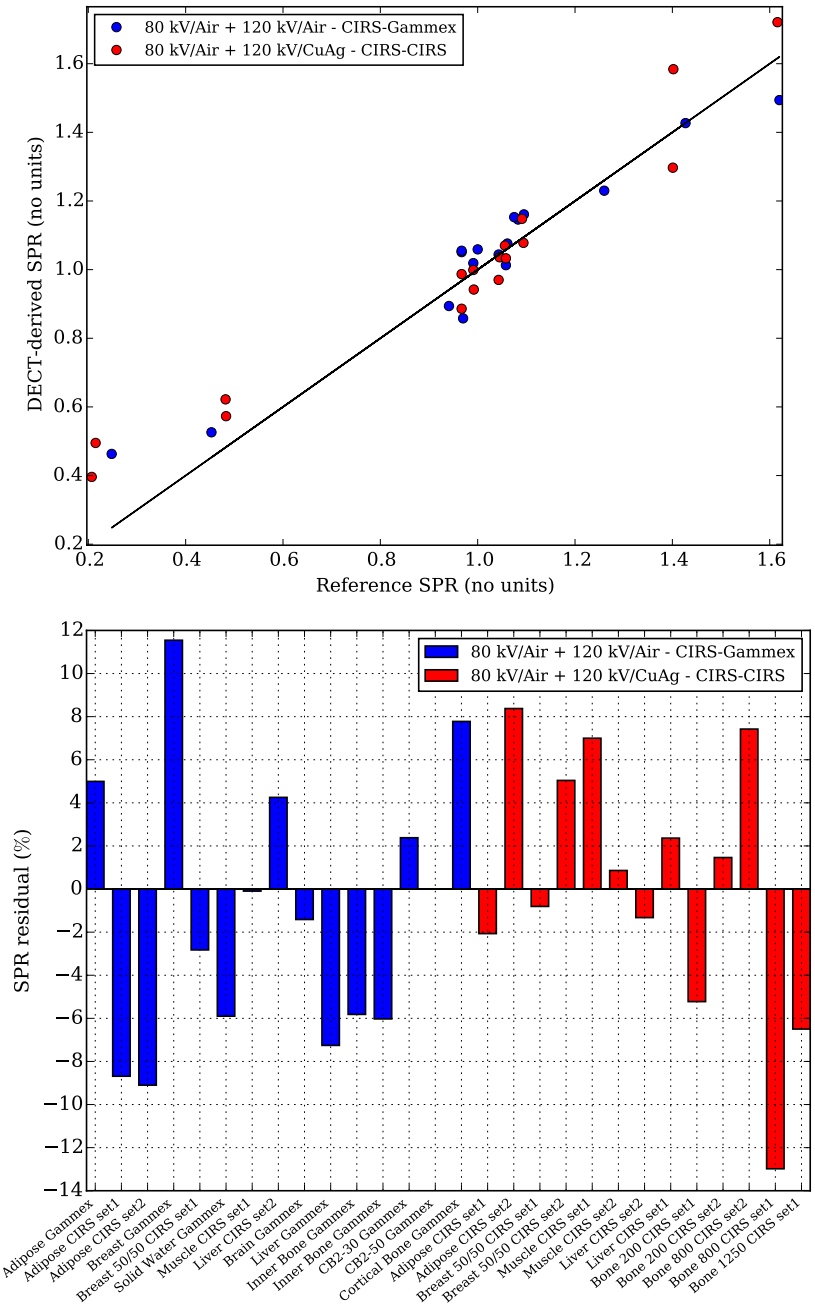

Figure 4.23: DECT-derived SPR values of the CIRS-Gammex (blue) and the CIRS-CIRS (red) phantom inserts for two dual-energy CBCT FKVS acquisitions versus reference values (top) and SPR residuals (bottom) for both phantom inserts sorted by increasing SPR value. Lung inserts were excluded from the residual plot.

4.6.2.3 SECT-derived SPR images

Figure 4.24 plots a line profile comparing the SPR image obtained through the HU-SPR curve of Figure 4.17 at 120 kV/Air with the experimentally determined SPR values (a), and the histogram of the SPR difference image (b). The SECT-derived image is less noisy with respect to the DECT-derived SPR image (Figure 4.19). This occurs because noise is propagated in DECT –and presumably enhanced– through the whole decomposition process and, afterwards, in the reconstruction step. In terms of RMS error, the SECT-image is comparable to the DECT-image. However, the SPR error histogram presents two peaks and none of them centered at zero (Figure 4.24-b). Moreover, SECT falls below lung tissue SPR accuracy as observed in the line profile or in the second wide peak centered at 0.4 on the SPR error histogram (Figure 4.24).

4.6.3 Discussion

Table 4.9 shows the percentage RMS errors obtained for several DE combinations when comparing DECT-derived SPR values with experimentally determined values. The SPR accuracy of these preliminary DE-CBCT acquisitions is far worst than the accuracy reported with diagnostic DECT systems, i.e. with RMS errors up to 1.2% [Hünemohr et al., 2014a; Hudobivnik et al., 2016]. Nevertheless, when looking at Table 4.9, a trend in the results has been observed which might explain these results.

Systematically, for the CIRS-CIRS and CIRS-Gammex phantoms, those DE combinations with high filtration –using the filters of the wheel or placing high purity filters after the collimator (see Table 4.9)– produced the worst results. The projection-based method used in this study relies on the exact knowledge of the source spectrum and the detector response (section 2.4). In addition, projection-based decomposition methods are known to be sensitive to spectrum alterations [Tremblay et al., 2014]. As the exact thicknesses of the wheel filters were not known, the nominal thicknesses were used instead. Moreover, the nominal filter composition was considered. Regarding the high purity filters taped to the collimator, placement errors (i.e. lack of orthogonality with respect to the beam axis) and source rotation might also modify the photon yield with respect to the estimated photon distribution. In addition, fluence corrections were not available for the acquisitions performed with a silver filter placed after the collimator (marked with a triangle in Table 4.9). Consequently, the uncertainty on the filter thicknesses and on the filter placement, might vary the photon yield due to their high attenuation properties and, thus, introduce some error in the decomposition scheme.

Another plausible explanation is that the source model used in this study is not optimal for high energies or for highly hardened beams, which was already pointed out in the discussion of [Vilches-Freixas et al., 2016a] (section 3.2). Moreover, the parametric source model was only calibrated close to the primary beam axis, it assumes a uniform 2D photon yield distribution, which might be incorrect in the presence of a filter. Indeed, specially on the phantom border of Figure 4.22 there is an overestimation of the phantom SPR compatible with a wrong estimation of the spectra 2D distribution due to the presence of the flattening filter (Figure 3.6), added before the experimental session that

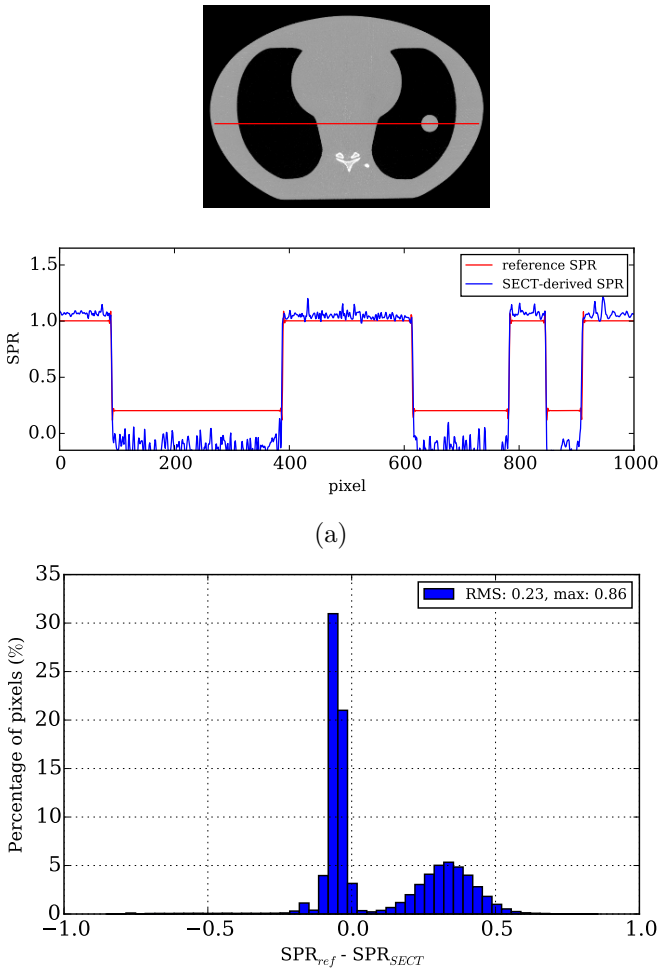

(a)

(b)

Figure 4.24: Results relative to the single-energy CBCT sequential acquisition at 120 kV/Air of the CIRS Thorax phantom. a) SPR profile comparing the reconstructed SPR image (blue) with the experimentally determined SPR values (red); b) histogram of the absolute SPR error. The corresponding RMS and maximum errors are indicated in the figure legend.

took place in November 2016. Furthermore, the source and the detector models should be validated against the different filter materials of the wheel.

In order to confirm these hypotheses, the next step would be to test the SPR accuracy with a calibration-based dual-energy decomposition method. Even if the current decomposition method actually relies on a calibration for both the source and the detector models, these models may need to be improved. The advantage of the polynomial

approach is that the source and the detector characteristics can be indirectly determined through a calibration procedure (section 2.4.2.2). One drawback of this approach is that a calibration per energy spectrum and tube settings, such as intensity and exposure time, should be performed and it might be tedious and time-consuming. Furthermore, it would also be worth investigating the performance of image-based decomposition approaches.

Except for the CIRS Thorax phantom, for which the collimator-shadow scatter correction was applied to, the other DE-CBCT acquisitions were not corrected for scatter. It is foreseen that results would improve with a proper scatter correction.

A double ring artifact around each phantom rod was visible in the reconstructed mass density images of Figure 4.20 –also visible in the SPR images– which might be due to the interpolation of projection images. This artifact might be less predominant if the projection to be interpolated had been backprojected at the isocenter instead of onto the detector (Figure 4.16).

BH-like artifacts are visible in the mass density images of Figures 4.20-4.22 but they are less present in the reconstructed SPR images. As already discussed in section 4.5, the base materials images, i.e. PMMA and Al, should not be affected by beam-hardening as the energy dependency is factored out in this decomposition process (equation 2.7). However, the choice of the basis material decomposition might have an influence on this assumption and the hypothesis that the linear attenuation coefficient of the object can be separated into an energy-dependent and an energy-independent part is not always valid. Equation 2.7 has to be verified for the entire range of the dual-energy spectra and it might not be true for too broad spectra. In addition, reconstruction artifacts such as streaks are present both in the mass density images and in the SPR images which might come from scatter. Improved SPR results are expected when these issues will be solved.

We observed for the same dual-energy spectra that FKVS results were slightly better than sequential results (Table 4.9). The main difference between both acquisitions is the number of frames of the LE and the HE projections after sinogram interpolation, i.e. 610 and 990 frames for the sequential and FKVS acquisitions, respectively. For the FKVS acquisitions, reconstructed mass density images exhibited less noise thanks to the increased number of projections which might influence the RED accuracy and, therefore, the SPR accuracy.

When comparing the SPR accuracy of the CIRS-Gammex phantom and the CIRS-CIRS phantom, for the same dual-energy CBCT FKVS acquisition, the CIRS-Gammex phantom provided better results. If we look at Table 4.9, the product of the tube current by the pulse length gives higher mAs values for the CIRS-Gammex phantom than for the CIRS-CIRS phantom. The smaller beam intensity of the CIRS-CIRS phantom acquisition causes more noise in the projections and it might impact the quality of the numerical solution (section 2.4.2.2).

4.6.4 Conclusions

The performance of the IR system on estimating the SPR of two tissue characterization phantoms and one anthropomorphic phantom has been evaluated. Preliminary results obtained on dual-energy CBCT sequential acquisitions and on dual-energy CBCT

FKVS acquisitions synchronized with the filter wheel of the IR are not optimal yet. Although the level of accuracy required to perform clinical treatment planning dose calculations with the reconstructed SPR images is not yet achieved, improvement paths have been identified. First, even if a 3 cm slit at the isocenter is used to reduce scatter, a remaining fraction of scatter contamination might still be present in the acquired projections of the CIRS-CIRS and CIRS-Gammex phantoms. Consequently, improved results are expected when applying the scatter correction implemented in the reconstruction pipeline of the IR. Second, the dual-energy material decomposition approach implemented in the projection domain is known to be sensitive to the correctness of the incident spectra, which is a required input to solve the non-linear system of equations (section 4.5.2.2). Inaccuracies on the chemical composition and the purity level of the additional filtration applied to the LE or the HE projections, wrong filter thickness estimation or suboptimal fluence correction, might alter the incident spectrum estimation and induce errors in the SPR estimation. The source and the detector models need also to be improved to better estimate the incident spectra. Moreover, the presence of noise in the projections, and a low SNR, might also influence the output of the material decomposition. Nevertheless, when comparing SECT- and DECT-derived SPR images of the CIRS Thorax phantom, DECT outperformed with respect to SECT, specially in the lung tissue region.

4.7 Conclusion

A literature overview on the existing methods to estimate the SPR from DECT acquisitions has been conducted. Two novel calibrated relations to estimate the SPR from dual-energy decomposition outputs have been proposed. Similar results in terms of accuracy were obtained when comparing the existing methods with the novel approaches. Most of the existing dual-energy decomposition methods for radiotherapy applications were found to be image-based. In order to determine whether projection-based approaches would be also suitable for proton therapy applications, a simulation-based comparative study between two image-based methods and one projection-based method has been conducted. Thanks to the development of new systems to perform dual-energy, such as dual-layer or photon-counting detectors (section 2.2), projection-based methods are becoming more attractive and, in the light of these results, should also be considered for proton SPR determination. Finally, the ability of the IR system to determine the SPR of real phantoms from dual-energy CBCT sequential and FKVS acquisitions using a projection-based dual-energy decomposition approach has been evaluated. Preliminary SPR images did not achieve the level of accuracy required to perform clinical treatment planning dose calculations. Some weak points have been individuated on the followed methodology and several ways for improving these results have been outlined to reach the ultimate goal of performing proton dose calculations on reconstructed SPR images using the IR system.

Chapter 5

DECT optimization for proton therapy

Contents

In the previous chapter, we compared several decomposition bases to estimate the proton SPR and the two main decomposition domains (image- or projection-based) in terms of SPR accuracy. The two-material decomposition approach implemented in the projection-domain was found to be a good choice: the results were comparable or slightly better than other methods implemented in the image-domain, and there is no need to implement a beam-hardening correction. In this chapter, the goal is to investigate the factors that would have an impact on the outcome of the dual-energy decomposition process, from the acquisition parameters to the post-processing, focusing entirely on projection-based approaches. To achieve this task, we tried to investigate which is the optimal dual-energy spectra, dose balance between energy levels, material decomposition pair of basis, and way of solving the inverse problem of material decomposition (section 2.4.2.2).

This chapter is organized in three parts. In the first part, based on simulations of X-ray images, we investigated the effect of various voltages and tin filtration combinations, and the influence of the dose allocation between the low energy (LE) and the high energy (HE) acquisitions on the SPR map accuracy and precision. This work has been published in the *Med. Phys.* journal in a full article format (see Appendix A). In the second part, we fixed the dual-energy spectra, the dose balance between energy channels and the method of solving the system of equations and we varied the decomposition basis: acrylic (PMMA) and aluminum, soft tissue and cortical bone, and water and compact bone. In the third part, keeping all the other parameters fixed, the inverse problem was solved using a polynomial approximation and an iterative convex optimization, and we compared the results.

5.1 Dual-energy spectra and dose balance

5.1.1 Introduction

Nowadays, there is a growing concern about the imparted doses in medical imaging applications, particularly for diagnostic procedures. By balancing the dose between the low (LE) and the high energy (HE) acquisitions, radiation dose levels of DECT imaging are not necessarily higher than those of SECT imaging [Henzler et al., 2012]. Due to the additional information contained in DECT data compared to SECT, it seems also feasible to further reduce radiation doses with dual-energy imaging. For that, the optimization of DECT acquisition protocols focusing on the figure of merit specific for each task, e.g. diagnostic or radiotherapy treatment planning, is mandatory. In addition, a careful study of the influence of the various acquisition parameters on the accuracy of the extracted data is of importance. Spectral optimization of dual-energy imaging has been conducted for cardiac, chest and mammography imaging applications [Xu et al., 2006;

Saito, 2007; Shkumat et al., 2007]. Additional spectral filtration has been optimized to improve the dual-energy performance in material discrimination tasks based on the dual-energy ratio [Granton et al., 2008; Primak et al., 2009]. In most of these works, the optimization of DECT acquisition settings, i.e. dose distribution between low and high energy acquisitions, tube voltage pair, filter material and thickness, is based on the contrast-to-noise ratio (CNR) or the signal-to-noise ratio (SNR) criterion. In a recent work [Rigie and La Rivière, 2016], a framework for optimizing spectral CT imaging parameters and hardware design with respect to material classification tasks has been proposed.
In this work, we have focused on investigating the effect of two factors, namely the dual-energy spectra and the dose balance between energy levels, to maximize the accuracy and the precision of SPR maps, which are figures of merit essential for proton therapy dose calculations. First, we have investigated the effect of various voltages and tin filtration combinations on the SPR. Second, holding the dose to the patient constant, we have studied the influence of the distribution of dose between the low and the high energy acquisitions on the reconstructed SPR images, using four representative dual-energy spectra. The SPR images of three slices of the Adult Female (AF) ICRP computational phantom (i.e. head, thorax and pelvis) have been reconstructed for the same four pairs of spectra. Then, the ranges of 70 MeV, 90 MeV and 100 MeV proton beams –which corresponded to a range in water of 40.8 mm, 64.0 mm and 77.2 mm, respectively– have been computed from the reconstructed SPR maps at different incident angles. The proton range accuracy of each setup has been estimated by calculating the mean range deviation over all irradiation angles and the root-mean-square (RMS) error. The gain in range accuracy, based on this dual-energy approach, has also been compared to a single-energy CT acquisition of the AF ICRP phantom at 120 kVp.

5.1.2 Materials and Methods

5.1.2.1 Image simulation

The 33-cm diameter Gammex RMI 467 (Gammex, Middleton, WI) tissue characterization phantom, which represents a medium-size body, was used to investigate the optimal dual-energy spectra and the optimal dose balance between energy levels. Sixteen inserts mimicking human tissue attenuation properties positioned as described in Figure 5.1 with mass densities ranging from 0.3 to 1.82 g·cm^{-3} and known chemical compositions were considered. The index-to-material mapping and the reference SPR values are provided in Figure 5.1.

The AF reference computational phantom of the International Commission on Radiological Protection (ICRP) [ICRP, 2009] was used as a virtual patient to investigate the influence of the previous results on the proton range estimation. This phantom represents an average female and it contains 140 organs made of 53 standard human tissues, whose mass density and chemical composition are provided in the same ICRP Publication 110 [ICRP, 2009]. Each voxel has a dimension of 1.774×1.775×4.84 mm^3. Three axial slices of different anatomical regions were selected to evaluate different human

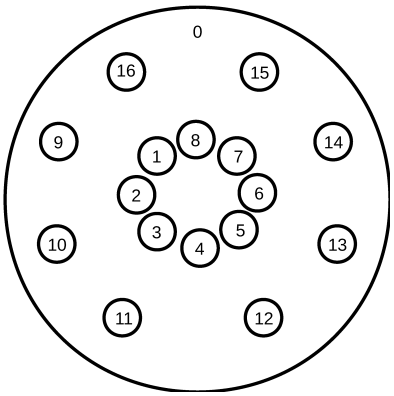

ID	Materials	SPR
0	Water	1.004
1	CB2-50% $CaCO_3$	1.439
2	BR12 Breast	0.972
3	SB3 Cortical Bone	1.634
4, 15	AP6 Adipose	0.939
5, 14	LV1 Liver	1.072
6	BRN-SR2 Brain	1.071
7, 12	Solid Water	1.002
8, 9	LN300 Lungs	0.284
10	LN450 Lungs	0.431
11	CB2-30% $CaCO_3$	1.271
13	IB3 Inner Bone	1.089
16	B200 Bone Mineral	1.098

Figure 5.1: Left: Gammex 467 phantom. Right: Insert ID, material name and reference SPR values.

tissues and irradiation geometries: head, thorax and pelvis (Figure 5.2).

For both phantoms, the electron density relative to water of each insert material or tissue m was estimated using:

$$\mathsf{RED}_m = \frac{\rho_m \left[\sum_i w_i \frac{Z_i}{A_i}\right]_m}{\rho_{\mathrm{w}} \left[\sum_i w_i \frac{Z_i}{A_i}\right]_{\mathrm{w}}} \tag{5.1}$$

where the label w refers to water, ρ is the mass density, Z_i is the atomic number, A_i the atomic mass and ω_i the fraction by weight of the i^{th} chemical element that composes the material m.

The reference stopping power values relative to water of the phantom inserts were computed using Bethe's equation without correction terms [Schneider et al., 1996; Yang et al., 2010]. A 200 MeV initial kinetic energy was used, and an ionization potential value of water of 78 eV was considered. Both the RED and the SPR reference values were computed with respect to G4-Water, i.e. water material from the Geant4 materials database, which slightly differs from Gammex Water material. Consequently, the reference SPR value of Gammex Water is 1.004 instead of 1 (Figure 5.1).

To make the study as realistic as possible, the irradiation geometry and the characteristics of a particular device, the Imaging Ring (IR) X-ray system (medPhoton, Salzburg, Austria), described by Rit *et al* [Rit et al., 2016], were employed in this study (see chapter 3 for further details). Nevertheless, the results of this study could be extrapolated for any other dual-spectrum device. Virtual CT acquisitions of the IR were carried out by means of deterministic simulations in GATE [Jan et al., 2004] v7.2 using the Fixed Forced Detection (FFD) actor. This deterministic module computes digitally reconstructed radiographs (DRR) using the reconstruction toolkit (RTK) [Rit et al., 2014] and the Geant4 database of X-ray cross sections. Fan-beam projections where

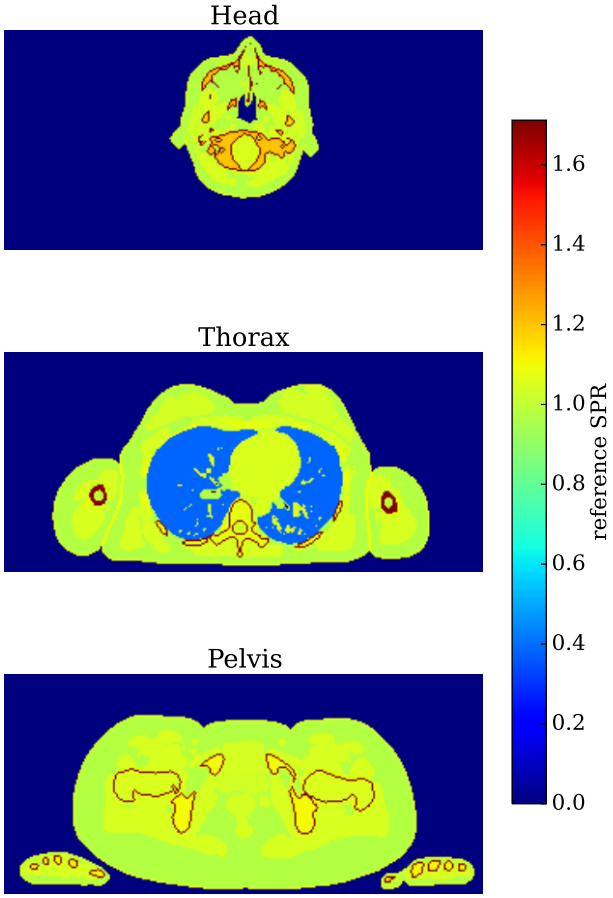

Figure 5.2: Reference SPR images for the head, thorax and pelvis slices of the AF ICRP phantom.

360 views of 807 pixels of 1 mm without scatter were considered for the Gammex phantom, whereas 600 projections of 1026 pixels of 1 mm without scatter were considered for the ICRP phantom. The source-to-isocenter distance was 626 mm and the source-to-detector distance was 1026 mm. For the realistic scenario, Poisson noise was applied to the projections to deliver a central dose D_c with each spectrum while delivering a total central dose of 20 mGy with the dual-energy acquisition. The level of Poisson noise depends on the number of primary photons per simulation, N_{prim}, required to deliver a central dose of primary radiation, D_c, which was determined analytically assuming an homogeneous water medium:

$$N_{prim} = \frac{D_c \; A_{beam}}{\int_E S(E) \; e^{-\mu_w(E) \; r} \; \frac{\mu_{en,w}(E)}{\rho_w} \; E \; dE} \tag{5.2}$$

where A_{beam} is the area covered by the beam at the isocenter considering a constant

flat field, S is the energy-dependent incident spectrum with unity area: $\int_E S(E) \cdot \mathrm{d}E = 1$, $\mu_{\mathrm{en,w}}(E)/\rho_{\mathrm{w}}$ and μ_{w} are respectively the energy-dependent mass energy-absorption coefficient and the linear attenuation coefficient of water taken from the NIST database [Hubbell and Seltzer, 2004], and r is the radius of the phantom. The central dose of D_{c} of 10 mGy per energy spectrum (20 mGy in total) was calculated at the center of a 33 cm diameter water phantom for the Gammex, the ICRP thorax slice and the ICRP pelvis slice, whereas a 20 cm diameter water phantom was considered for the ICRP head slice. The energy-dependent detector response used in this study was previously validated by Vilches-Freixas *et al* [Vilches-Freixas et al., 2016a].

For each projection angle, a low energy (LE) and a high energy (HE) intensity value were obtained:

$$I_{\mathrm{LE}} = \int_{E_{min}}^{E_{max}} S_{\mathrm{LE}}(E)\ D(E) \exp\left(-\int_L \mu(\ell, E)\mathrm{d}\ell\right) \mathrm{d}E \tag{5.3}$$

$$I_{\mathrm{HE}} = \int_{E_{min}}^{E_{max}} S_{\mathrm{HE}}(E)\ D(E) \exp\left(-\int_L \mu(\ell, E)\mathrm{d}\ell\right) \mathrm{d}E \tag{5.4}$$

where L is the line segment between the source and a detector pixel, I_{LE} and I_{HE} are the measured intensities, S_{LE} and S_{HE} are the weights of the polychromatic photon spectra, and $D(E)$ the detector response.

For each pair of X-ray spectra, the incident energy gap, ΔE, was calculated as the separation between the average energies of the incident spectra:

$$\Delta E = \int_0^{E_2} S_{HE}(E)\ E\ \mathrm{d}E - \int_0^{E_1} S_{LE}(E)\ E\ \mathrm{d}E \tag{5.5}$$

where E_1 and E_2 are the maximum energies of the LE and the HE spectra, respectively.

5.1.2.2 Dual-energy spectra optimization

SpekCalc [Poludniowski, 2007; Poludniowski and Evans, 2007; Poludniowski et al., 2009b] was used to generate the X-ray spectra from 60 kV to 140 kV with 2 kV steps, 10° anode angle, 2.5 mm Al total filtration (required minimum filtration according to the NCRPM (1989) [National Council on Radiation Protection and Measurements., 1989]) and 1000 mm air filtration. Each spectrum was filtered with pure tin (Sn), as suggested by Primak *et al* (2009) [Primak et al., 2009], with thicknesses ranging from 0 to 2.5 mm in 0.1 mm increments. For the LE acquisitions, the tube voltage was varied from 60 kV to 100 kV, whereas for the HE acquisitions it was varied from 80 kV to 140 kV. No tin filtration was considered for the LE acquisitions to maximize the energy gap, only the 2.5 mm Al inherent filtration. In total, 16926 tuples (21 LE voltages, 31 HE voltages and 26 Sn thicknesses) were evaluated.

In this spectra optimization study, the same dose at the center was considered for the low and the high energy acquisitions. In particular, a central dose D_{c} of 10 mGy with each voltage and filtration combination was used, and thus a total central dose of 20 mGy with the dual-energy acquisition.

For each (LE, HE, mm Sn) tuple, the reconstructed SPR image of the Gammex phantom was compared to the reference values (Figure 5.1). The relative accuracy and precision were calculated in a circular ROI centered at the center of the insert with a radius of 3/4 the size of the insert (i.e. 10 pixels radius). The relative accuracy (RA) and precision (RP) of the SPR averaged over all inserts were computed as follows:

$$\mathrm{RA} = \frac{1}{N}\sum_{m=1}^{N}\left(\frac{v_m^{\mathrm{ref}} - \overline{v}_m}{v_m^{\mathrm{ref}}}\right) \tag{5.6}$$

$$\mathrm{RP} = \sqrt{\frac{1}{N}\sum_{m=1}^{N}\left(\frac{\sigma_m}{v_m^{\mathrm{ref}}}\right)^2} \tag{5.7}$$

where v_m^{ref}, $\overline{v}_m$ and σ_m are respectively the reference SPR value (listed in Figure 5.1), the mean SPR value inside the ROI and the standard deviation inside the ROI for the m^{th} insert, with N equal to 16.

5.1.2.3 Fractional dose allocation optimization

The same irradiation setup as described above was used to estimate the optimal dose balance between voltages that minimizes the uncertainty and the precision of the SPR. Table 5.1 shows the four dual-energy spectra selected for this study, with incident energy gaps comprised between 30 keV and 49 keV. The first pair of dual-energy spectra corresponds to the Siemens Flash spectra [Primak et al., 2010]; the second one to a possible pair of dual-energy spectra generated with the medPhoton Imaging Ring; whereas the others correspond, respectively, to the optimal dual-energy spectra for solid water and bone tissue obtained from the results of Section B. The dose of the LE and the HE acquisitions are herein named $\mathrm{D_{LE}}$ and $\mathrm{D_{HE}}$, respectively. For each pair of dual-energy spectra, the proportion of $\mathrm{D_{LE}}$ ($\mathrm{D_{HE}}$) with respect to the total dose was varied from 10% (90%) to 90% (10%) by steps of 20% while keeping the phantom dose at the center to a constant value of 20 mGy. For each dose level, the corresponding Poisson noise was computed using Equation 5.2 and it was applied to the projections through the FFD actor of GATE. In total, considering the 4 pairs of dual-energy spectra and the 5 dose levels evaluated per spectra, 20 noise levels were computed with Equation 5.2. For each noise level, i.e. for each pair of dual-energy spectra and dose proportion, 25 realizations of noise in the projection images were generated to estimate the accuracy and the precision. Then, the SPR value inside a 10 pixels radius ROI inside each insert was computed for each set and compared to the reference values. The overall accuracy and precision of the SPR averaged over all inserts were also computed (Equations 5.6 and 5.7).

#	LE spectrum	HE spectrum	ΔE (keV)	Description
1	80 kVp	140 kVp + 0.4 mm Sn	43	Siemens Flash spectra
2	60 kVp	120 kVp + 0.6 mm Sn	48	medPhoton Imaging Ring spectra
3	90 kVp	110 kVp + 0.5 mm Sn	30	solid water optimal DE spectra
4	80 kVp	106 kVp + 2.2 mm Sn	49	bone tissue optimal DE spectra

Table 5.1: Dual-energy spectra selected for the dose allocation study and the assessment of the proton range accuracy. From left to right: low-energy spectrum, high-energy spectrum with additional tin filtration and the corresponding energy gap.

5.1.2.4 SPR determination

The proposed method to compute the SPR from dual-energy data in the projection domain is an adaptation of the two-steps procedure proposed by Farace [Farace, 2014] in the image domain. It consists of two steps: first, determination of the RED image through the two-material decomposition method proposed by Alvarez and Macovski [Alvarez and Macovski, 1976] implemented in the projection domain; second, determination of the SPR image using the poly-lines relations proposed by Kanematsu *et al* [Kanematsu et al., 2012].

The key idea of the two-materials method is that the linear attenuation coefficient of the scanned object at any spatial position $\boldsymbol{x}$ and energy E, $\mu(\boldsymbol{x}, E)$, can be expressed as a linear combination of two energy-dependent basis functions of two materials with energy-independent coefficients. Choosing water (w) and compact bone (b) as basis materials, it is assumed that

$$\mu(\boldsymbol{x}, E) = \rho_{\mathrm{w}}(\boldsymbol{x}) \left(\frac{\mu}{\rho}\right)_{\mathrm{w}} (E) + \rho_{\mathrm{b}}(\boldsymbol{x}) \left(\frac{\mu}{\rho}\right)_{\mathrm{b}} (E) \tag{5.8}$$

where μ/ρ denotes the energy-dependent mass attenuation coefficients and ρ the mass fraction per volume.

By performing an acquisition with LE and HE spectra, two sinograms of the same object are available. For every angle θ and pixel location $\boldsymbol{u}$, we have

$$\hat{I}_{\mathrm{LE}}(\theta, \boldsymbol{u}) = -\ln\left[\frac{I_{\mathrm{LE}}(\theta, \boldsymbol{u})}{I^0_{\mathrm{LE}}(\theta, \boldsymbol{u})}\right] \tag{5.9}$$

$$\hat{I}_{\mathrm{HE}}(\theta, \boldsymbol{u}) = -\ln\left[\frac{I_{\mathrm{HE}}(\theta, \boldsymbol{u})}{I^0_{\mathrm{HE}}(\theta, \boldsymbol{u})}\right] \tag{5.10}$$

where I_{LE} and I_{HE} are the intensities measured in the presence of the object, while I^0_{LE} and I^0_{HE} are the intensities measured in the absence of the object. The projection of the mass densities are given by

$$a_{\mathrm{w}}(\theta, \boldsymbol{u}) = \int_{L(\theta,\boldsymbol{u})} \rho_{\mathrm{w}}(\ell)\mathrm{d}\ell \tag{5.11}$$

$$a_{\mathrm{b}}(\theta, \boldsymbol{u}) = \int_{L(\theta,\boldsymbol{u})} \rho_{\mathrm{b}}(\ell)\mathrm{d}\ell \tag{5.12}$$

where $L(\theta, \boldsymbol{u})$ is the line segment between the source and a detector pixel located at position $\boldsymbol{u}$ for the view angle θ. The projected mass densities $\{a_{\mathrm{w}}, a_{\mathrm{b}}\}$ can be expressed as a polynomial function of the logarithmic transmission values $\{\hat{I}_{\mathrm{LE}}, \hat{I}_{\mathrm{HE}}\}$ [Lehmann et al., 1981; Chuang and Huang, 1988] at every angle θ and pixel location $\boldsymbol{u}$, i.e.,

$$a_{\mathrm{w}} = \mathcal{P}_{\mathrm{w}}(\hat{I}_{\mathrm{LE}}, \hat{I}_{\mathrm{HE}}) \tag{5.13}$$

$$a_{\mathrm{b}} = \mathcal{P}_{\mathrm{b}}(\hat{I}_{\mathrm{LE}}, \hat{I}_{\mathrm{HE}}) \tag{5.14}$$

The coefficients of the polynomial $\mathcal{P}_{\mathrm{w}}$ and $\mathcal{P}_{\mathrm{b}}$ can be obtained through a calibration procedure in the least square sense. Attenuation measurements were performed for two different photon spectra (labeled LE and HE) interposing slabs of two well-known materials with variable thicknesses. It is important that the calibration phantom covers all possible path length variations through each basis material, and combinations of path lengths through both materials [Stenner et al., 2007]. In this study, water thicknesses ranging from 0 to 38 cm with 1 mm steps and compact bone thicknesses comprised between 0 and 15 cm in 1 mm increments were used for the calibration. A fourth degree polynomial with fifteen terms was initially considered. A stability study to noise, similar to that conducted by Létang *et al* [Létang et al., 2004], was performed to determine which terms of the polynomial were more unstable and, thus, eliminated. Finally, a fourth degree polynomial with twelve terms was found to be adequate to solve this system of equations (see section 5.3.3.1 for further details).

Then, image reconstruction of water and compact bone mass densities were performed using the filtered backprojection (FBP) reconstruction of RTK on a 380×380 pixel grid with 1×1 mm^2 pixels size for the Gammex images, and on a 299×137 pixel grid with 1.775×1.775 mm^2 pixels size for the ICRP images.

Finally, on a pixel-by-pixel basis, the RED image was derived from the reconstructed mass density images, $\rho_{\mathrm{w}}(\boldsymbol{x})$ and $\rho_{\mathrm{b}}(\boldsymbol{x})$, the number of electrons per molecular weight of each basis material and the tabulated electron density of water (i.e. G4-water for consistency with reference RED and SPR values), $\rho_{e,\mathrm{w}}$, divided by the Avogradro's number, N_{A}:

$$\mathrm{RED}(\boldsymbol{x}) = \frac{\rho_{\mathrm{w}}(\boldsymbol{x}) \left[\sum_i w_i \frac{Z_i}{A_i}\right]_{\mathrm{w}} + \rho_{\mathrm{b}}(\boldsymbol{x}) \left[\sum_i w_i \frac{Z_i}{A_i}\right]_{\mathrm{b}}}{\left(\frac{\rho_{e,\mathrm{w}}}{N_{\mathrm{A}}}\right)} \tag{5.15}$$

The reconstructed RED values were directly converted into SPR through the piecewise linear relations of the RED and the ratio between SPR and RED of human tissues as suggested by Kanematsu [Kanematsu et al., 2012]. To reproduce Figure 1a of Kanematsu *et al* [Kanematsu et al., 2012], a selection of 92 ICRU 46 [Bethesda, 1992] body tissues, excluding obsolete or artificially extracted materials, were used to perform the calibration. The SPR values of these body tissues were calculated using Bethe's equation without correction terms at 200 MeV, as done for the Gammex and the ICRP SPR reference values.

5.1.2.5 Proton range prediction

To estimate the accuracy of the proton range prediction, three slices of the ICRP phantom were selected: head, thorax and pelvis. Three proton energies were considered: 70 MeV (head), 90 MeV (thorax) and 100 MeV (pelvis). The corresponding ranges in water R_{water}, according to the continuous slowing down approximation [Berger et al., 2011], were 40.8 mm, 64.0 mm and 77.2 mm, respectively. These beam energies have no clinical relevance, they have been chosen to avoid irradiating twice the same phantom area with coplanar beams. The proton range in the phantom computed at each angle θ, where θ ranges from 0 to 360° in 5° step around the center of the phantom, was determined as the phantom depth R_θ where the water equivalent thickness, defined as the integral of the phantom SPR along the proton beam path, matched the proton range in water:

$$R_{\text{water}} = \int_0^{R_\theta} \mathsf{SPR}_\theta(l)\ \mathrm{d}l \tag{5.16}$$

where SPR_θ is the 1D profile of the SPR image along the proton beam path for the incident angle θ. The SPR was computed for the dual-energy spectra shown in Table 5.1. To quantify the gain with respect to single-energy imaging, scanner simulations of the Gammex phantom performed at 120 kVp filtered with 0.2 mm Sn were used to generate a CT number to SPR calibration curve (Figure 5.3). A CT acquisition of the AF ICRP phantom at 120 kVp/Sn was used to derive the corresponding SPR map through this SECT calibration curve. Both for single-energy and dual-energy, two dose levels were considered: SPR images computed without imaging noise (infinite dose or ideal case) and SPR images computed with a 20 mGy central dose. For the latter, for each anatomical region and spectra, the range was assessed on 25 SPR images reconstructed from different noise realizations.

The proton range estimated from DECT and SECT SPR maps were compared to the range calculated from the reference SPR map (Figure 5.2).

For each imaging situation and noise setup, the histogram of the proton range differences over all irradiation angles was fitted with a Gaussian distribution ($\mu \pm \sigma$). In addition, the RMS error and the maximum error were also computed.

5.1.3 Results

5.1.3.1 Dual-energy spectra optimization

In this spectra optimization study, a total of 16926 tuples were considered by combining 21 LE voltages, 31 HE voltages and 26 Sn-thicknesses. For the realistic scenario (images with a 20 mGy central dose and equal dose weight per energy channel), the overall SPR accuracy and precision were plotted against the incident energy gap (Figure 5.4). The overall accuracy (Equation 5.6) was not strongly dependent on the spectra separation, with a minimum in the 25-35 keV range of energy gaps where the maximum separation is about 80 keV. In addition, dual-energy spectra combinations with

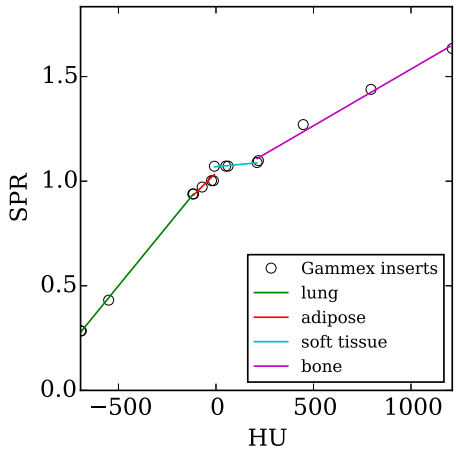

Figure 5.3: HU to SPR calibration curve for SECT scanner simulations of the Gammex phantom at 120 kVp/Sn. A piece-wise linear interpolation between HU and SPR values was used, divided in four segments: lung tissue, adipose tissue, soft tissue and bone tissue.

an energy gap above 30 keV resulted in an overall accuracy within ±0.6%. The overall precision (Equation 5.7) asymptotically approached a 4.7% level with increasing energy gap. This level of precision was achieved for energy gaps greater than 60 keV.

A zero precision was expected for the simulations without noise. However, images reconstructed from noiseless discrete projections always display residual noise caused by discrete filtering and image interpolation during backprojection. A constant value of 2.6 % was observed for all SPR images without noise. In other words, the horizontal line in Figure 5.4b would be shifted to 2.6% in the case of noiseless simulations. This residual noise level is also present in the noisy simulations of Figure 5.4 but combined with the photon noise.

To understand why the energy gap is not a good metric to determine the dual-energy spectra that minimizes the overall SPR accuracy, one representative insert per tissue group was selected: LN-300(8) for the low (RED<0.5), Solid Water(7) for the medium (0.5<RED<1.2) and CB2-50(1) for the high (RED>1.2) density. One optimal dual-energy spectra per tissue group was determined looking at the accuracy inside the corresponding ROI for all spectra combinations. Around this (LE, HE, Sn) tuple, orthogonal slices were plotted to study the dependence of the insert accuracy with the low voltage, the high voltage and the additional filtration. The plots relative to the ideal situation are shown in Figure 5.5. Different optimal points were found for different tissue types, which suggests tissue variability with respect to the optimal energy spectra.

To investigate why there are some energy windows that produce better accuracy results than others, the ratio between the theoretical linear attenuation coefficient (retrieved from NIST [Hubbell and Seltzer, 2004]) and the estimated value (obtained through Equation 5.8) as a function of the monochromatic energy was computed for the same Gammex inserts as in Figure 5.5: CB2-50, Solid Water and LN-300. For each

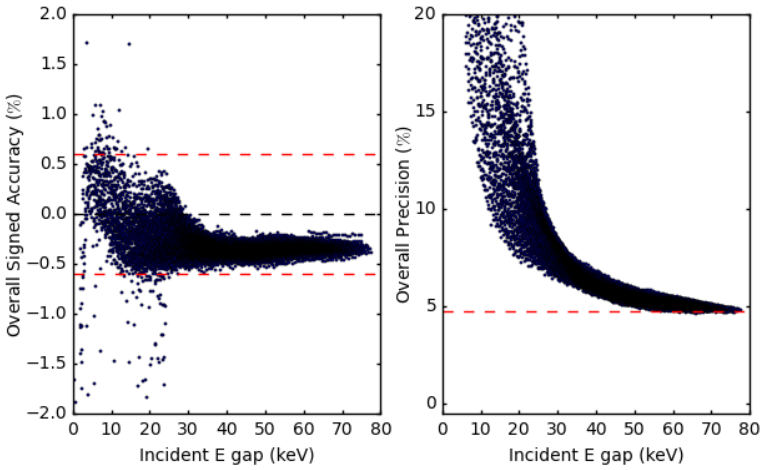

Figure 5.4: Overall SPR accuracy and precision as a function of the incident energy gap for the realistic acquisition scenario (20 mGy central dose) and the same dose weight per voltage. Each of the 16926 data points corresponds to a (LE, HE, mm Sn) combination. Horizontal dashed red lines indicate the ±0.6% accuracy level (left) and the 4.7% precision level (right).

insert, two pairs of dual-energy spectra were considered: one pair that maximizes the SPR accuracy and one that does not provide a good accuracy. Plot of the ratio between theoretical and estimated μ values for the three Gammex inserts is shown in Figure 5.6. The μ ratio being close to one for the entire range of the dual-energy spectra seems to correlate well with better SPR accuracy results. Solid water seems to be less dependent on the dual-energy spectra, as also shown in Figure 5.5, where most of the spectra provide a good level of accuracy. On the other hand, bone tissue and lung tissue present well-defined energy windows where the level of accuracy is optimal and areas where it is not.

5.1.3.2 Fractional dose allocation optimization

The impact of the dose balance between the low and the high energy projections was studied using 25 SPR images for each pair of dual-energy spectra of Table 5.1 and dose ratio (i.e. from 10% to 90%), obtained after decomposition and reconstruction of different noise realizations.

The boxplots of the overall precision (Equation 5.7) and accuracy (Equation 5.6) as a function of the dose distribution between the LE and the HE acquisitions are shown in Figure 5.7. The overall precision presented a minimum around 30% D_{LE} (70% D_{HE}) for all spectra. As shown in Figure 5.4, Figure 5.7 confirms that the precision improves when the energy separation between the incident energy spectra increases. In terms of accuracy, the overall accuracy is almost flat in the range 30%-70% D_{LE} (70%-30% D_{HE}). Around 90% D_{LE} (10% D_{HE}) the overall accuracy seems to be improved (Figure 5.7,

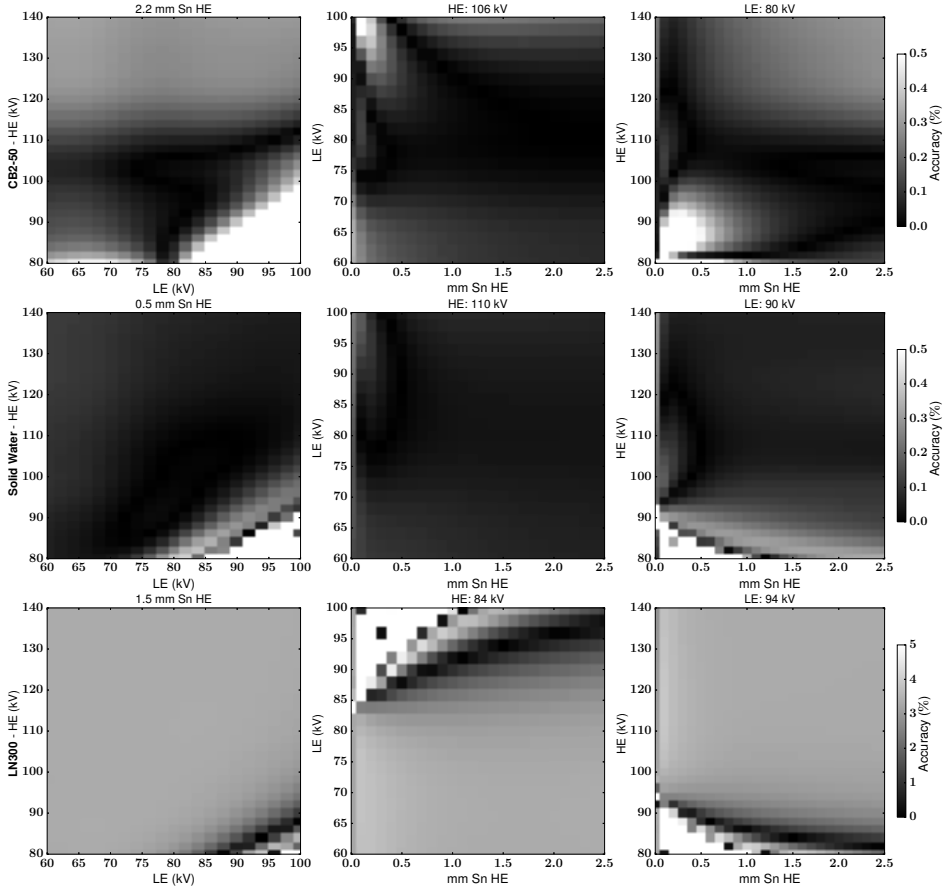

Figure 5.5: From top to bottom, SPR accuracy results as a function of the LE, HE and tin filtration for the insert: CB2-50, Solid Water and LN-300. From left to right: LE-HE plot at the optimal Sn thickness, LE-mm Sn plot at the optimal HE, HE-mm Sn plot at the optimal LE. The greyscale indicates the percentage error for the accuracy in absolute value. Note the different scale for the CB2-50 and the Solid Water with respect to the LN-300 insert. Data corresponding to the ideal situation, without noise.

right). However, the precision is two times larger than the 70% D_{LE} (30% D_{HE}) proportion (Figure 5.7, left) and noise therefore masks the validity of the accuracy at this point.

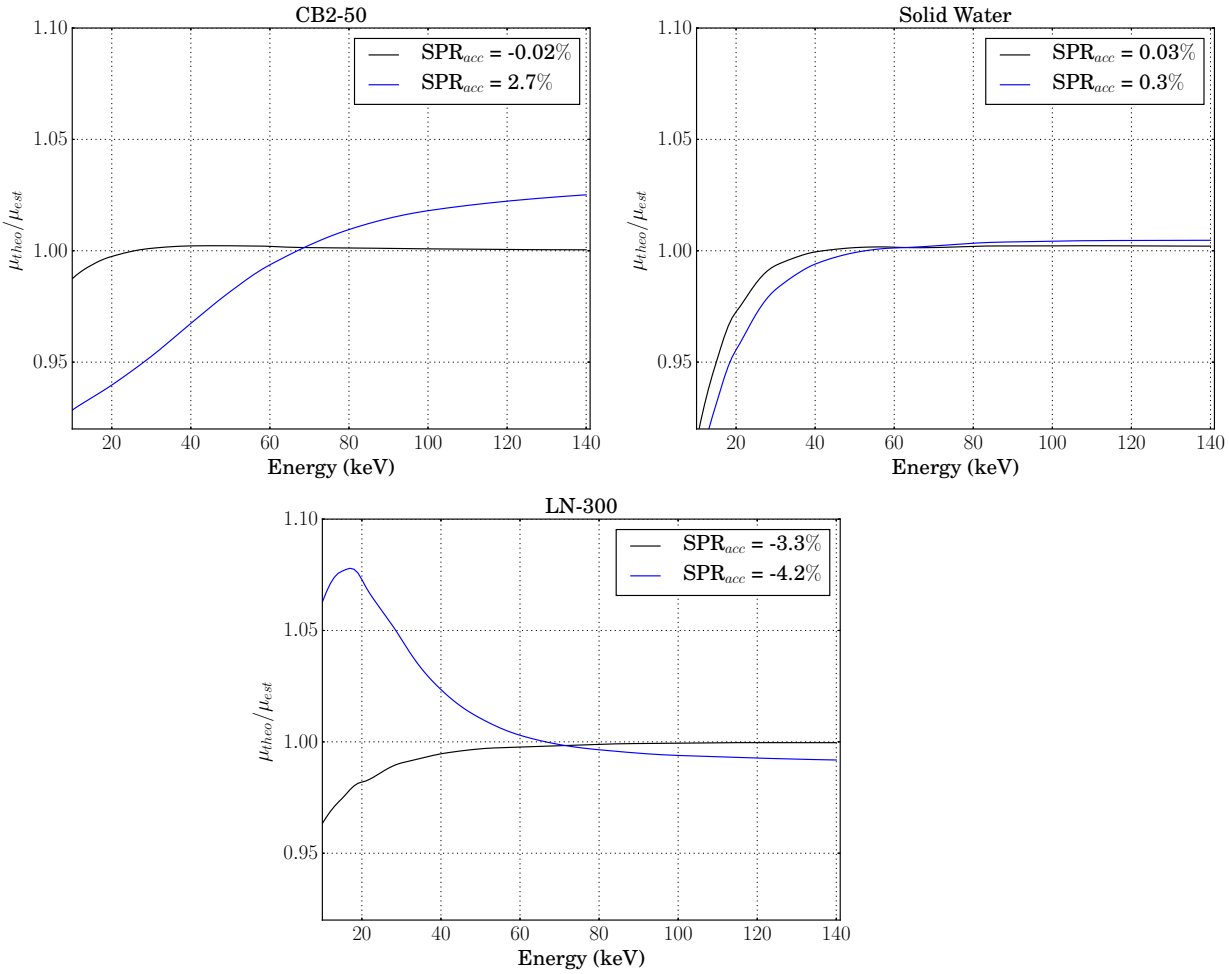

Figure 5.6: Ratio between the theoretical μ and the estimated μ value derived from Equation 5.8 as a function of the energy for three Gammex inserts. From left to right and top to bottom: CB2-50, Solid Water and LN-300. Legend shows the SPR accuracy corresponding to one optimal dual-energy spectra (black) and to one sub optimal dual-energy spectra (blue).

5.1.3.3 Proton range prediction

Proton beam irradiations were simulated from 360 directions in 5° step around the center of the ICRP phantom slices. The proton ranges for a 70 MeV, 90 MeV and 100 MeV were computed from the DECT-derived SPR images, the SECT-derived SPR images and from the reference SPR maps. Signed mean errors, maximum deviations and RMS errors on the proton range estimation over 360 directions at 70 MeV (head), 90 MeV (thorax) and 100 MeV (pelvis) are shown in Table 5.2 for the ideal situation (without noise) and the realistic scenario (at a central dose of 20 mGy).

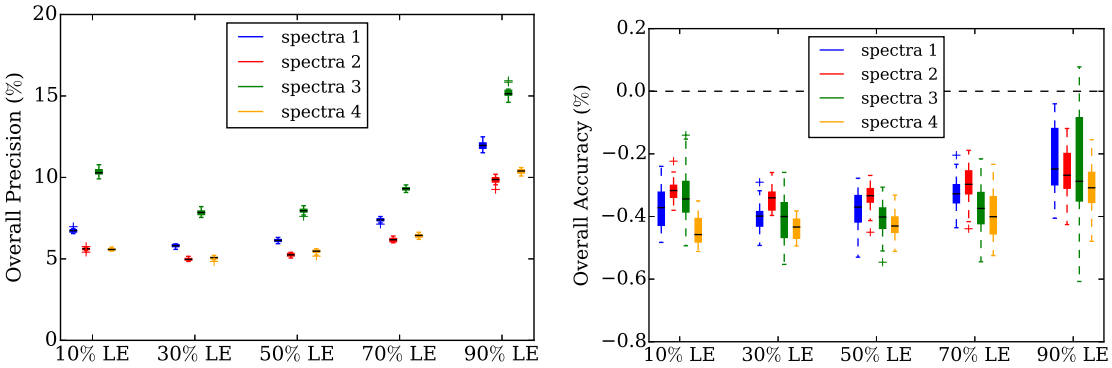

Figure 5.7: Overall precision (left) expressed in terms of the root-mean-squared (RMS) error, and overall accuracy (right) determined as the mean signed deviation, averaged over all inserts, as a function of the dose allocation between the LE and the HE acquisitions. The dual-energy spectra are described in Table 5.1.

		Without noise			20 mGy		
	Spectra	$\mu \pm \sigma$ (mm)	max (mm)	RMS (mm)	$\mu \pm \sigma$ (mm)	max (mm)	
Head	1	-0.04 ± 0.50	1.9	0.51	-0.05 ± 0.55	2.1	0.55
	2	-0.13 ± 0.55	1.9	0.56	-0.12 ± 0.56	2.1	0.57
	3	0.07 ± 0.49	1.9	0.50	0.07 ± 0.51	2.0	0.51
	4	-0.04 ± 0.51	1.9	0.51	-0.05 ± 0.53	2.1	0.54
	SECT	0.46 ± 0.67	1.9	0.81	0.47 ± 0.67	2.0	0.82
Thorax	1	-0.10 ± 0.70	2.7	0.71	-0.10 ± 0.73	3.8	0.74
	2	-0.14 ± 0.71	2.8	0.72	-0.15 ± 0.76	3.7	0.77
	3	0.00 ± 0.69	2.5	0.69	-0.00 ± 0.77	3.8	0.76
	4	-0.13 ± 0.68	2.6	0.69	-0.09 ± 0.74	3.8	0.75
	SECT	0.28 ± 0.81	3.2	0.86	0.29 ± 0.82	3.5	0.87
Pelvis	1	-0.15 ± 0.52	1.9	0.55	-0.23 ± 0.64	3.0	0.70
	2	-0.18 ± 0.56	1.8	0.59	-0.24 ± 0.61	2.0	0.66
	3	-0.13 ± 0.50	1.9	0.51	-0.20 ± 0.71	2.9	0.74
	4	-0.15 ± 0.52	1.8	0.55	-0.23 ± 0.61	2.0	0.65
	SECT	0.09 ± 0.58	1.8	0.59	0.11 ± 0.64	2.0	0.65

Table 5.2: Signed mean errors ($\mu \pm \sigma$), maximum deviations on the proton range estimation (max) and root-mean square (RMS) errors over 360 directions at 5° steps for the ideal situation (without noise) and the realistic scenario (at 20 mGy).

5.1.4 Discussion

This simulations-based study comparing many pairs of dual-energy spectra demonstrates that the energy separation between the incident spectra had a strong influence on the SPR precision. It was observed that above an energy gap of 60 keV the precision asymptotically tends to a 4.7 % level. This result is in agreement with Primak *et al* (2009) [Primak et al., 2009], in which they established a relation between the dual-energy ratio of two materials and the image quality. They found that a small difference between the dual-energy spectra resulted in a significant increase of the noise. To improve image quality, they optimized the additional filtration to increase the energy gap.

Our study indicates that the energy gap is not a good metric to determine the optimal spectra when looking at the SPR accuracy averaged over all tissues. The reason is that a large variability of the optimal spectra was observed when studying each phantom material separately (Figure 5.5). Therefore, the optimization of the dual-energy spectra must be based on the materials present in the anatomical region traversed by the proton beams. This result confirms that the optimal spectra in dual-energy imaging is task [Richard and Siewerdsen, 2007], site and patient dependent.

The choice of the material basis (water and compact bone), the choice of the order of the polynomial, the presence of crossed terms in the polynomial and the choice of the dual-energy spectra are factors that determine the correctness of Equation 5.8, which is the main hypothesis of the employed decomposition method. In addition, to obtain acceptable results in terms of accuracy, the validity of Equation 5.8 has to be verified within the spectral energy range of the incident spectra (Figure 5.6).

With respect to the dose allocation study, it was found that the dose balance between energy levels was not critical for the SPR estimation. In fact, the overall accuracy was almost flat in the 30-70% D_{LE} range (Figure 5.7, right). This result agrees with a previous study [Vilches-Freixas et al., 2015] conducted for an image-based decomposition method and a different figure of merit: the accuracy on the extracted Z_{eff}. A plausible explanation is that even if the high energy spectrum is more penetrating than the low energy spectrum, this effect is compensated with the poorer efficiency of the detector response at high energy (Figure 1 of [Vilches-Freixas et al., 2016a]). On the other hand, the precision presents a minimum slightly shifted in favor of lower dose for the lower voltage spectrum (i.e. 30% LE-dose). Shkumat *et al* (2007) [Shkumat et al., 2007] came to the same conclusion; the optimal image quality, in terms of SNR, was achieved when one third of the total dose was imparted with the LE acquisition.

Two scenarios were evaluated to determine the accuracy of the proton range prediction: an ideal case with an infinite dose, i.e. X-ray simulations without noise, and a realistic situation with a 20 mGy central dose. The SPR images of the ICRP phantom were reconstructed using four representative dual-energy spectra (see Table 5.1). The differences between the four pairs of spectra in Table 5.2 were small ($|\mu| < 0.2$ mm) and not significant (two-tailed paired t-test, $p > 0.1$) due to the variability between beams (standard deviation $\sigma > 0.49$ mm). In practice, precision could therefore drive the choice of spectra, i.e., the energy gap (Figure 5.4, right). When comparing DECT range errors with SECT range errors, all dual-energy spectra provided a range improvement for the

head and for the thorax slices. Although this was not the case for the pelvis slice, this confirms the limitations of SECT, with variations from site-to-site and the results would have been different if another calibration curve had been used than the one in Figure 3, as observed by [Arbor et al., 2015]. All pairs of DECT spectra seemed robuster on average over all sites. Based on these results, the gain in SPR accuracy obtained when optimizing the dual-energy spectra based on the materials traversed by the proton path is not translated into improved proton range estimation, as comparable range differences were obtained with the four dual-energy spectra.

For radiotherapy applications, based on the As Low As Reasonably Achievable (ALARA) principle, a trade-off between dose and image noise should be found. On the one side, an imaging dose lower than 20 mGy might not be appropriate as it would trigger excessive image noise. On the other side, increasing the dose or implementing a regularized reconstruction algorithm instead of using filtered-back-projection could be valid alternatives to reduce image noise. Signed mean errors and RMS errors for the realistic scenario were found to be comparable to those of the noiseless situation (infinite dose), particularly for the head and the thorax slices, despite a rather small increase in the maximum error values (Table 5.2). For the pelvis slice a higher impact of noise on the range results was observed. Nevertheless, according to these results, the presence of noise in the SPR image seems to have a rather low impact on the range estimation as noise is averaged along the voxels of the beam path.

Uncertainties in the beam direction, such as changes in density and tissue inhomegeneites caused by movement, patient misalignment or anatomical changes, or uncertainties in determining the SPR of tissues, have a severe impact on the proton range and can cause severe damages to the patient, such as target miss or accidental exposure of organs-at-risk. Benefits of using dual-energy imaging for treatment planning to improve the estimation of the SPR of tissues, as an alternative to single-energy CT calibration, assuming a non-moving target have been evaluated in this work. However, it should be noted that a 3.5% range uncertainty is commonly associated to the single-energy calibration curve between CT numbers and SPR values using a real CT scanner system but range errors obtained in Table 5.2 are much lower than 3.5%. The reason is that in this simulation-based study, we only focused on the range uncertainty associated to the conversion of CT numbers into SPR values. We have considered an idealized irradiation setup, neglecting real CT scanner issues such as X-ray scatter, motion artifacts and time stability. Moreover, besides the uncertainties in the longitudinal direction, other sources of uncertainty exist in proton therapy such as density changes perpendicular to the beam direction, the effect of lateral beam penumbra or incorrect proton scatter modeling in analytical treatment planning systems [Paganetti, 2012], which might have a severe dosimetric impact in proton therapy dose calculations.

In this work, we propose a full projection-based decomposition method framework for the treatment planning of proton therapy. Despite the fact that no consensus has been reached within the community to prefer one method over the others, nor a decomposition domain (projection– or image– domain) for the SPR estimation, projection-based methods present the advantage to be intrinsically less affected by beam-hardening than

image-based approaches. One assumption of projection-based methods is that the same information per tube voltage is available at each projection angle. This prerequisite can be seen as a disadvantage when using dual-source scanners as independent rotations around the patient are performed, however, with the advent of technological developments, this requirement can be fulfilled by using dual-layer detectors or photon counting detectors systems, for which it is possible to acquire low and high energy projections at the same angle. Fast-kV switching imaging systems equipped with a synchronized filter wheel, such as the Imaging Ring, approach this requirement on the condition that interpolation of consecutive projections is performed. Besides, the proposed method to estimate the SPR images from dual-energy data in the projection-domain is an adaptation of the two-steps procedure proposed by Farace *et al* in the image-domain, which produced comparable results with respect to Hünemohr's approach [Hünemohr et al., 2014a].

One limitation of this study is that the investigated acquisition parameters (i.e. spectral separation and dose allocation) are only meaningful for dual-spectrum scanners but not for dual-detector systems. In addition, we have used a projection-based decomposition algorithm to evaluate the acquisition parameters and it would be interesting to repeat the same study using an image-based decomposition algorithm. However, image-based methods require the implementation of a beam-hardening correction for each X-ray spectra.

Another limitation of this study is the fact that the LE spectrum is not filtered. This definitely bias the results in terms of optimal spectra. This would have required to use an additional parameter (width of the LE filter).

For each dual-energy spectra evaluated, a virtual image-simulation calibration curve, interposing slabs of two materials of known thickness and composition, was performed to solve the system of equations 5.3 and 5.4. In this case, the dual-energy spectra were an input of this virtual simulation and we assumed that the spectra were perfectly known. A realistic detector response model has been used and a Poisson noise proportional to a certain dose value has been applied to the projections, but we have neglected scattered photons. We might expect a significant effect of scatter on the material decomposition, and scatter-compensation techniques prior to the decomposition should be implemented for large X-ray beams [Sossin et al., 2014], such as cone-beam irradiations.

5.1.5 Conclusion

This study evaluated the impact of the dual-energy spectra and the dose allocation between energy levels on the proton stopping power ratio accuracy and precision based on a projection-based dual-energy decomposition approach, which can guide the choice of spectra for dual-energy CT for protontherapy. The effect of the SPR accuracy and precision on the proton range estimation was also investigated. An ideal situation without noise and a realistic acquisition with a total central dose of 20 mGy were considered. The precision was improved increasing the energy separation between the incident spectra, whereas the accuracy showed little dependence to the energy gap. The dose balance between energy levels was not found to be sensitive for the SPR estimation. In terms of

SPR accuracy, the optimal pair of dual-energy spectra was material dependent but, on a heterogeneous anthropomorphic phantom, there was no significant difference in range accuracy and, therefore, the choice of spectra could be driven by the precision, i.e., the energy gap.

5.2 Material decomposition basis

5.2.1 Introduction

One of the assumptions of projection-based decomposition methods (see section 2.4.2) is that the linear attenuation coefficient of the scanned object at any energy can be expressed as a linear combination of two energy-dependent basis functions with two energy-independent coefficients. These energy-dependent bases can either be the two main interaction processes of photons with matter at the energy range of diagnostic CT (photoelectric effect and Compton scattering) or the energy-dependent mass attenuation coefficients of two basis materials (see section 2.4.2.1). For the latter, another assumption is that human tissues can be expressed as a combination of two materials. Typically, soft tissue and cortical bone, water and compact bone or acrylic (PMMA) and aluminum are chosen as pairs of basis materials [Heismann et al., 2012; Chuang and Huang, 1988]. This simulation-based study aimed at comparing the SPR accuracy when decomposing the dual-energy sinograms into these three sets of basis.

5.2.2 Materials and Methods

The same dual-energy spectra and irradiation setup employed in section 4.5 were used to perform the basis material comparison. Four slices of the ICRP phantom were used to simulate a human body irradiation and thirteen ROIs placed in homogeneous material areas (see Figure 4.11) were considered. The LE and HE sinograms of the ICRP phantom were decomposed into the tabulated materials of the NIST database [Linstrom and Mallard, (retrieved December 6, 2016)]: acrylic (PMMA) and aluminum, soft tissue and cortical bone, and water and compact bone. The corresponding mass density images and the corresponding SPR images were derived following the procedure described in section 4.5.2.2. Relative SPR differences over the thirteen ROIs were computed by comparing the SPR image reconstructed with each material basis to the reference SPR values listed in Table 4.6, computed from the chemical composition of human tissues provided in the ICRP publication [ICRP, 2009] and Bethe's equation.

5.2.3 Results and Discussion

Figure 5.8 plots the relative SPR errors for each ROI and decomposition basis. The RMS SPR error over the thirteen ROIs was 0.55% for the PMMA and Al basis, 0.54% for the soft tissue and cortical bone basis, and 0.71% for the water and compact bone basis. The water and compact bone decomposition basis produced worst results for the pelvis slice (ROIs 4a-4d) than for the other anatomical regions. The soft tissue and

cortical bone basis and the PMMA and Al basis behaved in a similar manner over all anatomical regions.

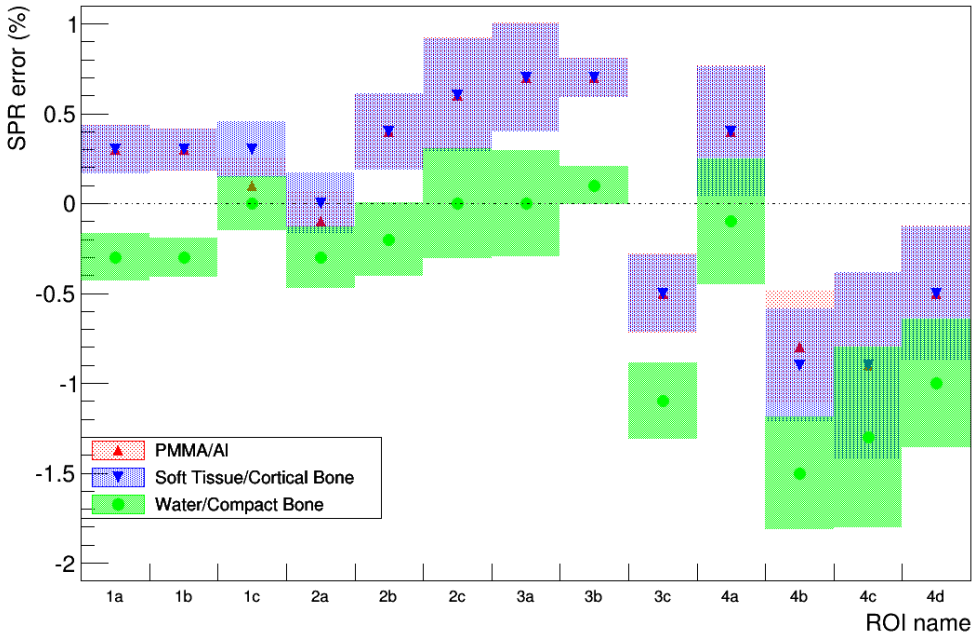

Figure 5.8: Relative SPR errors for each of the thirteen ROIs (see Figure 4.11 for the placement of the ROIs on the four ICRP slices) obtained with each decomposition basis: PMMA and aluminum, soft tissue and cortical bone, and water and compact bone.

5.2.4 Conclusion

Three material decomposition bases, typically used to represent human tissues, were compared in terms of proton SPR accuracy: PMMA and aluminum, soft tissue and cortical bone, and water and compact bone. Comparable results were obtained with the three basis which suggests that the assumption that the linear attenuation coefficient of the scanned object can be expressed as a linear combination of two basis materials is valid in the diagnostic CT energy range for human tissues if a proper pair of basis materials is chosen.

5.3 System inversion

5.3.1 Introduction

When performing a dual-energy acquisition, two-energy projection datasets of the same object are acquired (see equations 2.10-2.11). To decompose into the two sino-

grams of the decomposition basis (see section 2.4.2.1), one needs to solve the system of equations for the line integrals A_i $(i = 1, 2)$. Section 2.4.2.2 illustrated in detail the two main approaches to solve this system of equations. On the one hand, when scanner specific information is known *a priori*, such as the source energy spectra and the detector response, the non-linear equations can be directly solved using the *simplex method* of Nelder and Mead [Nelder and Mead, 1965], following [Schlomka et al., 2008], i.e., accounting for the statistics of the measurements by estimating the most likelihood. On the other hand, the unknowns A_i can be expressed as a polynomial expansion of the logarithmic transmission values at LE (m_{LE}) and HE (m_{HE}) and the coefficients of these polynomials can be determined by performing a calibration using two materials with known properties and increasing thicknesses [Lehmann et al., 1981; Chuang and Huang, 1988].

The aim of this study was to compare the dual-energy decomposition output when solving the system of equations using the polynomial approximation or when using iterative convex optimization. The other variables, such as the dual-energy spectra, the material basis and the dose balance between energy levels, were kept constant. For the polynomial approach, the sub-optimal terms of the polynomial were discarded based on a mathematical criterion. Two variants were considered for the iterative convex optimization: first, the system unknowns A_i were initialized to zero; second, the output of the polynomial approach was used as *a priori* information to initialize A_i.

5.3.2 Materials and Methods

The tissue characterization 467 Gammex phantom (Gammex, Middleton, WI) was used in this study (see Figure 5.1). Water and compact bone were selected as pair of basis materials for the decomposition process. The optimization of the polynomial was carried out for one dual-energy photon spectra: LE: 80 kV and HE: 140 kV + 2.5 mm Sn. The same dual-energy spectra was used to compare the reconstructed RED images with both approaches and a Poisson noise level corresponding to 20 mGy at the center of the Gammex phantom with an equal dose split between the LE and the HE spectra was considered.

5.3.2.1 Polynomial optimization

Based on a mathematical criterion, a stability study to noise, similar to that conducted by Létang *et al* [Létang et al., 2004], was performed to determine which terms of the polynomial were more unstable and, therefore, eliminated.

In the calibration stage, to study the stability of polynomial terms to noise, a Poisson sampling was done to the incident photon spectra, $N_{0,\mathrm{LE}}$ and $N_{0,\mathrm{HE}}$, to simulate acquisitions with noise:

$$N_{0,\mathrm{LE}}(E) = \mathrm{Poisson}\ (\mathrm{N_{pix,LE}}\ \mathrm{S_{LE}(E)}) \tag{5.17}$$

$$N_{0,\mathrm{HE}}(E) = \mathrm{Poisson}\ (\mathrm{N_{pix,HE}}\ \mathrm{S_{HE}(E)}) \tag{5.18}$$

where $N_{\text{pix,LE}}$ and $N_{\text{pix,HE}}$ are the expected number of photons in each pixel of the detector of the LE and HE spectra (see equation B.2), respectively, and S_{LE} and S_{LE} the incident LE and HE spectra. Then, the logarithm of the transmission values at LE and HE were computed as follows:

$$m_{\text{LE}} = -\ln \int_E \frac{N_{0,\text{LE}}(E)\ D(E) \exp\left(-A_1\ f_1(E) - A_2\ f_2(E)\right)}{N_{0,\text{LE}}\ D(E)}\ \mathrm{d}E \tag{5.19}$$

$$m_{\text{HE}} = -\ln \int_E \frac{N_{0,\text{HE}}(E)\ D(E) \exp\left(-A_1\ f_1(E) - A_2\ f_2(E)\right)}{N_{0,\text{HE}}\ D(E)}\ \mathrm{d}E \tag{5.20}$$

where D(E) is the energy-dependent detector response of the flat panel detector, and A_1 and A_2 are the areal density values of water and compact bone basis materials, respectively.

A_1 and A_2 were expressed as a polynomial expansion of m_{LE} and m_{HE} with polynomial coefficients $\{b_i\}$ and $\{c_i\}$, as in equations 2.14 and 2.15. To simplify the notation, $x \equiv m_{\text{LE}}$ and $y \equiv m_{\text{HE}}$. Létang *et al* [Létang et al., 2004] concluded that a third order polynomial was more convenient rather than a second order polynomial. We decided to start the optimization procedure with a fourth degree polynomial with fifteen terms:

$$\{1, x, y, x \cdot y, x^2, y^2, x^3, y^3, y \cdot x^2, x \cdot y^2, y \cdot x^3, x \cdot y^3, x^2 \cdot y^2, x^4, y^4\} \tag{5.21}$$

The calibration procedure was repeated for 30 noise realizations and the coefficients $\{b_i\}$ and $\{c_i\}$ were determined at each run. Then, the coefficient of variation (CV) of each coefficient, defined as the ratio of the standard deviation to the mean, was computed and the coefficient presenting the highest variation was excluded. The procedure was repeated excluding one coefficient at a time, until all coefficients showed a CV below 1 %.

5.3.2.2 RED comparison

In both situations, i.e. calibration approach and iterative convex optimization, image reconstructions of water and compact bone mass densities ρ were obtained using filtered backprojection on a 380×380×1 grid with 1×1×1 mm^3 voxels size, i.e., in the central slice only. On a pixel-by-pixel basis, the RED image was derived from equation 5.15. The estimated RED images of the Gammex phantom obtained by the numerical solution method and by the calibration approach were compared to the ground-truth values. The relative accuracy and precision were calculated in a ROI of 3/4 the size of the insert. The absolute accuracy and the precision of the RED averaged over all inserts and excluding the lung tissue inserts were also computed (see equations 5.6 and 5.7).

5.3.3 Results and Discussion

5.3.3.1 Polynomial optimization

The optimal polynomial was found to be a fourth degree polynomial with twelve terms:

$$\{1, x, y, x \cdot y, x^2, y^2, x^3, y \cdot x^2, y \cdot x^3, x \cdot y^3, x^2 \cdot y^2, x^4\} \tag{5.22}$$

To test the goodness of the polynomial approach and the eventual dependence on the energy spectra, the optimized polynomial (equation 5.22) was used to reconstruct the mass density images of the basis materials and to reconstruct the linear attenuation coefficient image (μ-image) at 100 keV, according to equation 4.10, using two different DE spectra: 80 kV/140 kV+2.5 mm Sn (71 keV incident energy gap) and 78 kV/94 kV+0.1 mm Sn (12 keV incident energy gap). The two reconstructed μ-images were compared with the reference μ-values at 100 keV. Line profile comparisons and percentage difference images are shown in Figures 5.9 and 5.10, respectively. Higher percentage errors were observed at the border of the reconstructed μ-image using the DE spectra 78 kV/94 kV+0.1 mm Sn and the optimized polynomial for the 80 kV/140 kV+2.5 mm Sn spectra (equation 5.22). To understand why the highest error was obtained at the image border, i.e. for small traversed phantom thicknesses, the nominal areal density values used in the calibration stage were plotted against the reconstructed areal density values using the polynomial of equation 5.22 (Figure 5.11). For low areal density values, the agreement between nominal and reconstructed data points was found to be sub-optimal for the 78 kV/94 kV+0.1 mm Sn spectra. This result suggests that a spectra-specific polynomial optimization is preferable. Indeed, the polynomial optimization was repeated for the 78 kV/94 kV+0.1 mm Sn spectra and the optimal polynomial resulted to be the initial fourth degree polynomial with fifteen terms (equation 5.21).

5.3.3.2 RED comparison

RED images of the Gammex phantom were obtained following the calibration approach and by numerical solution. For the latter, two variants were considered: first, areal density values A_1 and A_2 were initialized to zero; second, the results of the calibration approach were used as *a priori*. For the iterative convex optimization, the maximum number of iterations was set to 10^4.

Table 5.3 shows the results of the RED estimation in terms of the percentage accuracy averaged over all inserts and the precision expressed as the RMS error. The computation time required for both approaches using one single processor is also indicated. Comparable results were obtained for the calibration approach and for the two variants of the iterative convex optimization.

5.3.4 Conclusions

A mathematical criterion to exclude the unnecessary terms of the polynomial was established. A fourth degree polynomial with twelve terms resulted to be a good candidate for the dual-energy spectra investigated. Nevertheless, this optimized polynomial was found to be invalid when using a very different dual-energy spectra, which suggests that a spectra-specific polynomial optimization should be carried out instead.

No significant differences were observed in terms of accuracy and precision when comparing the relative electron density images reconstructed by solving the system of equations numerically or when using the polynomial approach. Both approaches con-

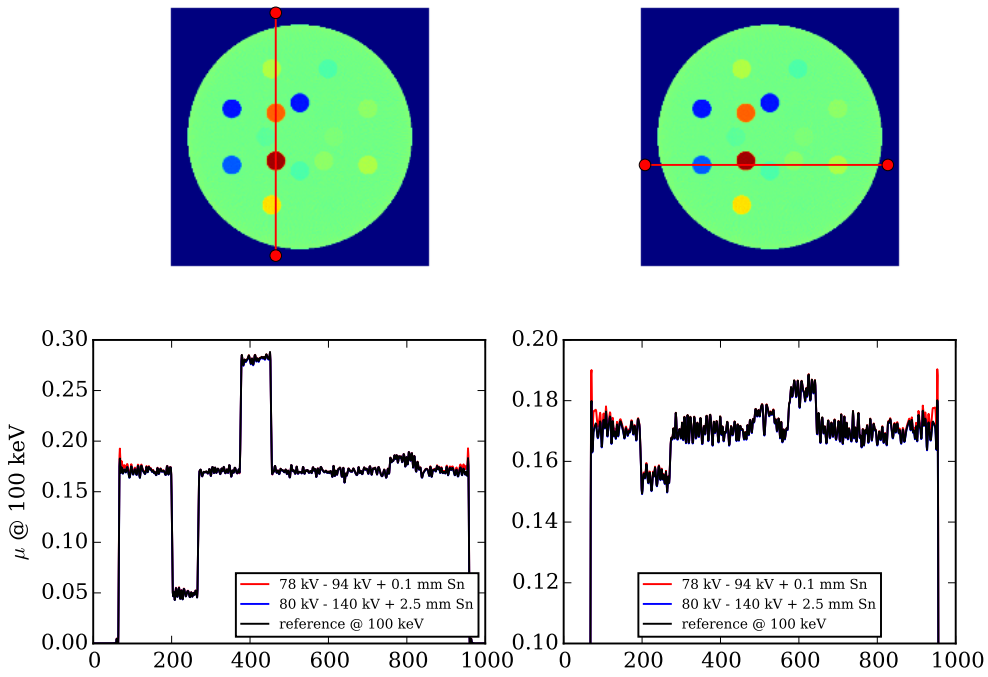

Figure 5.9: Top: reference linear attenuation maps at 100 keV showing the position of horizontal and vertical line profiles (red). Bottom: horizontal (left) and vertical (right) line profiles comparing two reconstructed images at different dual-energy spectra with the reference μ-image at 100 keV.

verged to comparable RED images. On the one hand, the numerical approach was found to be more demanding in terms of computation time. On the other hand, the calibration approach would require a polynomial optimization for the given dual-energy spectra prior to decomposition.

5.4 Conclusion

Several factors that could impact the outcome of the dual-energy decomposition process were investigated, namely: the dual-energy spectra, the dose balance between energy levels, the material decomposition bases and the way of solving the non-linear system of equations inherent to the dual-energy decomposition. For all of these studies, dual-energy decomposition was performed in the projection domain. Different figures of merit were employed in these comparisons: from the goodness of the reconstructed linear attenuation coefficient to the proton range accuracy in the patient.

Increasing the incident energy gap between the dual-energy spectra reduced the noise in the reconstructed images. The optimal pair of dual-energy spectra in terms of SPR

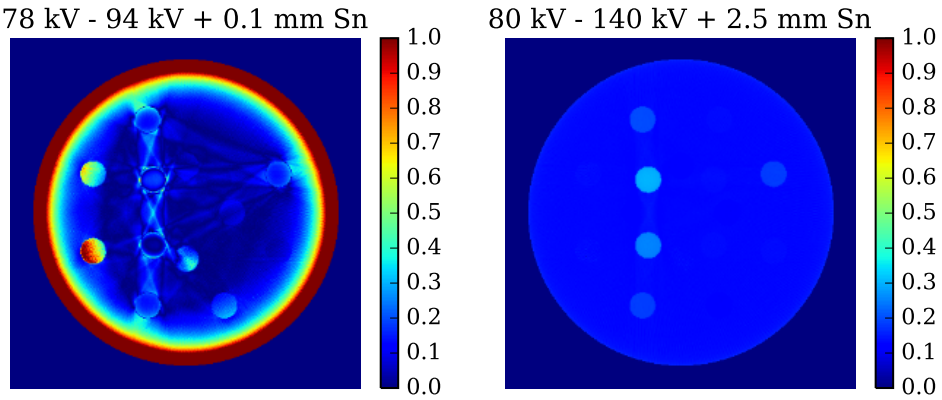

Figure 5.10: Percentage different images when comparing the reconstructed μ-images at two different dual-energy spectra obtained through the optimized polynomial (equation 5.22) with the reference values at 100 keV. Colorbar indicates the percentage relative error.

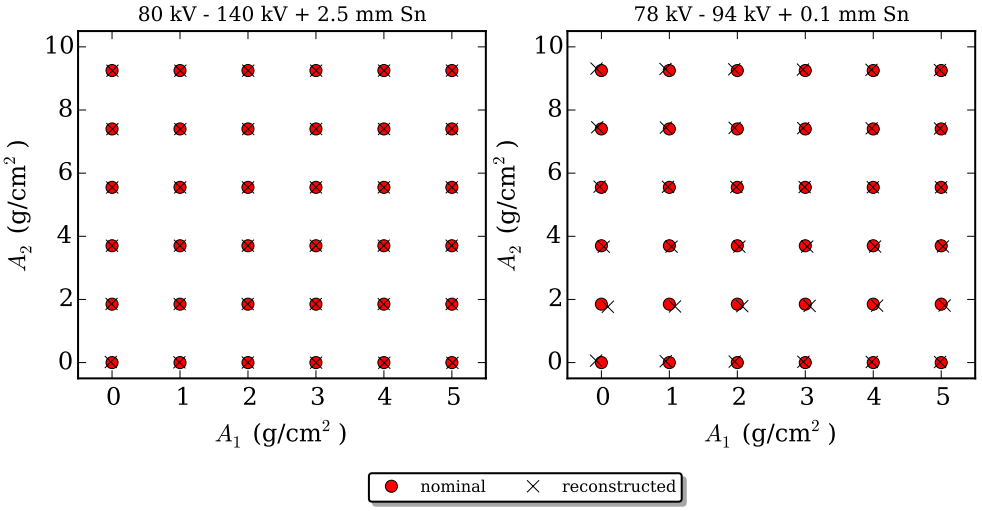

Figure 5.11: Nominal areal density values A_i $(i = 1, 2)$ in g/cm^2 (red dots) and reconstructed areal density values (black crosses) through the optimized polynomial (equation 5.22) using two different dual-energy spectra.

accuracy was found to be material dependent, however, when computing the range on an anthropomorphic phantom, there was no significant difference in range accuracy. Therefore, for proton treatment planning, the choice of the spectra should be guided by the precision, i.e. the energy gap. In addition, the presence of noise in the SPR images seems to have a rather low impact on the range estimation as noise is averaged along the voxels of the beam path. Regarding the dose balance between the low-energy and

Method	$\overline{x} \pm RMS$	$\overline{x} \pm RMS$ (no lungs)	CPU time
Polynomial	0.7 ± 5.2	0.7 ± 3.3	14 sec
Numerical initialized to 0	0.7 ± 5.2	0.7 ± 3.4	2 h 30 min
Numerical with *a priori*	0.7 ± 5.2	0.7 ± 3.3	1 h 20 min

Table 5.3: RED results in terms of accuracy and precision for the different approaches considered: polynomial solution and iterative convex optimization with and without *a priori* (i.e. initialized with the polynomial output). The last column indicates the computational time using one single processor.

the high-energy acquisition, the optimal image quality is achieved when one third of the dose is imparted with the low-energy acquisition. A comparison of three pairs of decomposition basis (i.e. PMMA and aluminum, soft tissue and cortical bone, water and compact bone) was carried out to decompose human tissue materials and no significant differences were observed. Depending on whether scanner information, such as the source spectrum and the detector response, is available, the non-linear system of equations can either be solved with an iterative optimization or based on a calibration to indirectly estimate the scanner characteristics. Comparable results were obtained in terms of accuracy. The numerical approach was found to be computationally demanding, but the calibration approach required a spectra-specific polynomial optimization to ensure a correct decomposition.

In view of these results, as the Imaging Ring (IR) system has been previously characterized (see chapter 3), the direct inversion of the non-linear system of equations using the approach proposed by Schlomka *et al* [Schlomka et al., 2008] seems a good approach to estimate the SPR of real phantoms from DE-CBCT acquisitions using the IR system.

Chapter 6

Deriving the ionization potential

Contents

The mean excitation energy, sometimes referred to as the average ionization potential or I-value, is a controversial issue as there is no consensus on how to establish reference values for different media. In this chapter, the goal was two-fold. On the one hand, to review some of the works that have investigated the influence of the mean excitation energy of human tissues on the proton range. On the other hand, to evaluate the feasibility of an experimental setup designed to extract volumetric distributions of the I-value of patients combining two tomographic imaging modalities: proton CT and dual-energy CT. Possible fields of application of these 3D-maps have also been identified.

6.1 Impact of the I-value on the proton range

In proton therapy, the range of protons in patients is determined from the stopping power ratio (SPR) of tissues relative to water along the beam path. One of the parameters required to compute the SPR is the mean excitation energy of the medium and that

of water (Equation 1.12), which is a measure of the ability of a target system to absorb kinetic energy from a projectile [Sabin et al., 2013]. Consequently, the uncertainty associated to the I-value of different media influences the SPR calculation and, thus, the proton range. A 10% variation of the mean excitation energy modifies the SPR by about 1.1-1.3% [Schneider et al., 1996]. Yang *et al* [Yang et al., 2012] came to a similar result: a 10% variation in the elemental I-values introduces a 1% variation of the stopping power of water and human tissues and less than 1.4% when computing the SPRs. Although the I-value of a material is a well-defined quantity and only depends on the properties of the medium [ICRU, 1993], there are large uncertainties associated to its determination. It may be obtained either theoretically or experimentally (section 1.1.3.5).

Due to the limited knowledge of I-values, the *sub-millimeter* precision claimed to be achievable in proton and ion therapy has been questioned by Andreo [Andreo, 2009] who concluded that talking about a *sub-centimeter* precision was more appropriate. The reasons are manifold. To start with, even if water is a reference material commonly used in treatment planning, a generally accepted mean excitation energy for liquid water has not been established yet [Besemer et al., 2013]. Values obtained by theoretical or experimental means are found to vary as much as 20%. Moreover, values deduced from experiments are generally higher [Sabin et al., 2013]. An overview of some of the values found in the literature for liquid water, either measured or calculated, are shown in Table 6.1.

I (eV)	Reference
75	[Ritchie et al., 1978], Dielectric response function
79.7 ± 2	[Bichsel and Hiraoka, 1992], Ionization curves, 70 MeV protons
81.8	[Dingfelder et al., 1999], Dielectric response function
80	[Bichsel et al., 2000], C-ions, 290 MeV/u
77	[Krämer et al., 2000], Depth dose curves, C-ions
75 ± 3	Recommended value in ICRU Reports 37 [ICRU, 1984] and 49 [ICRU, 1993]
67.2	Recommended value in ICRU Report 73 [ICRU, 2005]
78 ± 2	Recommended value in Errata ICRU Report 73 [Sigmund et al., 2009]

Table 6.1: I-values for liquid water found in the literature.

The I-value of 75 ± 3 eV for water, suggested by the publications ICRU Reports 37 [ICRU, 1984] and 49 [ICRU, 1993], has long been accepted. The latest suggested value by the ICRU, which replaces the value of 67.2 eV in ICRU Report 73 [ICRU, 2005], is 78 ± 2 eV [Sigmund et al., 2009]. When varying the I-value for water between 75 eV and 80 eV, it results in a SPR variation between 0.8% and 1.2% in the therapeutic energy range [Paganetti, 2012]. Soltani-Nabipour *et al* [Soltani-Nabipour et al., 2009] obtained a variation of about 1.5 mm in range when varying the I-value for water from 72 eV to 78 eV, i.e. considering the accepted value of 75 eV ± 3 eV of experimental uncertainty [ICRU, 1984, 1993]. Andreo [Andreo, 2009] studied the differences in the energy-deposition distributions in water irradiated by protons and carbon ions of different energies. He observed a substantial spread of the Bragg Peak (BP) position of proton

and carbon ion beams up to 6 mm when using the triplet of recommended I-values for water in ICRU Reports 37 [ICRU, 1984, 1993; Sigmund et al., 2009] (Table 6.1). In addition, the spread in the BP position was found to be energy dependent, increasing with energy, and similar for protons and carbons having analogous ranges in water.

Elemental I-values are generally derived from experimental data [ICRU, 1993], but, for compounds and mixtures, there is limited experimental data. When the value of a medium is not known neither experimentally nor based on the theory, it is computed by Bragg's additivity rule (see Equation 1.10) based on its tabulated chemical composition and mass density. Reference human tissue compositions [Woodard and White, 1986; White et al., 1987; ICRU, 1992; ICRP, 2009] are average values obtained under different conditions and, thus, are expected to be approximated [Andreo, 2009]. As a consequence, the available I-values for human tissues are average estimates. Moreover, because this rule is an approximation and it ignores the effects of chemical bonds, the I-value estimates of human tissues have large uncertainties, up to 10-15% [ICRU, 1984; Andreo, 2009]. The uncertainty in the I-value for tissues might result in a range uncertainty of 1.5% [Paganetti, 2012].

There is a large variability on the I-values for similar organs or human tissues reported in ICRU Publications [ICRU, 1984, 1989, 1992]. [Andreo, 2009] observed a spread of the BP position with range differences up to 0.3 g/cm^2 when considering four different types of soft tissue (considered almost identical in clinical practice [Besemer et al., 2013]), with I-values ranging from 70.8 eV to 74.9 eV. When varying the I-value of skeletal muscle and female soft tissue by $\pm$10% with respect to its tabulated value, he observed a range variation up to 0.7 g/cm^2.

Finally, as stated in ICRU Report 44 [ICRU, 1989], instead of assuming common body-tissue compositions for all individuals, the variations in the composition of similar organs or human tissues should not be neglected [Andreo, 2009; España and Paganetti, 2010]. For this reason, instead of using a conversion between patient CT numbers and SPRs, some authors suggest that it would be more appropriate to determine the tissue composition along the proton beam path for each patient individually [Andreo, 2009; Besemer et al., 2013].

Unlike analytical pencil-beam dose calculation algorithms, where dose to water or water-equivalent dose is typically reported [Paganetti, 2012], MC dose calculations report dose to medium and a conversion from patient CT numbers to material composition and mass densities is required [Schneider et al., 2000; Paganetti, 2009]. At present, the most widely used approach to assign material type and mass density at each voxel of the CT scan is the one proposed by [Schneider et al., 2000]. [Landry et al., 2013a] improved tissue quantification by identifying the carbon, oxygen, calcium and phosphor contents using DECT information, i.e. (Z_{eff}, RED). MC algorithms compute the I-value of each CT voxel through the Bragg additivity rule based on its chemical composition and, therefore, neglects chemical bonds introducing the above-mentioned uncertainty up to 10-15% for human tissues [Andreo, 2009]. Alternatively, for a proton treatment plan based on MC, the SPR maps reconstructed from X-ray or proton CT images can be converted voxel-by-voxel into water equivalent materials. Then, the mass density in each voxel is adjusted

to reach the reconstructed SPR value of the voxel [Arbor et al., 2015]. However, it has been mentioned that reporting dose to medium provides more accurate dosimetric results than reporting dose to water or water-equivalent dose [Paganetti, 2009]. One drawback of this approach is that by setting all CT voxels to water, and by just adjusting the mass density to match the SPR value, we lose information on the chemical composition, i.e. on the atomic number and on the I-value, therefore, on the lateral scattering, which might result in wrong lateral dose calculation. According to the study conducted by [Arbor et al., 2015] in the liver region of the ICRP phantom, range uncertainties introduced by this wrong material compositions were below 0.05 mm, which corresponded to the statistical range uncertainty accepted in their study. However, that might not be the case for tissue materials that significantly differ from water. To answer this question, a simulation-based experiment to quantify the error in the longitudinal and transverse direction of the beam path associated to this approximation was performed, the results of which are presented in Appendix D.

[Besemer et al., 2013] were the first to quantify the clinical impact of I-value uncertainties on proton dose distributions within patient geometries. They observed that uncertainties in the I-value (i.e. tissue I-values were varied by $\pm 10\%$ of the nominal values) introduced a range uncertainty up to 1.9% of the beam range and variations in the mean dose to the target volume and to the OARs up to 3.5%, these differences being more significant for deep seated tumors. Consequently, to reduce clinical margins and to improve the outcome of proton therapy treatments, it is fundamental to reduce the uncertainty in the I-value of human tissues.

6.2 Estimation of the I-value from DECT and pCT

Previous studies, listed in section 6.1, provided valuable insights on the impact of the I-value uncertainties on the proton range estimation. Motivated by these statements, this work investigated the feasibility of extracting the volumetric distribution of the ionization potential of an object by combining two tomographic imaging modalities: proton CT and dual-energy CT. The former provided the patient distribution of the stopping power relative to water and the latter the distribution of the relative electron density. As a result, 3D I-value maps of the imaged object were obtained.

6.2.1 Materials and Methods

6.2.1.1 Phantoms

The 33-cm diameter Gammex RMI 467 (Gammex, Middleton, WI) tissue characterization phantom (Figure 5.1) was used in this simulation-based study. This phantom has been described in detail in section 5.1.2.1.

6.2.1.2 RED determination

Virtual CT acquisitions of the Gammex phantom were obtained by means of deterministic simulations in GATE [Jan et al., 2004] v7.2 using the Fixed-Forced Detection (FFD) actor. The irradiation geometry and the detector response model of the Imaging Ring (IR) system were considered. The dual-energy spectra were 60 kV and 124 kV/Sn. Poisson noise was applied to the projections to deliver a central dose of 20 mGy with the dual-energy acquisition while keeping a dose balance between the low and the high energy acquisitions (equation 5.2).

The basis material decomposition method proposed by Alvarez and Macovski [Alvarez and Macovski, 1976] was implemented in the projection domain to extract the RED map from the Compton cross section of tissues (section 2.4.2.1). The RED image was reconstructed using filtered backprojection with 380×380×1 voxels of 1×1×1 mm^3.

6.2.1.3 SPR determinaton

The conceptual design of the proton CT scanner used in this study is illustrated in Figure 6.1. The simulated proton CT scanner corresponded to an ideal detector composed of two planes: one at the entrance and one at the exit of the phantom. An incident proton beam of 300 MeV was used. Like in the dual-energy acquisition, a 20 mGy central dose was considered. Due to MCS, protons are deflected many times along their path and, as a consequence, protons do not travel following a straight line but a curved path. An estimate of the position, energy and direction of each proton in a list mode manner before and after the phantom enables the computation of a maximum likelihood estimate of the proton trajectory known as the Most Likely Path (MLP) [Schulte et al., 2008]. By measuring the energy loss after the phantom, the stopping power relative to water (SPR) of the object was reconstructed based on a filtered backprojection algorithm developed by [Rit et al., 2013] to include the MLP formalism. SPR reconstructed images had dimensions of 380×380×1 mm^3. As a fraction of the incident protons undergoes nuclear interactions while traversing the medium, the exit detector tracks both primary and secondary protons. These events bias the SPR reconstruction as the small angle MCS Gaussian approximation is no longer valid (section 1.1.2). Consequently, to filter out these events, a 3σ cut on the exit energy and on the exit angular distribution was applied prior to image reconstruction. For further details on the proton CT scanner implementation and on the SPR reconstruction, the reader is referred to [Quiñones, 2016].

6.2.1.4 I-value determination

The ionization potential image was estimated through Bethe's equation without correction terms (Equation 1.12). The RED image of the phantom under study was determined from dual-energy CT acquisitions, whereas the corresponding SPR map was directly obtained through proton CT simulations. Assuming an I-value for water equal to 78 eV (Table 6.1), the mean excitation energy value of the object can be estimated

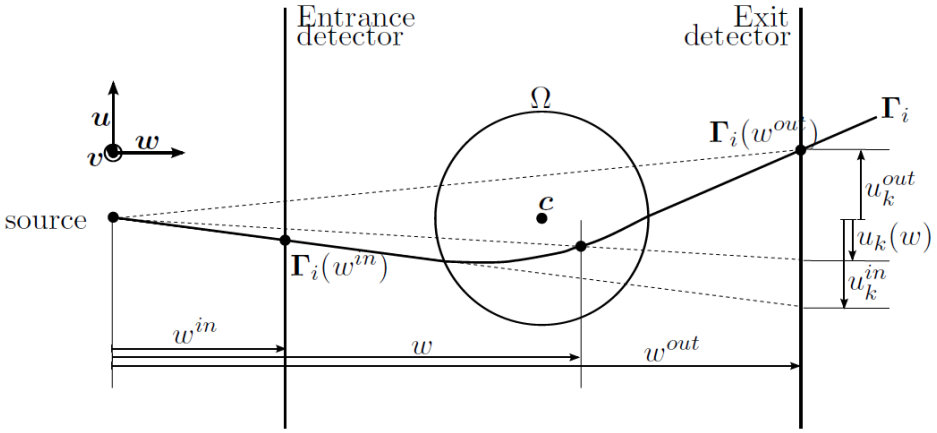

Figure 6.1: Schematic top view of the proton CT scanner used in this study. u and v define the orientation of the detectors, whereas ω defines the source-to-isocenter direction. $\Gamma_i(\omega^{in})$, $\Gamma_i(\omega^{out})$ and Γ_i represent the entrance position, the exit position and the most likely path, respectively. Figure extracted from [Quiñones, 2016].

in a pixel-by-pixel basis solving equation 1.12 for I as follows:

$$I_m(\boldsymbol{x}) = \frac{2m_e c^2\beta^2}{(1-\beta^2)} \exp\left(-\frac{\mathrm{SPR}(\boldsymbol{x})}{\mathrm{RED}(\boldsymbol{x})}\left[\ln\frac{2m_e c^2\beta^2}{I_{\mathrm{w}}(1-\beta^2)} - \beta^2\right] - \beta^2\right) \tag{6.1}$$

Reference SPR values of the Gammex phantom inserts, with known chemical composition and mass density, were determined through the weighted sum of mass stopping powers for the atomic constituents (Equation 1.11). Theoretical RED values were determined from the chemical composition and equation 1.13. Reference I-values for the phantom inserts were calculated using Bragg additivity rule and the elemental I-values given in Tables 2.8 and 2.11 of the ICRU49 report [ICRU, 1993]. The I-value in a region of interest (ROI) inside each phantom insert was taken and it was compared to the theoretical value. Instead of taking the mean value inside each ROI, we took the median value for robustness to outliers.

6.2.2 Results

The top row of Figure 6.2 displays the reconstructed SPR image obtained through proton CT, the RED map obtained through dual-energy CT and the reconstructed ionization potential map determined combining both imaging modalities. The row below shows the corresponding percentage difference maps when comparing the reconstructed values with the reference values. RED and I-maps were much noisier compared to the SPR map.

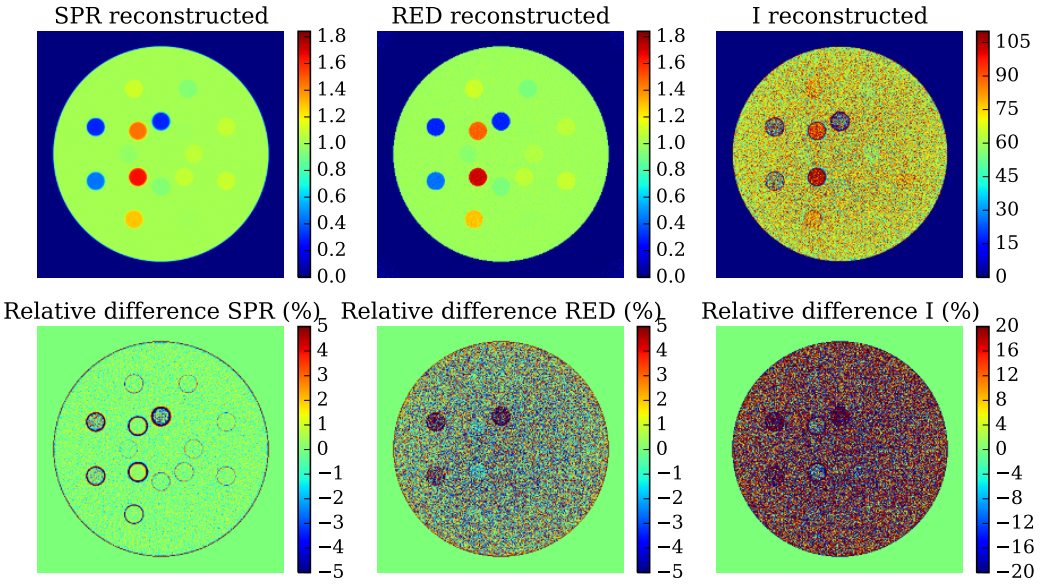

Figure 6.2: From left to right, top row: reconstructed SPR image obtained through proton CT, reconstructed RED image obtained through dual-energy CT and reconstructed I-value image determined by solving the Bethe's equation for I; below, percentage difference maps when comparing reconstructed SPR, RED and I-value images with reference values, respectively.

To quantify the accuracy and the precision of the proposed method, we took the median value in a ROI inside each phantom insert. Figure 6.3 plots the relative error with the corresponding error bars for all inserts sorted by increasing mass density. The error in extracting the I-value was within $\pm$ 3% for all inserts except for 3: the lung inhale (LN-300) and the lung exhale (LN-450) with errors around 8% and 4%, respectively, and the high density insert cortical bone (SB3) with an error around 4%. The signed mean of the errors and the root-mean-square error averaging over all inserts were -0.09% $\pm$ 5% for the RED, 0.07% $\pm$ 1.1% for the SPR and 1.5% $\pm$ 54% (0.9% $\pm$ 29% excluding lung inserts) for the I-values. Lung inserts presented the largest error bars, so the worst precision. We observed that the accuracy of the I-values was extremely dependent on the RED accuracy. To understand that, we performed an error propagation analysis of the I-value as a function of the uncertainties associated to SPR and RED.

Error propagation analysis To simplify the notation, $m_e c^2$ and $\ln\left[2m_e c^2\beta^2/I_{\mathrm{w}}(1-\beta^2)-\beta^2\right]$ are herein named A and B, respectively. Equation 6.1 can be rewritten as:

$$I_m(\boldsymbol{x}) = \frac{2A\beta^2}{(1-\beta^2)}\exp\left(-\frac{\mathrm{SPR}(\boldsymbol{x})}{\mathrm{RED}(\boldsymbol{x})}B-\beta^2\right) \tag{6.2}$$

Assuming that RED and SPR are independent variables, since they are measured by two different means, the variance formula to calculate the error propagation of I_m (s_I) as a function of the uncertainties associated to SPR (s^2_{SPR}) and RED (s^2_{RED}) is given by:

$$s_I^2 = \left(\frac{\partial I_m}{\partial \text{SPR}}\right)^2 s^2_{\text{SPR}} + \left(\frac{\partial I_m}{\partial \text{RED}}\right)^2 s^2_{\text{RED}} \tag{6.3}$$

and

$$\frac{\partial I_m}{\partial \text{SPR}} = I_m \left(\frac{-1}{\text{RED}} B\right) \tag{6.4}$$

$$\frac{\partial I_m}{\partial \text{RED}} = I_m \left(\frac{1}{\text{RED}^2} B\right) \tag{6.5}$$

thus, after reverting the notation, we obtain the following expression for the I-value variance:

$$s_I^2 = \left(\frac{I_m^2}{\text{RED}^2}\right) \left(\ln \frac{2m_e c^2 \beta^2}{I_{\text{w}}(1-\beta^2)} - \beta^2\right)^2 \left[s^2_{\text{SPR}} + \left(\frac{1}{\text{RED}^2}\right) s^2_{\text{RED}}\right] \tag{6.6}$$

From Equations 6.4-6.5 we see that the contribution of the RED error is inversely weighted by an additional RED term with respect to the SPR error.

6.2.3 Discussion

The RED map of the Gammex phantom was determined from dual-energy CT acquisitions. Unlike conventional use of DECT for proton therapy, where the proton SPR is derived from the dual-energy output (see chapter 4), the SPR map of the phantom under study was directly obtained using proton CT. Assuming an I-value for water equal to 78 eV, the I-map of the object was estimated in a pixel-by-pixel basis solving equation 1.12 for I (equation 6.1).

The SPR expression used to extract the I-value of the object (equation 1.12) could be a matter of discussion. At present, there is no clear consensus on which is the most appropriate approach to compute theoretical SPR values [Ödén et al., 2015; Doolan et al., 2016]. On the one hand, the approach used in this study is the one proposed by Schneider *et al* [Schneider et al., 1996], later used by Yang *et al* [Yang et al., 2010], which neglects shell, density, Barkas and Bloch correction terms (see section 1.1.2.1). On the other hand, Bethe-Bloch [Bethe, 1930; Bloch, 1933] theory, which accounts for all mentioned corrections, has been widely used in proton therapy to compute the stopping power of human tissues. This formalism is not valid for proton energies below 1 MeV but it was found to have a negligible clinical impact [Doolan et al., 2016]. Oden *et al* [Ödén et al., 2015] compared Schneider's approach with the SRIM software [Ziegler et al., 2010], which incorporates all mentioned corrections, and concluded that equation 1.12 could be safely used because SPR errors below 0.1% were obtained across 72

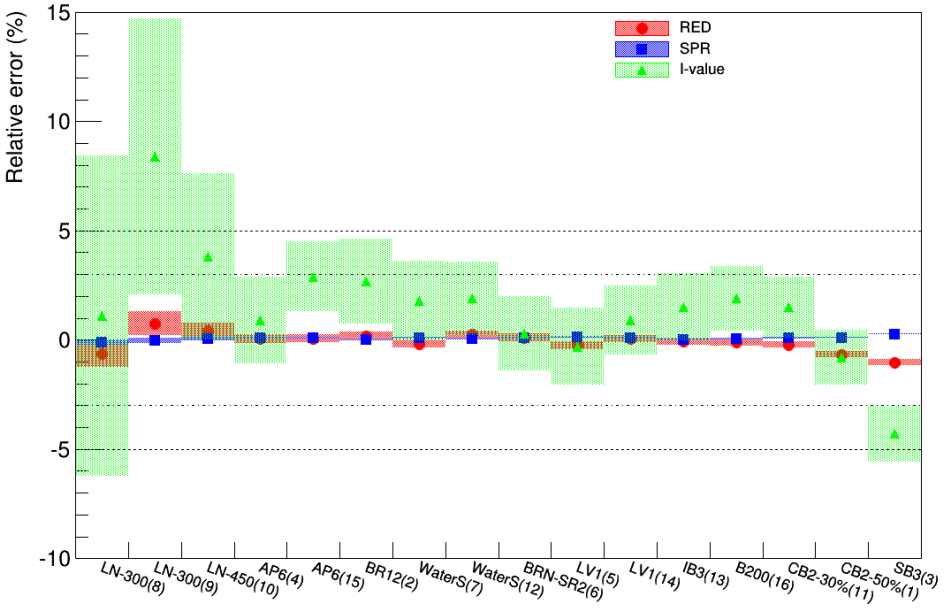

Figure 6.3: Plot of the relative RED, SPR and I-value errors with the corresponding error bars for all inserts sorted by increasing mass density. The numbers in the abscissa labels correspond to the inserts position inside the Gammex phantom (see Figure 5.1).

biological tissues. Furthermore, they concluded that elemental I-values of the ICRU Report 37 [ICRU, 1984] provided better agreement with experimental data than Janni's tabulated I-values [Janni, 1982]. In a recent work, Doolan *et al* [Doolan et al., 2016] did an inter-comparison of four existing SPR models for proton therapy: Bichsel's [Bichsel, 1972], Janni's [Janni, 1982] and ICRU's [ICRU, 1993] formulas to compute the absolute stopping power of tissues, and Schneider's [Schneider et al., 1996] to compute the relative stopping power. The SPR value of eleven plastic materials was experimentally determined and it was compared against the four theoretical approaches. The first three approaches account for different effects (i.e. shell and/or density corrections) and use different set of elemental I-values. To determine the relative SPR, the absolute stopping power of the tissue was divided by the absolute stopping power of water over the same range of energies. They concluded that Bichsel's approach using Bichsel's I-values and Schneider's approximation using ICRU elemental I-values lead to the lowest errors. Therefore, based on these studies, equation 1.12 can be safely used to determine the SPR and also to derive the I-value distribution of the object under study.

One obvious limitation of this simulation-based study is the fact that the considered proton CT scanner is assumed to be ideal in terms of detector response. In addition, no clinical proton CT scanners are available at the moment, just prototypes, so the clinical implementation of this technique is far from being immediate. Nevertheless, proton CT

radiography is already possible with commercial multi-layer ionization chambers [Farace et al., 2016] and, consequently, two-dimensional I-maps would be immediately available with current technology.

The combination of DECT and proton CT for determining the I-value should also be evaluated against means of calculation of the I-value from measurement of the SPR and the range, as discussed in section 1.1.3.5.

The difficulty of experimentally extracting the mean excitation energy of compounds or mixtures has long been stated [ICRU, 1984, 1989, 1992; Andreo, 2009; Besemer et al., 2013]. The Bragg additivity rule, neglecting chemical bounds and assuming a constant and general chemical composition for human tissues, is used instead [Andreo, 2009; España and Paganetti, 2010; Besemer et al., 2013]. One immediate application of the 3-D I-value images, reconstructed by combining proton CT (proton radiography) and DECT (dual-energy radiography) imaging, is to determine the intra-organ or intra-tissue I-value variability by performing organ or tissue segmentation.

Furthermore, if the proposed imaging modality is applied to a large number of individuals, representative of different population groups (e.g. infants, children, female adults, male adults, ill and healthy individuals, etc.), it would be possible to derive the intra-group and inter-group I-value variability for a given organ or tissue. Consequently, the proposed imaging technique could be used to extract valuable experimental reference data of human tissue I-values, which is currently lacking.

Another possible field of application of reconstructed I-value images is to improve the accuracy of MC dose calculations. On the one side, the scattering angle (θ_0) is related to the radiation length (X_0) (see equation 1.4) which is a property of the material. On the other side, the radiation length depends on the square of the atomic number and, at the same time, there exists a relation between the logarithm of the I-value and the effective atomic number. Consequently, from the I-value images, it would be possible to derive the radiation length map of the object and, together with the SPR map information, an improvement on the lateral dose computation is foreseen. However, there exist some other alternatives to improve dose computations. To start with, an alternative to the proposed approach is the combination of scattering power maps (δ-maps), reconstructed from scattering proton CT, with the SPR-maps, reconstructed from energy loss proton CT, which has already been investigated by Quiñones *et al* [Quiñones, 2016]. Furthermore, a simple derivation of the scattering power ratio of a tissue material to water from RED maps, e.g. obtained from dual-energy imaging, is also possible through a conversion function [Kanematsu et al., 2012]. Moreover, the Z_{eff} maps reconstructed from dual-energy imaging could also be used to derive the radiation length maps of the object being imaged. Consequently, unlike the application of I-value maps to derive intra-organ and intra- or inter-group I-value variability which is straightforward, the interest of using I-value maps to improve dose calculations has to be justified and, therefore, it requires further investigation and developments.

6.2.4 Conclusions

We have conducted a feasibility study based on simulations to extract the I-map of an object combining dual-energy CT and proton CT acquisitions. From these preliminary results, it seems feasible to do so. We obtained estimation errors of I within 3% for all phantom inserts, except for two lung inserts and for one bone insert which showed higher errors, up to 8%. The observed I inaccuracies in this study were mainly due to inaccuracies of the RED map. With optimized acquisition protocols and by choosing the most appropriate decomposition basis, we could improve the RED estimation. Moreover, to improve the precision, it seems desirable to adjust the dose balance towards the dual-energy CT acquisition. The proposed imaging technique could be a good candidate to extract volumetric distributions of the mean excitation energy of objects or patients. These maps could be used to determine the intra-organ or intra-tissue variability and, when applied to a large number of individuals, to determine the inter-group tissue variability. Furthermore, Monte Carlo dose computations could benefit from this additional material information and improve lateral dose distributions.

6.3 Conclusion

The determination of the proton range in the patient lacks of accuracy because of the limited knowledge on the mean excitation energy or I-value of different media, which is one of the components required to compute proton stopping powers. By combining two imaging modalities, proton CT and dual-energy CT, it seems feasible to derive volumetric I-value distributions of the imaged object. The proposed imaging technique could be used to extract experimental reference data of human tissue I-values, which is currently lacking and we believe it would add a valuable insight.

Chapter 7

Conclusions and future works

The works presented in this thesis aimed at improving the SPR estimation using dual-energy imaging, motivated by the need for a precise treatment plan in proton therapy. The thesis work also included the evaluation of the performance of the Imaging Ring system, which is a CBCT scanner equipped with a fast-kV switching X-ray source synchronized with a filter wheel, to determine the SPR of phantoms through dual-energy imaging.

One objective of this thesis was to propose a model for the source and the detector response in energy of the IR system in order to perform image simulations in GATE and dual-energy decomposition of phantom data. An experimental procedure to calibrate and validate the source and the detector models of a CBCT unit has been proposed and it has been evaluated on three commercial systems. For some applications, such as the implementation of MC scatter corrections, having separate and validated models of the source and the detector of the system under study is mandatory. However, for other purposes, as in most dual-energy applications, the product of the source energy spectrum by the detector response in energy is enough. Another experimental procedure has been proposed to simultaneously assess the validity of the source and the detector response models. One future approach that we are currently considering relies on making use of the experimental setup designed for the before-mentioned model assessment to implement more sophisticated procedures to determine the source and the detector model of the system, such as [Sidky et al., 2005]. Having a model of a CBCT unit in a research framework is extremely important because it allows to take decisions based on image simulations. For example, image simulations are the most practical tool to decide the most convenient composition and thickness of the filter wheel materials (Chapter 5) – depending on the final application, i.e., diagnostics, material segmentation, SPR map determination, etc.

The idea of extracting patient information to improve material discrimination, namely the effective atomic number and the relative electron density, by performing two acquisitions at different beam spectra was already proposed in the 1970s. Due to limitations of the first DECT scanners, such as low resolution or reconstruction arti-

facts due to movement, dual-energy was not spread clinically until 2006, when the first commercial dual-energy scanner solved most of these limitations. It was not until 2009 that dual-energy imaging was first proposed as a valid alternative to single-energy CT to improve proton therapy dose calculations. There are mainly two approaches to use dual-energy data to determine the SPR image of the patient. First, to directly reconstruct the SPR image from DECT output (sections 4.2-4.3). Alternatively, we can also combine the dual-energy output to reconstruct monochromatic CT images at a certain energy, and then use the lookup table HU-SPR relation to determine the SPR image. Unlike polychromatic images, these pseudo-monochromatic images are more exempt of beam hardening, metal artifacts and exhibit more tissue contrast (section 2.3). The main advantage of the former is that the SPR map is patient-specific, whereas the latter is based on a conversion between HU and SPR determined using tissue substitutes and it does not account for intra- and inter- patient variations. The advantage of the latter approach is that it is compatible with current TPSs which rely on a CT number to SPR conversion. Nevertheless, this is only an algorithmic limitation of current TPSs and new generation TPSs should move towards the incorporation of DECT-derived SPR images of the patient into the dose calculation pipeline.

A literature overview on the existing methods to estimate the SPR from DECT data revealed that most of the decomposition approaches for radiotherapy applications were image-based. There are several ways of combining dual-energy outputs to get the SPR or other relevant parameters for proton therapy dose calculations. We proposed to reconstruct the electronic cross section at a certain energy level and the RED from the mass density images resulting from the BMD approach. Two calibrated relations to estimate the SPR from these dual-energy outputs have been proposed: between the electronic cross section and the logarithm of the ionization potential, and between the electronic cross section and the ratio between the SPR over RED. Then, when compared with the existing methods, similar results in terms of SPR accuracy have been obtained. Furthermore, a simulation-based study has been conducted to determine whether projection-based decomposition approaches were suitable for proton therapy applications. In the light of these results and with the development of new imaging systems, such as dual-layer or photon counting detectors, we concluded that projection-based methods should also be considered for proton SPR determination.

Another objective of this PhD work was the optimization of acquisition protocols for proton therapy purposes. To that end, parameters that could have an influence on the decomposition output have been evaluated using a projection-based decomposition method: from the acquisition settings to the post-processing. In particular, we have evaluated the impact of the dual-energy spectra, the dose allocation between energy levels, the choice of the decomposition basis, and the way of solving the non-linear system of equations of the dual-energy problem on the SPR accuracy and precision. Then, based on simulations, the translation of these results onto the proton range accuracy using anthropomorphic phantoms has been evaluated. The work reported in this thesis shows that the SPR precision improves when increasing the energy separation between the incident spectra, whereas the accuracy shows little dependence on the energy gap.

Moreover, the dose balance between energy levels is not sensitive for the SPR accuracy, but the SPR precision, i.e. image noise, improves when one third of the total dose is imparted with the LE acquisition. The optimal pair of dual-energy spectra is material dependent, however, the gain in SPR accuracy was not translated to improved proton range estimation when performing measurements on a heterogeneous anthropomorphic phantom. Consequently, for proton therapy applications, the choice of the spectra may be driven by the precision, i.e., the energy gap. Furthermore, no significant differences have been found when comparing three decomposition bases. Depending on whether scanner information is available, such as the source spectrum or the detector response, the non-linear system of equations can either be solved analytically with an iterative optimization approach, more computationally demanding, or based on a calibration to indirectly estimate the scanner characteristics interposing slabs of known material and thickness to the photon beam. Future steps will be to validate these simulation-based results on real data acquisitions. In particular, it would be interesting to perform DECT acquisitions at different imaging doses to experimentally determine the impact of the noise on the proton range estimation.

The limited knowledge on the mean excitation energy of compounds and mixtures, such as human body tissues, introduces some uncertainty when computing the SPR and, thus, when determining the proton range. Bragg additivity rule is alternatively used to determine the I-value of tissues, but it is an approximation and it is based on tabulated data of average human tissues. We designed a simulation-based study combining two tomographic imaging modalities, proton CT and dual-energy CT, to investigate whether it was possible to derive the volumetric mean excitation energy distribution of the object being imaged. Promising results have been achieved but the proposed imaging technique is not yet technically possible because of proton CT imaging. One application of this imaging technique is the possibility to experimentally determine reference data of human tissue I-values, currently lacking, and to derive intra-tissue and inter-patient I-values variability. Future steps will be to derive the mean excitation energy distribution of phantom materials and/or animal tissues by performing proton radiography and dual-energy radiography with equipment already available in most proton therapy facilities [Farace et al., 2016].

Nowadays, there are several technological solutions to perform dual-energy. The advantages and limitations of each scanner have been reviewed. The IR system is one of the first commercially available systems capable of performing dual-energy CBCT FKVS acquisitions with each pulse synchronized with a filter wheel. This system gives the possibility to perform multi-energy imaging by interleaving patient projections acquired at different voltages and with different beam filtration. In this thesis we evaluated the performance of the IR system to estimate the proton SPR of real phantoms by performing dual-energy CBCT sequential and FKVS acquisitions. To minimize the scatter contamination at the projection level, we performed dual-energy CBCT acquisitions with a slit of 3 cm at the isocenter. We have also investigated the possibility of exploiting the information behind the collimator jaws to estimate the remaining scatter contribution on the measured transmission signal and to perform scatter correction off-line. Comparable re-

sults with respect to scatter deconvolution approaches have been obtained. We have also seen that linear interpolation between consecutive projections, to implement dual-energy decomposition in the projection domain, provides images of enough quality. Nevertheless, the accuracy level reached so far is not enough to clinically use the reconstructed SPR images with the IR for proton dose calculations, but some fields of improvement have been identified. To start with, the implemented projection-based decomposition approach relies on the perfect knowledge of the source spectrum and the detector response whose models might not be correctly determined for very hardened beams. In addition, inaccuracies on the filter thickness or on the chemical composition might modify the incident spectrum and induce errors in the SPR estimation. The presence of noise in the projections and a low SNR might also influence the output of the material decomposition. Future work would be to improve the source and the detector response models and to validate them against the filter materials of the wheel to better estimate the incident spectra. Even if we already do a calibration via the model, it would be interesting to evaluate the SPR accuracy with a calibration-based dual-energy decomposition method, for which the knowledge of the source and detector models is not required as they are indirectly determined through a calibration. Furthermore, image-based decomposition methods could also be evaluated.

In this thesis, we have conducted many simulation-based studies rather than experimental ones. Even if a noise-dose relation has been established and Poisson noise has been applied to the projections to deliver a given central dose value, we have performed our studies in an ideal scenario, exempt of motion artifacts, CT number instability over time and scatter contamination. Furthermore, what is lacking in this PhD thesis is an exhaustive quantification of the eventual gain of dual-energy CT with respect to single-energy CT with experimental data and to solve the noise problem encountered when decomposing dual-energy data using a projection-based approach. The best way to compare the performance of both imaging modalities would be to compute proton dose distributions based on the reconstructed SPR maps with DECT and SECT.

The IR system has been developed for IGRT and, therefore, we can image the patient at the treatment position. One interesting DE imaging application with the IR system, or with an analogous scanner, is the possibility to perform Adaptive Proton Therapy (APT) by re-planning the treatment on the SPR images reconstructed from DE-CBCT acquisitions recorded at the treatment position. Nowadays, there is increasing interest in using CBCT images for dose calculations both in photon and in proton therapy [Niu et al., 2010; Park et al., 2015; Landry et al., 2015]. The question of whether or not we can use DE-CBCT images for treatment planning to compute proton dose distributions has been partially addressed in this thesis. All CBCT scans have been performed with a 2 cm or 3 cm slit aperture at the isocenter. Future works include the evaluation of the SPR accuracy with DE-CBCT acquisitions without slit, i.e. open field, but a better scatter correction seems required as it has a strong influence on the material decomposition outcome [Sossin et al., 2014]. Furthermore, *in-vivo* treatment plan verification techniques based on the detection of secondary radiation, such as PET and prompt gamma imaging, could benefit from DE imaging at the treatment position to determine the elemental

composition of body tissues, namely the oxygen, carbon, phosphor and calcium tissue contents, with higher accuracy with respect to SECT [Landry et al., 2013a].

Projection-based decomposition methods consists in two steps: first, decomposition of CT datasets into basis material sinograms; second, reconstruction of these basis sinograms. As pointed out when reconstructing SPR maps from real data phantom acquisitions (section 4.6), this two-step approach seems to be susceptible to noise. We observed that the presence of noise in the CT projections might have an influence on the outcome of the material decomposition as it introduces some instability at the decomposition step. To overcome these limitations, the possibility to decompose and to reconstruct dual-energy (or spectral) data in one step is raising interest within the community. Iterative methods with regularization are current lines of investigation [Schmidt et al., 2015; Sidky et al., 2016; Foygel Barber et al., 2016].

The energy-dependence of the linear attenuation coefficient of different tissues, which allows for material segmentation with dual-energy imaging, could be further exploited to extract additional tissue information by moving from DE to multi-energy imaging. There are different approaches to perform multi-energy imaging with the current technology, either at the source level or at the detector level. On the one hand, multi-energy imaging at the source level can be performed by filtering the incident spectrum with different materials at a time. The IR system with the filter wheel synchronized with the beam pulse allows for multi-energy imaging by filtering the incident spectrum with up to four different materials. Projections with different filtration would be sequentially acquired and a proper sinogram interpolation would be required to sample the projections at the same angle in order to implement projection-based decomposition schemes. On the other hand, at the detector level, multi-energy imaging can be implemented making use of photon-counting detectors systems which are capable of recording the incident spectrum within different energy bins or windows. One drawback of these systems is that the detector technology is not mature yet [Atak and Shikhaliev, 2015] and some issues need to be solved before being clinically available, such as charge sharing, pile-up, energy sensitivity, etc. Once both system technologies are comparable, it would be interesting to evaluate the performance of both approaches. In addition, it would be worth to investigate whether photon counting detectors could be used in CBCT scanners to combine the advantage of both technologies, i.e. energy resolved volumetric acquisitions with reduced patient dose with respect to fan-beam systems.

The main goal of this thesis work was to use DE imaging to reduce margins in proton therapy. In clinical practice, lateral and range margins are added to the CTV for each beam in the TPS. We have mainly focused on investigating approaches to perform DE decomposition to reduce the uncertainty associated to the conversion of HU to SPR values, typically performed with SECT imaging, which has a 1% error associated. When accounting for BH artifacts only, it contributes up to 1.1% and 1.8% of the proton range in water for soft tissue and for bone, respectively [Schaffner and Pedroni, 1998; Paganetti, 2012]. However, there are other scanner related uncertainties, such as CT numbers stability over time, i.e. day-to-day variations, and besides BH artifacts there are scatter artifacts, specially with CBCT scanners, that additionally contribute to the

range uncertainty. Despite this range error values, more conservative margins such as 3.5% +1 mm –which may vary from one institution to the other– are being used instead. Margins are taken as a geometric concept, as in the photon world, for which these margins are mainly used to determine lateral errors [Both, 2012]. The next step is to directly plan proton treatments on SPR images reconstructed from DECT imaging, combined with personalized and beam-specific margins [Park et al., 2012]. It could open a new line of research and it should give more confidence to clinicians and medical physicists to reduce margins in proton therapy, to reduce target volumes and, therefore, to decrease the probability of complications and late effects.

Appendix A

List of Publications

In this chapter, the list of publications, both journals and conferences papers, communications and scientific dissemination derived from the development of the thesis is given.

A.1 Journal articles

[**J1**] G. Vilches-Freixas, J. M. Létang, S. Brousmiche, E. Romero, M. Vila Oliva, H. Deutschmann, P. Keuschnigg, P. Steininger, and S. Rit, "Technical Note : Procedure for the calibration and validation of kilo-voltage cone-beam CT models," *Med. Phys.*, vol. 43, no. 9, pp. 5199–5204, 2016.

[**J2**] G. Vilches-Freixas, J. M. Létang, N. Ducros, and S. Rit, "Optimization of dual-energy CT acquisitions for proton therapy using projection-based decomposition," *Med. Phys.*, vol. 44, no. 9, pp. 4548–4558, 2017.

[**J3**] G. Vilches-Freixas, V. T. Taasti, L. P. Muren, J. B. B. Petersen, J. M. Létang, D. C. Hansen, and S. Rit, "Comparison of projection- and image-based methods for proton stopping power estimation using dual energy CT," *PhiRo*, vol. 3, pp. 28–36, 2017.

A.2 Conference articles

[**A1**] G. Vilches-Freixas, J. M. Létang, N. Ducros, and S. Rit, "Dual-energy CT spectra optimization for proton treatment planning," *The 4th International Conference on Image Formation in X-Ray Computed Tomography*, Jul 2016, Bamberg, Germany, pp.585-588.

A.3 Communications

[**C1**] G. Vilches-Freixas, J. M. Létang, K. Presich , P. Steininger, and S. Rit, "PO-0959: Optimal dose balance between energy levels for material decomposition with dual-energy X-ray CT, 3rd *ESTRO* Forum 2015, April 2015, Barcelona, Spain. Poster presentation.

[**C2**] G. Vilches-Freixas, J. M. Létang, and S. Rit, "EP-1847: Comparison of stopping power estimators from dual-energy computed tomography for proton therapy", *ESTRO* 2016, April 2016, Turin, Italy. Poster presentation.

[**C3**] G. Vilches-Freixas, J. M. Létang, and S. Rit, "Comparison of stopping power estimators from dual-energy computed tomography for proton therapy", Dual-energy workshop @ ESTRO 2016, April 2016, Turin, Italy. Oral presentation.

[**C4**] G. Vilches-Freixas, C. T. Quiñones, J. M. Létang, and S. Rit, "Estimation of the ionization potential map from dual-energy CT and proton CT," *PTCOG 55*, May 2016, Prague, Czech Republic. Oral presentation.

[**C5**] G. Vilches-Freixas, J. M. Létang, N. Ducros, and S. Rit, "Dual-energy CT spectra optimization for proton treatment planning," *CT meeting* 2016, July 2016, Bamberg, Germany. Oral presentation.

[**C6**] G. Vilches-Freixas, V. T. Taasti, L. P. Muren, J. B. B. Petersen, J. M. Létang, D. C. Hansen, and S. Rit, "Stopping power ratio estimation for proton therapy dose calculations using projection- vs. image-based dual-energy CT methods, *PTCOG 56*, May 2017, Yokohama, Japan. Poster presentation.

[**C7**] V. T. Taasti, G. Vilches-Freixas, L. P. Muren, J. B. B. Petersen, J. M. Létang, D. C. Hansen, and S. Rit, "Comparison of projection- and image-based methods for proton stopping power estimation using dual energy CT," *BiGART* 2017, Aarhus, Denmark. Oral presentation.

A.4 Scientific dissemination

[**O1**] *Ma thèse en 180 secondes* - MT180s. 3rd price of the Jury at the regional final of Université de Lyon.

Appendix B

Noise - dose relation

Most of the works presented in this thesis are based on CT imaging simulations. Poisson noise was applied to the projections to simulate a realistic scenario. To relate the level of Poisson noise to the imaging dose, a relation between the dose value at the center of the phantom and the number of primary photons per simulation is derived in this chapter.

B.1 Image simulations

Most of the image simulations of the Imaging Ring (IR) system carried out in this PhD thesis were performed using the Fixed Forced Detection (FFD) actor implemented in GATE [Jan et al., 2004] v7.2. This deterministic module computes digitally reconstructed radiographs (DRR) using the reconstruction toolkit (RTK) [Rit et al., 2014] and the Geant4 database of X-ray cross sections. The source-to-isocenter distance was 626 mm and the source-to-detector distance was 1026 mm. The tissue characterization Gammex 467 phantom (Gammex, Middleton, WI) and the anthropomorphic female (AF) computational phantom of the ICRP [ICRP, 2009] were used in the simulations. Fan-beam projections with 360 views of 807 pixels of 1 mm were considered for the Gammex phantom, whereas 600 projections of 1026 pixels of 1 mm were considered for the ICRP phantom. Scattered particles were not considered in the simulation to approximate ideal conditions with anti-scatter grids. The energy-dependent detector response used in the simulations was previously validated by [Vilches-Freixas et al., 2016a]. To simulate a realistic scenario, Poisson noise was applied to the projections to deliver a central dose D_c with each spectrum.

The level of Poisson noise depends on the number of primary photons per simulation, N_{prim}, required to deliver a central dose of primary radiation, D_c, which was determined

analytically (see equation B.7) assuming an homogeneous and cylindrical water medium:

$$N_{\text{prim}} = \frac{D_{\text{c}}\ A_{\text{beam}}}{\int_E S(E)\ e^{-\mu_{\text{w}}(E)\ r}\ \left(\frac{\mu_{en}(E)}{\rho}\right)_{\text{w}}\ E\ \text{d}E} \tag{B.1}$$

where A_{beam} is the area covered by the beam at the isocenter considering a constant flat field, S is the energy-dependent incident spectrum with unity area: $\int_E S(E)\ \text{d}E = 1$, $(\mu_{en}(E)/\rho)_{\text{w}}$ and μ_{w} are respectively the energy-dependent mass energy-absorption coefficient and the linear attenuation coefficient of water taken from the NIST database [Hubbell and Seltzer, 2004], and r is the radius of the phantom.

The required input of the FFD actor is the expected number of photons in each pixel of the detector, N_{pix}, which can be computed from the number of primary photons per simulation, N_{prim}, as follows:

$$N_{\text{pix}} = \frac{N_{\text{prim}}}{K_{\text{proj}}}\ \frac{A_{\text{det}'}}{A_{\text{beam}'}}\ \frac{1}{p} \tag{B.2}$$

where K_{proj} is the number of projections of the simulation, $A_{\text{det}'}$ is the area of the detector (i.e. fan beam slit) in mm^2, $A_{\text{beam}'}$ is the area covered by the beam at the detector level in mm^2, and p is the number of pixels of the detector.

B.2 Dose at the center of the phantom

For a monoenergetic beam, the analytical expression for the absorbed dose in water at the center of a cylindrical or spherical phantom is given by:

$$D_i = N_i\ \left(\frac{\mu_{en}}{\rho}\right)_{\text{w},i}\ E_i \tag{B.3}$$

with N_i the number of photons of energy E_i that reach the center of the phantom per unit surface, $(\mu_{en}(E)/\rho)_{\text{w},i}$ the mass energy absorption coefficient of water at the i-th energy and E_i the energy of the photons.

Similarly, for a polychromatic beam the total absorbed dose, D_T, can be expressed as the sum of the dose deposited by each monoenergetic energy that composes the polychromatic spectrum:

$$D_T = \sum_i^N D_i = \sum_i^N N_i\ \left(\frac{\mu_{en}}{\rho}\right)_{\text{w},i}\ E_i \tag{B.4}$$

N_i is equal to the total number of incident photons that reach the center of the phantom per unit surface, N_T, multiplied by the weight of the i-th energy, ω_i, of the polychromatic spectrum. Furthermore, N_T can be expressed as the total number of incident photons without phantom to an area of 1 mm$\times$1 mm, $N_{0,T}$, multiplied by the attenuation of half phantom according to the Beer-Lambert law (see equation 1.22).

$$D_T = N_T \sum_i^N \omega_i \left(\frac{\mu_{en}}{\rho}\right)_{\mathrm{w},i} E_i = N_{0,T} \sum_i^N \omega_i \, e^{-\mu_{i,\mathrm{w}} \, r} \left(\frac{\mu_{en}}{\rho}\right)_{\mathrm{w},i} E_i \tag{B.5}$$

It is possible to establish a relation between $N_{0,T}$ and the total primary number N_{prim}.

$$N_{0,T} = \frac{N_{\mathrm{prim}}}{A_{\mathrm{beam}}} \tag{B.6}$$

Substituting Equation B.6 into Equation B.5, we obtain the final expression of the absorbed dose at the center of a water phantom irradiated with a polychromatic beam, over K_{proj} projections, and a total number of incident photons N_{prim}.

$$D_T = \frac{N_{\mathrm{prim}}}{A_{\mathrm{beam}}} \sum_i^N \omega_i \, e^{-\mu_{i,\mathrm{w}} \, r} \left(\frac{\mu_{en}}{\rho}\right)_{\mathrm{w},i} E_i \tag{B.7}$$

The analytical expression to compute the absorbed dose at the center of the water phantom (Equation B.7) was verified using the split exponential Track Length Estimator (seTLE) Dose Actor, which is based on a variance reduction technique [Smekens et al., 2009, 2014]. The results of the comparison, carried out for two beam spectra and for two dose levels per spectrum, are shown in Table B.1. It is worth mentioning that the seTLE Dose Actor records both the primary and the secondary radiation whilst in the analytical expression only the primary radiation is accounted for.

N_{prim}	D_T prim + sec (σ_{D_T})	D_T prim	D_{theo}	Rel. diff. (%)	E
7.20×10^6	9.7 (2) $\times 10^{-7}$	9.18×10^{-7}	9.27×10^{-7}	1.0	120 kV Cu + Ag
7.06×10^7	9.58 (5) $\times 10^{-6}$	9.03×10^{-6}	9.09×10^{-6}	0.6	120 kV Cu + Ag
7.20×10^6	3.22 (8) $\times 10^{-7}$	2.98×10^{-7}	3.08×10^{-7}	3.0	60 kV
6.95×10^7	3.13 (4) $\times 10^{-6}$	2.89×10^{-6}	2.97×10^{-6}	2.6	60 kV

Table B.1: Comparison of the seTLE actor output and the analytically determined dose values (D_{theo}) for different number of primaries N_{prim} and beam qualities. prim stands for primary radiation and sec for secondary radiation. The relative difference (Rel. diff. % column) has been computed between the theoretical dose and the primary dose recorded at the center.

Appendix C

Reference SPR values

In March 2016, a measurement session was carried out at the Heidelberg Ion-beam Therapy center (HIT, Germany) to determine the reference SPR values of three phantom materials: twelve inserts of the Gammex RMI 467 (Gammex, Middleton, United States of America), eighteen inserts of the CIRS 062 (CIRS, Norfolk, United States of America) and the CIRS Dynamic Thorax phantom with a lung tumor insert (CIRS, Norfolk, United States of America).

As discussed in section 1.2.3.1, the SPR of a material x of known thickness a can be determined experimentally by measuring the shift in the Bragg peak position when interposing this material to the beam (BP_x) with respect to the Bragg peak position in water without insert ($BP_{w/o}$).

$$SPR_x = \frac{BP_{w/o} - BP_x}{a} = \frac{\Delta P}{a} \tag{C.1}$$

where ΔP and a have to be expressed in the same units (e.g. mm), because SPR is dimensionless.

As the diameter of the Gammex and the CIRS rods were 2.8 cm and 3 cm, respectively, we decided to perform the SPR measurements with carbon beams because they present a reduced spot size in air at the isocenter with respect to proton beams. A 310.6 MeV/u carbon beam was used which corresponds to a depth in water of 182.5 mm. First, we measured with the Peakfinder water column (PTW, Freiburg, Germany) the Depth Dose Distribution (DDD) of the carbon beam without any insert at a resolution of 50 µm. Then, an insert at a time was interposed to the carbon beam and we measured the DDD at a resolution of 100 µm. The experimental setup is illustrated in Figure C.1.

For each DDD, a fifth degree polynomial fit was done to the data at the peak region, defined as the 70% proximal and distal edge range with respect to the maximum. To extract the range value, which corresponds to the 80% distal edge with respect to the Bragg peak position, a linear interpolation was done to the fitted data (Figure C.2). The exact length of each insert material was determined using a caliper with a precision of ± 10 µm. The resulting SPR values determined for each phantom insert are shown

in Tables C.1, C.2 and C.3.

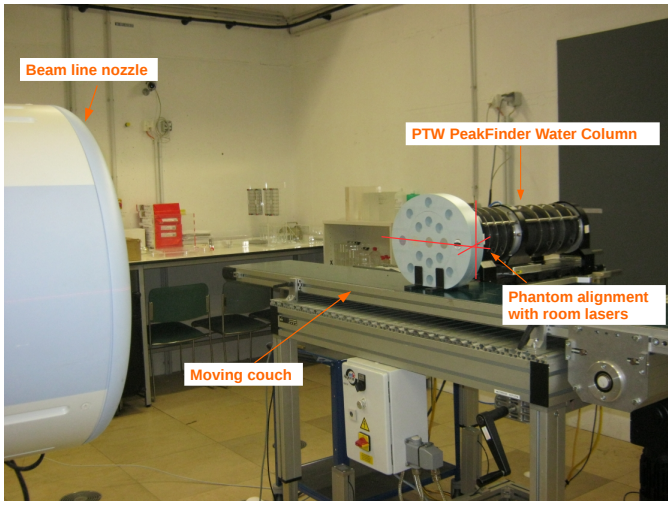

Figure C.1: Experimental setup to determine the Bragg Peak position

Insert	SPR	Insert	SPR
Lung inhale set 1	0.215	Lung inhale set 2	0.207
Lung exhale set 1	0.482	Lung exhale set 2	0.483
Adipose set 1	0.967	Adipose set 2	0.967
Breast 50/50 set 1	0.991	Breast 50/50 set 2	0.992
Muscle set 1	1.043	Muscle set 2	1.045
Liver set 1	1.058	Liver set 2	1.056
Trabecular Bone set 1	1.091	Trabecular Bone set 2	1.094
Dense Bone 800 set 1	1.402	Dense Bone 800 set 2	1.401
Bone 1250	1.616	Plastic Water	1.005

Table C.1: CIRS 062M phantom. set 1: black line on the capsule; set 2: no line.

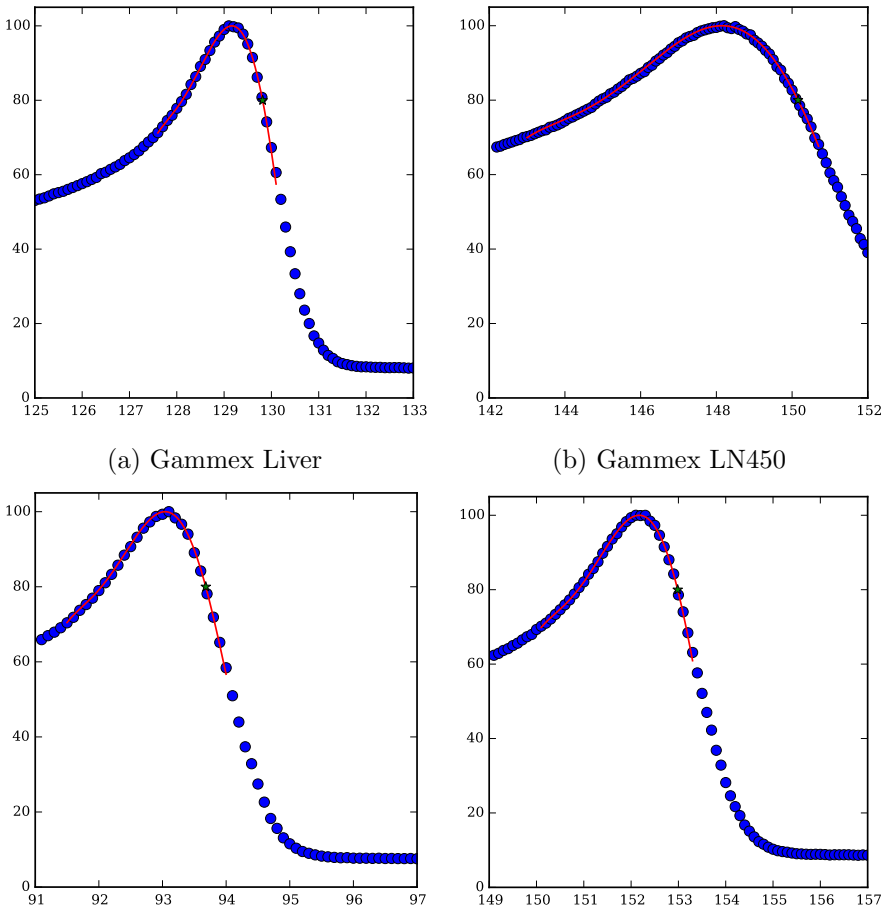

(a) Gammex Liver (b) Gammex LN450

(c) Gammex CB2-30% (d) CIRS Dynamic Thorax Lung tissue

Figure C.2: Measured depth-dose distributions (dots), fifth degree polynomial fit in the 70% proximal to distal region (red line) and range position (green star) at the 80% distal edge.

Insert	SPR	Insert	SPR
LN-300 Lung	0.248	LN-300 Lung*	0.248
LN-450 Lung	0.453	LN-450 Lung*	0.455
AP6 Adipose	0.941	AP6 Adipose*	0.941
BR-12 Avg. Breast	0.970	BR-12 Avg. Breast*	0.971
CT Solid Water	1.000	CT Solid Water*	1.000
BRN-SR2 Brain	1.061	BRN-SR2 Brain*	1.062
LV1 Liver	1.075	LV1 Liver*	1.076
IB3 Inner Bone	1.083	IB3 Inner Bone*	1.083
B200 Bone Mineral	1.095	B200 Bone Mineral*	1.094
CB2 Resin 30% CaCO3	1.260	CB2 Resin 30% CaCO3*	1.258
CB2 Resin 50% CaCO3	1.427	CB2 Resin 50% CaCO3*	1.427
SB3 Cortical Bone	1.620	SB3 Cortical Bone*	1.621

Table C.2: Gammex 467 phantom. Left) ΔP value computed from the DDD measurements without etiquette: the average 0.2 mm etiquette thickness was subtracted to the measured a value to compute the SPR. Right *) ΔP value computed from the DDD measurements with etiquette minus the average 0.5 mm water equivalent length of the etiquette.

Insert	SPR
Lung Insert Thorax Phantom	0.191
Plastic Water DT Thorax Phantom	0.988
Lung Tissue Thorax Phantom	0.197

Table C.3: CIRS Dynamic Thorax phantom

Appendix D

Conversion into water-equivalent materials

D.1 Introduction

To compute patient dose distributions of a proton treatment plan based on MC, a conversion from patient CT numbers to material composition and mass densities is required [Schneider et al., 2000; Paganetti, 2009]. Another approach consists in coverting SPR maps voxel-by-voxel into water equivalent materials and in adjusting the mass density in each voxel to match its reconstructed SPR value [Arbor et al., 2015]. The immediate consequence of converting patient CT voxels into water equivalent materials is that we lose information on the chemical composition, i.e. we make the assumption that all voxels have the same chemical composition.

Motivated by this approximation, a simulation-based study was designed to qualitatively study the impact of this wrong material assignment on the transverse dose distribution, at the Bragg Peak depth. We also verified that there were no significant range errors in the longitudinal direction of the proton pencil beam.

D.2 Materials and Methods

A 50 cm phantom box (material M, mass density ρ) was irradiated with proton beams of 150 MeV and 250 MeV of initial squared shape of 10 mm and beam intensity of 10^6 protons. These proton energies corresponded to a mean proton path of 158.3 mm and 381.0 mm in water, respectively. Five human tissue materials M, extracted from GATE's material database [Jan et al., 2004], were considered: adipose, liver, cartilage, spine bone and rib bone. MC simulations in GATE with a Dose Actor attached to the phantom volume were performed. When computing the dose deposit, two different setups were considered for each material (Table D.1): first, material M was assigned to the phantom box; second, water material with mass density ρ corresponding to the

SPR of M computed at 300 MeV was assigned to the phantom box. For the first part of the study, the 2D dose distribution was laterally integrated to obtain the depth dose distribution. The BP curves were fitted with a fifth degree polynomial. To extract the range value, which corresponds to the 80% distal edge with respect to the BP position, a linear interpolation was done to the fitted data. For each material, range values obtained with the two setups and for both proton energies were compared. For the second part of the study, the normalized lateral dose profiles, at 150 MeV and 250 MeV, were compared for both irradiation setups at the BP position, at the BP-2 mm and at the BP-4 mm.

D.3 Results and Discussion

The corresponding absolute and relative range errors at 150 MeV and 250 MeV when assigning the material M to the phantom voxels or when assigning water equivalent material with mass density equal to the SPR value of M are summarized in Table D.1. Those materials having a chemical composition or a mass density much different from that of water, i.e. adipose and rib bone tissues, exhibit a larger range difference when computing the depth-dose deposit in the material M or in the water equivalent medium. Nevertheless, relative range errors were comprised between -0.4% and 0.4% for the 150 MeV beam, and between -0.2% and 0.3% for the 250 MeV beam. Consequently, with respect to the longitudinal depth-dose comparison, we can conclude that it is accurate to convert patient CT voxels into water equivalent materials.

Material M	ρ	ΔR_1 (mm)	$\%R_1$	ΔR_2 (mm)	$\%R_2$
Adipose	0.920	-	-	-	-
Water eq. adipose @ 78 eV	0.951	-0.7	-0.4%	-0.8	-0.2%
Liver	1.060	-	-		
Water eq. liver @ 78 eV	1.064	-0.2	-0.13%	-0.4	-0.11%
Cartilage	1.100	-	-		
Water eq. cartilage @ 78 eV	1.093	-0.09	-0.06%	-0.14	-0.04%
Spine bone	1.420	-	-		
Water eq. spine bone @ 78 eV	1.341	0.16	0.14%	0.2	0.07%
Rib bone	1.920	-	-		
Water eq. rib bone @ 78 eV	1.724	0.4	0.4%	0.6	0.3%

Table D.1: Absolute range errors at 150 MeV (ΔR_1) and 250 MeV (ΔR_2), and the corresponding relative range errors ($\%R_1$) and ($\%R_2$), respectively, caused by wrong material assignment. When the material M is assigned to the phantom voxels, ρ corresponds to its mass density value (expressed in g/cm^3), whereas ρ equals the SPR value of M computed at 300 MeV using an I-value for water of 78 eV when water equivalent material is assigned.

The transverse dose profiles at the BP position (80% distal edge), at BP -2 mm, and at BP -4 mm; for the adipose, the cartilage and the rib bone tissues are shown in

Figures D.1, D.2 and D.3, respectively. On the one hand, small lateral dose differences are observed for the cartilage tissue between the pure material and the water equivalent material. The differences are larger for the 250 MeV proton energy beam. On the other hand, lateral dose differences become more significant for the adipose and the rib bone tissues. Dose profiles in rib bone are wider than the ones in the water equivalent rib bone, whereas lateral dose profiles are wider for the water equivalent adipose tissue than for the pure adipose tissue. These results are reasonable because scattering strongly depends on the atomic number of the traversed material.

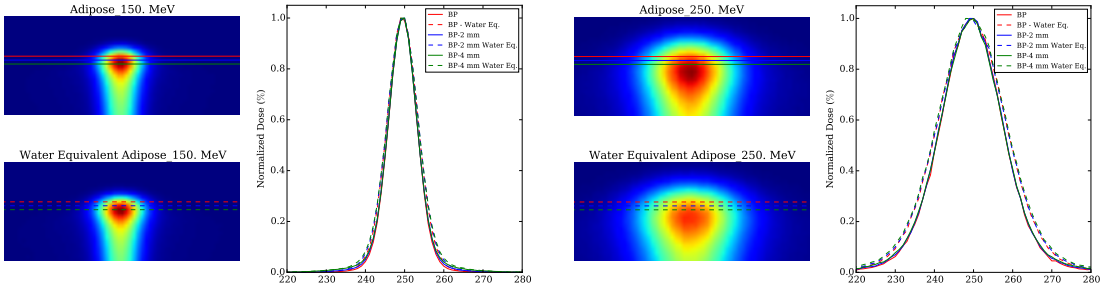

Figure D.1: Transverse dose profiles at the Bragg Peak (BP) position (red), at the BP-2 mm (blue) and at the BP-4 mm (green) for the adipose tissue (solid line) and the water equivalent adipose tissue (dashed line) at 150 MeV (left) and 250 MeV (right).

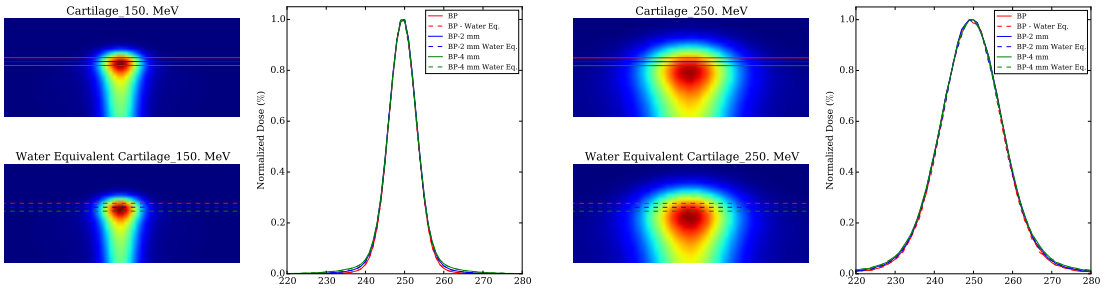

Figure D.2: Transverse dose profiles at the Bragg Peak (BP) position (red), at the BP-2 mm (blue) and at the BP-4 mm (green) for the cartilage tissue (solid line) and the water equivalent cartilage tissue (dashed line) at 150 MeV (left) and 250 MeV (right).

Regarding the qualitative lateral dose profile comparison, these results suggest that the conversion into water equivalent materials is accurate for most tissues close to water, but it is no longer applicable for materials having a chemical composition much different from that of water. Nevertheless, a 50 cm homogeneous material cube as the one used in this study is not a realistic irradiation setup when dealing with patients.

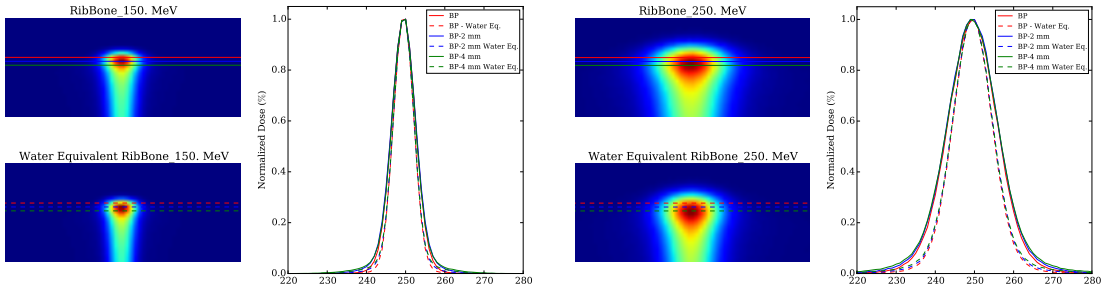

Figure D.3: Transverse dose profiles at the Bragg Peak (BP) position (red), at the BP-2 mm (blue) and at the BP-4 mm (green) for the rib bone tissue (solid line) and the water equivalent rib bone tissue (dashed line) at 150 MeV (left) and 250 MeV (right).

D.4 Conclusions

The aim of this simulation-based experiment was to investigate the impact of converting CT voxels into water equivalent materials on the longitudinal and on the lateral dose distributions. From these results we can conclude that the conversion into water equivalent materials could be used in a MC proton dose calculation framework to reproduce patient treatment plans. However, special care should be taken for materials with mass densities and chemical compositions much different from that of water, as this approximation has some limits. For two reasons: first, because the proton energy loss depends on the electron density of the traversed media and thus, on the mass density, which would introduce errors in the range estimation; second, because scattering strongly depends on the atomic number and, therefore, lateral dose profiles would not be correct. Moreover, special care should be taken for deeply seated tumors as lateral dose differences become more significant at higher proton energies.

Appendix E

Résumé étendu

Les images tomodensitométriques (Computed Tomography en Anglais, CT) montrent la distribution spatiale du coefficient d'atténuation linéaire de l'objet dont on prend l'image. Deux objets ayant une densité massique et une composition élémentaire différentes peuvent montrer la même atténuation et, en conséquence, ne peuvent pas être différenciées avec un scanner CT. Cependant, si on profite de la dépendance énergétique du coefficient d'atténuation des tissus, deux matériaux peuvent être différenciés en enregistrant l'atténuation à différents spectres. Ceci est le principe de base de l'imagerie bi-énergie, auquel faisait déjà référence en 1973 Sir Hounsfield dans l'article qui décrivait l'invention du scanner CT [Hounsfield, 1973].

La proton thérapie est une modalité de traitement du cancer qui utilise des faisceaux de protons pour endommager les cellules cancérigènes en les empêchant de grandir et se diviser. En principe, la portée de protons est finie et contrôlable en ajustant leur énergie cinétique. La réduction de la dose intégrale que reçoit le patient par rapport aux photons permet, pour la même dose à la tumeur, une radiothérapie plus conforme. Les systèmes de planification de traitement actuels se basent sur une image CT de l'anatomie du patient pour concevoir le plan de traitement. Le pouvoir d'arrêt des protons relatif à l'eau (Stopping Power Ratio en anglais, SPR) est déterminé à partir des unités Hounsfield (Hounsfield Units en anglais, HU) pour calculer la dose absorbée au patient. Les protons sont plus vulnérables que les photons aux modifications du SPR du tissu dans la direction du faisceau dues au mouvement, au mauvais positionnement ou aux changements anatomiques. De plus, les inexactitudes issues du CT de planification et intrinsèques à la conversion HU-SPR contribuent énormément à l'incertitude sur la portée des protons. Dans la pratique clinique, des marges de sécurité s'ajoutent au volume de traitement pour tenir compte de ces incertitudes au détriment de la capacité d'épargner les tissus autour de la tumeur. L'usage de l'imagerie bi-énergie (Dual-energy en anglais, DE) pour les plans de traitement avec protons a été proposé pour la première fois en 2009 pour mieux estimer le SPR du patient par rapport à l'imagerie mono-énergie.

Les travaux présentés dans cette thèse visaient à améliorer l'estimation du SPR en utilisant l'imagerie bi-énergie, en ayant pour but de réduire l'incertitude sur la prédiction

de la portée des protons dans le patient. Cette thèse est appliquée à un nouveau système d'imagerie, l'Imaging Ring (IR), un scanner tomodensitométrique conique (Cone-Beam CT en anglais, CBCT) développé pour la radiothérapie guidée par l'image (Image-guided Radiotherapy en anglais, IGRT). L'IR est équipé d'une source de rayons X avec un système d'alternance rapide du voltage (Fast-kV switching en anglais, FKVS), synchronisé avec une roue contenant des filtres de différents matériaux qui permet des acquisitions de tomodensitométries coniques multi-énergie.

Un objectif de la thèse était de proposer un modèle pour la source et la réponse en énergie du détecteur du système IR pour réaliser des simulations de l'IR avec GATE et des décompositions bi-énergie de fantômes numériques. Une procédure expérimentale pour calibrer et valider les modèles de source et détecteur d'une unité CBCT a été proposée et a été évaluée avec trois systèmes commerciaux. Pour certaines applications, comme l'implémentation de corrections Monte Carlo (MC) du diffusé, le fait d'avoir des modèles séparés et validés de la source et du détecteur du système étudié est nécessaire. Néanmoins, pour d'autres objectifs, comme dans la plupart des applications de la bi-énergie, le produit des spectres énergétiques de la source par la réponse en énergie du détecteur est suffisant. Une autre procédure expérimentale a été proposée pour estimer simultanément la validité des modèles de la source et de la réponse du détecteur. Le fait d'avoir un modèle d'une unité CBCT dans un cadre de recherche est extrêmement important car cela permet de prendre des décisions basées sur des simulations d'images contrôlées. Par exemple, les simulations d'images sont l'outil le plus pratique pour décider de la composition et de l'épaisseur les plus appropriées des matériaux des filtres de la roue (Chapitre 5) en fonction de l'application finale, par exemple le diagnostic, la segmentation en matériaux, la détermination de la carte du SPR, etc.

L'idée d'obtenir des informations sur les tissus du patient en réalisant deux acquisitions avec des faisceaux ayant des spectres différents pour améliorer la distinction des matériaux, notamment le nombre atomique et la densité électronique relative, fut déjà proposée pendant les années 70. A cause des limitations des premiers scanners DECT, telles que la basse résolution ou les artefacts de reconstruction dus au mouvement, la bi-énergie ne s'est pas répandue dans la pratique clinique jusqu'à 2006, quand le premier scanner commercial bi-énergie a résolu la plupart de ces limitations. Ce n'est qu'en 2009 que l'imagerie bi-énergie a été proposée pour la première fois comme une alternative valide à la CT mono-énergie pour améliorer les calculs de dose en proton thérapie. Il y a principalement deux approches pour utiliser les données bi-énergie pour déterminer l'image SPR du patient. La première est de reconstruire directement l'image SPR à partir des données du DECT (sections 4.2-4.3). De manière alternative, on peut aussi combiner les données de la bi-énergie pour reconstruire des images CT monochromatiques à une certaine énergie, et utiliser alors la table de conversion (lookup table en anglais) HU-SPR pour déterminer l'image SPR. Contrairement aux images polychromatiques, ces pseudo-images monochromatiques sont moins susceptibles au durcissement de faisceau, aux artefacts métalliques et elles montrent plus de contraste des tissus (section 2.3). Le principal avantage de la première approche est que la carte du SPR est spécifique au patient tandis que la deuxième approche est basée sur une conversion entre

HU et SPR déterminée en utilisant des substituts plastiques aux tissus et ne tient donc pas compte des variations intra- et inter-patient. L'avantage de la deuxième approche est qu'elle est compatible avec les TPS actuels qui se basent sur les HU de la CT pour la conversion SPR. Néanmoins, celle-ci est seulement une limitation algorithmique des actuels TPS et la nouvelle génération de TPS devrait incorporer les images SPR du patient dérivées du DECT dans les processus de calcul de dose.

Une vue d'ensemble de la littérature sur les méthodes existantes pour estimer le SPR à partir des donnés DECT a montré que la plupart des approches de décomposition pour des applications en radiothérapie étaient basées dans le domaine image. Il y a plusieurs manières de combiner les données de sortie de la bi-énergie pour obtenir le SPR ou d'autres paramètres pertinents pour les calculs de dose en proton thérapie. On a proposé de reconstruire la section efficace électronique à un certain niveau d'énergie ainsi que la densité électronique relative à l'eau (Relative Electron Density en anglais, RED) à partir des images de densité obtenues par l'approche de décomposition en matériaux. Deux relations calibrées pour estimer le SPR à partir de ces données de sortie bi-énergie ont été proposées : entre la section efficace électronique et le logarithme du potentiel d'ionisation, et entre la section efficace électronique et le ratio SPR/RED. Ces relations ont été comparées aux méthodes existantes et les résultats obtenus ont été similaires en termes de justesse du SPR. En outre, une étude basée sur des simulations a été réalisée pour déterminer si les approches de décomposition basées sur les projections étaient indiquées pour des applications en proton thérapie. A la vue de ces résultats et avec le développement de nouveaux systèmes d'imagerie comme les systèmes bi-couches ou les détecteurs à comptage de photons, nous avons conclu que les méthodes basées sur les projections devraient aussi être envisagées pour déterminer le SPR des protons.

Un autre objectif de cette thèse a été l'optimisation de protocoles d'acquisition pour la proton thérapie. Avec cette finalité, les paramètres qui pourraient avoir une influence sur les données de sortie de la décomposition ont été évalués en utilisant une méthode de décomposition basée sur les projections, des paramètres d'acquisition au post-traitement. En particulier, nous avons évalué l'impact des spectres bi-énergie, la répartition de la dose entre les niveaux d'énergie, le choix des bases de décomposition, et la manière de résoudre le système d'équations non linéaires du problème de la bi-énergie utilisant comme figure de mérite la justesse et la précision du SPR. Ensuite, sur la base de ces simulations, le transfert de ces résultats sur la justesse de la portée des protons a été évalué en utilisant des fantômes anthropomorphiques numériques. Le travail exposé dans cette thèse montre que la précision du SPR s'améliore quand on augmente la séparation énergétique entre les spectres incidents, tandis que la justesse montre une faible dépendance à cette séparation énergétique. De plus, la répartition de la dose entre les niveaux d'énergie n'est pas sensible pour la justesse du SPR, mais elle l'est pour la précision du SPR, c'est-à-dire que le bruit de l'image diminue quand un tiers de la dose totale est donné avec l'acquisition de basse énergie. La paire de spectres bi-énergie optimale dépend du matériau, cependant, le gain en justesse du SPR ne se traduisait pas en une estimation améliorée de la portée des protons quand on réalisait des mesures sur des fantômes anthropomorphiques hétérogènes. En conséquence, pour

des applications en proton thérapie, le choix des spectres devrait être motivé par la précision, c'est-à-dire la séparation énergétique. De plus, nous n'avons pas trouvé de différences significatives en comparant les trois bases de décomposition. En fonction de si l'information du scanner est disponible, comme les spectres de la source ou la réponse du détecteur, le système d'équation non-linéaires peut être résolu soit avec une approche d'optimisation itérative, avec temps de calcul plus élevé, soit sur la base d'une calibration pour estimer indirectement les caractéristiques du scanner en interposant des plaques de matériau et d'épaisseur connus devant le faisceau de rayons X. Les prochaines étapes permettront de valider ces résultats basés sur des simulations par l'acquisition de données réelles. Concrètement, ce serait intéressant de réaliser des acquisitions DECT à différentes doses d'imagerie pour déterminer de manière expérimentale l'impact du bruit sur l'estimation de la portée des protons.

La connaissance limitée sur l'énergie moyenne d'excitation (ou potentiel d'ionisation) de composés et mélanges, comme les tissus du corps humain, introduit une incertitude quand on calcule le SPR et, en conséquence, quand on détermine la portée des protons. La loi d'additivité de Bragg est utilisée comme alternative pour déterminer les potentiels d'ionisation des tissus, mais elle est une approximation et elle est basée sur des tableaux de données moyennées des tissus humains. Nous avons mis en place une étude basée sur des simulations qui combine deux modalités d'images tomographiques, CT proton et CT bi-énergie, pour vérifier s'il était possible de déduire la distribution volumétrique moyenne d'énergie d'excitation de l'objet imagé. Nous avons obtenu des résultats prometteurs, mais la technique d'imagerie proposée n'est pas encore réalisable parce qu'il n'y a pas encore de scanners CT proton cliniques. L'intérêt clinique de cette technique d'imagerie est la possibilité de déterminer de manière expérimentale des données de référence de potentiels d'ionisation de tissus humains, qui manquent actuellement, et de dériver la variabilité inter-patients de ces potentiels d'ionisation. Les prochaines étapes serviront à déterminer la distribution d'énergie moyenne d'excitation des matériaux des fantômes et/ou des tissus d'animaux en réalisant des radiographies avec protons et radiographies bi-énergie, en utilisant des équipements déjà disponibles dans la plupart des centres de proton thérapie [Farace et al., 2016].

Actuellement, il existe plusieurs solutions technologiques pour réaliser des images bi-énergétiques. Les avantages et les limitations de chaque scanner ont été revués. Le système IR est l'un des premiers systèmes commerciaux disponibles capable de réaliser des acquisitions bi-énergie CBCT FKVS à chaque impulsion synchronisé avec une roue contenant des filtres. Ce système offre la possibilité de réaliser des images multi-énergie en insérant des projections du patient acquises à différents voltages et filtrations. Dans cette thèse, nous avons évalué la performance du système IR pour estimer le SPR de fantômes réels en réalisant des acquisitions séquentielles bi-énergie CBCT et FKVS. Pour minimiser la contamination due au diffusé au niveau de la projection, nous avons réalisé des acquisitions bi-énergie CBCT avec une fente de 3 cm à l'isocentre. Nous avons aussi étudié la possibilité d'exploiter l'information derrière les lames du collimateur pour estimer la contribution résiduelle du diffusé au signal de transmission mesuré et de réaliser des corrections du diffusé hors-ligne. Nous avons obtenu des résultats

comparables aux approches de déconvolution de correction du diffusé. On a aussi observé que l'interpolation linéaire entre projections consécutives pour implémenter des décompositions bi-énergie dans le domaine de la projection donne des images de qualité suffisante. Néanmoins, le niveau de justesse atteint pour l'instant n'est pas suffisant pour l'utilisation clinique des images du SPR reconstruites avec l'IR pour des calculs de dose de protons, même si quelques voies d'amélioration ont été identifiées. Pour commencer, l'approche de la décomposition implémentée basée sur les projections se base sur la connaissance parfaite des spectres de la source et de la réponse du détecteur, dont les modèles pourraient ne pas être correctement déterminés pour des faisceaux très durcis. En outre, les inexactitudes sur l'épaisseur des filtres ou sur la composition chimique pourraient modifier les spectres incidents et induire des erreurs sur l'estimation du SPR. La présence de bruit dans les projections et un faible rapport signal sur bruit (Signal Noise Ratio en anglais, SNR) peuvent aussi avoir une influence sur les données de sortie de la décomposition en matériaux. De futurs travaux pourraient être l'amélioration des modèles de la source et de la réponse du détecteur et leur validation par rapport aux matériaux des filtres de la roue pour mieux estimer les spectres incidents. Au lieu de faire la calibration proposée des modèles, il serait intéressant d'évaluer la justesse du SPR avec une méthode de décomposition bi-énergie basée sur d'autres mesures de calibrations, pour lesquelles nous n'aurions pas besoin de connaître les modèles de source ni détecteur car ils sont déterminés indirectement par la calibration. En outre, les méthodes de décomposition basées sur l'image CT pourraient aussi être évaluées.

Dans cette thèse, nous avons réalisé plusieurs études basées sur des données simulées plutôt que des données expérimentales. Même si un rapport bruit-dose a été établi et que du bruit de Poisson a été appliqué aux projections correspondant à une valeur de dose centrale déterminée, nous avons réalisées nos études dans un cadre idéal, exempt d'artefacts de mouvement, instabilité temporelle du nombre CT et de contamination due au rayonnement diffusé. D'autre part, il manque dans cette thèse une quantification exhaustive de l'éventuel gain de la CT bi-énergie par rapport à la CT mono-énergie avec des données expérimentales. Il faudrait enfin résoudre le problème du bruit observé quand on décompose les données de bi-énergie avec une approche basée sur les projections. La meilleure manière de comparer la performance des deux modalités d'imagerie serait de calculer des distributions de dose de protons basées sur les cartes du SPR reconstruites avec des images DECT et SECT de patients.

Le système IR a été développé pour l'IGRT et, donc, on peut acquérir des images du patient dans la position de traitement. Une application intéressante de l'imagerie bi-énergie avec le système IR, ou avec un scanner similaire, est la possibilité de réaliser la proton thérapie adaptative (Adaptive Proton Therapy en anglais, APT) en re-planifiant le traitement avec les images du SPR reconstruites à partir des acquisitions DE-CBCT enregistrées à la position de traitement. De nos jours, il y a un intérêt croissant dans l'utilisation d'images CBCT pour les calculs de dose, en photon comme en proton thérapie [Niu et al., 2010; Park et al., 2015; Landry et al., 2015]. La question de si on peut ou pas utiliser les images DE-CBCT pour calculer les distributions de dose de protons a été partiellement évoquée dans cette thèse. Tous les scanners CBCT ont été

réalisés avec une fente de 2 ou 3 cm à l'isocentre. Les travaux futurs incluront l'évaluation de la justesse du SPR avec des acquisitions DE-CBCT sans fente, c'est-à-dire à champ ouvert, mais une meilleure correction du rayonnement diffusé semblerait nécessaire dû à la forte influence sur le résultat de la décomposition en matériaux [Sossin et al., 2014]. En outre, les techniques de vérification *in-vivo* basées sur la détection des particules secondaires, comme la tomodensitometrie par emission de positrons (TEP) et l'imagerie gamma rapide (prompt-gamma), pourraient bénéficier de l'imagerie bi-énergie en position de traitement pour déterminer la composition élémentaire des tissus du corps, notamment les contenus d'oxygène, carbone, phosphore et calcium, avec une justesse plus élevée par rapport au SECT [Landry et al., 2013a].

Les méthodes de décomposition basées sur les projections consistent en deux étapes : la première, la décomposition des projections en sinogrammes de base de matériaux; la deuxième, la reconstruction CT de ces sinogrammes de base. Comme remarqué pendant la reconstruction de cartes du SPR à partir des acquisitions de données réelles des fantômes (section 4.6), cette approche en deux étapes semblerait être sensible au bruit. On a observé que la présence de bruit dans les projections CT pourrait avoir une influence sur le résultat de la décomposition du matériau car elle introduit une instabilité à l'étape de décomposition. Pour dépasser cette limitation, la possibilité de décomposer et reconstruire des données bi-énergie (ou spectrales) en une seule étape a sucité l'intérêt de la communauté. Des méthodes itératives avec régularisation sont actuellement investiguées [Schmidt et al., 2015; Sidky et al., 2016; Foygel Barber et al., 2016].

La dépendance énergétique des coefficients d'atténuation linéaires de différents tissus, laquelle permet la segmentation en matériaux par imagerie bi-énergie, pourrait être plus exploitée pour obtenir une information additionnelle du tissu en passant de l'imagerie bi-énergie à la multi-énergie. Il y a différentes approches pour réaliser cette imagerie multi-énergie avec la technologie actuelle, au niveau de la source comme au niveau du détecteur. D'un côté, l'imagerie multi-énergie au niveau de la source peut être réalisée en filtrant le spectre incident avec différents matériaux en même temps. Le système IR avec la roue contenant des filtres synchronisée avec l'émission du faisceau permet l'imagerie multi-énergie en filtrant le spectre incident avec jusqu'à quatre matériaux différents. Les projections avec différents filtres seraient acquises séquentiellement et une bonne interpolation des sinogrammes serait nécessaire pour échantillonner les projections au même angle pour implémenter schémas de décomposition basés sur les projections. D'un autre côté, au niveau du détecteur, l'imagerie multi-énergie peut être implémentée en utilisant les systèmes de comptage de photons qui sont capables d'enregistrer le spectre incident en différentes boîtes d'énergie ou fenêtres. Un inconvénient de ces systèmes est que la technologie du détecteur n'a pas encore abouti [Atak and Shikhaliev, 2015] et certains problèmes doivent être résolus avant qu'elle soit disponible en clinique, comme le partage de charge, l'empilement, la sensibilité énergetique, etc. Une fois que les deux technologies seront comparables, ce serait intéressant d'évaluer la performance des deux approches. De plus, ce serait également intéressant d'investiguer si les détecteurs à comptage de photons peuvent être utilisés en scanners CBCT pour combiner les avantages des deux

technologies, c'est-à-dire les acquisitions volumétriques résolues en énergie.

L'objectif principal de cette thèse était d'utiliser l'imagerie bi-énergie pour réduire les marges de traitement en proton thérapie. Dans la pratique clinique, des marges latérales et de portée sont ajoutées au CTV pour chaque faisceau dans le TPS. On s'est principalement intéressé à l'étude des approches pour réaliser la décomposition bi-énergie dans le but de réduire l'incertitude associée à la conversion des HU en valeurs de SPR, normalement réalisée avec une image SECT, laquelle a 1% d'erreur associée. Quand on considère uniquement les artefacts de durcissement du faisceau, cela contribue jusqu'à un 1.1% et 1.8% de la portée des protons dans l'eau pour les tissus mous et l'os respectivement [Schaffner and Pedroni, 1998; Paganetti, 2012]. Néanmoins, il y a d'autres incertitudes liées au scanner, comme la stabilité temporelle des nombres CT, c'est-à-dire les variations jour après jour, et les artefacts dus au rayonnement diffusé, particulièrement avec les scanners CBCT, qui contribuent par ailleurs à l'incertitude de la portée. Malgré ces valeurs d'erreur de la portée, des marges plus conservatrices comme 3.5% +1 mm qui peuvent varier d'une institution à une autre- sont actuellement utilisées à la place. Les marges sont prises comme un concept géométrique comme dans le milieu des photons, dans lequel ces marges sont principalement utilisées pour tenir compte des incertitudes latérales [Both, 2012]. La prochaine étape est de planifier directement les traitements sur la base d'images du SPR reconstruites à partir d'images DECT, combinée à des marges personnalisées et spécifiques aux faisceaux [Park et al., 2012]. Cela pourrait ouvrir une nouvelle ligne d'étude et devrait donner davantage de confiance aux cliniciens et physiciens médicaux pour réduire les marges en proton thérapie, pour réduire les volumes de traitement et ainsi diminuer la probabilité de complications et effets tardifs.

Bibliography

A. Akbarzadeh, M. R. Ay, H. Ghadiri, S. Sarkar, and H. Zaidi. Measurement of scattered radiation in a volumetric 64-slice CT scanner using three experimental techniques. *Phys. Med. Biol.*, 55(8):2269–80, 2010. Cited on pages 68 and 69.

P. Alaei and E. Spezi. Imaging dose from cone beam computed tomography in radiation therapy. *Phys. Medica*, 31(7):647–658, 2015. Cited on page 52.

R. E. Alvarez and A. Macovski. Energy-selective reconstructions in X-ray computerized tomography. *Phys. Med. Biol.*, 21(5):733–744, 1976. Cited on pages 35, 44, 45, 47, 81, 90, 91, 100, 107, 127, and 150.

U. Amaldi and G. Kraft. Radiotherapy with beams of carbon ions. *Reports Prog. Phys.*, 68(8):1861–1882, 2005. Cited on pages 5 and 17.

P. Andreo. On the clinical spatial resolution achievable with protons and heavier charged particle radiotherapy. *Phys. Med. Biol.*, 54, 2009. Cited on pages 16, 30, 147, 148, and 155.

N. Arbor, D. Dauvergne, G. Dedes, J. M. Létang, K. Parodi, C. T. Quiñones, E. Testa, and S. Rit. Monte Carlo Comparison of X-ray and Proton CT for Range Calculations of Proton Therapy Beams. *Phys. Med. Biol.*, 60:7585, 2015. Cited on pages XV, 27, 79, 100, 136, 149, and 172.

W. Assmann, S. Kellnberger, S. Reinhardt, S. Lehrack, A. Edlich, P. G. Thirolf, M. Moser, G. Dollinger, M. Omar, V. Ntziachristos, and K. Parodi. Ionoacoustic characterization of the proton Bragg peak with submillimeter accuracy. *Med. Phys.*, 42(2):567–74, jan 2015. Cited on page 33.

H. Atak and P. M. Shikhaliev. Dual energy CT with photon counting and dual source systems: comparative evaluation. *Phys. Med. Biol.*, 60(23):8949–8975, 2015. Cited on pages 161 and 181.

F. Bamberg, A. Dierks, K. Nikolaou, M. Reiser, C. Becker, and T. Johnson. Metal artifact reduction by dual energy computed tomography using monoenergetic extrapolation. *Eur. Radiol.*, 21(7):1424–1429, 2011. Cited on page 42.

D. Barkas and W. H. Evans. *Nuclear research emulsions*. 1963. Cited on page 9.

M. Bazalova and F. Verhaegen. Tissue segmentation issues in Monte Carlo treatment planning for proton radiotherapy. In *48th PTCOG Conf.*, 2009. Cited on page 42.

M. Bazalova, J.-F. Carrier, L. Beaulieu, and F. Verhaegen. Tissue segmentation in Monte Carlo treatment planning: a simulation study using dual-energy CT images. *Radiother. Oncol.*, 86(1):93–98, 2008a. Cited on page 42.

M. Bazalova, J.-F. Carrier, L. Beaulieu, and F. Verhaegen. Dual-energy CT-based material extraction for tissue segmentation in Monte Carlo dose calculations. *Phys. Med. Biol.*, 53(9):2439–2456, 2008b. Cited on pages 42, 43, 76, 77, 81, 83, and 100.

M. Bazalova, H. Zhou, P. J. Keall, and E. E. Graves. Kilovoltage beam Monte Carlo dose calculations in submillimeter voxels for small animal radiotherapy. *Med. Phys.*, 36(11):4991–4999, 2009. Cited on page 32.

L. Beaulieu, M. Bazalova, C. Furstoss, and F. Verhaegen. SU-FF-T-408: Tissue Inhomogeneities in Monte Carlo Treatment Planning for Proton Therapy. *Med. Phys.*, 36 (6):2616–2616, jun 2009. Cited on pages 32 and 42.

M. J. Berger, J. S. Coursey, M. A. Zucker, and J. Chang. ESTAR, ASTAR, PSTAR : Stopping-Power and Range Tables for Electrons, Protons, and Helium Ions. *NIST, http://www.nist.gov/pml/data/star/index.cfm*, 2011. Cited on page 129.

M. J. Berger, J. H. Hubbell, S. M. Seltzer, J. Chang, J. S. Coursey, R. Sukumar, et al. *XCOM: Photon Cross Section Database* (version 1.5), 2010. National Institute of Standards and Technology, Gaithersburg, MD. Cited on page 93.

M. Bertram, J. Wiegert, and G. Rose. Scatter correction for cone-beam computed tomography using simulated object models. *Proc. SPIE*, 6142:61421C, 2006. Cited on page 67.

A. Besemer, H. Paganetti, and B. Bednarz. The clinical impact of uncertainties in the mean excitation energy of human tissues during proton therapy. *Phys. Med. Biol.*, 58 (4):887–902, 2013. Cited on pages 147, 148, 149, and 155.

H. Bethe. Zur Theorie des Durchgangs schneller Korpuskularstrahlen durch Materie. *Ann. Phys.*, 397(3):325–400, 1930. Cited on pages 9 and 153.

M. Bethesda. Report N. 46: Photon, Electron, Proton and Neutron Interaction Data for Body Tissues. Technical report, 1992. Cited on page 128.

N. Bhatia, D. Tisseur, S. Valton, and J. M. Létang. Separable scatter model of the detector and object contributions using continuously thickness-adapted kernels in CBCT. *J. Xray. Sci. Technol.*, 24(5):723–732, 2016. Cited on page 67.

H. Bichsel. *Passage of charged particles through matter*. American Institute of Physics Handbook ed E D Gray, New York: McGraw-Hill, 1972. Cited on pages 27 and 154.

H. Bichsel and T. Hiraoka. Energy loss of 70 MeV protons in elements. *Nucl. Inst. Methods Phys. Res. B*, 66(3):345–351, apr 1992. Cited on page 147.

H. Bichsel, T. Hiraoka, and K. Omata. Aspects of fast-ion dosimetry. *Radiat. Res.*, 153 (2):208–19, feb 2000. Cited on page 147.

F. Bloch. Bremsvermögen von Atomen mit mehreren Elektronen. *Zeitschrift für Phys.*, 81(5-6):363–376, may 1933. Cited on pages 9, 15, and 153.

S. Both. Proton Treatment Planning : From Physics to Clinical Reality. In *AAPM Spring Clin. Meet.*, 2012. Cited on pages 28, 162, and 182.

A. E. Bourque, J.-F. Carrier, and H. Bouchard. A stoichiometric calibration method for dual energy computed tomography. *Phys. Med. Biol.*, 59(8):2059–88, 2014. Cited on pages XVIII, 44, 74, 76, 77, 78, 80, 81, 82, 83, 89, and 90.

H. Braun, Y. Kyriakou, M. Kachelrieß, and W. A. Kalender. The influence of the heel effect in cone-beam computed tomography : artifacts in standard and novel. *Phys. Med. Biol.*, 55:6005–6021, 2010. Cited on page 60.

B. Brendel, F. Bergner, K. Brown, and T. Koehler. Penalized likelihood decomposition for dual layer spectral CT. *Proc. 4th Intl. Mtg. image Form. X-ray CT*, pages 41–44, 2016. Cited on page 100.

R. A. Brooks. A quantitative theory of the Hounsfield unit and its application to dual energy scanning. *J. Comput. Assist. Tomogr.*, 1(4):487–493, 1977. Cited on pages 36, 43, 75, and 76.

R. A. Brooks and G. Di Chiro. Beam hardening in x-ray reconstructive tomography. *Phys. Med. Biol.*, 21(3):390–398, may 1976. Cited on pages 43 and 95.

C. E. Cann, G. Gamsu, F. A. Birnberg, and W. R. Webb. Quantification of calcium in solitary pulmonary nodules using single- and dual-energy CT. *Radiology*, 145(2): 493–496, nov 1982. Cited on page 36.

H. N. Cardinal and A. Fenster. An accurate method for direct dual-energy calibration and decomposition. *Med. Phys.*, 17(3):327–341, 1990. Cited on page 48.

G. T. Y. Chen, R. P. Singh, J. R. Castro, J. T. Lyman, and J. M. Quivey. Treatment planning for heavy ion radiotherapy. *Int. J. Radiat. Oncol. Biol. Phys.*, 5(10):1809–1819, oct 1979. Cited on page 26.

G. D. Chiro, R. A. Brooks, R. M. Kessler, G. S. Johnston, A. E. Jones, J. R. Herdt, and W. T. Sheridan. Tissue signatures with dual-energy computed tomography. *Radiology*, 131(2):521–523, may 1979. Cited on page 36.

K.-S. Chuang and H. K. Huang. Comparison of four dual energy image decomposition methods. *Phys. Med. Biol.*, 33(4):455, 1988. Cited on pages 36, 48, 100, 128, 138, and 140.

A. M. Cormack. Representation of a function by its line integrals, with some radiological applications. *J. Appl. Phys.*, 34(9):2722–2727, sep 1963. Cited on page 32.

G. X. Ding, D. M. Duggan, and C. W. Coffey. Characteristics of kilovoltage x-ray beams used for cone-beam computed tomography in radiation therapy. *Phys. Med. Biol.*, 52 (6):1595–1615, 2007. Cited on page 52.

G. X. Ding, P. Munro, J. Pawlowski, A. Malcolm, and C. W. Coffey. Reducing radiation exposure to patients from kV-CBCT imaging. *Radiother. Oncol.*, 97(3):585–592, 2010. Cited on page 52.

M. Dingfelder, D. Hantke, M. Inokuti, and H. G. Paretzke. Electron inelastic-scattering cross sections in liquid water. *Radiat. Phys. Chem.*, 53(1):1–18, jan 1999. Cited on page 147.

P. J. Doolan, C.-A. Collins-Fekete, M. F. Dias, T. A. Ruggieri, D. D'Souza, and J. Seco. Inter-comparison of relative stopping power estimation models for proton therapy. *Phys. Med. Biol.*, 61(22):8085–8104, 2016. Cited on pages 27, 29, 153, and 154.

P. Downes, R. Jarvis, E. Radu, I. Kawrakow, and E. Spezi. Monte Carlo simulation and patient dosimetry for a kilovoltage cone-beam CT unit Monte Carlo simulation and patient dosimetry for a kilovoltage cone-beam CT unit. *Med Phys*, 36(9):4156–4167, 2009. Cited on page 52.

P. B. Dunscombe, D. E. Katz, and A. J. Stacey. Some practical aspects of dual-energy CT scanning. *Br. J. Radiol.*, 57(673):82–7, jan 1984. Cited on page 36.

S. España and H. Paganetti. The impact of uncertainties in the CT conversion algorithm when predicting proton beam ranges in patients from dose and PET-activity distributions. *Phys. Med. Biol.*, 55(24):7557–7571, 2010. Cited on pages 148 and 155.

U. Fano. Penetrations of protons, alpha particles, and mesons. In *Stud. Penetration Charg. Part. Matter*, page 1133:287. 1964. Cited on page 15.

P. Farace. Comment on "Experimental verification of ion stopping power prediction from dual energy CT data in tissue surrogates". *Phys. Med. Biol.*, 59(22):7081–7084, nov 2014. Cited on pages 79, 89, 91, and 127.

P. Farace, R. Righetto, and A. Meijers. Pencil beam proton radiography using a multilayer ionization chamber. *Phys. Med. Biol.*, 61(11):4078–87, jun 2016. Cited on pages 155, 159, and 179.

M. K. Fix, D. Frei, W. Volken, E. J. Born, D. M. Aebersold, and P. Manser. Macro Monte Carlo for dose calculation of proton beams. *Phys. Med. Biol.*, 58(7):2027–44, 2013. Cited on pages XIV and 13.

T. G. Flohr, C. H. McCollough, H. Bruder, M. Petersilka, K. Gruber, C. Süß, M. Grasruck, K. Stierstorfer, B. Krauss, R. Raupach, A. N. Primak, A. Küttner, S. Achenbach, C. Becker, A. Kopp, and B. M. Ohnesorge. First performance evaluation of a dual-source CT (DSCT) system. *Eur. Radiol.*, 16(2):256–268, 2006. Cited on pages XVI, 36, 37, and 38.

R. Foygel Barber, E. Y. Sidky, T. Gilat Schmidt, and X. Pan. An algorithm for constrained one-step inversion of spectral CT data. *Phys. Med. Biol.*, 61(10):3784–3818, 2016. Cited on pages 48, 161, and 181.

M. Goitein. Applications of computed tomography in radiotherapy treatment planning. *Prog. Med. Radiat. Phys.*, I:195–293, 1982. Cited on page 29.

M. Goitein. Calculation of the uncertainty in the dose delivered during radiation therapy. *Med. Phys.*, 12(5):608–612, sep 1985. Cited on page 30.

B. Gottschalk. Passive Beam Spreading in Proton Radiation Therapy. Technical report, Harvard High Energy Physics Laboratory, 2004. Cited on page 11.

P. V. Granton, S. I. Pollmann, N. L. Ford, M. Drangova, and D. W. Holdsworth. Implementation of dual- and triple-energy cone-beam micro-CT for postreconstruction material decomposition. *Med. Phys.*, 35(11):5030–5042, 2008. Cited on page 122.

P. V. Granton, M. Podesta, G. Landry, S. Nijsten, G. Bootsma, and F. Verhaegen. A combined dose calculation and verification method for a small animal precision irradiator based on onboard imaging. *Med. Phys.*, 39(7):4155–4166, 2012. Cited on page 52.

L. Grevillot. *Monte Carlo simulation of active scanning proton therapy system with Gate/ Geant4: Towards a better patient dose quality assurance.* PhD thesis, INSA de Lyon, 2011. Cited on page 29.

D. Han, J. V. Siebers, and J. F. Williamson. A linear, separable two-parameter model for dual energy CT imaging of proton stopping power computation. *Med. Phys.*, 43 (1):600–612, 2016. Cited on pages 44, 74, 79, 80, 81, 89, and 99.

D. C. Hansen, J. Seco, T. S. Sørensen, J. B. B. Petersen, J. E. Wildberger, F. Verhaegen, and G. Landry. A simulation study on proton computed tomography (CT) stopping power accuracy using dual energy CT scans as benchmark. *Acta Oncol. (Madr).*, 54 (July):1638–1642, 2015. Cited on pages 74, 79, and 99.

D. J. Hawkes, D. F. Jackson, and R. P. Parker. Tissue analysis by dual-energy computed tomography. *Br. J. Radiol.*, 59(702):537–542, jun 1986. Cited on page 36.

B. J. Heismann, B. Schmidt, and T. Flohr. *Spectral Computed Tomography Development*. SPIE PRESS, Bellingham, Washington, USA, 2012. Cited on pages XVI, 32, 36, 37, 38, 39, 41, 45, 47, and 138.

A. Hemmingsson, B. Jung, and C. Ytterbergh. Dual energy computed tomography: simulated monoenergetic and material-selective imaging. *J Comput Assist Tomogr*, 10(3):490–499, 1986. Cited on page 36.

P. Henriquet, E. Testa, M. Chevallier, D. Dauvergne, G. Dedes, N. Freud, J. Krimmer, J. M. Létang, C. Ray, M.-H. Richard, and F. Sauli. Interaction vertex imaging (IVI) for carbon ion therapy monitoring: a feasibility study. *Phys. Med. Biol.*, 57(14):4655–69, jul 2012. Cited on page 33.

T. Henzler, C. Fink, S. O. Schoenberg, and U. J. Schoepf. Dual-energy CT: radiation dose aspects., 2012. Cited on page 121.

G. N. Hounsfield. Computerized transverse axial scanning (tomography): I. Description of system. *Br. J. Radiol.*, 46(552):1016–1022, 1973. Cited on pages 35 and 176.

R.-F. Hsu. Mean excitation energy of the elements for proton penetration in matter. *J. Norm. Univ.*, 24:318–352, 1979. Cited on pages 15 and 16.

J. H. Hubbell and S. M. Seltzer. Tables of x-ray mass attenuation coefficients and mass energy-absorption coefficients (version 1.4), 2004. National Institute of Standards and Technology, Gaithersburg, MD. Cited on pages XV, 35, 53, 76, 125, 130, and 166.

N. Hudobivnik, F. Schwarz, T. Johnson, L. Agolli, G. Dedes, T. Tessonnier, F. Verhaegen, C. Thieke, C. Belka, W. H. Sommer, K. Parodi, and G. Landry. Comparison of proton therapy treatment planning for head tumors with a pencil beam algorithm on dual and single energy CT images. *Med Phys*, 43(1):495–504, 2016. Cited on page 116.

B. F. B. Huisman, J. M. Létang, É. Testa, and D. Sarrut. Accelerated prompt gamma estimation for clinical proton therapy simulations. *Phys. Med. Biol.*, 61(21):7725–7743, nov 2016. Cited on page 33.

N. Hünemohr, B. Krauss, J. Dinkel, C. Gillmann, B. Ackermann, O. Jäkel, and S. Greilich. Ion range estimation by using dual energy computed tomography. *Z. Med. Phys.*, 23(4):300–313, 2013. Cited on pages 74 and 77.

N. Hünemohr, B. Krauss, C. Tremmel, B. Ackermann, O. Jäkel, and S. Greilich. Experimental verification of ion stopping power prediction from dual energy CT data in tissue surrogates. *Phys. Med. Biol.*, 59(1):83–96, 2014a. Cited on pages 44, 74, 77, 81, 116, and 137.

N. Hünemohr, N. Niebuhr, and S. Greilich. Reply to Comment on Experimental verification of ion stopping power prediction from dual energy CT data in tissue surrogates'. *Phys. Med. Biol.*, 59(22):7085–7087, nov 2014b. Cited on page 89.

N. Hünemohr, H. Paganetti, S. Greilich, O. Jäkel, and J. Seco. Tissue decomposition from dual energy CT data for MC based dose calculation in particle therapy. *Med. Phys.*, 41(6):061714, 2014c. Cited on pages 74, 76, 77, and 78.

ICRP. Adult Reference Computational Phantoms. ICRP Publi(Ann. ICRP 39 (2)), 2009. Cited on pages 26, 80, 85, 90, 122, 138, 148, and 165.

ICRU. *ICRU Report 37, Stopping Powers for Electrons and Positrons.* 1984. Cited on pages 16, 30, 147, 148, 154, and 155.

ICRU. *ICRU Report 44 - Tissue Substitutes in Radiation Dosimetry and Measurement.* 1989. Cited on pages XVII, 77, 78, 148, and 155.

ICRU. Photon, electron, proton and neutron interaction data for body tissues. *ICRU Rep. No. 46*, 1992. Cited on pages XVIII, 14, 26, 79, 80, 81, 82, 93, 148, and 155.

ICRU. *ICRU Report 49, Stopping Powers and Ranges for Protons and Alpha Particles.* American Association of Physicists in Medicine, 1993. Cited on pages XV, 9, 15, 16, 27, 30, 78, 80, 94, 147, 148, 151, and 154.

ICRU. *ICRU Report 62, Prescribing, Recording and Reporting Photon Beam Therapy (Supplement to ICRU Report 50).* 1999. Cited on page 19.

ICRU. *ICRU Report 71, Prescribing, Recording, and Reporting Electron Beam Therapy.* 2004. Cited on pages XV and 20.

ICRU. *ICRU Report 73, Stopping of ions heavier than helium*, volume 5. 2005. Cited on pages 30 and 147.

ICRU. *ICRU Report 78, Prescribing, Recording and Reporting Proton Beam Therapy*, volume 7. 2007. Cited on pages XV, 28, and 31.

D. J. Indelicato, T. Merchant, N. Laperriere, Y. Lassen, S. Vennarini, S. Wolden, W. Hartsell, M. Pankuch, P. Brandal, C. C. K. Law, R. Taylor, S. Laskar, M. F. Okcu, E. Bouffet, H. Mandeville, T. Björk-Eriksson, K. Nilsson, H. Nyström, L. S. Constine, M. Story, B. Timmermann, K. Roberts, and R. D. Kortmann. Consensus Report From the Stockholm Pediatric Proton Therapy Conference. *Int. J. Radiat. Oncol. Biol. Phys.*, 96(2):387–392, 2016. Cited on page 17.

D. F. Jackson and D. J. Hawkes. X-ray attenuation coefficients of elements and mixtures. *Phys. Reports - Rev. Sect. Phys. Lett.*, 70(3):169–233, 1981. Cited on pages 21, 23, 44, 77, 79, and 99.

O. Jäkel. Heavy ion radiotherapy. In *Schlegel W., Bortfeld T. Grosu A.L. (Eds), New Technol. Radiat. Oncol.*, pages 365–378. Springer, Heidelberg, 2006. Cited on pages 18 and 29.

O. Jäkel, D. Schulz-Ertner, C. P. Karger, A. Nikoghosyan, and J. Debus. Heavy ion therapy: status and perspectives. *Technol. Cancer Res. Treat.*, 2(5):377–387, oct 2003. Cited on page 18.

S. Jan, G. Santin, D. Strul, S. Staelens, K. Assié, and D. Autret. GATE : a simulation toolkit for PET and SPECT. *Phys. Med. Biol.*, 49:4543–4561, 2004. Cited on pages 56, 94, 123, 150, 165, and 172.

J. F. Janni. Energy loss, range, path length, time-of-flight, straggling, multiple scattering, and nuclear interaction probability. In two parts. Part 1. For 63 compounds. Part 2. For elements $1 < Z < 92$. *At. Data Nucl. Data Tables*, 27(2-3):147–339, mar 1982. Cited on pages 27 and 154.

H. E. Johns and J. R. Cunningham. *The physics of radiology*. Charles C. Thomas, 4th edition, 1983. Cited on page 76.

W. A. Kalender, W. H. Perman, J. R. Vetter, and E. Klotz. Evaluation of a prototype dual-energy computed tomographic apparatus. I. Phantom studies. *Med. Phys.*, 13 (3):334–339, 1986. Cited on page 38.

W. A. Kalender, E. Klotz, and C. Suess. Vertebral bone mineral analysis: an integrated approach with CT. *Radiology*, 164(2):419–423, aug 1987. Cited on page 36.

N. Kanematsu, T. Inaniwa, and Y. Koba. Relationship between electron density and effective densities of body tissues for stopping, scattering, and nuclear interactions of proton and ion beams. *Med. Phys.*, 39(2):1016–1020, 2012. Cited on pages XVIII, 79, 81, 82, 89, 91, 92, 94, 99, 107, 127, 128, and 155.

M. Karçaaltncaba and A. Akta. Dual-energy CT revisited with multidetector CT: review of principles and clinical applications. *Diagn. Interv. Radiol.*, 17(3):181–194, 2011. Cited on page 41.

F. Kelcz, P. M. Joseph, and S. K. Hilal. Noise considerations in dual energy CT scanning. *Med. Phys.*, 6(5):418–425, 1979. Cited on page 36.

P. Keuschnigg, D. Kellner, K. Fritscher, A. Zechner, U. Mayer, P. Huber, F. Sedlmayer, H. Deutschmann, and P. Steininger. Nine-degrees-of-freedom flexmap for a cone-beam computed tomography imaging device with independently movable source and detector. *Med. Phys.*, 44(1):132–142, jan 2017. Cited on page 51.

F. M. Khan. *The physics of radiation therapy*. Lippincott Williams & Wilkins, 3rd edition, 2003. Cited on page 75.

A.-C. Knopf and A. Lomax. In vivo proton range verification: a review. *Phys. Med. Biol.*, 58(58):131–160, 2013. Cited on pages 12, 30, 32, and 33.

M. Krämer, O. Jäkel, T. Haberer, G. Kraft, D. Schardt, and U. Weber. Treatment planning for heavy-ion radiotherapy: physical beam model and dose optimization. *Phys. Med. Biol.*, 45(11):3299–3317, nov 2000. Cited on page 147.

M. Krämer, E. Scifoni, C. Schuy, M. Rovituso, W. Tinganelli, A. Maier, R. Kaderka, W. Kraft-Weyrather, S. Brons, T. Tessonnier, K. Parodi, and M. Durante. Helium ions for radiotherapy? Physical and biological verifications of a novel treatment modality. *Med. Phys.*, 43(4):1995–2004, apr 2016. Cited on page 18.

Y. Kyriakou and W. A. Kalender. Efficiency of antiscatter grids for flat-detector CT. *Phys. Med. Biol.*, 52(20):6275–6293, oct 2007. Cited on page 67.

J. J. W. Lagendijk, B. W. Raaymakers, C. A. T. V. den Berg, M. A. Moerland, M. E. Philippens, and M. van Vulpen. MR guidance in radiotherapy. *Phys. Med. Biol.*, 59 (21):R349, 2014. Cited on page 32.

G. Landry, B. Reniers, P. V. Granton, B. Van Rooijen, L. Beaulieu, J. E. Wildberger, and F. Verhaegen. Extracting atomic numbers and electron densities from a dual source dual energy CT scanner: Experiments and a simulation model. *Radiother. Oncol.*, 100(3):375–379, 2011. Cited on pages 76 and 77.

G. Landry, K. Parodi, J. E. Wildberger, and F. Verhaegen. Deriving concentrations of oxygen and carbon in human tissues using single- and dual-energy CT for ion therapy applications. *Phys. Med. Biol.*, 58(15):5029–48, 2013a. Cited on pages 148, 161, and 181.

G. Landry, J. Seco, M. Gaudreault, and F. Verhaegen. Deriving effective atomic numbers from DECT based on a parameterization of the ratio of high and low linear attenuation coefficients. *Phys. Med. Biol.*, 58(19):6851–6866, 2013b. Cited on pages 44, 74, and 77.

G. Landry, R. Nijhuis, G. Dedes, J. Handrack, C. Thieke, G. Janssens, J. Orban de Xivry, M. Reiner, F. Kamp, J. J. Wilkens, C. Paganelli, M. Riboldi, G. Baroni, U. Ganswindt, C. Belka, and K. Parodi. Investigating CT to CBCT image registration for head and neck proton therapy as a tool for daily dose recalculation. *Med. Phys.*, 42(3):1354–66, 2015. Cited on pages 160 and 180.

L. A. Lehmann, R. E. Alvarez, A. Macovski, W. R. Brody, N. J. Pelc, S. J. Riederer, and a. L. Hall. Generalized image combinations in dual KVP digital radiography. *Med. Phys.*, 8(5):659–667, 1981. Cited on pages 36, 48, 128, and 140.

W. R. Leo. *Techniques for Nuclear and Particle Physics Experiments - A How-to Approach*. Springer-Verlag Berlin Heidelberg GmbH, second edition, 1994. Cited on pages 9 and 11.

J.-M. Létang, N. Freud, and G. Peix. Signal-to-noise ratio criterion for the optimization of dual-energy acquisition using virtual x-ray imaging: application to glass wool. *J. Electron. Imaging*, 13(3):436, 2004. Cited on pages 41, 128, 140, and 141.

W. Levin, H. Kooy, J. Loeffler, and T. Delaney. Proton beam therapy. *Br. J. Cancer*, 93(8):849–854, oct 2005. Cited on pages XIV, 10, and 17.

H. Li, W. Giles, L. Ren, J. Bowsher, and F.-F. Yin. Implementation of dual-energy technique for virtual monochromatic and linearly mixed CBCTs. *Med. Phys.*, 39(10): 6056, 2012. Cited on pages 42, 47, and 80.

P. Linstrom and W. Mallard. *NIST Standard Reference Database Number 69*, (retrieved December 6, 2016). National Institute of Standards and Technology, Gaithersburg, MD. Cited on pages 91 and 138.

A. J. Lomax. Charged particle therapy: the physics of interaction. *Cancer J.*, 15(4): 285–91, jul 2009. Cited on page 12.

Y. Long and J. A. Fessler. Multi-material decomposition using statistical image reconstruction for spectral CT. *IEEE Trans. Med. Imaging*, 33(8):1614–1626, 2014. Cited on page 46.

C. Maaß, M. Baer, and M. Kachelrieß. Image-based dual energy CT using optimized precorrection functions: A practical new approach to material decomposition in the image domain. *Med. Phys.*, 36(8):3818–3829, 2009. Cited on page 43.

A. Mairani, T. T. Böhlen, A. Schiavi, T. Tessonnier, S. Molinelli, S. Brons, G. Battistoni, K. Parodi, and V. Patera. A Monte Carlo-based treatment planning tool for proton therapy. *Phys. Med. Biol.*, 58(8):2471–90, 2013. Cited on page 30.

W. Marshall, E. Hall, A. Doost-Hoseini, R. Alvarez, A. Macovski, and D. Cassel. An implementation of dual energy CT scanning. *J. Comput. Assist. Tomogr.*, 8(4):745–749, aug 1984. Cited on page 36.

W. V. Mayneord. The significance of the roentgen. *Acta Union Int. Against Cancer*, 2: 271282, 1937. Cited on page 75.

C. H. McCollough, S. Leng, L. Yu, and J. G. Fletcher. Dual- and Multi-Energy CT: Principles, Technical Approaches, and Clinical Applications. *Radiology*, 276(3):637–653, 2015. Cited on pages XVI, 37, 38, 39, 40, 41, and 42.

P. R. S. Mendonça. A flexible method for Mutlti-Material Decomposition of Dual-Energy CT Images. In *IEEE Trans. Med. Imaging*, volume 33, pages 1–20, 2014. Cited on pages 44 and 46.

C. Möhler, P. Wohlfahrt, C. Richter, and S. Greilich. Range prediction for tissue mixtures based on dual-energy CT. *Phys. Med. Biol.*, 61:N268–N275, 2016. Cited on pages 74, 78, 80, 81, and 89.

National Council on Radiation Protection and Measurements. Medical X-ray, electron beam, and gamma-ray protection for energies up to 50 MeV : (equipment design, performance, and use) : recommendations of the National Council on Radiation Protection and Measurements. *NCRP Rep.*, (no 102), 1989. Cited on page 125.

J. A. Nelder and R. Mead. A Simplex Method for Function Minimization. *Comput. J.*, 7(4):308–313, jan 1965. Cited on pages 47, 92, and 140.

W. D. Newhauser and R. Zhang. The physics of proton therapy. *Phys. Med. Biol.*, 60 (8):R155, 2015. Cited on pages XIV, 8, 12, 14, and 17.

T. Niu, M. Sun, J. Star-Lack, H. Gao, Q. Fan, and L. Zhu. Shading correction for on-board cone-beam CT in radiation therapy using planning MDCT images. *Med. Phys.*, 37(10):5395–5406, 2010. Cited on pages 160 and 180.

J. Ödén, J. Zimmerman, R. Bujila, P. Nowik, and G. Poludniowski. Technical Note: On the calculation of stopping-power ratio for stoichiometric calibration in proton therapy. *Med. Phys.*, 42(9):5252–5257, 2015. Cited on pages 27 and 153.

K. C. Oeffinger, A. C. Mertens, C. A. Sklar, T. Kawashima, M. M. Hudson, A. T. Meadows, D. L. Friedman, N. Marina, W. Hobbie, N. S. Kadan-Lottick, C. L. Schwartz, W. Leisenring, and L. L. Robison. Chronic Health Conditions in Adult Survivors of Childhood Cancer. *N. Engl. J. Med.*, 355:1572–82, 2006. Cited on page 17.

B. Ohnesorge, T. Flohr, and K. Klingenbeck-Regn. Efficient object scatter correction algorithm for third and fourth generation CT scanners. *Eur. Radiol.*, 9:563–569, 1999. Cited on page 67.

T. Okada, T. Kamada, H. Tsuji, J.-E. Mizoe, M. Baba, S. Kato, S. Yamada, S. Sugahara, S. Yasuda, N. Yamamoto, R. Imai, A. Hasegawa, H. Imada, H. Kiyohara, K. Jingu, M. Shinoto, and H. Tsujii. Carbon Ion Radiotherapy: Clinical Experiences at National Institute of Radiological Science (NIRS). *J. Radiat. Res.*, 51(4):355–364, 2010. Cited on page 6.

H. Paganetti. Dose to water versus dose to medium in proton beam therapy. *Phys. Med. Biol*, 54:4399–4421, 2009. Cited on pages 21, 26, 148, 149, and 172.

H. Paganetti. Proton therapy: History and rationale. In H. Paganetti, editor, *Prot. Ther. Physics, Ser. Med. Phys. Biomed. Eng.*, chapter 1, pages 1–19. Taylor & Francis, 2011. Cited on pages 6 and 17.

H. Paganetti. Range uncertainties in proton therapy and the role of Monte Carlo simulations. *Phys. Med. Biol.*, 57(11):R99–R117, 2012. Cited on pages 12, 29, 30, 136, 147, 148, 161, and 182.

H. Paganetti and T. Bortfeld. *Proton beam radiotherapy - The state of the art.* Number October. 2005. Cited on page 17.

P. C. Park, X. R. Zhu, A. K. Lee, N. Sahoo, A. D. Melancon, L. Zhang, and L. Dong. A beam-specific planning target volume (PTV) design for proton therapy to account for setup and range uncertainties. *Int. J. Radiat. Oncol. Biol. Phys.*, 82(2):1–15, 2012. Cited on pages 30, 162, and 182.

P. C. Park, J. P. Cheung, X. R. Zhu, A. K. Lee, N. Sahoo, S. L. Tucker, W. Liu, H. Li, R. Mohan, L. E. Court, and L. Dong. Statistical assessment of proton treatment plans under setup and range uncertainties. *Int. J. Radiat. Oncol. Biol. Phys.*, 86(5): 1007–1013, 2013. Cited on page 30.

Y.-K. Park, G. C. Sharp, J. Phillips, and B. A. Winey. Proton dose calculation on scatter-corrected CBCT image: Feasibility study for adaptive proton therapy. *Med. Phys.*, 42(8):4449–4459, 2015. Cited on pages 160 and 180.

E. Pessis, J. M. Sverzut, R. Campagna, H. Guerini, A. Feydy, and J. L. Drapé. Reduction of Metal Artifact with Dual-Energy CT: Virtual Monospectral Imaging with Fast Kilovoltage Switching and Metal Artifact Reduction Software. *Semin. Musculoskelet. Radiol.*, 19(5):446–455, dec 2015. Cited on page 42.

G. Poludniowski, P. M. Evans, V. N. Hansen, and S. Webb. An efficient Monte Carlo-based algorithm for scatter correction in keV cone-beam CT. *Phys. Med. Biol.*, 54 (12):3847–3864, 2009a. Cited on page 52.

G. Poludniowski, G. Landry, F. DeBlois, P. M. Evans, and F. Verhaegen. SpekCalc: a program to calculate photon spectra from tungsten anode x-ray tubes. *Phys. Med. Biol.*, 54(19):N433–N438, 2009b. Cited on pages 55 and 125.

G. Poludniowski, P. M. Evans, A. Kavanagh, and S. Webb. Removal and effects of scatter-glare in cone-beam CT with an amorphous-silicon flat-panel detector. *Phys. Med. Biol.*, 56(6):1837–1851, 2011. Cited on pages 54 and 67.

G. G. Poludniowski. Calculation of x-ray spectra emerging from an x-ray tube. Part II. X-ray production and filtration in x-ray targets. *Med. Phys.*, 34(6):2175–2186, 2007. Cited on page 125.

G. G. Poludniowski and P. M. Evans. Calculation of x-ray spectra emerging from an x-ray tube. Part I. electron penetration characteristics in x-ray targets. *Med. Phys.*, 34(6):2164–2174, 2007. Cited on page 125.

A. N. Primak, J. C. Ramirez Giraldo, X. Liu, L. Yu, and C. H. McCollough. Improved dual-energy material discrimination for dual-source CT by means of additional spectral filtration. *Med. Phys.*, 36(4):1359–1369, 2009. Cited on pages 122, 125, and 135.

A. N. Primak, J. Carlos, R. Giraldo, C. D. Eusemann, B. Schmidt, B. Kantor, J. G. Fletcher, and H. Cynthia. Dual-source dual-energy CT with additional tin filtration: Dose and image quality evaluation in phantoms and in-vivo. *AJR Am J Roentgenol*, 195(5):1164–1174, 2010. Cited on page 126.

C. T. Quiñones. *Proton Computed Tomography*. PhD thesis, INSA de Lyon, 2016. Cited on pages XIV, XXI, 7, 150, 151, and 155.

C. T. Quiñones, J. M. Létang, and S. Rit. Filtered back-projection reconstruction for attenuation proton CT along most likely paths. *Phys. Med. Biol.*, 61(9):3258–3278, 2016. Cited on page 32.

L. I. Ramos Garcia, J. F. Pérez Azorin, and J. F. Almansa. A new method to measure electron density and effective atomic number using dual-energy CT images. *Phys. Med. Biol.*, 61(1):265–279, 2016. Cited on pages 44, 74, and 77.

M. Randazzo and M. Tambasco. A rapid noninvasive characterization of CT x-ray sources. *Med. Phys.*, 42(7):3960–3968, 2015. Cited on pages 52 and 60.

V. Rebuffel and J. M. Dinten. Dual-energy X-ray imaging: Benefits and limits, 2007. Cited on page 41.

S. Richard and J. H. Siewerdsen. Optimization of dual-energy imaging systems using generalized NEQ and imaging task. *Med. Phys.*, 34(1):127–139, 2007. Cited on page 135.

D. S. Rigie and P. J. La Rivière. Optimizing spectral CT parameters for material classification tasks. *Phys. Med. Biol.*, 61:4599–4623, 2016. Cited on page 122.

S. Rit, G. Dedes, N. Freud, D. Sarrut, and J. M. Létang. Filtered backprojection proton CT reconstruction along most likely paths. *Med. Phys.*, 40(3):031103–1–9, feb 2013. Cited on page 150.

S. Rit, M. Vila Oliva, S. Brousmiche, R. Labarbe, D. Sarrut, and G. C. Sharp. The Reconstruction Toolkit (RTK), an open-source cone-beam CT reconstruction toolkit based on the Insight Toolkit (ITK). *J. Phys. Conf. Ser.*, 489:012079, 2014. Cited on pages 92, 94, 123, and 165.

S. Rit, R. Clackdoyle, P. Keuschnigg, and P. Steininger. Filtered-backprojection reconstruction for a cone-beam computed tomography scanner with independent source and detector rotations. *Med. Phys.*, 43(5):2344–2352, 2016. Cited on pages 51, 106, and 123.

R. Ritchie, R. Hamm, J. Turner, and H. Wright. The interaction of swift electrons with liquid water. In *Sixth Symp. Microdosim. Brussels, Belgium, May 22-26, 1978*, pages 345–354. Harwood Academic, 1978. Cited on page 147.

D. A. Roberts, V. N. Hansen, A. C. Niven, M. G. Thompson, J. Seco, and P. M. Evans. A low Z linac and flat panel imager: comparison with the conventional imaging approach. *Phys. Med. Biol.*, 53(22):6305–6319, 2008. Cited on page 56.

E. Roessl and R. Proksa. K-edge imaging in x-ray computed tomography using multi-bin photon counting detectors. *Phys. Med. Biol.*, 52(15):4679–4696, 2007. Cited on page 46.

B. Rombi, S. Vennarini, L. Vinante, D. Ravanelli, and M. Amichetti. Proton radiotherapy for pediatric tumors: review of first clinical results. *Ital. J. Pediatr.*, 40(1):74, 2014. Cited on pages XV, 17, and 18.

E.-P. Rührnschopf, K. Klingenbeck, and E.-P. Ru. A general framework and review of scatter correction methods in x-ray cone-beam computerized tomography . Part 1 : Scatter compensation approaches. *Med. Phys.*, 38(7):4296–4311, jun 2011. Cited on page 67.

R. A. Rutherford, B. R. Pullan, and I. Isherwood. Measurement of effective atomic number and electron density using an EMI scanner. *Neuroradiology*, 11(1):15–21, 1976. Cited on pages 35 and 43.

E.-P. Ruhrnschopf and and K. Klingenbeck. A general framework and review of scatter correction methods in cone beam CT. Part 2: Scatter estimation approaches. *Med. Phys.*, 38(9):5186, aug 2011. Cited on page 67.

J. R. Sabin, J. Oddershede, and S. P. A. Sauer. On the Determination of the Mean Excitation Energy of Water. *Adv. Quantum Chem.*, 65:63–77, 2013. Cited on page 147.

M. Saito. Dual-energy approach to contrast-enhanced mammography using the balanced filter method: spectral optimization and preliminary phantom measurement. *Med. Phys.*, 34(2007):4236–4246, 2007. Cited on page 122.

M. Saito. Potential of dual-energy subtraction for converting CT numbers to electron density based on a single linear relationship. *Med. Phys.*, 39(4):2021–2030, 2012. Cited on pages 43, 74, 76, 77, 91, and 93.

B. Schaffner and E. Pedroni. The precision of proton range calculations in proton radiotherapy treatment planning: experimental verification of the relation between CT-HU and proton stopping power. *Phys. Med. Biol.*, 43(6):1579–1592, jun 1998. Cited on pages 27, 29, 161, and 182.

B. Schaffner, E. Pedroni, and A. Lomax. Dose calculation models for proton treatment planning using a dynamic beam delivery system: an attempt to include density heterogeneity effects in the analytical dose calculation. *Phys. Med. Biol.*, 44(1):27–41, 1999. Cited on page 29.

J. P. Schlomka, E. Roessl, R. Dorscheid, S. Dill, G. Martens, T. Istel, C. Bäumer, C. Herrmann, R. Steadman, G. Zeitler, A. Livne, and R. Proksa. Experimental feasibility of multi-energy photon-counting K-edge imaging in pre-clinical computed tomography. *Phys. Med. Biol.*, 53(15):4031–4047, 2008. Cited on pages 41, 47, 92, 140, and 145.

M. A. Schmidt and G. S. Payne. Radiotherapy planning using MRI. *Phys. Med. Biol*, 60(22):R323–R361, 2015. Cited on page 21.

T. G. Schmidt, R. F. Barber, and E. Sidky. Experimental investigation of a one-step material decomposition algorithm for Spectral CT. In *Third Work. Med. Appl. Spectrosc. X-ray Detect.*, CERN, Switzerland, 2015. Cited on pages 48, 161, and 181.

U. Schneider, E. Pedroni, and A. Lomax. The calibration of CT Hounsfield units for radiotherapy treatment planning. *Phys. Med. Biol.*, 41:111–124, 1996. Cited on pages XV, 17, 25, 26, 27, 28, 44, 74, 77, 94, 123, 147, 153, and 154.

W. Schneider, T. Bortfeld, and W. Schlegel. Correlation between CT numbers and tissue parameters needed for Monte Carlo simulations of clinical dose distrions. *Phys Med Biol*, pages 459–478, 2000. Cited on pages 42, 148, and 172.

J. Schuemann, S. Dowdell, C. Grassberger, C. H. Min, and H. Paganetti. Site-specific range uncertainties caused by dose calculation algorithms for proton therapy. *Phys. Med. Biol.*, 59(15):4007–4031, 2014. Cited on page 30.

R. W. Schulte, S. N. Penfold, J. T. Tafas, and K. E. Schubert. A maximum likelihood proton path formalism for application in proton computed tomography. *Med. Phys.*, 35(11):4849–4856, oct 2008. Cited on page 150.

N. A. Shkumat, J. H. Siewerdsen, A. C. Dhanantwari, D. B. Williams, S. Richard, N. S. Paul, J. Yorkston, and R. Van Metter. Optimization of image acquisition techniques for dual-energy imaging. *Med Phys*, 10:3904–3915, 2007. Cited on pages 122 and 135.

E. Y. Sidky, L. Yu, X. Pan, Y. Zou, and M. Vannier. A robust method of x-ray source spectrum estimation from transmission measurements: Demonstrated on computer simulated, scatter-free transmission data. *J. Appl. Phys.*, 97(12), 2005. Cited on page 157.

E. Y. Sidky, T. Gilat-Schmidt, and X. Pan. Direct inversion of spectral CT data into a materials decomposition and the effect of multiple soft tissues. In *2014 IEEE Nucl. Sci. Symp. Med. Imaging Conf. NSS/MIC 2014*, pages 1–3. IEEE, nov 2016. Cited on pages 48, 161, and 181.

J. H. Siewerdsen and D. A. Jaffray. Cone-beam computed tomography with a flat-panel imager: magnitude and effects of x-ray scatter. *Med. Phys.*, 28(2):220–31, feb 2001. Cited on page 67.

J. H. Siewerdsen, M. J. Daly, B. Bakhtiar, D. J. Moseley, S. Richard, H. Keller, and D. A. Jaffray. A simple, direct method for x-ray scatter estimation and correction in digital radiography and cone-beam CT. *Med. Phys.*, 33(1):187–197, 2006. Cited on pages XVII, 67, 68, 69, and 102.

P. Sigmund, A. Schinner, and H. Paul. Errata and Addenda for ICRU Report 73 , Stopping of Ions Heavier than Helium. *J. ICRU*, 5(1):1–10, 2009. Cited on pages 30, 85, 94, 147, and 148.

J. M. Slater. From X-Rays to Ion Beams: A Short History of Radiation Therapy. In *Ion Beam Ther. Biol. Andm. Physics, Biomed. Eng. U. Linz*, volume 320, chapter 1, pages 3–16. Springer-Verlag, Berlin Heidelberg, 2012. Cited on pages 4, 6, 17, and 18.

F. Smekens, N. Freud, J. M. Létang, J.-F. Adam, C. Ferrero, H. Elleaume, A. Bravin, F. Estève, and D. Babot. Simulation of dose deposition in stereotactic synchrotron radiation therapy: a fast approach combining Monte Carlo and deterministic algorithms. *Phys. Med. Biol.*, 54(15):4671–4685, aug 2009. Cited on page 167.

F. Smekens, J. M. Létang, C. Noblet, S. Chiavassa, G. Delpon, N. Freud, S. Rit, and D. Sarrut. Split exponential track length estimator for Monte-Carlo simulations of small-animal radiation therapy. *Phys. Med. Biol.*, 59(24):7703–7715, dec 2014. Cited on page 167.

J. Soltani-Nabipour, D. Sardari, and G. H. Cata-Danil. Sensitivity of the Bragg peak curve to the average ionization potential of the stopping medium. *Rom. Reports Phys.*, 54(3-4):321–330, 2009. Cited on page 147.

A. Sossin, J. Tabary, V. Rebuffel, J.-M. Létang, N. Freud, L. Verger, and L. Verger. Influence of Scattering on Material Quantification Using Multi - Energy X - ray Imaging. In *Proc. IEEE Nucl. Sci. Symp. Med. Imaging Conf.*, number 1, pages 1–5, 2014. Cited on pages 67, 137, 160, and 181.

E. Spezi, P. Downes, E. Radu, R. Jarvis, and P. Downes. Monte Carlo simulation of an x-ray volume imaging cone beam CT unit Monte Carlo simulation of an x-ray volume imaging cone beam CT unit. *Med Phys*, 36(1):127–136, 2009. Cited on page 52.

J. Star-Lack, M. Sun, A. Kaestner, R. Hassanein, G. Virshup, T. Berkus, and M. Oelhafen. Efficient scatter correction using asymmetric kernels. *Proc. SPIE*, 7258(12): 72581–12, 2009. Cited on page 67.

J. Starman, J. Star-Lack, G. Virshup, E. Shapiro, and R. Fahrig. A nonlinear lag correction algorithm for a-Si flat-panel x-ray detectors. *Med. Phys.*, 39(10):6035–6047, 2012. Cited on page 54.

P. Stenner, T. Berkus, and M. Kachelrieß. Empirical Dual Energy Calibration (EDEC) for cone-beam computed tomography. *Med Phys*, 34(9):3630–3640, 2007. Cited on page 128.

R. Stone, J. Lawrence, and P. Aebersold. A Preliminary Report on the Use of Fast Neutrons in the Treatment of Malignant Disease 1. *Radiology*, 1940. Cited on page 6.

M. Sun and J. M. Star-Lack. Improved scatter correction using adaptive scatter kernel superposition. *Phys. Med. Biol.*, 55(22):6695–6720, 2010. Cited on page 67.

V. T. Taasti, J. B. B. Petersen, L. P. Muren, J. Thygesen, and D. C. Hansen. A robust empirical parametrization of proton stopping power using dual energy CT. *Med. Phys.*, 43(10):5547–5560, 2016. Cited on pages 74, 79, 91, 92, and 99.

K. Taguchi and J. S. Iwanczyk. Vision 20/20: Single photon counting x-ray detectors in medical imaging. *Med. Phys.*, 40(10):100901, 2013. Cited on page 40.

J. Thariat, J.-M. Hannoun-Levi, A. Sun Myint, T. Vuong, and J.-P. Gérard. Past, present, and future of radiotherapy for the benefit of patients. *Nat. Rev. Clin. Oncol.*, 10(1):52–60, 2012. Cited on pages 5 and 18.

R. S. Thing, U. Bernchou, E. Mainegra-Hing, and C. Brink. Patient-specific scatter correction in clinical cone beam computed tomography imaging made possible by the combination of Monte Carlo simulations and a ray tracing algorithm. *Acta Oncol.*, 52 (7):1477–83, 2013. Cited on page 71.

M. Torikoshi, T. Tsunoo, M. Sasaki, M. Endo, Y. Noda, Y. Ohno, T. Kohno, K. Hyodo, K. Uesugi, and N. Yagi. Electron density measurement with dual-energy x-ray CT using synchrotron radiation. *Phys. Med. Biol.*, 48(5):673–685, 2003. Cited on page 43.

J.-É. Tremblay, S. Bedwani, and H. Bouchard. A theoretical comparison of tissue parameter extraction methods for dual energy computed tomography. *Med. Phys.*, 41 (8):081905, 2014. Cited on pages 26, 44, 83, 90, 100, and 116.

H. Tsujii, J.-E. Mizoe, T. Kamada, M. Baba, S. Kato, H. Kato, H. Tsuji, S. Yamada, S. Yasuda, T. Ohno, T. Yanagi, A. Hasegawa, T. Sugawara, H. Ezawa, S. Kandatsu, K. Yoshikawa, R. Kishimoto, and T. Miyamoto. Overview of clinical experiences on carbon ion radiotherapy at NIRS. *Radiother. Oncol.*, 73, Supple:S41–S49, dec 2004. Cited on page 6.

J. K. Van Abbema, M.-j. V. Goethem, M. J. W. Greuter, A. V. D. Schaaf, S. Brandenburg, and E. R. V. D. Graaf. Relative electron density determination using a physics based parameterization of photon interactions in medical DECT. *Phys. Med. Biol.*, 60:3825–3846, 2015. Cited on pages 44, 74, and 77.

W. Van Elmpt, G. Landry, M. Das, and F. Verhaegen. Dual energy CT in radiotherapy: Current applications and future outlook. *Radiother. Oncol.*, 119(1):137–144, 2016. Cited on pages 41, 42, and 90.

D. Verellen, M. De Ridder, N. Linthout, K. Tournel, G. Soete, and S. G. Innovations in image-guided radiotherapy. *Nat Rev Cancer*, 7(12):949–960, dec 2007. Cited on page 32.

G. Vilches-Freixas, J.-M. Létang, K. Presich, P. Steininger, and S. Rit. Optimal dose balance between energy levels for material decomposition with dual-energy X-ray CT. *Radiother. Oncol.*, 115:S506–S507, 2015. Cited on page 135.

G. Vilches-Freixas, J. M. Létang, S. Brousmiche, E. Romero, M. Vila Oliva, H. Deutschmann, P. Keuschnigg, P. Steininger, and S. Rit. Technical Note : Procedure for the calibration and validation of kilo-voltage cone-beam CT models. *Med. Phys.*, 43:5199–5204, 2016a. Cited on pages 51, 83, 116, 125, 135, and 165.

G. Vilches-Freixas, J.-M. Létang, and S. Rit. Comparison of stopping power estimators-from dual-energy computed tomographyfor proton therapy. *Radiother. Oncol.*, 119(5): S869, 2016b. Cited on pages 81 and 100.

X. Wang, D. Meier, K. Taguchi, D. J. Wagenaar, B. E. Patt, and E. C. Frey. Material separation in x-ray CT with energy resolved photon-counting detectors. *Med. Phys.*, 38(3):1534–46, 2011. Cited on page 36.

D. R. White, H. Q. Woodard, and S. M. Hammond. Average soft-tissue and bone models for use in radiation dosimetry. *Br. J. Radiol.*, 60(804):907–913, 1987. Cited on pages XVII, 26, 77, 78, 81, and 148.

J. F. Williamson, S. Li, S. Devic, B. Whiting, and F. A. Lerma. On two-parameter models of photon cross sections: application to dual-energy CT imaging. *Med. Phys.*, 33(11):4115–4129, oct 2006. Cited on pages 44 and 81.

R. R. Wilson. Radiological Use of Fast Protons. *Radiology*, 47(5):487–491, nov 1946. Cited on page 6.

H. Q. Woodard and D. R. White. The composition of body tissues. *Br. J. Radiol.*, 59 (708):1209–18, 1986. Cited on pages 26, 81, and 148.

T. Xu, J. L. Ducote, J. T. Wong, and S. Molloi. Feasibility of real time dual-energy imaging based on a flat panel detector for coronary artery calcium quantification. *Med. Phys.*, 33(2006):1612–1622, 2006. Cited on page 121.

Y. Xue, R. Ruan, X. Hu, Y. Kuang, J. Wang, Y. Long, and T. Niu. Statistical image-domain multimaterial decomposition for dual-energy CT. *Med. Phys.*, 44(3):886–901, mar 2017. Cited on page 46.

M. Yang. *Dual energy computed tomography for proton therapy treatment planning*. PhD thesis, The University of Texas, 2011. Cited on page 100.

M. Yang, G. Virshup, J. Clayton, X. R. Zhu, R. Mohan, and L. Dong. Theoretical variance analysis of single- and dual-energy computed tomography methods for calculating proton stopping power ratios of biological tissues. *Phys. Med. Biol.*, 55(5): 1343–1362, 2010. Cited on pages XVII, 32, 74, 76, 77, 78, 81, 89, 100, 123, and 153.

M. Yang, X. R. Zhu, P. C. Park, U. Titt, R. Mohan, G. Virshup, J. E. Clayton, and L. Dong. Comprehensive analysis of proton range uncertainties related to patient stopping-power-ratio estimation using the stoichiometric calibration. *Phys. Med. Biol.*, 57(13):4095–4115, 2012. Cited on pages 17, 26, 29, 30, 74, and 147.

L. Yu, S. Leng, and C. H. McCollough. Dual-energy CT-based monochromatic imaging. *AJR. Am. J. Roentgenol.*, 199(5 Suppl):S9–S15, 2012. Cited on pages 41 and 80.

L. Yu, Z. Li, S. Leng, and C. H. McCollough. Dual-source multi-energy CT with triple or quadruple x-ray beams. In *Proc. SPIE Int. Soc. Opt. Eng.*, volume 9783, 2016. Cited on pages XVI and 40.

D. Zhang, X. Li, and B. Liu. Objective characterization of GE discovery CT750 HD scanner: gemstone spectral imaging mode. *Med. Phys.*, 38(3):1178–88, mar 2011. Cited on page 38.

R. Zhang, R. M. Howell, A. Giebeler, P. J. Taddei, A. Mahajan, and W. D. Newhauser. Comparison of risk of radiogenic second cancer following photon and proton craniospinal irradiation for a pediatric medulloblastoma patient. *Phys. Med. Biol.*, 58(4): 807–23, 2013. Cited on page 17.

J. Zhu and S. N. Penfold. Dosimetric comparison of stopping power calibration with dual-energy CT and single-energy CT in proton therapy treatment planning. *Med Phys*, 43(6):2845–2854, 2016. Cited on page 74.

L. Zhu, Y. Xie, J. Wang, and L. Xing. Scatter correction for cone-beam CT in radiation therapy. *Med. Phys.*, 36(6):2258–2268, 2009. Cited on page 66.

J. F. Ziegler. The Stopping of Energetic Light Ions in Elemental Matter. *J.Appl.Phys/Rev.Appl.Phys.*, 85(1999):1249–1272, 1999. Cited on page 9.

J. F. Ziegler, M. D. Ziegler, and J. P. Biersack. SRIM - The stopping and range of ions in matter (2010). *Nucl. Instruments Methods Phys. Res. Sect. B Beam Interact. with Mater. Atoms*, 268(11-12):1818–1823, 2010. Cited on page 153.

Y. Zou and M. D. Silver. Analysis of Fast kV-switching in Dual Energy CT using a Pre- reconstruction Decomposition Technique. In J. Hsieh and E. Samei, editors, *Proc. SPIE, Med. Imaging Phys. Med. Imaging*, volume 6913, pages 691313–1–12. International Society for Optics and Photonics, mar 2008. Cited on page 38.